Dissertation
submitted to the
Combined Faculties for the Natural Sciences and for Mathematics
of the Ruperto-Carola University of
Heidelberg, Germany
for the degree of
Doctor of Natural Sciences

presented by

Diplom-Physicist: **Sven Krohn**
born in: Saarbrücken

Oral examination: 14th November, 2001

Inelastic collisions and recombination between electrons and molecular ions

Referees: **Prof. Dr. Andreas Wolf**
Prof. Dr. Frank Arnold

Kurzfassung

Inelastische Kollisionen und Rekombination zwischen Elektronen und Molekülionen

Inelastische Kollisionen zwischen Molekülionen und langsamen Elektronen spielen eine wichtige Rolle in natürlich vorkommenden ionisierten Umgebungen und schließen interessante Wechselwirkungsmechanismen mit ein, die auch Gegenstand intensiver theoretischer Studien sind. Am Schwerionenspeicherring TSR des Max-Planck-Instituts für Kernphysik wurden verschiedene Experimente zur Untersuchung von Kollisionen kleiner Molekülionen mit langsamen Elektronen durchgeführt. Mit Hilfe des Coulomb-Explosion-Imagings war es möglich, die Vibrationskühlung der gespeicherten homonuklearen Molekülionen H_2^+ und D_2^+ direkt zu beobachten und es konnte gezeigt werden, dass die Kühlung auf super-elastische Kollisionen (SEC) zurückzuführen ist, bei denen interne Anregungsenergie auf das gestreute Elektron übertragen wird. Dieser Prozess ist eng verwandt mit der dissoziative Rekombination (DR). Für die unteren Vibrationszustände von H_2^+ und D_2^+ wurden erstmals absolute DR und SEC Ratenkoeffizienten gemessen. Die Bestimmung der atomaren Endzustände in der DR von LiH^+ und $^4HeH^+$ mit langsamen Elektronen war Gegenstand weiterer Experimente. Die elektronische Struktur von LiH, ^4HeH und ihrer Ionen ist derart, dass DR nur durch eine nicht-adiabatische Kopplung der Elektron- und Kernbewegung bei kleine Atomabständen stattfinden kann. Die Experimente zeigten die bevorzugte Bevölkerung der höchsten, bei diesen Reaktionen energetisch erreichbaren atomaren Endzustände. Des weiteren wurde der absolute Ratenkoeffizient für die DR von LiH^+ Ionen mit langsamen Elektronen gemessen.

Abstract

Inelastic collisions and recombination between electrons and molecular ions

Inelastic collisions between molecular ions and slow electrons play an important role in naturally occurring ionized media and involve interesting interaction mechanisms which are also under intense theoretical study. Several experiments focused on the collision of small molecular ions with electrons were carried out at the heavy-ion storage ring TSR, located at the Max-Planck-Institut für Kernphysik, Heidelberg. Using the Coulomb explosion imaging technique it was possible to monitor vibrational cooling of the stored homonuclear molecular ions H_2^+ and D_2^+ and it could be shown that the cooling is only due to the interaction of electrons with the molecular ions in super-elastic collisions (SEC) where internal energy is transferred to the scattered electron. This process is closely related to dissociative recombination (DR). For the DR and SEC of H_2^+ and D_2^+ ions with near-zero kinetic energy electrons absolute vibrational state specific rate coefficients were measured for the first time. Another series of experiments was focused on the investigation of final fragment states in the DR of LiH^+ and $^4HeH^+$. The electronic structure of these ions and the corresponding neutral molecules is such that DR proceeds via a non-adiabatic coupling of electronic and vibrational motion at short internuclear distances. The experiments revealed a dominant population of the highest energetically accessible final fragment states in such reactions. In addition, also the absolute rate coefficient for the DR of LiH^+ molecules with slow electrons was measured.

Für meine Eltern

Contents

1. Introduction

The understanding of the dynamics both of highly excited and of internally cold molecular systems in collisions with electrons is an active field of research in basic molecular physics and also of importance in various natural environments, such as astrophysical plasmas. An example for an astrophysical plasma finding great interest is the primordial gas - the state of matter before the formation of the first stars - where the positively charged diatomic molecular ions H_2^+ , HD^+ , LiH^+ and $^4HeH^+$ were abundant. In the early universe, these molecular ions played an important role in the formation of the first generation of galaxies and stars after the Big-Bang[1, 2].
In consequence of the expansion the primordial gas cooled off and photoionization of atoms became gradually ineffective. This led to an increased abundance of neutral atoms (e.g. H, He and Li), formed by radiative recombinations with electrons. In a next step various small molecular ions were created in radiative association processes and the radiative cooling of these ions, such as LiH^+ and $^4HeH^+$, resulted in an additional cooling of the primordial gas, due to the transformation of translational energy of the atoms into radiation. This additional cooling gave rise to the gravitational collapse of the primordial clouds and the formation of a first generation of stars. The understanding of the processes that took place in primordial clouds requires detailed knowledge about not only the formation but also the depletion mechanism of the molecular ions. In the cooling primordial gas photodissociation became of less importance and dynamics of electron-ion collision processes started to play a relevant role. The dominant destruction process was the dissociative recombination (DR) of the molecular ions with electrons. The DR cross section is therefore of particular interest for the modeling of the molecular abundances in the primordial gas[2].
The most abundant molecular ion in the primordial gas, H_2^+ , has DR rate coefficients strongly dependent on the vibrational excitation ($\alpha_{DR} \approx 1 - 10 \times 10^{-8}\,\mathrm{cm}^3/\mathrm{s}$, for the lower vibrational states), as will be shown in Chapter 5.
Because homonuclear diatomic molecules, such as H_2^+ , do not cool radiatively due to a missing dipole moment (lifetime for quadrupole transitions is of the order of 10^6 s[3]), the vibrational excitation of the H_2^+ molecules has to be taken into account in the models. But, as will be shown in Chapter 5, recombination of an H_2^+ (or D_2^+) molecule with slow electrons does not always lead to dissociation. The formed neutral hydrogen molecules can autoionize (inverse recombination process) again. This scattering process is called super-elastic collision (SEC) if internal excitation

energy is transferred to the escaping electron. The electron induced vibrational de-excitation (SEC) of H_2^+ (D_2^+) turned out to be the dominant process after the recombination with cross sections between one and two orders of magnitude larger than that for DR (see Chapter 5). Part of this work was focused on the detailed understanding of the two competing processes, DR and SEC.

The heteronuclear diatomic molecular ions $^4HeH^+$ and LiH^+, which were also abundant in the primordial gas, relax vibrationally on a time scale between milliseconds and seconds. Thus, the DR rate coefficient for the vibrational ground state is most important. While the DR rate coefficient for $^4HeH^+$ in the vibrational ground state has been already measured[4], the absolute DR rate coefficient for LiH^+ in collisions with zero kinetic energy electrons was determined for the first time in this work.

Besides the importance of the DR rate coefficients for astrophysical models, the different processes are also of interest from a more fundamental point of view. There are basically two different models DR is thought to proceed through, the so-called crossing and non-crossing mode DR. In the crossing mode DR, a doubly excited potential curve of the neutral molecule is intersecting the potential curve of the ground electronic state of the molecular ion (typically close to the vibrational ground state), whereas in the non-crossing mode DR there is no such curve crossing. In the non-crossing mode DR a coupling of the electron and nuclear motion is needed, whereas the crossing mode DR can go by a pure electronic transition (see Sec. 2.1). The DR of hydrogen molecular ions is a prominent example for the crossing-mode, whereas the DR of $^4HeH^+$ and LiH^+ are examples for the non-crossing mode. Experimental studies of the latter type of DR at the TSR, performed in the present work, concentrated on the question how the energetically accessible final atomic fragment states are populated. This question is approached in this thesis for $^4HeH^+$ using an established technique based on imaging of the DR fragments and for LiH^+ using a novel method of analyzing the field ionization of the Li fragments (see Chapter 3).

The different processes discussed above can be investigated under well controlled conditions by storing fast ($v/c \approx 2 - 3\,\%$) molecular ion beams in the heavy-ion storage ring TSR. The usage of storage rings for DR measurements, starting about ten years ago, has improved greatly the understanding of the recombination processes between electrons and molecular ions. Storage rings have two principal advantages. Firstly, infrared-active ions can be stored and cooled vibrationally by spontaneous emission of radiation. Secondly, the molecular ion beam can be merged with an intense and cold electron beam in the so-called electron cooler. The electron velocity and therefore the collision energy can easily be varied by changing the acceleration voltage, which allows for the investigation of the energy dependence of the DR process. The merged beam geometry allows for an efficient detection of the recombination products.

This present thesis is structured as follows: In Chapter 2 the different mechanisms of DR and SEC of diatomic molecular ions with electrons are briefly discussed. Additionally some properties of the studied molecular ions are summarized. The experimental principles used to study the properties of DR and SEC, namely the Coulomb explosion imaging (CEI) and the recombination fragment imaging (RFI), are introduced in Chapter 3. The experimental apparatus, such as the used ion sources, the storage ring TSR together with the electron cooler and the CEI and RFI setups are discussed in Chapter 4. First experimental results on the absolute DR rate coefficient for the vibrational ground state and higher vibrational states of H_2^+ and D_2^+ are discussed in Chapter 5. Furthermore, first absolute SEC rate coefficients for the lower vibrational states of these molecular ions are presented. A comparison of the DR and SEC rate coefficients reveals the dominance of the autoionization with respect to the dissociation which was up to now thought to play a minor role in the recombination of hydrogen molecular ions with electrons.

Final state measurements for the DR of $^4HeH^+$ and LiH^+ , following the so-called non-crossing mode DR and a first measurement of the absolute DR rate coefficient of LiH^+ are described in detail in Chapter 6. For both molecular ions the dominant population of the highest possible final fragment states was observed which might be a peculiarity of the non-crossing mode DR.

2. Electron collision processes of small molecular ions

2.1 Dissociative recombination

Dissociative recombination (DR) of a diatomic molecular ion AB^+ with an electron is described by the following process

$$\mathrm{AB}^+(vJ) + e^- \longrightarrow \mathrm{A}(nl) + \mathrm{B}(n'l'), \tag{2.1}$$

where vJ is the initial ro-vibrational state of the molecular ion and nl and $n'l'$ are the final states of the fragments A and B, respectively.

For molecules with an electronic configuration where a doubly excited electronic state of the neutral molecule crosses the ground electronic state of the ion, DR can proceed via two different paths. The basic DR process is described by a di-electronic recombination in which the incident electron gets captured into the doubly excited neutral state. This so-called *direct* DR is a pure electronic process and the coupling is described by the electronic Hamilton operator $\mathbf{H}_e(r, R)$ (Eq. A.6). In a second possible DR process, often referred to as *indirect* DR, the incoming electron gets first captured into a neutral vibrationally excited Rydberg state which is then predissociated by the doubly excited state. The recombination in the indirect DR is driven by the nuclear kinetic energy operator $\mathbf{T}_N$ (see Eq. A.13) and the transformation of the kinetic energy of the incident electron to the nuclear motion of the molecule. This non-Born-Oppenheimer recombination process is competing with the direct recombination into the doubly excited neutral state.

The DR mechanism for molecular ions which lack a doubly excited neutral state crossing their ground electronic state occurs via a nonadiabatic coupling to one of the neutral molecular Rydberg states at short internuclear distances. As in the indirect process, the recombination in driven by the nuclear kinetic energy operator $\mathbf{T}_N$.

The different DR processes mentioned above are discussed in more detail in this section.

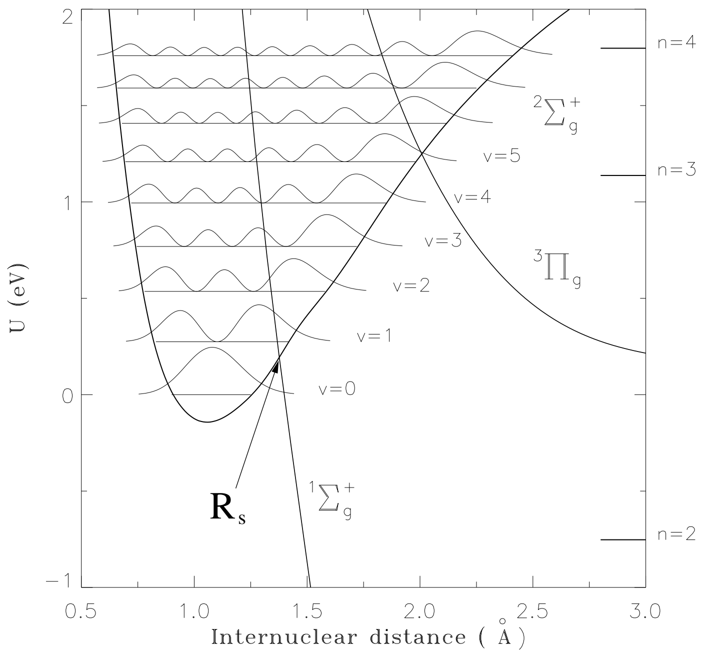

Figure 2.1: *The ground electronic state $^2\Sigma_g^+$ of H_2^+ [5] and the doubly excited $^1\Sigma_g^+$ dissociative state [6] of H_2. Additionally shown is another doubly excited state belonging to the Q_1 series and the nuclear wavefunctions squared $|\chi_v(R)|^2$ $(J = 0)$. The final fragment state energies of the excited atomic hydrogen $(n = 2 - 4)$ are depicted on the right.*

2.1.1 DR with curve crossing: basic and resonant processes

Basic DR process

The so-called direct DR is a dielectronic process in which an electron gets captured into a repulsive, doubly excited resonant state followed by the dissociation of the neutral molecule. This process has been first explained by Bates [7]. The hydrogen molecular ion is an example for a system with a doubly excited state crossing the electronic ground state of the ion, see Fig. 2.1. The direct DR of H_2^+ is described schematically by:

$$\mathrm{H}_2^+ + e^- \longrightarrow \mathrm{H_2}^{**} \longrightarrow \mathrm{H} + \mathrm{H}. \tag{2.2}$$

The doubly excited state has a $(2\pi\sigma_u)^2$ configuration.

In competition to the dissociation an electron can be emitted again through autoionization, the reverse electron capture process. Due to the vanishing electronic coupling between the doubly excited neutral state and the ionic state at distances larger than the separation at which both curves cross (denoted by R_S in Fig. 2.1), autoionization is becoming unlikely.

A classical formalism describing the direct DR was discussed by Bardsley and Biondi [8] and will be only briefly reviewed.

The DR cross section σ_{DR} as a function of the collision energy is often expressed as a product of the cross section for the electron capture σ_{cap} and the probability for the dissociation to occur (i.e. the complement of the autoionization probability), which is often called *survival factor*

$S(E)$[1]

$$\sigma_{DR}(E) = \sigma_{cap}(E)\, S(E). \tag{2.3}$$

The survival factor, as a function of the internuclear separation, was estimated by Bardsley [9] assuming a classical trajectory $R(t)$ for the dissociating atomic fragments to

$$S(R) = exp\left(-\int \frac{1}{\tau(R(t))}dt\right), \tag{2.4}$$

where $\tau(R)$ is the autoionization lifetime τ. In a classical picture recombination with electrons at a collision energy E can only occur at an internuclear distance R_c where the vertical transition energy to the doubly excited state is identical with the collision energy E. The autoionization lifetime is proportional to the inverse capture width $\Gamma(R)$ and can be written as [8]

$$\tau(R) = \frac{\hbar}{\Gamma(R)} = \frac{\hbar}{2\pi|\mathcal{V}(R)|^2} \tag{2.5}$$

with

$$\mathcal{V}(R) = \langle\, \Phi_{AB}(r,R) \,|\, \mathbf{H_e}(\mathbf{r},\mathbf{R}) \,|\, \Phi_{AB^+}(r,R)\phi(r)\,\rangle\,, \tag{2.6}$$

where $\mathbf{H_e}(\mathbf{r},\mathbf{R})$ denotes the electronic Hamilton operator (Eq. A.6), describing the interaction between the electronic state of the ion $\Phi_{AB^+}(r,R)$ and the free electron $\phi(r)$ and the electronic state of the neutral molecule $\Phi_{AB}(r,R)$. Using Eq. 2.5, the survival factor can be written as

$$S(R) = exp\left(-\frac{1}{\hbar}\int_{R_c}^{R_s} \frac{\Gamma(R)}{v(R_c,R_s)}dR\right), \tag{2.7}$$

where R_c denotes the internuclear separation at which the recombination occurred, R_s (see Fig. 2.1) the distance at which the doubly excited neutral state of the molecule crosses the electronic ground state of the molecular ion and $v(R_c,R_s)$ the velocity of the dissociating fragments. The cross section σ_{cap} for the electron capture is expressed by [8]

$$\sigma_{cap}(E) = \frac{\pi^2\hbar^2}{2m_eE}\left(\frac{g_n}{g_i}\right)|\chi_i(R_c)|^2\Gamma(R_c)\left|\frac{dV_i}{dR}\right|^{-1}, \tag{2.8}$$

where g_i and g_n are the multiplicities of the electronic states of the molecular ion and the neutral molecule, respectively, V_i the electronic potential curve of the ion and $\chi_i(R)$ the nuclear wavefunction of the molecular ion.

Influence of resonances on DR

The indirect DR, first proposed by Bardsley [10], is a resonant three-stage process in which a free electron is first captured into a vibrationally excited neutral molecular Rydberg state followed

---

[1] This assumption cannot be fully justified but is very useful for a qualitative description of the DR process, see Bardsley [9].

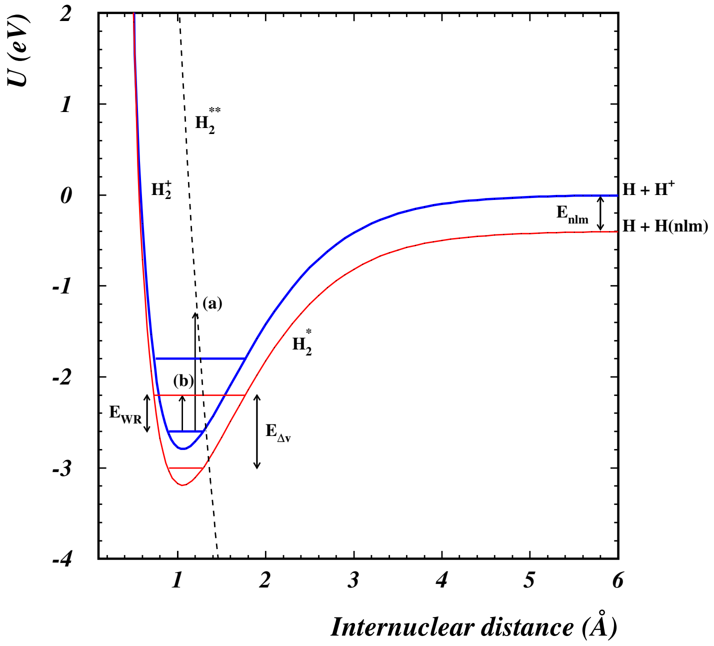

Figure 2.2: *Schematic drawing of the ground electronic state of H_2^+, the lowest doubly excited neutral state of H_2 and a Rydberg state of H_2. The recombination processes in the direct and indirect DR are marked by (a) and (b), respectively.*

by a radiationless transition (predissociation) to the repulsive, doubly excited state. Indirect DR is a non-Born-Oppenheimer process in which the energy of the incoming electron is transferred to the nuclear motion of an H_2 Rydberg state. The Rydberg states $(1s\sigma_g nlm)$ are converging to the ground electronic state of H_2^+ $(1s\sigma_g)$. The indirect DR of H_2^+ is described by

$$H_2^+(v) + e^- \longrightarrow H_2{}^*(v') \longrightarrow H_2{}^{**} \longrightarrow H + H. \tag{2.9}$$

Due to the discrete ro-vibrational energy spectra of the neutral Rydberg states indirect DR is a resonant process. Some Rydberg states are strongly coupled to the dissociation continuum and have a short autoionization lifetime [11, 12]. The interference between direct and indirect DR leads to so-called window resonances in the total DR cross section which are mostly destructive, i.e. they lower the DR cross section. In the multichannel quantum defect theory (MQDT) approach to DR [11] these interferences are included and it has been shown that the cross section near window resonances takes the form of a peak, a dip or a Fano profile [13], depending on the relative magnitudes of the direct recombination matrix elements and the matrix elements for the interaction of the Rydberg state with the electron ion continuum (autoionization) and with the dissociative state (DR) [14].

The potential curves of higher neutral Rydberg states $(1s\sigma_g nlm)$ are described in a good approximation by the ground electronic state of H_2^+ $(1s\sigma_g)$, shifted by the binding energy E_{nlm} of the atomic Rydberg state (nlm). The energy position E_{WR} of a window resonance in the DR cross section for a vibrational excitation Δv can therefore be estimated, neglecting rotational excitation, to

$$E_{WR} = E_{\Delta v} - E_{nlm}, \tag{2.10}$$

where $E_{\Delta v}$ denotes the vibrational level spacing, see Fig. 2.2.

2.1.2 Non-crossing mode DR

For molecules that lack a doubly excited state crossing the ionic potential curve one would expect the DR cross section to be small. The molecular ions LiH$^+$, ^{4}HeH$^+$ and H$_3^+$ are examples for such molecules. However, experimental studies of the DR of these molecular ion at ion storage rings yielded high rate coefficients, $\alpha \approx 7 \times 10^{-9}\,\mathrm{cm}^3/\mathrm{s}$ for ^{4}HeH$^+$ [4], $\alpha \approx 6 \times 10^{-7}\,\mathrm{cm}^3/\mathrm{s}$ for LiH$^+$ [15] (see Sec. 6.1.2) and $\alpha \approx 1 \times 10^{-7}\,\mathrm{cm}^3/\mathrm{s}$ for H$_3^+$ [16, 17], as compared to e.g. $\alpha \approx 2 \times 10^{-8}\,\mathrm{cm}^3/\mathrm{s}$ for H$_2^+$ (see Chapter 5).

For the studied molecular ion ^{4}HeH$^+$ (see Sec. 6.2) two theoretical calculations, based on $R-$matrix theory and MQDT by Sarpal, Tennyson and Morgan [18] and Guberman [19], respectively, were performed and a reasonable agreement with the experimental results was obtained. Both calculations assumed that at short internuclear separations a nonadiabatic coupling exists between the ground electronic state of ^{4}HeH$^+$ (plus a free electron) and the neutral Rydberg states of ^{4}HeH. Both theories described the DR with the same mechanism but predicted the population of different final fragment states. The dominant dissociation routes are $X^2\Sigma^+$ and $C^2\Sigma^+$ in the calculations by Sarpal *et al.* and Guberman, respectively. The $C^2\Sigma^+$ state is connected to H($n = 2$) + He($2s^2$) which has been experimentally shown to be the dominant process, see Sec. 6.2 and references therein. The MQDT calculations for the DR of ^{4}HeH$^+$ by Guberman will therefore be briefly discussed.

The coupling matrix element describing the capture into a Rydberg state with an effective principal quantum number n^* is given by a matrix element over the total Hamiltonian (Eq. A.2). The matrix element over the electronic ($\mathbf{H}_e$) and the nuclear-nuclear ($\mathbf{V}_N$) Hamiltonian vanishes and the matrix element over the nuclear kinetic energy operator $\mathbf{T}_N^v$ (Eq. A.13) is given by [20]

$$T_{v,d} = \rho^{1/2} \left\langle \psi_d^{n^*} \chi_d^{n^*} \left| \mathbf{T}_N^v \right| \psi_v^{l,k} \chi_v \right\rangle, \tag{2.11}$$

where ρ denotes the density of states. The dissociative and ion wavefunctions are labeled d and v, respectively, and ψ and χ describe the many-electron and vibrational wavefunctions, respectively. $\psi_v^{l,k}$ includes the free electron orbital and the angular momentum and the wavenumber of the electron are denoted by the label l and k, respectively. The matrix element $T_{v,d}$ falls off as $(1/n^*)^{3/2}$ [20].

The “direct” DR cross section (i.e. the one not involving any Rydberg resonances similar to those depicted in Fig. 2.2) for an ion in a vibrational level v is given by [11]

$$\sigma_v = \frac{\pi}{2k^2} \left(\frac{g_n}{g_i} \right) \frac{4\pi^2 T_{v,d}^2}{\left(1 + \sum_{v'} \pi^2 T_{v',d}^2 \right)^2}, \tag{2.12}$$

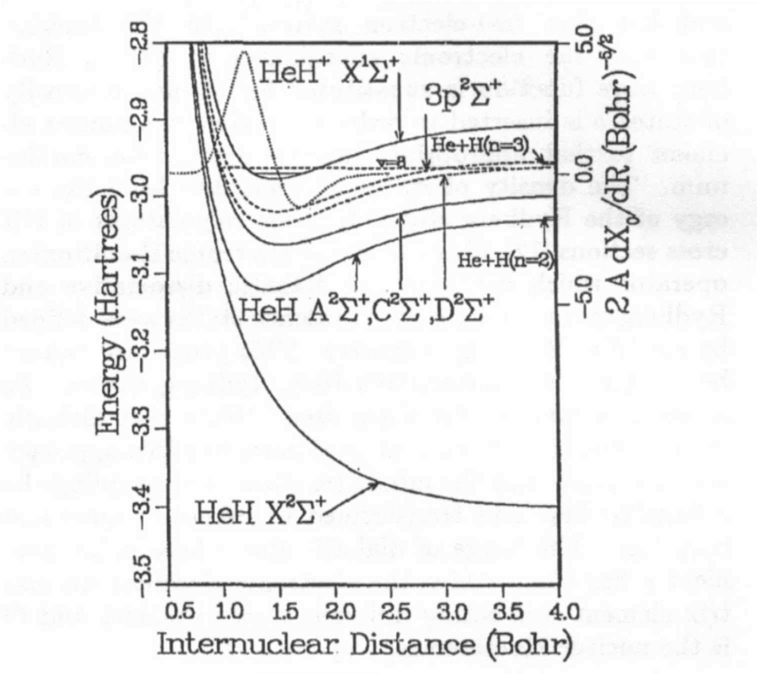

Figure 2.3: *The calculated HeH dissociative potential-energy curves (solid lines), the $n = 3$ Rydberg states (dashed lines), and the HeH$^+$ ground state (slid line) with the $v = 0$ level are shown. The $v = 8$ resonance level of the $D^2\Sigma^+$ state is shown as the dashed line. The dotted line shows the product, $2A(R)d\chi_0/dR$, with its ordinate axis on the right. Plot taken from Ref. [19].*

where k is the wavenumber of the incident electron, g_n and g_i are the statistical weights of the neutral and ion state, respectively and v' is an index running over the energetically open ion vibrational levels as final states of autoionization. The interaction matrix element

$$\langle \psi_d \chi_d | \mathbf{T}_N^v | \psi_v \chi_v \rangle \tag{2.13}$$

can be written as

$$-\frac{\hbar^2}{2\mu} \left\langle \chi_d \middle| B(R) + 2A(R)\frac{\partial}{\partial R} \middle| \chi_v \right\rangle , \tag{2.14}$$

with

$$B(R) = \left\langle \psi_d \middle| \frac{\partial^2}{\partial R^2} \middle| \psi_v \right\rangle \tag{2.15}$$

and

$$A(R) = \left\langle \psi_d \middle| \frac{\partial}{\partial R} \middle| \psi_v \right\rangle . \tag{2.16}$$

S. Guberman [19] showed that the second term in Eq. 2.14 is large at small internuclear distances (see Fig. 2.3 from Ref. [19]). Thus, the term $A(R)$ is non-negligible and the Born-Oppenheimer approximation (Sec. A.1) is not valid at these internuclear distances.

For ^{4}HeH$^+$ there are presently no further calculations available for the partial DR cross section of energetically accessible dissociation paths at larger collision energies.

For the second studied molecular ion, LiH^+ (see Sec. 6.1.2), no such calculations are presently available. As will be discussed in Sec. 2.3.3, LiH^+ is a weakly bound molecule. Thus, DR of LiH^+ in the vibrational ground state with low kinetic energy electron can proceed via a various number of neutral Rydberg states, see Fig. 6.2 (Sec. 6.1.3). Applying the scaling law for the coupling matrix element $T_{v,d} \propto (1/n^*)^{3/2}$, DR is expected to proceed via the lower neutral Rydberg states. In Sec. 6.1 an experiment studying the final fragment states in the DR of LiH^+ with zero kinetic energy electrons is discussed and it will be shown, that the coupling to the highest energetically accessible neutral Rydberg states is stronger than the coupling to lower lying Rydberg states which is contradictory to the predicted results using the scaling law discussed before.

2.2 Super-elastic collisions

The homonuclear isotopomers of the hydrogen molecular ion do not possess a dipole moment which is needed for a radiative cooling. Thus, storing of such an ion in a storage ring is expected to be insufficient for obtaining internally cold molecules. But, vibrational cooling of the homonuclear hydrogen molecules H_2^+ and D_2^+ has been observed in several experiments at different storage rings in the past [21, 22]. The cooling mechanism was ascribed to different processes. M. Larsson *et al.* [21] claimed collisions with the residual rest gas for the observed removal of vibrational excitation in D_2^+ , whereas W. van der Zande *et al.* [22] assigned the observed vibrational cooling of H_2^+ to electron-ion collisions in the electron cooler and conjecture vibrational state specific DR rate coefficients being responsible for the cooling. Another possible cooling mechanism, the channel of super-elastic collisions (SEC) of electrons with vibrationally excited molecular ions, was ruled out as an efficient cooling process. This conclusion was based on the results of calculations of the SEC rate coefficients by Sarpal and Tennyson [23] and Nakashima *et al.* [24]. For collisions with low kinetic energy electrons SECs are described by

$$\begin{array}{ccc} \mathrm{H_2}^+(v) + e^-(E) \;\longrightarrow\; \mathrm{H_2}^+(v') \;+\; e^-(E+\Delta E) & , \\ (v' < v, \Delta E > 0) & , \end{array} \tag{2.17}$$

where a part of the internal excitation energy of the molecule (ro-vibrational excitation) is transferred to the scattered electron by autoionization of the doubly excited intermediate state H_2^{**} (see Eq. 2.2). Experimental evidence for SEC was found by Tanabe *et al.* [25] in DR experiments with H_2^+ ions and Saito *et al.* [26] with H_2^+ and D_2^+ ions. First SEC rate coefficients for the lower vibrational states were obtained from vibrational population measurements presented in Sec. 5.4 of this thesis (see also Krohn *et al.* [27]) and estimated by to be of the order of (1-4) $\times 10^{-6}\ \mathrm{cm^3 s^{-1}}$ and therefore about an order of magnitude larger than calculated values [23, 24]. A detailed study of SEC processes within the present work, giving experimental values for the SEC rate coefficients, is discribed in Chapter 5.

2.3 Some properties of the studied molecular ions

2.3.1 H_2^+ and its isotopomers

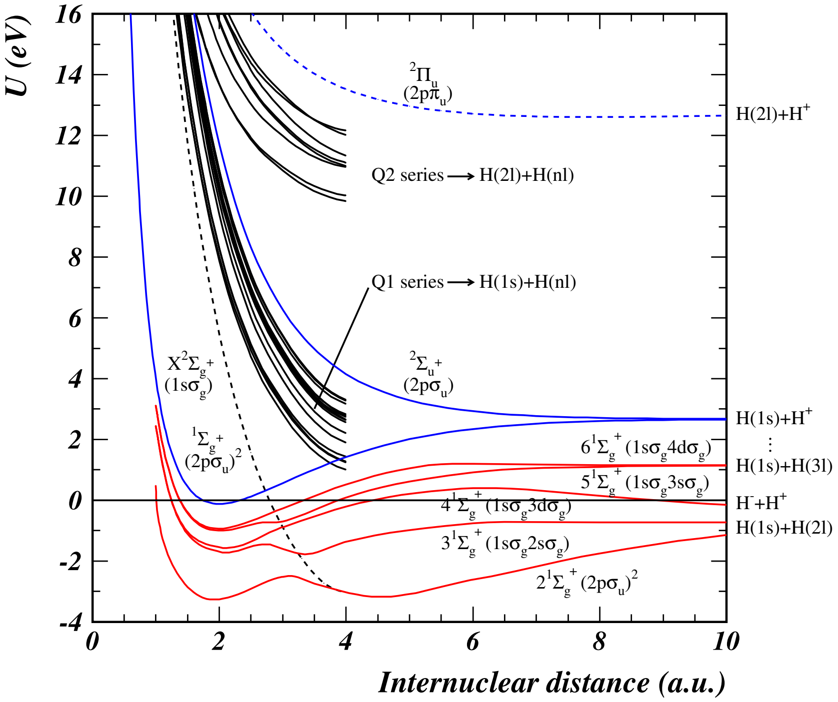

Figure 2.4: *Potential energy curves of H_2^+ and H_2. Solid blue lines: adiabatic curves of the two lowest ionic states, calculated for HD^+ in Ref. [28]. Dashed blue curve: Born-Oppenheimer curve of the second excited ionic state [29]. Solid red curves: adiabatic curves of the lowest excited bound states of H_2 [30], showing avoided crossing with the lowest Q_1 curve (dashed black line) [6, 31]. Solid black lines: states from the antibonding Q_1 and Q_2 series [6]. To the right, the atomic fragment states are noted.*

H_2^+ is the simplest diatomic molecular ion and therefore often used to compare theoretical models with experimental results. The electronic structure is identical for all its isotopomers. In Fig. 2.4 the $(1s\sigma_g)^2\Sigma_g^+$ and $(2p\sigma_u)^2\Sigma_u^+$ potential energy curves of H_2^+ [5] are plotted together with the two series of doubly excited neutral states [6], often referred to as Q_1 and Q_2 series. The doubly excited neutral states play an important role in the direct and indirect DR, as discussed in Sec.2.1.1. The ro-vibrational energy levels structures are different for all isotopomers due to their reduced masses, see Eq. A.14. The dissociation energies from the vibrational ground state range from $E_d \approx 2.65\,\text{eV}$ to $E_d \approx 2.70\,\text{eV}$ (Sec. B.2, Tab. B.2) for H_2^+, HD^+ and D_2^+. The binding length is $R_e \approx 1.06\,\text{Å}$ [32] for all isotopomers. There is a principal difference between HD^+ on one hand and H_2^+ and D_2^+ on the other. The heteronuclear molecule HD^+ possesses a dipole moment. The radiative relaxation times for ro-vibrational transitions are between 10 ms and 60 ms [33] and a complete cooling into the vibrational ground state has been observed after about 500 ms of storage [34]. The homonuclear diatomic ions H_2^+ and D_2^+ lack such a dipole moment and the radiative lifetimes for quadrupol transitions are of the order of 10^6 s [3]. These lifetimes are much too long to observe ro-vibrational cooling in storage ring experiments.

Thus, first experiments investigating the DR of the molecular hydrogen ion at heavy-ion storage rings have been performed at vibrationally cold HD^+. A first DR cross section measurement for HD^+ has been carried out at the TSR [35, 36]. In the following years the DR cross section of HD^+ has also been measured at other storage rings, such as CRYRING [37], Sweden, and TARN II [38], Japan. Further studies of the DR of HD^+ in Heidelberg were focused on the investigation of the branching ratio into the final fragment states at different collision energies [39, 31], vibrational state specific DR rate coefficients [40] and the threshold structure of the DR cross section at the opening of additional final fragment states [41].

Experimental studies of the dependence of the DR cross section of H_2^+ on the vibrational population have been carried out at the storage rings CRYRING [22], Stockholm, and ASTRID [42, 43], Aarhus. In the experiment at the ASTRID storage ring the population of the higher vibrational states has been reduced by photodissociation of these states, whereas the higher vibrational states have been depeleted in the CRYRING experiments by electron-ion collisions. In both experiments a lower DR cross section for the vibrationally colder H_2^+ ion beams [22, 42, 43] has been measured.

2.3.2 The helium hydride ion: $^4HeH^+$

The helium hydride ion $^4HeH^+$ has a binding length of $R_e = 0.774\,\text{Å}$ [44]. The dissociation energy for the vibrational ground state amounts to $E_D \approx 1.85\,\text{eV}$ (Append. D.1). Some additional spectroscopic data are summarized in Append. D.1. In Fig. 2.5 the potential energy curves for the $X^1\Sigma^+$ ground electronic state of $^4HeH^+$ and for some excited electronic states are shown. The calculations were performed by A. Orel *et al.* [45]. Additionally plotted are some important singly excited Rydberg states and a series of doubly excited states of the neutral ^4HeH molecule [45]. HeH is an excimer, i.e. the $X^2\Sigma^+$ ground state potential is repulsive and the excited states are bound (Fig. 2.5). All doubly excited states of HeH are energetically several eV higher than the electronic ground state of $^4HeH^+$. $^4HeH^+$ is therefore an example for a molecular ion which recombines with slow electrons via a non-crossing process [19].

Due to the short radiative lifetimes of ro-vibrational transitions (Append. D.2), $^4HeH^+$ cools vibrationally into its ground state on a time scale of several ms, which is short compared to typical storage times in the TSR of up to about a minute. DR of a vibrationally cold $^4HeH^+$ ion with zero kinetic energy electrons has two possible final fragment channels, $\mathrm{He}(1s^2) + \mathrm{H}(1\mathrm{s})$ and $\mathrm{He}(1s^2) + \mathrm{H}(2\mathrm{l})$. The next higher fragment state (i.e. $\mathrm{He}(1s^2) + \mathrm{H}(3\mathrm{l})$) opens at a collision energy $E = 333\,\mathrm{meV}$.

Radiative cooling of ^{4}HeH$^+$ ions in a Planck radiation field

The temperatures in ion sources are typically a few hundreds of Kelvin. The ions produced in these sources are therefore rotationally and vibrationally excited when injected in the storage ring. The rotational and vibrational cooling of stored polar molecules into a thermal equilibrium at 300 K, according to the ring temperature, occurs via emission and absorption of radiation. The spontaneous and stimulated emission are responsible for cooling and the absorption for heading. The coefficients describing these three processes are commonly known as the Einstein coefficients [32].

For several experiments performed at storage rings it is important to know if an ion beam can get into a thermal equilibrium with the environment while stored in the ring, e.g. cooling of stored CH$^+$ [46]. A simple model can be used to simulate the cooling of an ensemble of stored ions in a radiation field corresponding to a temperature of $T = 300\,\mathrm{K}$ [47, 48].

The ^{4}HeH$^+$ molecule cools within several ms in its vibrational groundstate, see Tab. D.3 for the radiative lifetimes of the lower vibrational states. Therefore only the time needed for rotational cooling into an equilibrium with the thermal radiation of the ring is of importance for the study of the recombination of ^{4}HeH$^+$ with electrons.

In our model only the lowest 6 rotational states ($J = 0 - 5$) have been considered. This assumption is reasonably because of the rather large rotational constant of ^{4}HeH$^+$ (see Table D.2). The excitation energy for ^{4}HeH$^+$ ($J = 5$) is $\approx 120\,\mathrm{meV}$, or expressed in a temperature $\approx 1400\,\mathrm{K}$, whereas the ion source temperature is less than 1000 K.

The energy density $\rho_T(\bar{\nu})$ of the radiation field at a temperature T is given by the Planck distribution law for a particular wavenumber ν and can be written as

$$\rho_T(\bar{\nu}) = 8\pi h \, \frac{\bar{\nu}^3}{e^{(hc\bar{\nu}/k_B T)} - 1}, \tag{2.18}$$

where c is the speed of light and k_B the Boltzmann constant.

The Einstein coefficient $A_{J,J-1}$ gives the probability for a spontaneous transition per time interval from $J \longrightarrow J - 1$. The dipole moment matrix element $|\mu|$ is approximately constant for lower rotational states (see Appendix D.2) and $A_{J,J-1}$ can be written as

$$A_{J,J-1} = \frac{16\pi^3 \bar{\nu}^3_{J,J-1}}{3\epsilon_0 h} \, \frac{J}{2J+1} \, |\mu|^2. \tag{2.19}$$

The dipole moment matrix element for the transition $J = 5 \longrightarrow J = 4$ can be obtained from Eq. D.4. The Einstein coefficient $A_{5,4}$ has been calculated by Datz and Larsson [49] and the

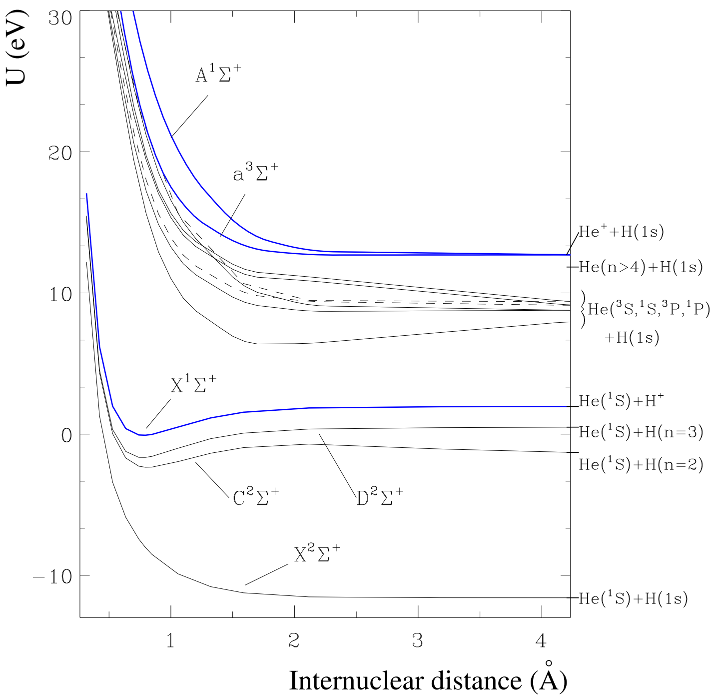

Figure 2.5: *Potential energy curves for the $^1\Sigma^+$ and $^3\Sigma^+$ states of HeH$^+$, the singly excited $^2\Sigma^+$ states and the doubly excited states of HeH [45] together with the corresponding asymptotic atomic states.*

transition wavenumber is given by

$$\bar{\nu}_{J,J-1} = 2B_{0,0}J, \tag{2.20}$$

where $B_{0,0}$ denotes the rotational constant for the ro-vibrational ground state, see Table D.2. The product of the Einstein coefficient $B_{J,J-1}$ and the energy density $\rho_T(\bar{\nu}_{J,J-1})$ for the transition $J \longrightarrow J-1$ represents the probability for a stimulated transition per time unit and $\rho_T(\bar{\nu}_{J-1,J})B_{J-1,J}$ the absorption from $J-1 \longrightarrow J$. Both coefficients can be written as:

$$B_{J,J-1} = \frac{1}{6\epsilon_0\hbar^2}\,\frac{J}{2J+1}\,|\mu|^2 \qquad B_{J-1,J} = \frac{2J+1}{2(J-1)+1}\,B_{J,J-1}. \tag{2.21}$$

Einstein has shown that the coefficients for spontaneous emission and stimulated emission are related by

$$A_{J,J-1} = 8\pi h\bar{\nu}^3\,B_{J,J-1}. \tag{2.22}$$

The time evolution of the population p_J of a rotational state changes according to the rate equation:

$$\dot{p}_J \;=\; p_J\{-A_{J,J-1} - \rho_T(\bar{\nu}_{J,J-1})B_{J,J-1} - \rho_T(\bar{\nu}_{J,J+1})B_{J,J+1}\} +$$

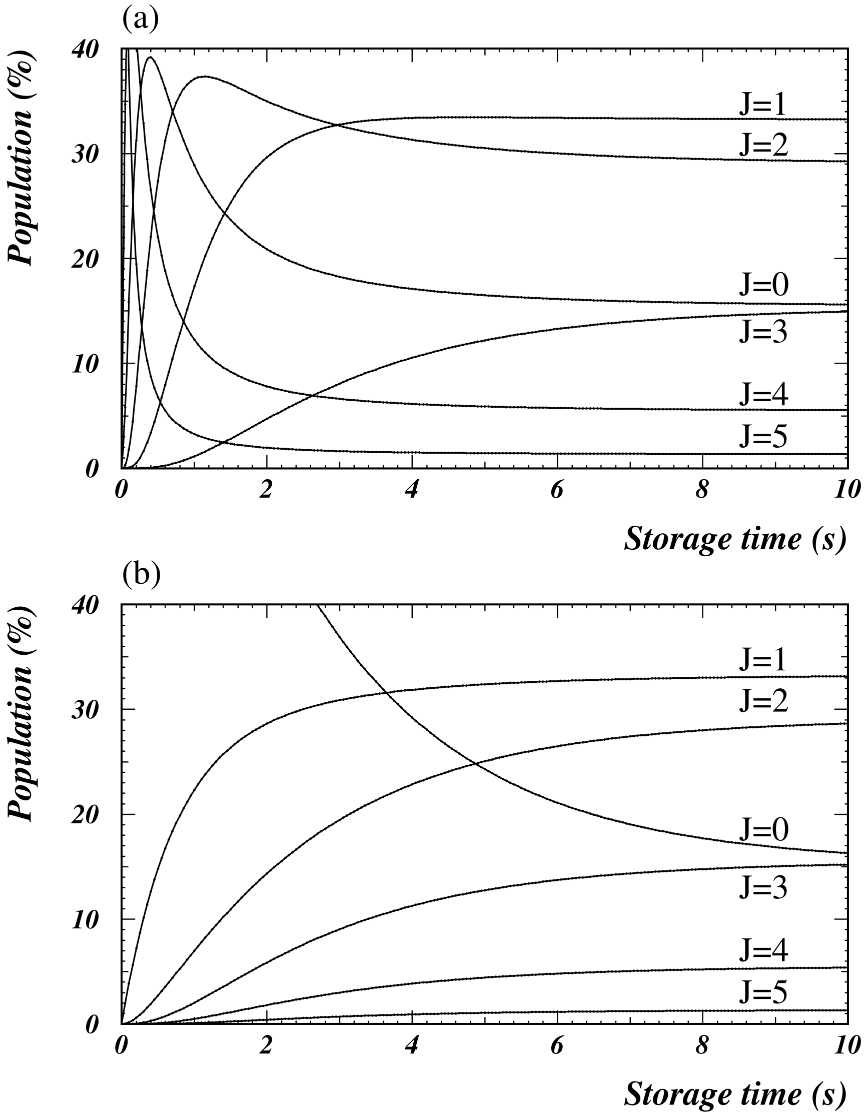

Figure 2.6: *Calculated rotational cooling for two different initial population distributions in a Planck radiation field corresponding to* $T = 300\,K$*. In case (a) 100 % of the molecules where in* $J = 5$ *and in case (b) 100 % where in* $J = 0$ *at* $t = 0\,s$*. For both cases an almost complete thermal equilibrium is reached in less than 10 s.*

$$\begin{aligned} & p_{J+1}\{A_{J+1,J} + \rho_T(\bar{\nu}_{J+1,J})B_{J+1,J}\} + \\ & p_{J-1}\{\rho_T(\bar{\nu}_{J-1,J})B_{J-1,J}\}. \end{aligned} \tag{2.23}$$

The set of coupled rate equations for all considered rotational states can be solved as explained in Appendix E.

The population p_J in a thermal equilibrium corresponding to a temperature T is given by a

Boltzmann distribution and can be written as

$$p_J = Z^{-1}(2J+1)e^{(-E_J/k_BT)} \quad \text{with} \quad Z = \sum_{J=0}^{J_{max}} (2J+1)e^{(-E_J/k_BT)}, \tag{2.24}$$

where E_J denotes the energy of the rotational excitation and Z the partition function.

Fig. 2.6 shows the calculated rotational cooling for two different initial rotational population distributions. In case (a) 100 % of the molecules where in $J = 5$ at $t = 0\,\mathrm{s}$ and in case (b) 100 % where in $J = 5$. For both initial distributions an almost complete cooling into thermal equilibrium corresponding to the temperature $T = 300\,\mathrm{K}$ (see Eq. 2.24) in less than 10 s can be observed.

2.3.3 The lithium hydride ion: LiH$^+$

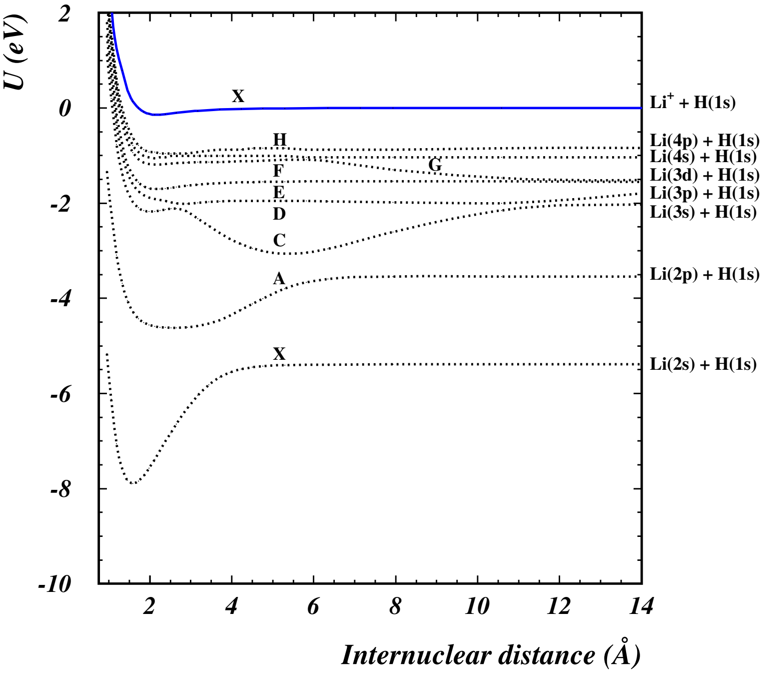

Figure 2.7: *Adiabatic potential energy curves for the $X^1\Sigma^+$ states (dotted lines) of LiH [50] and the ground electronic state $X^2\Sigma^+$ of LiH$^+$ (solid line) [51] together with the corresponding asymptotic atomic states.*

The lithium hydride ion LiH$^+$ is a weakly bound molecule with a dissociation energy of $E_D \approx 116\,\mathrm{meV}$ [51] for the vibrational ground state and a binding length $R_e \approx 2.17\,\text{Å}$ [51]. In Append. C some spectroscopic data are presented. To our knowledge LiH$^+$ has never been studied experimentally and only observed in a mass spectrometer [52]. Fig. 2.7 shows the adiabatic

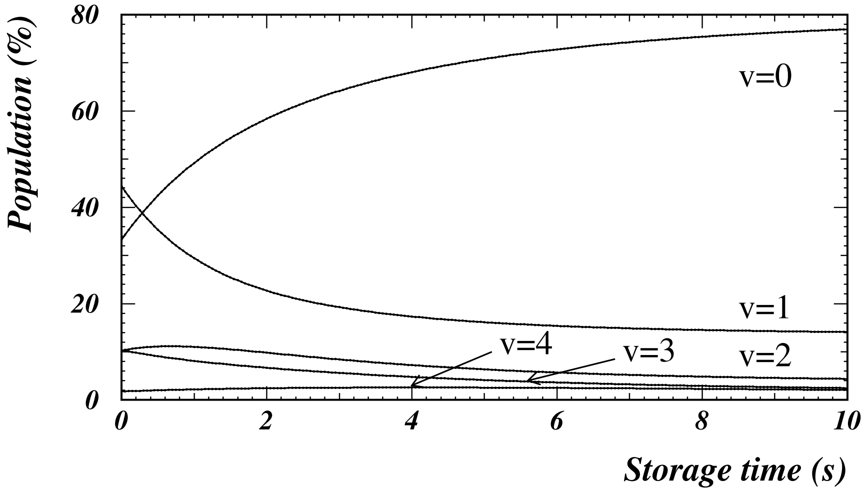

Figure 2.8: *Calculated vibrational cooling of LiH$^+$ (solid lines) in a Planck radiation field corresponding to a temperature of $T = 300\,K$. For the initial population values from a Coulomb explosion imaging measurement [54] were taken.*

potential energy curve for the $^2\Sigma^+$ ground electronic state of LiH$^+$ from *ab initio* calculations by Berriche and Gadéa [51]. *Ab initio* adiabatic and diabatic potential energy curves for almost all states of LiH below the ionic limit (Li$^+$ + H$^-$) were calculated by Boutalib and Gadéa [50]. In Fig. 2.7 the adiabatic curves are plotted together with the corresponding asymptotic atomic states. Presently there are no doubly excited neutral states known crossing the $X^2\Sigma^+$ state of LiH$^+$. The excitation of the Li and H atom requires much more energy than a single excitation of a Li atom. The potential energy curves corresponding to the final atomic fragment states Li($2s$)+H($n = 2$) are lying several eV above the ground electronic state of LiH$^+$ and do not play a role in the studied low-kinetic electron-ion collisions. These states are not shown in Fig. 2.7 for the sake of clarity. Thus, LiH$^+$ recombines with slow electrons via a non-adiabatic coupling at short internuclear distances, see Sec. 2.1.2. Due to the exceptional low binding energy high Rydberg fragment states can be reached energetically by recombinations with near-zero kinetic energy electrons. A review on spectroscopy and structure of the lithium hydride diatomic molecules and ions has been given by Stwalley and Zemke [53].

Vibrational cooling of LiH$^+$

The time scale for vibrational cooling of LiH$^+$ into thermal equilibrium is of particular interest for the DR measurements and will be studied here. LiH$^+$ in the ground electronic state possesses a rather large dipole moment ($\approx 0.5 - 3\,$Debye) [55], but the binding energy is only $\approx 120\,$meV and hence the vibrational level spacing small. The probability for spontaneous transitions are therefore small and the radiative lifetimes long, see Appendix C.3.

A model for the vibrational population can be developed similar to that for the rotational cooling of ^{4}HeH$^+$ (Sec. 2.3.2). The modeled time evolution is shown in Fig. 2.8. For the initial population values from a Coulomb explosion imaging (CEI) measurement [54] measured at the storeage time $t = 0.5\,\mathrm{s}$ were chosen, see also Tab. 6.1 in Sec. 6.1. The modeled cooling shows that a stored LiH$^+$ ion beam should be almost in a complete thermal equilibrium with the storage ring walls after about 7 s.

3. Background of the experimental technique

This chapter describes the principles and the theoretical background of the experimental methods used in the present work to study the properties of molecular ions and their interaction with electrons using fast ion beams in a heavy ion storage ring. In the first part the Coulomb explosion imaging technique will be explained and its application to measurements of the vibrational population evolution of stored molecular ions discussed. In the second part the projected fragment imaging technique used for dissociative recombination (DR) measurements will be presented. Details of the experimental setup are given in Chapter 4 and for example in the review article [56].

3.1 The Coulomb explosion imaging principle

In order to study molecular ions by Coulomb explosion imaging (CEI) [57] they are accelerated to velocities of several a.u.[1]. When such a molecular ion collides with a thin foil its binding electrons get stripped off on a time scale of $\approx 10^{-17}$ s. Moreover, if the thickness of the target foils are less than 100 Å typical dwell times of the molecule inside the target are $\leq 10^{-16}$ s. The time scales are short compared to vibrational and rotational times which are about 10^{-14} s and 10^{-12} s, respectively. Thus, the attractive binding force between the molecular constituents is abruptly replaced by a pure repelling Coulomb force and the charged molecular fragments start to repel each other. The Coulomb energy is completely converted into kinetic energy after several μm of flight and the exploding fragments then move with their asymptotic velocities. The microscopic binding distance of about 1 Å is thus transformed into a macroscopic distance (few centimeters) after several meters of flight. The resulting distance between the particles, determined by the center-of-mass motion, the flight distance and the asymptotic velocities, can be measured by a three-dimensional (3D) detector system. The distance perpendicular to the ion beam direction is measured using an imaging system, whereas the spatial component parallel to the ion beam direction is retrieved by measuring the impact time difference between the fragments on the detector. In Fig. 3.1 the Coulomb explosion process is shown schematically for

---

[1] 1 a.u.=αc, where α denotes the fine structure constant and c the speed of light

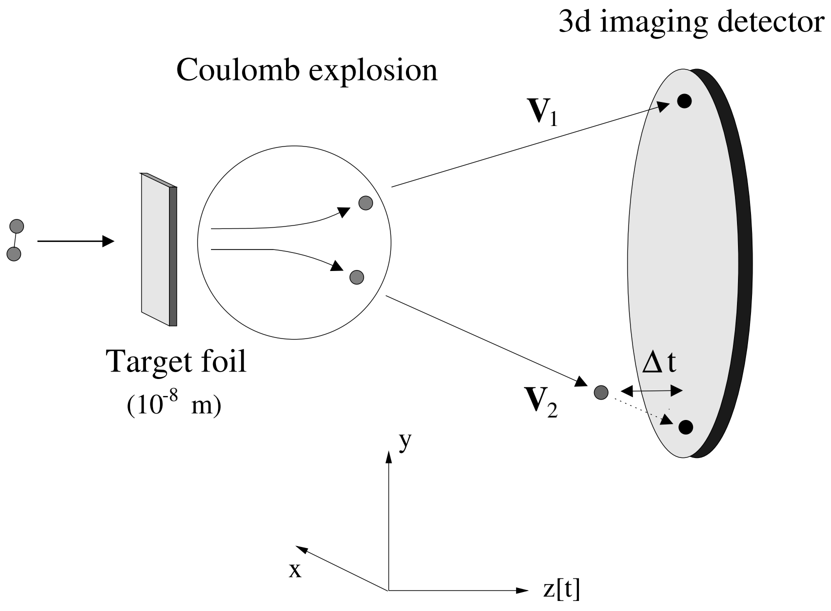

Figure 3.1: *Schematic sketch of the Coulomb explosion of a diatomic molecule.*

a diatomic molecular ion.

By calculating the asymptotic velocities of all fragments from the measured fragment distances information can be retrieved about the molecular structure prior to the Coulomb explosion. In case of a diatomic molecule, the final velocity vectors $\mathbf{V}_1$,$\mathbf{V}_2$ contain this information. Measuring the velocity vectors for many events one obtains a distribution of the asymptotic fragment velocities $\mathrm{P}(\mathbf{V}_1,\mathbf{V}_2)$, the so-called *V-space distribution*. This distribution is directly related to the internuclear distance distribution (often referred to as *R-space distribution*), which for a pure quantum state (e.g. ro-vibrational ground state) is given by the square of the nuclear wavefunction if the internal ro-vibrational excitation energy of the exploding molecules is small compared to the dissociation energy, i.e. the Coulomb energy. For H_2^+ and D_2^+ , discussed in this work, the kinetic energy releases are about $10 - 25\,\mathrm{eV}$ for the vibrational ground state and $5 - 25\,\mathrm{eV}$ for the higher vibrational states, whereas the internal vibrational energies of H_2^+ and D_2^+ are $\approx 0.14\,\mathrm{eV}$ and $\approx 2.2\,\mathrm{eV}$ for $v = 0$ and $v = 10$, respectively. Thus, in these cases the internal kinetic energies of the molecule are sizable and have to be taken into account.

Even for the thinnest target, however, part of the Coulomb explosion occurs inside the target foil and the positively charged atomic fragments will interact with the target. The charge state of the atomic fragments can change several times due to electron capture and stripping. The effective repulsion potential is therefore different from a pure Coulomb potential. This effect is furthermore increased by additional screening effects caused by target electrons The strongest perturbation is caused by multiple small angle scattering, which leads to a smearing of the asymptotic velocities of the dissociating fragments [58, 59, 60]. A further effect occurs due to *wake-fields* [61] caused by fragments when passing the foil. A positively charged particle changes the local electron density in the target and forms a negative wake. Trailing positive fragments get attracted and the molecular axis aligns towards the beam direction giving rise to a reorientation of the molecule and an anisotropy in the orientation distribution. The probability to find the molecular axis aligned parallel to the beam axis is therefore increased. More target effects are taken into account by a Monte-Carlo calculation when performing the $R-$space to $V-$space transformation.

3.2 Vibrational population from CEI measurements

In this section a method for obtaining vibrational population distributions from CEI measurements will be discussed and the characteristic shapes of kinetic energy distributions for Coulomb explosion of molecules in an initial vibrational state v will be derived.

3.2.1 Theoretical aspects of the Coulomb explosion

Neglecting the internal energy of the molecule the relative velocity $v(t)$ between the dissociating fragments of a diatomic molecule as a function of the internuclear distance depends on the initial distance $R = r(t = 0)$ and is given by conservation of energy as

$$\begin{aligned} E_{total} = \frac{Q_1 Q_2 e^2}{R} &= E_{Coul}(t) + E_k(t) \\ &= \frac{Q_1 Q_2 e^2}{r(t)} + \frac{1}{2}\mu v(t)^2 \\ \text{with} \quad \lim_{t\to\infty} E_{total} &= \frac{1}{2}\mu v^2 \end{aligned} \tag{3.1}$$

where Q_1 and Q_2 are the fragment charge states, e the elementary charge, E_{Coul} the Coulomb energy and μ the reduced mass of the molecule. The asymptotic fragment velocity $v = V_2 - V_1$ can then easily be calculated by

$$v(R) = e\sqrt{\frac{2Q_1 Q_2}{\mu R}}\,. \tag{3.2}$$

Integrating over the velocity $v(t)$ in Eq. 3.1 gives a relation between the time t after the explosion and the fragment distance $r(t)$ and one can estimate the time for the transformation of 99 % of the Coulomb energy into kinetic energy which typically amounts to about hundred femtoseconds or $\approx 0.1\,\mu$m if expressed in a flight distance.

In this semi-classical description of the Coulomb explosion process, the distribution of the asymptotic velocities $P(v)_{v,J}$ of the fragments (V-space distribution) is related to the internuclear distance distribution $P'_{v,J}(R)$ (R-space distribution) according to

$$P_{v,J}(v(R)) = P'_{vJ}(R)\left|\frac{dv}{dR}\right|^{-1} \tag{3.3}$$

$$\text{with} \qquad P'_{vJ}(R) \;=\; \Psi^2_{vJ}(R), \tag{3.4}$$

where $\Psi_{vJ}(R)$ is the nuclear wavefunction for the ro-vibrational state vJ and $v(R)$ the asymptotic fragment velocity from Eq. 3.2.

The initial momentum of the nuclei prior to the explosion has to be taken into account since the contribution to the total kinetic energy release is about 10 % for the higher vibrational states. The correct quantum-mechanical distribution $Q_{vJ}(v)$ of the asymptotic fragment velocities in their center-of-mass frame of reference can be obtained by projecting the initial nuclear wavefunction $\Psi_{vJ}(R)$ on Coulomb wavefunctions $\chi_C(R;k,J)$. The Coulomb wavefunction for a given total kinetic energy E_k is characterized by the initial angular momentum J and the wavenumber k, where

$$k = \frac{1}{\hbar}\sqrt{\frac{2E_k m_1 m_2}{m_1+m_2}} \tag{3.5}$$

and m_1, m_2 are the fragment masses. The V-space distribution $Q_{vJ}(v)$ for an initial state vJ is expressed by

$$Q_{vJ}(v) \;=\; Q'_{vJ}(k)\left|\frac{dv}{dk}\right|^{-1} \tag{3.6}$$

$$\;=\; |C_{vJ}(k)|^2\left|\frac{dv}{dk}\right|^{-1} \tag{3.7}$$

with

$$C_{vJ}(k) = \int_0^\infty \chi^*_C(R;k,J)\Psi_{vJ}(R)dR. \tag{3.8}$$

The ion source temperature was about 500 K-600 K [34]. This corresponds to a rotational excitation, assuming a Boltzmann distribution, with $\approx 90\,\%$ of the rotational population in $J = 0-6$ and $J = 0-4$ for D_2^+ and H_2^+ , respectively. For these low J values the experiment cannot resolve the differences in the V-space distributions from Eq. 3.7, as discussed by Amitay *et al.* [34]. Thus, for simplicity, $J = 0$ was assumed throughout the calculations. The V-space distribution was therefore taken to be

$$Q_v(v) = |C_{vJ=0}(k)|^2\left|\frac{dv}{dk}\right|^{-1} \tag{3.9}$$

and the corresponding kinetic energy distribution by

$$Q_v(E_k) = |C_{vJ=0}(k)|^2\left|\frac{dE_k}{dk}\right|^{-1}. \tag{3.10}$$

The function $Q_v(v)$ represents the V-space distribution for the dissociation of a molecular ion via a pure Coulomb potential.

3.2.2 Monte-Carlo simulation of the Coulomb explosion and the detector system

The V-space distribution derived in the previous section neglects all effects happening inside the target foil, i.e. charge exchange, electron screening, multiple scattering and wake-fields. To take the first three processes into account a Monte-Carlo simulation has been developed [59] and tested in Coulomb explosion experiments with several molecular ions, see for instance Ref. [62] and references therein. The main input parameters in the simulation are the target thickness and the target composition[2]. The wake effect has not yet been implemented successfully in the Monte-Carlo simulation. To minimize the influence of the wake effect on the measured fragment distance distribution a cut is applied to the data sample. Events get discarded if the angle Φ between the beam direction (z-, or time-component) and the molecular axis deduced from the asymptotic velocities of the dissociating fragments is smaller than typically 60°, i.e. $\cos\Phi < 0.5$. This cut is therefore often referred to as *cosine-cut.* With this cosine-cut those events are discarded which are strongest influenced by the wake field effects.

The simulation computes for each vibrational state specific R-space distribution, the classical trajectories of the dissociating fragments, taking into account multiple scattering, electron screening and charge exchange. From the simulated trajectories the asymptotic fragment velocities behind the target foil and thus the V-space distribution is obtained.

To compare the measured distributions with the simulated V-space distributions a second Monte-Carlo simulation is employed which includes the finite detector resolution of $\approx 0.1\,\mathrm{mm}$ and $\approx 1\,\mathrm{mm}$ in the directions perpendicular and parallel to the ion beam, respectively. Furthermore, the beam size is taken into account as well as the efficiency of the detector. The realisation of the three-dimensional fragment distance measurement and the resolutions obtained are discussed in Sec. 4.3.

In this approach the internal energy of the molecular ion is not yet taken into account. To include these contributions the following procedure was applied for each vibrational state:

1. Calculating the quantum-mechanical distribution $Q_v(v)$ of the asymptotic fragment velocities
2. Calculating backwards an effective R-space distribution $P_v^*(R)$ using the semi-classical relation in Eq. 3.4
3. Using the effective R-space distribution $P_v^*(R)$ as the initial R distribution for the Monte-Carlo simulations, to yield the modified distributions $P_v^*(v)$ or $P_v^*(E_k)$

---

[2] The two different target compositions used are build up of a metal grid and a thin layer of either Formvar resin or **D**iamond-**L**ike **C**arbon (DLC), see also Sec. 4.3.

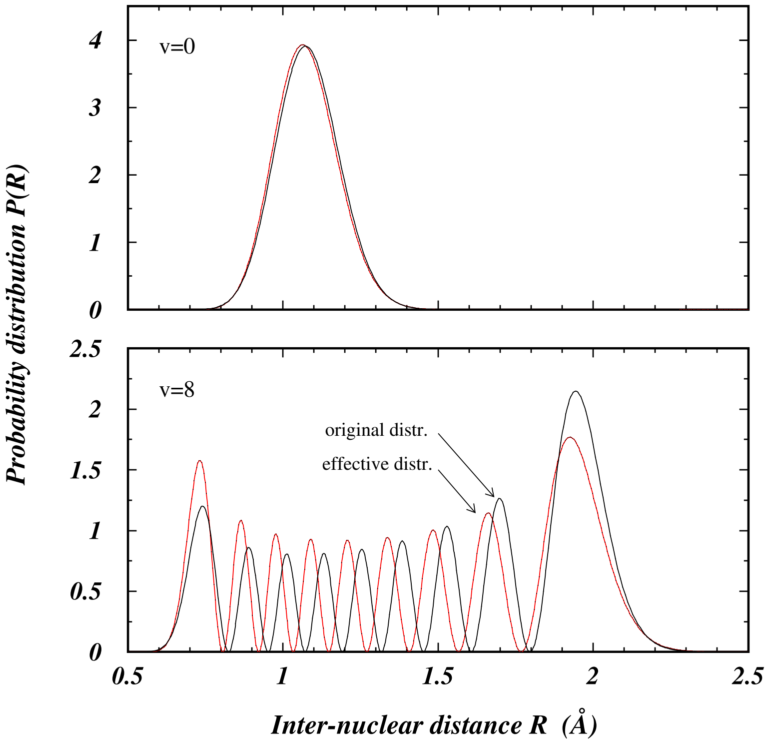

Figure 3.2: *Comparison of the R-space distributions $P_v(R)$ for vibrational states $v = 0$ and $v = 8$ of D_2^+ with the effective functions $P_v^*(R)$ (see text for further descriptions).*

In Fig. 3.2 the original R-space distributions $P_0(R)$ and $P_8(R)$ for D_2^+ [3] are shown as well as the effective functions $P_0^*(v)$ and $P_8^*(v)$ obtained following the procedure explained above. Clearly a shift in the center-position of the humps in the effective distribution for $v = 8$ towards smaller internuclear distances compared to the positions in the original R-space distribution can be seen, whereas the two distributions for the vibrational ground state are almost identical. A shift in the R-space distribution towards smaller internuclear distances, corresponding to a higher total potential Coulomb energy, gives rise to a shift in the V-space distribution to higher velocities and therefore to a higher total kinetic energy release which accounts for the internal excitation energy. For D_2^+ in the vibrational state $v = 8$, the internal energy is about 10 % of the total potential Coulomb energy and less than 1 % for the vibrational ground state, therefore the differences in the two distributions is more pronounced for $v = 8$.

3.2.3 Evaluation of vibrational populations

The vibrational state specific shape of the simulated functions $P_v^*(E_k)$ for the kinetic energy release can be used to evaluate the relative vibrational population $p_v(t)$ $[\sum_v p_v(t) \equiv 1]$ as a

---

[3] The nuclear wavefunctions square have been calculated using *Level*7.0 [63]

function of the storage time t in the TSR.

The time evolution of the relative vibrational population $p_v(t)$ can be obtained by comparing the function

$$P(E_k;t) = \sum_v p_v(t) P_v^*(E_k) \tag{3.11}$$

to the measured and normalized kinetic energy spectra; $P_v^*(E_k)$ are the (normalized) kinetic energy distributions for an ensemble of ions in a vibrational state v.

To perform the comparison the simulated kinetic energy distributions $P_v^*(E_k)$ are transformed into distributions $P_v^*(d)$ of the three-dimensional fragment distances d using the second Monte-Carlo simulation. The relative vibrational population $p_v(t)$ can then be obtained by fitting the function

$$P(d;t) = \sum_v p_v(t) P_v^*(d) \tag{3.12}$$

to the measured and normalized fragment distance spectra.

The kinetic energy E_k is related to the three-dimension fragment distance d by

$$d = L \frac{E_k}{E_i} \frac{m_1 + m_2}{\sqrt{m_1 m_2}}, \tag{3.13}$$

where E_i is the molecular ion energy E_i, L the distance from the target to the detector system and m_1 and m_2 are the masses of the exploding particles.

3.3 Recombination fragment imaging

The DR of a diatomic molecular ion with electrons can be studied in more detail by measuring the distance of the dissociating fragments after a free flight path of several meters. The fragment distance contains information about the relation between the initial vibrational state and the final atomic fragment states (here often called state-to-state relation). The recombination fragment imaging (RFI) technique has been developed [39] to study these state-to-state contributions and its practical realization will be discussed in Sec. 4.5.

The projection of the three-dimensional (3D) distance between the DR fragments onto a plane perpendicular to the beam direction leads to a projected-distance spectrum characterized by the kinetic energy release E_k in the molecular frame-of-reference of the DR process. Thus each initial-to-final DR channel, corresponding to a specific kinetic energy release, can be extracted from a measured fragment distance spectrum. However, the ability for extracting the involved DR channels is limited by the number of channels and their differences in the kinetic energy release, as will be discussed in Chapter 4.4. The kinetic energy release E_k for the recombination of a molecular ion in the ro-vibrational state vJ with electrons at a relative energy E is

$$E_k = E_{vJ} + E - E_{nn'} \quad , \tag{3.14}$$

where

$$E_{vJ} = E_v + J(J+1)B. \tag{3.15}$$

E_{vJ} is the excitation energy of the molecular ion, with E_v the ro-vibrational energy for $J = 0$ and B the rotational constant of the molecular ion[4]. The energy of the final asymptotic state nn' of the atomic DR fragments is denoted as $E_{nn'}$. The influence of the electron and ion beam velocity spread; given basically by the transverse electron temperature ($kT_\perp \approx 15\,\mathrm{meV}$); is small and therefore neglected. Using Eqs. 3.14 and 3.15 the kinetic energy release E_k for recombination with zero kinetic energy electrons ($E = 0\,\mathrm{eV}$) can be directly calculated for each initial-to-final state-to-state DR channel $vJnn'$, with the initial state vJ and the final state nn' and will be denoted as $E_k^{vJnn'}$. Defining all energies in Eqs. 3.14 and 3.15 relative to the ro-vibrational ground state of the molecular ion, a DR channel is energetically open if $E_k^{vJnn'} > 0$.

Molecular ions, with an energy E_i in the laboratory frame, recombine with electrons at a distance S from the detector and fall apart under an angle θ, where θ is defined as the angle between the internuclear axis and the beam direction, see Fig. 3.3. The distance D of the two fragments in the plane perpendicular to the beam direction is then given by

$$\begin{aligned} D &= d \sin\theta \\ &= S\delta_{vJnn'} \sin\theta \end{aligned} \tag{3.16}$$

where

$$\delta_{vJnn'} = \frac{m_1 + m_2}{\sqrt{m_1 m_2}} \sqrt{\frac{E_k^{vJnn'}}{E_i}} \quad , \tag{3.17}$$

The fragment masses are denoted by m_1 and m_2 and d is the three-dimensional fragment distance, and E_i denotes the ion beam energy.

Recombinations do not occur at a fix distance S from the detector, in fact the interaction region of the electrons with the ion beam is typically more than 1 m (see the description of the electron cooler in Sec. 4.5). Thus the value for S is ranging from s_1 to s_2. The angular distribution of the fragments can be expressed in Legendre polynomials $P_{vJnn'}^k$ of the order k (only even k for symmetry reasons) and the distribution of projected distances for a state-to-state DR channel $vJnn'$ can therefore be written as

$$P_{vJnn'}(D) = P_{vJnn'}^0(D) + a_2 P_{vJnn'}^2(D) + \cdots \tag{3.18}$$

---

[4] All rotational excitation energies have been calculated using the rotational constant for the ro-vibrational ground state.

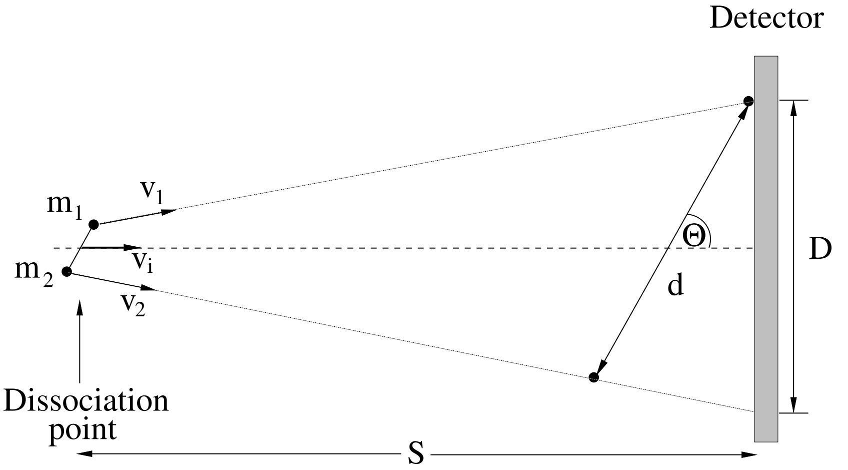

Figure 3.3: *Schematic drawing of the dissociation process of a diatomic molecule and the definition of the angle θ and the fragment distances and velocities.*

The fragment distance distribution $P^0_{vJnn'}(D)$ corresponding to an isotropic distribution of θ (i.e. $k = 0$) in the molecular frame-of-reference is given by [64]

$$P^0_{vJnn'}(D) = \begin{cases} \dfrac{1}{(s_2 - s_1)\delta_{vJnn'}} \left(\arccos \dfrac{D}{s_2\delta_{vJnn'}} - \arccos \dfrac{D}{s_1\delta_{vJnn'}} \right) \\ \qquad \text{for } 0 \leq D \leq s_1\delta_{vJnn'} \\[2ex] \dfrac{1}{(s_2 - s_1)\delta_{vJnn'}} \arccos \dfrac{D}{s_2\delta_{vJnn'}} \\ \qquad \text{for } s_1\delta_{vJnn'} \leq D \leq s_2\delta_{vJnn'} \\[2ex] 0 \qquad \text{otherwise.} \end{cases} \tag{3.19}$$

The first anisotropic component (i.e. k=2) in Eq. 3.18 is

$$P^2_{vJnn'}(D) = \begin{cases} \dfrac{1}{4(s_2 - s_1)\delta_{vJnn'}} \left(\arccos \dfrac{D}{s_2\delta_{vJnn'}} - \arccos \dfrac{D}{s_1\delta_{vJnn'}} \right) \\ - \dfrac{3D}{4(s_2 - s_1)\delta^2_{vJnn'}} \left(\dfrac{\Gamma_2}{s_2^2} - \dfrac{\Gamma_1}{s_1^2} \right) \\ \qquad \text{for } 0 \leq D \leq s_1\delta_{vJnn'} \\[2ex] \dfrac{1}{4(s_2 - s_1)\delta_{vJnn'}} \arccos \dfrac{D}{s_2\delta_{vJnn'}} \\ - \dfrac{3D}{4(s_2 - s_1)\delta^2_{vJnn'}} \dfrac{\Gamma_2}{s_2^2} \\ \qquad \text{for } s_1\delta_{vJnn'} \leq D \leq s_2\delta_{vJnn'} \\[2ex] 0 \qquad \text{otherwise,} \end{cases} \tag{3.20}$$

where

$$\Gamma_{1,2} = \sqrt{s_{1,2}^2 - \frac{D}{\delta_{vJnn'}}}. \tag{3.21}$$

The anisotropy coefficient a_2 can range from -1 to 2. For experiments performed with zero kinetic energy electrons the anisotropy coefficient is $a_2 = 0$ and the dissociation is therefore isotropic in θ.

Molecular ions are rotationally excited when created in an ion source and it is reasonable to assume an initial Boltzmann distribution corresponding to $T_{rot} = 600 \pm 150\,\mathrm{K}$ for the rotational population, as discussed in more detail for the production of HD^+ [34] in the same ion source. Assuming the DR rate coefficient for a given vibrational state v being independent of the rotational state J, the initial rotational temperature will stay approximately constant over the whole storage time. For each vibrational state a distribution of projected distances including the rotational excitation can be derived.

According to our assumptions the population p_J of each rotational state J is proportional to the multiplicity of that state weighted with a Boltzmann factor, i.e.

$$p_J \propto \beta(J) = (2J+1)e^{-J(J+1)B/kT_{rot}}, \tag{3.22}$$

where $\beta(J)$ takes care of the nuclear spin statistics, which for homonuclear diatomic molecules, gives rise to a J dependent degeneracy, due to symmetry reasons [65]. In particular, for H_2^+ (nuclear spin of hydrogen[5] $I = 1/2$), $\beta(J = \mathrm{odd})/\beta(J = \mathrm{even})$=3, while for D_2^+ (nuclear spin of deuterium $I = 1$), $\beta(J = \mathrm{odd})/\beta(J = \mathrm{even})$=1/2. The projected fragment distance distribution for a vibrational state v dissociating into the final states n, n' is thus given by

$$P_{vnn'}(D) = \sum_J p_J P_{vJnn'}(D). \tag{3.23}$$

The projected fragment distance distribution $P^{(E)}(D;t)$, measured at time t after injection and normalized to unity, is a linear combination of the normalized functions $P_{vnn'}(D)$ for all energetically possible DR channels ($E_{k,vJnn'} \geq 0$):

$$P(D;t) = \sum_{vnn'} q_{vnn'}(t) P_{vnn'}(D), \tag{3.24}$$

with the coefficients $q_{vnn'}(t)$ representing the contribution of the corresponding DR channel to the measured spectrum. The coefficients $q_{vnn'}(t)$ are proportional to the time-dependent population $p_v(t)$ of the vibrational state v and the time-independent DR rate coefficient $\alpha_{vnn'}(E)$:

$$q_{vnn'}(t) \sim \alpha_{vnn'}(E) p_v(t). \tag{3.25}$$

---

[5] The proton spin quantum number was first determined by measurements of the intensity of spectral lines of H_2 corresponding to transitions between levels with either even or odd J, see Ref. [66].

4. Experimental apparatus and procedures

In this chapter the different ion sources and accelerators used for the experiments discussed in the framework of this thesis will be described as well as the heavy ion storage ring TSR with its components and properties. Furthermore, the Coulomb explosion imaging (CEI) setup and the DR fragment detector system will be explained. The last two sections will focus on the electron cooler and the principle of cross section measurements.

4.1 Ion production and acceleration

At the Max-Planck-Institut für Kernphysik in Heidelberg, several ion sources and accelerators are presently used to provide molecular ion beams for experiments at the heavy ion storage ring TSR. The single-ended van-de-Graaff and the Tandem accelerator use electrostatic fields whereas the third accelerator consists of two radio-frequency quadrupoles (RFQ) together with eight seven-gap resonators operating with oscillating electric fields [67, 68].
The single-ended van-de-Graaff accelerator provides positively charged molecular ions produced by a Penning source. The maximum terminal voltage is 2.5 MV. This accelerator has been used to produce a 1 MeV H_2^+ beam (beam intensity $\approx 1\,\mu$A) through electron impact ionisation of a neutral hydrogen gas.
The second electrostatic accelerator, a so-called Tandem accelerator, uses twice the positive terminal voltage. The maximum terminal voltage is about +11.5 MV. Negatively charged ions from either a cesium sputter source or a duoplasmatron source get accelerated towards the positively charged terminal of the Tandem. Part of the electrons get stripped off the ion by collisions with either a nitrogen gas target or carbon atoms of thin stripping foils. Furthermore, the gas stripping allows for removing atoms of a molecular ion beam. In case of LiH^+, the ion beam has been produced by stripping off two electrons and a proton from a LiH_2^- ion produced in a cesium sputter source. The beam current reached was ≈ 150 pA.
In the last two years the RFQ accelerator has been additionally used for the acceleration of positively charged molecules, together with a high current ion beam source, the so-called CHORDIS (**C**old or **HO**t **R**eflex **D**ischarge **I**on **S**ource) source, developed at the GSI in Darmstadt [69]. Due to the geometry of the acceleration cavity of the RFQ and the frequency of the driving RF field, the energy of the ion beam is restricted to 500 keV/a.m.u., or 250 keV/a.m.u. if only half

of the RFQ system is used [70]. These energies correspond to ion beam velocities of 3.3 % and 2.3 % of the speed of light, respectively. Seven-gap resonators following the RFQ system allow for an additional acceleration to an energy of 1000 keV/a.m.u. A drawback of the RFQ system is its limitation to a maximum mass-to-charge ratio of 9:1, however, beam current of up to 1 mA can be achieved.

The three accelerators are connected via a transfer beam line to the storage ring. The transfer beam line consists of several dipole magnets for mass separation, focusing units and a post-accelerator, which is build up of several RF resonator structures which can be used for a further acceleration. An HD^+ beam from the RFQ has recently been accelerated to 16 MeV [71] using the post-accelerator.

Accelerator	Molecular ion	Ion source	Precursors	Beam energy	TSR rigidity
van-de-Graaff	H_2^+	Penning	H_2	1.0 MeV	0.20 Tm
Tandem	LiH^+	Penning	LiH_2^-	6.0 MeV	0.98 Tm
RFQ	H_2^+	CHORDIS	H_2	2.0 MeV	0.28 Tm
	D_2^+	CHORDIS	D_2	2.0 MeV	0.57 Tm
	$^4HeH^+$	CHORDIS	$^4He + H_2$	2.5 MeV	0.50 Tm

Table 4.1: *Summarized beam parameters for the molecular ions studied in the framework of this thesis.*

4.2 The heavy ion storage ring TSR

The heavy ion storag ring TSR (see Fig. 4.1) started operation in May 1988 [72] and was in the beginning mainly used for experiments with atomic ions. In the recent years it has been taken advantage of the capability to store molecular ions up to a minute. These storage times are long compared to typical radiative lifetimes of molecular vibrational states and allow for a complete thermalization with the background radiation field at around $T = 300\,\mathrm{K}$. At these temperatures most molecular ions are completely relaxed to their ground state and a defined inital quantum state is reached.

The TSR consists of eight dipole magnets, twenty quadrupole magnets and twelve sextupole magnets bending and focusing the ion beam on a closed orbit of 55.4 m circumference. The injection as well as the extraction of ions is done with the same electrostatic septum, see Fig. 4.1. To increase the ion beam current stored in the TSR the multi-turn injection technique can be used. This technique allows for stored ion beam currents increased by a factor up to 40 compared to an ion beam current of a single injection. The number of stored molecules N ranges from $\sim 10^5 - 10^8$ per multi-turn injection corresponding to an ion current $I_i \sim 0.01 - 10\,\mu\mathrm{A}$ for a

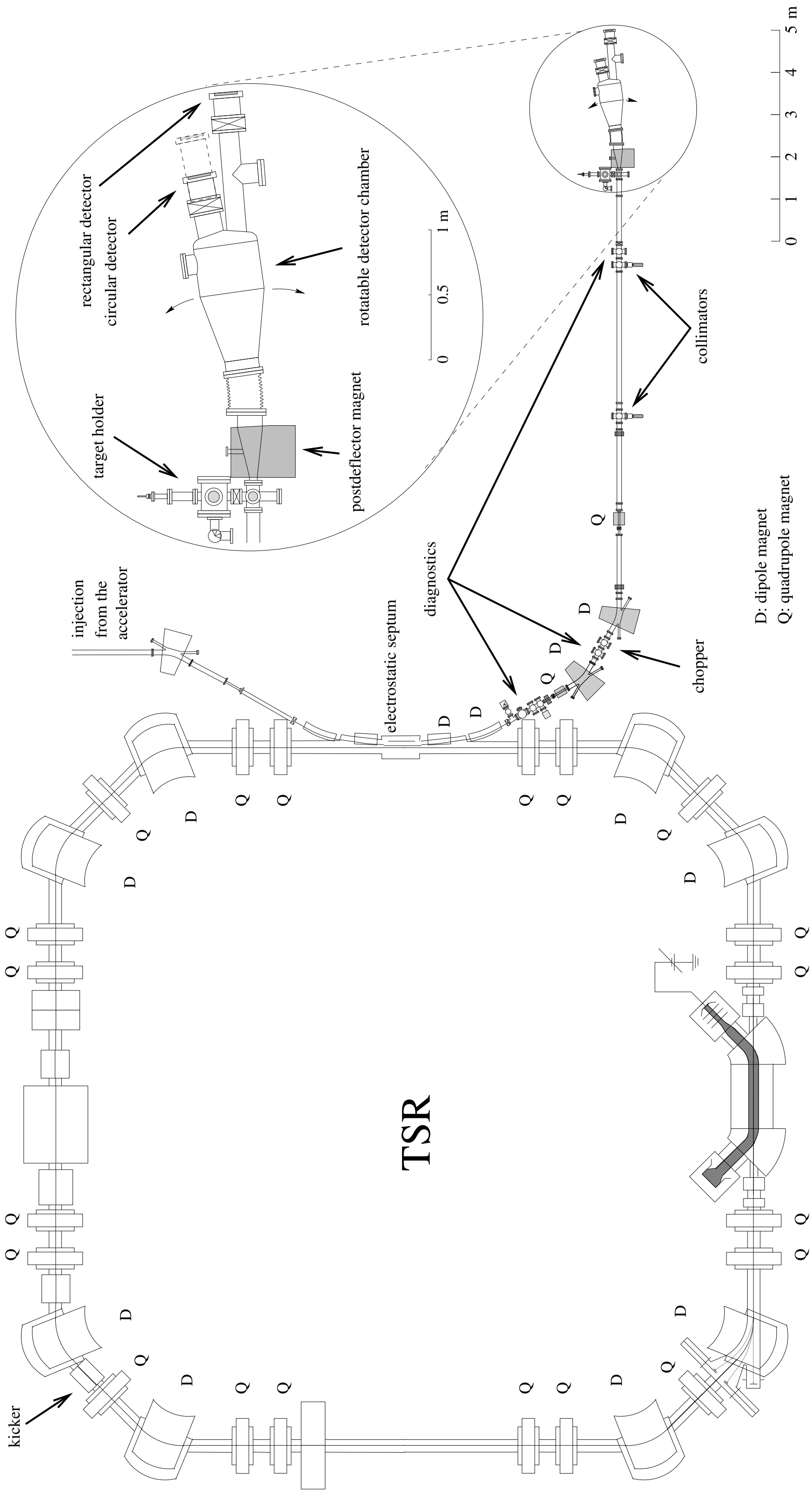

Figure 4.1: *The heavy ion storage ring TSR together with the injection beamline and the Coulomb explosion imaging experiment. The main part of the CEI setup is enlarged.*

typical ion velocity $v_i \sim 3\,\%$ of the speed of light, according to the relation

$$I_i = N_i\, q_i\, v_i / L, \tag{4.1}$$

where q_i is the ion charge and L the ring circumference. The maximum magnetic field of the dipole magnets restricts the beam energy. An ion with mass m_i moves in the magnetic field B of the dipole on a curvature with a radius ρ due to the Lorentz force. The so-called rigidity $B\rho$ of the TSR is therefore defined as

$$B\rho = \frac{m_i v_i}{q_i}. \tag{4.2}$$

The radius of curvature in the dipole magnets is $\rho = 1.15\,\mathrm{m}$ and the maximum rigidity of the TSR is $(B\rho)_{max}$=1.4 Tm.
The maximum storage time in the TSR is limited by collisions with residual gas molecules. Typical $1/e$ beam lifetimes were 15 s for LiH$^+$, 18 s for ^{4}HeH$^+$ and about 20 s for H_2^+ and D_2^+ . The residual gas pressure inside the TSR is on average 3×10^{-11} mbar, depending on the temperature inside the building the TSR is located in. About 90 % of the residual gas is hydrogen and the other constituents are atomic argon and molecular nitrogen, oxygen and carbon.

4.2.1 Slow extraction

The slow extraction technique [73, 74] allows to continuously remove a small fraction of the stored molecules. The extraction rate ranges from $10^2\,\mathrm{s}^{-1}$ to $10^4\,\mathrm{s}^{-1}$. The extracted molecules pass the extraction beam line, consisting of a set of two dipole magnets, magnetic septa, quadrupol magnets, collimators each and three diagnostic units (see Fig. 4.1) before impinging on the target of the Coulomb explosion imaging setup. The principle of the slow extraction has been explained in detail in Ref. [75, 62] and only a short description will be given here. The extraction is done by a resonant transverse RF field applied to the stored ion beam which drives part of the ions to unstable phase space regions from which they can be extracted using the electrostatic septum. The efficiency of the slow extraction has been studied extensively [76].

4.3 The Coulomb explosion imaging setup

In Fig. 4.2 the Coulomb explosion imaging (CEI) setup is shown schematically. This CEI setup allows for measuring the three-dimensional distance of the atomic or molecular fragments emerging from the target foil, situated either at position 1 or position 2. The experiment consists of a chopper, two collimators (0.5 mm to 5 mm diameter) to reduce the beam divergence (±0.17 mrad), a postdeflector magnetic field for charge and mass separation of the exploding fragments and two detectors (rectangular and circular shape) for three-dimensional fragment imaging. The electrostatic chopper (a parallel plate capacitor) can be switched on in about 500 ns and deflects the molecular ion beam to the wall. The switching is triggered by a fragment hitting

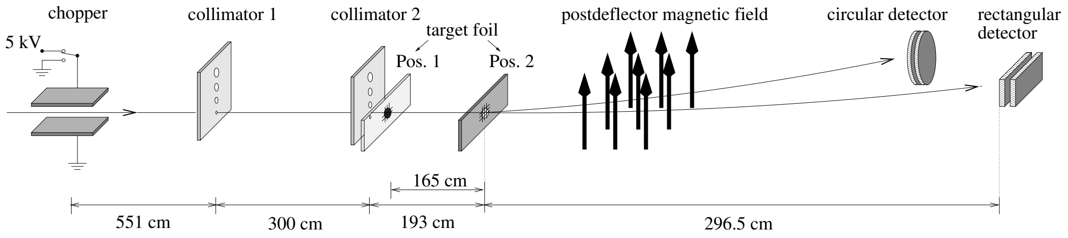

Figure 4.2: *The Coulomb explosion imaging setup at the TSR. Shown are the two positions of the target foils used in the experiments and the two different detector systems.*

the particle detector. As mentioned above the maximum rate of extracted ions is $10^4\,\mathrm{s}^{-1}$ and small compared to the inverse switching time of the chopper. Thus we can study one molecule at a time. After a read-out cycle the chopper is switched off again and a new measurement can be performed. Two target positions are possible in the present experimental setup, 296.5 cm and 461.5 cm away from the rectangular detector. Two different types of targets are used in the CEI experiments, Formvar resin [77] and **D**iamond-**L**ike **C**arbon (DLC) [78]. The density of Formvar and DLC is $1.2\,\mathrm{g/cm}^3$ and $2\,\mathrm{g/cm}^3$, respectively. Typical target thicknesses used in CEI measurements are between 30 Å and 60 Å for DLC targets [79, 80] and around 80 Å for Formvar targets [62]. DLC targets have several advantages compared to the Formvar targets, e.g. smaller thickness and less pin-holes (see Ref. [62] for more details).

The two detectors have been developed at the Weizmann Institute of Science [81] and are build up as shown schematically in Fig. 4.3 for the circular detector. Each detector consists of a mylar foil with a CsI layer, a microchannel plate (MCP) in chevron layout, a kapton foil with a phosphor layer on the front side and a set of anode strips on the back side. The circular detector has a diameter of 118 mm and the size of the rectangular detector is $76 \times 93\,\mathrm{mm}^2$. The mylar foil with the CsI layer increases the detection efficiency up to 100 %. Electrons get released from the mylar foil once an ion impinges and accelerated to about 100 eV towards the MCP. The microchannels in a MCP improve the spatial resolution of the detector system. Inside the MCP a cloud of about 10^7 to 10^8 electrons get produced and further accelerated with 2.5 kV once they leave the plate towards the phosphor screen where they produce a visible light spot with a diameter of a few hundred micrometer. A CCD camera images the phosphor screen with either a 25 Hz or 50 Hz frame rate. Each frame is digitized by a *Frame Threshold Supressor* (FTS). The FTP sends pixel position and light intensity to a VME-computer if a minimum intensity is reached. An event consists of a cluster of pixels and a software routine calculates the intensity weighted center position of each cluster. The spatial resolution for the components of the fragment distances perpendicular to the beam direction is therefore better than the actual pixel distance and amounts to about 0.1 mm.

The third spatial component, e.g. parallel to the beam direction, is obtained by measuring the impact time of the fragments on the detector. The measurement of the impact time is done with

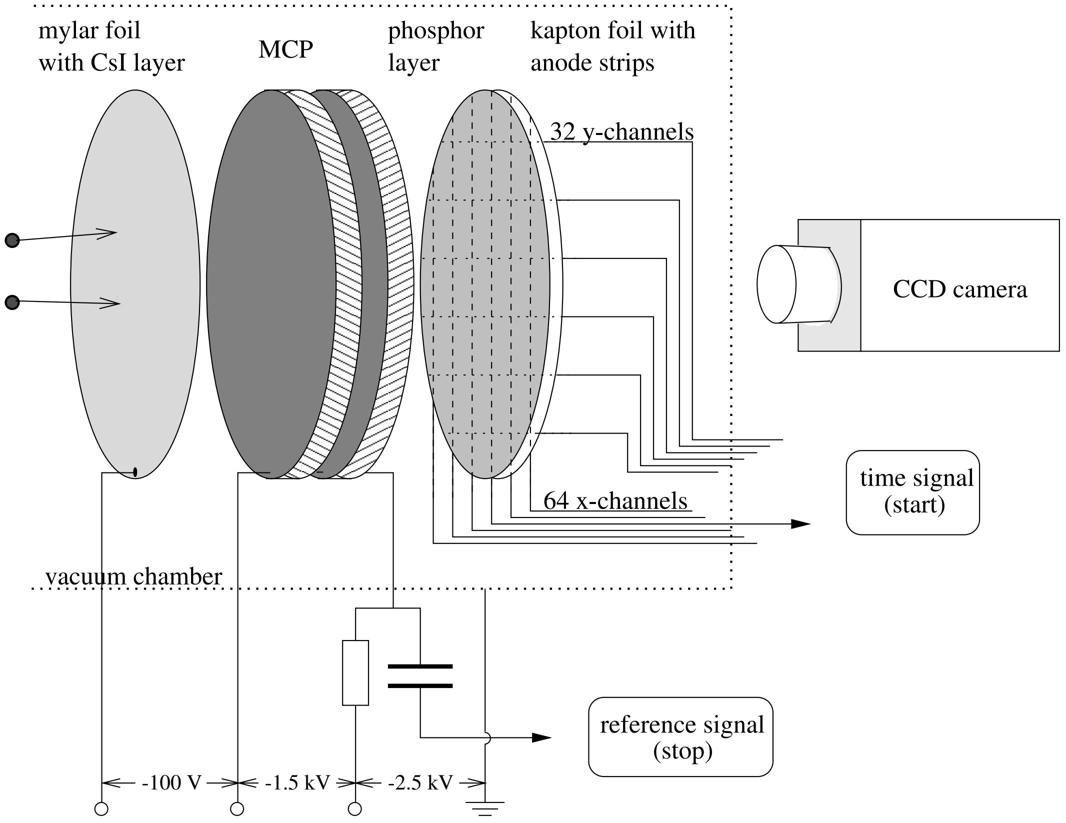

Figure 4.3: *Schematic drawing of the circular detector of the Coulomb explosion imaging system. The CCD camera and timing signals are connected to a data acquisition system consisting of a FTS, Q-ADC moduls and a VME computer. The rectangular detector system has 93 x-channels and no y-channels.*

the set of anode strips on the kapton foil (93 in case of the rectangular detector). Each strip is connected to an amplifier and a combination of a *Constant Fraction Discriminator* (CFD) and an *Analog Digital Converter* (ADC) in a CAMAC-Crate which is connected to the VME-computer. When a bunch of electrons hits the phosphor screen a fast signal in some adjacent strips is induced. Each signal triggers the CFD which gives a negative NIM-signal of 16 mA to the ADC. The ADC cumulates the current from the CFD until a common stop-signal arrives. The common stop signal is obtained from the induced signal on the back of the MCP and serves as an arbitrary definition of the zero-point time, which is sufficient since only time differences are needed. The integrated charge is digitized by the ADC and transfered to the VME-computer. A systematic study of the time resolution has been done by M. Scheffel [82] and led to the development of a new electronic board for the signal amplification coming from the anode strips. With this setup we are able to get a time resolution of about 100 ps (H_2^+ measurement) and 60 ps (D_2^+ measurement) with the old and new amplifier, respectively. A time resolution of 100 ps corresponds to a spatial resolution in beam direction (beam velocity $\sim 0.03c$) of ~ 1 mm.

A more detailed description of the detectors and the electronics has been given elsewhere [75].

4.4 The electron cooler

This section gives a short overview on the setup of the electron cooler device. Further parts deal with the properties of the electron beam and the calculation of the relative energies between the electrons and ions, so-called beam dragging effects and the relation between cross section and rate coefficient.

4.4.1 The electron beam as a cooling device

The electron cooler shown in Fig. 4.4 is used as a cooling device for the stored ion beams as well as a target for recombination experiments. The magnetic field guiding the electron beam from the electron gun to the collector is realized by five solenoidal and two toroidal coils [83]. The guiding field B_{int}[1] in the electron-ion interaction region amounts to typically $\approx 2-4\,\mathrm{mT}$. The electrons are produced by a thermocathode (diameter $D_i = 3/8''$) with a temperature of about $kT_i = 120\,\mathrm{meV}$ [84]. The emission of the electrons from the cathode is space-charge limited and the electron current I_e is given by

$$I_e = PU_{cath}^{3/2}, \tag{4.3}$$

where U_{cath} is the cathode voltage and P the perveance, which is defined by the geometry of the cathode. For both, an efficient phase-space cooling and recombination experiments a cold electron beam is needed. This can be attained by adiabatic transverse expansion of the electron beam (initial temperature $kT_{\perp i} \sim 120\,\mathrm{meV}$) in the straight section after acceleration and before the toroid section (see Fig. 4.4) [85]. The transverse electron temperature $kT_\perp$ after adiabatic expansion is

$$kT_\perp = \frac{B}{B_i} kT_{\perp i}, \tag{4.4}$$

where B_i and B are the magnetic fields prior to and after the expansion, respectively. The ratio $\alpha = B_i/B$ is called *expansion factor*[2] and it is possible to adjust it between 1 and 30 by varying B. The lowest possible transverse temperature is therefore $kT_\perp \sim 4\,\mathrm{meV}$. The electron beam diameter D_{eb} after expansion is related to the cathode diameter D_i by

$$D_{eb} = \sqrt{\frac{B_i}{B}} D_i = \sqrt{\alpha} D_i. \tag{4.5}$$

---

[1] The guiding magnetic field can be calculated from the adjusted bit-values of the solenoid$_{+2}$ (S_{+2}) coil by $B_{int} = 0.1093 * S_{+2} \times 10^{-2}\,\mathrm{mT}$.

[2] The expansion factor can be calculated from the adjusted bit-values of the gun-solenoid(S_G.) and the solenoid$_{+2}$ (S_{+2}) coil by $\alpha = 3.7422 S_G/S_{+2} + 0.003631$.

The longitudinal temperature of the electrons is reduced to $kT_{||} \sim 0.1\,\mathrm{meV}$ because of the fast acceleration [86]. Due to the different temperatures of the transverse and longitudinal component of the electron beam, the distribution of the electron velocity $\mathbf{v_e}$ is described by a *flattened* Maxwellian distribution [87], with

$$f(\mathbf{v_e}) = \frac{m_e}{2\pi kT_\perp}\left(\frac{m_e}{2\pi kT_{||}}\right)^{1/2} \times \exp\left(-\frac{m_e v_{e\perp}^2}{2kT_\perp} - \frac{m_e v_{e||}^2}{2kT_{||}}\right), \tag{4.6}$$

where $v_e = (v_{e\perp}^2 + v_{e||}^2)^{1/2}$.

The electron-ion interaction in the electron cooler gives rise to a phase-space cooling of the stored ion beam, i.e. reduction of the transverse and longitudinal momentum spread of the ions, due to the so-called electron cooling force. The phase-space cooling reduces the width of the horizontal and the vertical beam profile which can be observed as a function of the cooling time [88] using a beam profile monitor (BPM) [89]; the typical width of a cold ion beam is about 1 mm (FWHM). The cooling force is most efficient at matched electron and ion beam velocities, i.e.

$$\langle\, \mathbf{v}_i \,\rangle = \langle\, \mathbf{v}_e \,\rangle\,, \tag{4.7}$$

with the non-relativistic electron and ion energies

$$E_e = \frac{1}{2} m_e \langle\, \mathbf{v_e} \,\rangle^2 \tag{4.8}$$

and

$$E_i = \frac{1}{2} m_i \langle\, \mathbf{v_i} \,\rangle^2\,, \tag{4.9}$$

respectively. Thus, the corresponding electron energy $E_c = (m_e/m_i)E_i$ is called *cooling energy*. Electron-ion interactions in the electron cooler drag the ion beam velocity towards that of the electrons, i.e. $\langle\, \mathbf{v_i} \,\rangle = \langle\, \mathbf{v_e} \,\rangle$. The so-called *dragging forces* will be discussed in Sec. 4.4.4. Thus, the energy of the stored ion beam is determined after a certain storage time by the electron energy, with $E_i = (m_i/m_e)E_e = (m_i/m_e)E_c$.

4.4.2 The electron beam as a target for collision experiments

The electron beam can be used as a target for collision experiments by changing the electron energy E_e, i.e. changing the cathode voltage U_{cath}. It has been mentioned in the previous section, that ion beam dragging forces reduce the collision energy. Thus, the measurement time at a certain collision energy has to be short compared to the time scale on which the collision energy is significantly changed due to the dragging effects. The measurement time at a certain collision energy was typically 25 ms in the experiments presented in this work, see Sec. 4.6 for more details.

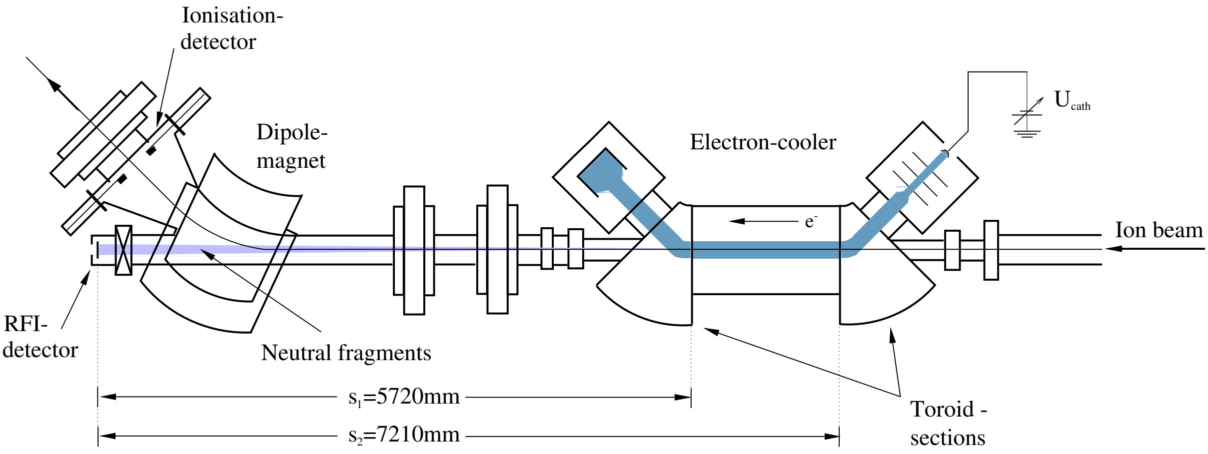

Figure 4.4: *Schematic drawing of the drift region between the electron cooler and the detector setup. Shown are the positions of the recombination fragment imaging detector (RFI detector) and the ionisation-detector. The values s_1 and s_2 correspond to the minimum and maximum flight distances of the neutral fragments from the DR process.*

We define the relative electron-ion velocity $\mathbf{v}'$ as

$$\mathbf{v}' = \mathbf{v}_e - \mathbf{v}_i \tag{4.10}$$

$$\text{with} \quad v' = |\mathbf{v}'| \tag{4.11}$$

and the mean relative electron-ion velocity $\mathbf{v}$ as

$$\mathbf{v} = \langle \mathbf{v}_e \rangle - \langle \mathbf{v}_i \rangle , \tag{4.12}$$

$$\text{with} \quad v = |\mathbf{v}| = \sqrt{\langle v_e \rangle^2 + \langle v_i \rangle^2 - 2 \langle v_e \rangle \langle v_i \rangle \, cos\phi} \tag{4.13}$$

where ϕ is the angle between the electron and ion beam and $\mathbf{v}_e$ and $\mathbf{v}_i$ is the velocity of the electrons and ions, respectively. It should be mentioned that to obtain a relative velocity $v = 0$, the electron and ion beams have to be coaxial, i.e. $\phi = 0$, see Eq. 4.13. The electron mass m_e is small compared to the ion mass m_i ($m_i \approx 10^4 m_e$), i.e. the reduced mass μ of the electrons and the ions is identical with the electron mass m_e. Thus, for an angle $\phi = 0$ the relative energy E can be written as

$$E = \frac{1}{2} m_e v^2 \tag{4.14}$$

$$= \left(\sqrt{E_e} - \sqrt{E_c} \right)^2 , \tag{4.15}$$

with $E_c = (m_e/m_i)E_i$.

E_c is the *cooling energy* (see above), i.e. the electron energy at matched electron and ion velocities. After the electron cooling of the ion beam, the variance of $\mathbf{v}$ is dominated by the variance of the velocity $\mathbf{v_e}$ of the electrons.

The velocities of the molecular ions studied in the present work were small ($\beta = v_i/c \leq 5\,\%$) such that the non-relativistic approximation was sufficient. The correct relativistic expression for the electron-ion energy is [90]:

$$E \simeq E_e\left(1+\frac{E_i}{m_ic^2}\right)+\frac{m_e}{m_i}E_i-\sqrt{\left(\left(\frac{m_e}{m_i}E_i\right)^2+2m_ic^2\frac{m_e}{m_i}E_i\right)\left(\frac{E_e^2}{m_e^2c^4}+2\frac{E_e}{m_ec^2}\right)}\,. \tag{4.16}$$

The electron energy is not only determined by the cathode voltage at high electron densities ($n_e \sim 10^6 - 10^7\,\mathrm{cm}^{-3}$). The cathode voltage felt by the electrons in the inner part of the electron beam is screened by electrons further outside and the effective electron energy E_e is reduced by about 10 %. The electron energy $E_e(r)$ as a function of the distance r from the beam center is modified by a space-charge potential $U_{sc}(r)$ and can be expressed by

$$E_e(r) = eU_{cath} - eU_{sc}(r, U_{cath}). \tag{4.17}$$

The density profile $n_e(r)$ of the electron beam is in a good approximation homogeneous [88] and can be calculated from the electron current I_e by,

$$n_e = \frac{I_e}{ev_e\pi R_{eb}^2}. \tag{4.18}$$

Then, the shape of $U_{sc}(r)$ is parabolic inside and logarithmic outside the electron beam (radius R_{eb}) with respect to the symmetry axis, defined by the electron beam direction. Denoting the diameter of the beam tube by $R_T (R_T = 100\,\mathrm{mm})$ the space-charge potential is given by

$$U_{sc}(r) = \begin{cases} \frac{en_eR_{eb}^2}{4\epsilon_0}\left(1-\frac{r^2}{R_{eb}^2}+2\ln\frac{R_T}{R_{eb}}\right) & : \; r \leq R_{eb} \\ \frac{en_eR_{eb}^2}{2\epsilon_0}\ln\frac{R_T}{r} & : \; r \geq R_{eb}\;. \end{cases} \tag{4.19}$$

The constant ϵ_0 denotes the permittivity of the free space. The electron beam diameter in the presented experiments varied from 25 mm to 35 mm whereas the diameter of the phase-space cooled ion beams were typically ~ 1 mm (FWHM).

The electron density depends on the electron velocity v_e (Eq. 4.18) which again depends, via the space-charge potential, on the electron density (Eq. 4.19). Therefore, an iterative calculation of v_e is needed. The ion energy at cooling (i.e. $v_e = v_i$) can be determined from the electron energy function $E_e(r)$. Taking into account the Gaussian-like space-charge profile of the ion beam with a radius σ the mean electron energy $\langle E_e \rangle$ is given by

$$\langle E_e \rangle = \frac{\int E_e(r)e^{-\frac{1}{2}\left(\frac{r}{\sigma}\right)^2}2\pi r dr}{\int e^{-\frac{1}{2}\left(\frac{r}{\sigma}\right)^2}2\pi r dr}. \tag{4.20}$$

The specific electron beam properties in the different experiments are presented in Tab. 4.2. The electron energy E_e corresponds to the energy in the beam center. The relative collision energy

	Molecule	E_i MeV	U_{cath} V	I_e mA	E_e eV	n_e $10^6\,\mathrm{cm}^{-3}$	$kT_\perp$ meV	R_{eb} mm	α	B_{int} mT
	LiH^+	6.024	452.3	11.2	411.9	8.48	11.86	14.77	9.61	4.19
	$^4HeH^+$	2.410	293.9	5.9	262.4	13.44	28.50	9.53	4.00	2.09
CD	H_2^+	0.996	300.0	6.5	271.1	6.07	11.88	14.77	9.61	4.19
DR	H_2^+	1.996	584.4	15.3	535.3	10.85	12.67	14.29	9.00	4.20
CS	H_2^+	3.119	926.9	31.0	849.1	16.35	11.86	14.77	9.61	4.19
CD	D_2^+	1.934	289.8	5.9	263.2	5.55	11.79	14.81	9.67	4.19
CS	D_2^+	6.328	939.5	31.4	861.3	16.44	11.86	14.77	9.61	4.19

Table 4.2: *Electron beam parameters for the different recombination experiments at relative energy $E = 0\,\mathrm{eV}$, i.e. matching velocity of electron and ion beam. The expansion factor of the electron beam is given by the value α and the guiding magnetic field in the interaction region by B_{int}. The longitudinal temperature in all experiments was $kT_{||} \approx 0.1\,\mathrm{meV}$. Type of experiment: (CD): Combined CEI and DR; (DR) DR; (CS) cross section.*

can be changed by varying the cathode voltage. For typical electron beam parameters (see Tab. 4.2) the mean electron energy $\langle E_e \rangle$ is in a good approximation identical with $E_e(r = 0)$ and the ratio between $\langle E_e \rangle$ and the adjusted electron energy (i.e. eU_{cath}) is $\langle E_e \rangle / eU_{cath} \approx 90\,\%$. The variance of E_e is expected to be of the same order, i.e. $\sigma(E_e)/E_e \approx 10^{-5}$ and results in a negligible smearing of the electron velocity distribution.

4.4.3 Rate coefficients and cross sections

The rate coefficient $\alpha(E)$, e.g. for the DR with electrons at a relative collision energy E, can be calculated from a measured fragment rate $R(E)$ by

$$\alpha(E) = \frac{R(E)}{n_e(E)\eta N_i}, \tag{4.21}$$

where n_e is the electron density and $\eta = L/C$ is the ratio between the length of the merged electron-ion beam in the electron cooler ($L = s_2 - s_1 \approx 1.5\,\mathrm{m}$, see Fig. 4.4) and the circumference of the TSR ($C = 55.4\,\mathrm{m}$). The electron density n_e can be derived from the measured electron current I_e and the radius of the electron beam R_{eb} using Eq. 4.18.

As has been mentioned before the acceleration and expansion of the electron beam leads to different temperatures in the transverse and longitudinal component and the electron velocity distribution is described by the *flattened* Maxwellian distribution in Eq. 4.6. The measured DR rate coefficient $\alpha(E)$ is a convolution of the DR cross section $\sigma(E)$ with the *flattened* Maxwellian velocity distribution $f(v, \mathbf{v}')$ and given by

$$\alpha(E) = \langle \sigma(v')v' \rangle = \int \sigma(v')v' f(v, \mathbf{v}') d^3v', \tag{4.22}$$

with $d^3v' = 2\pi v'_\perp dv'_\perp dv'_{||}$.

The electron velocity distribution function at a collision energy $E \neq 0$ is given by

$$f(v, \mathbf{v}') = \frac{m_e}{2\pi kT_\perp} \left(\frac{m_e}{2\pi kT_{||}}\right)^{1/2} \times \exp\left(-\frac{m_e v'^2_\perp}{2kT_\perp} - \frac{m_e(v'_{||} - v)^2}{2kT_{||}}\right). \tag{4.23}$$

where $v' = (v'^2_\perp + v'^2_{||})^{1/2}$.

For collision energies E larger than $kT_\perp$, the cross section $\sigma(v)$ can be directly obtained from the ratio between $\langle \sigma(v)v \rangle$ and the collision velocity v.

The shape of the electron energy distribution in the center-of-mass frame of reference is dependent on the collision energy E [87]. At low E (i.e. $E \ll (kT_\perp)^2/(kT_{||}) \approx 0.2\,\mathrm{meV}$) the energy distribution is asymmetric and the width is limited by the transversal electron temperature ($kT_{||} \approx 12\,\mathrm{meV}$). At large E the distribution is nearly Gaussian with a full width at half maximum (FWHM) of $\Delta E \approx 4(EkT_{||}\ln 2)^{1/2}(\approx 0.1\,\mathrm{eV}$ for $E = 10\,\mathrm{eV})$. Hence, the resolution for measuring narrow resonances decreases with increasing relative energy E.

The measured rate coefficients α_{aniso} at $E = 0\,\mathrm{eV}$ is convoluted with a flattened Maxwellian velocity distribution (characterized by $kT_{||} \leq kT_\perp$) and can be compared to a rate coefficient α_{iso}, convoluted with an isotropic Maxwellian velocity distributions (i.e. $kT_{||} = kT_\perp$), as both rate coefficients are related by [91]:

$$\alpha_{iso} = \alpha_{aniso} \left[\sqrt{\frac{t+1}{t}} \arctan\sqrt{t}\right]^{-1}, \tag{4.24}$$

with the anisotropy parameter t, defined as:

$$t = \frac{kT_\perp - kT_{||}}{kT_{||}}. \tag{4.25}$$

If the longitudinal temperature $kT_{||}$ is much lower than the transverse temperature $kT_\perp$, Eq. 4.24 reduces to

$$\alpha_{iso} \approx \alpha_{aniso} \left(\frac{\pi}{2}\right)^{-1}. \tag{4.26}$$

4.4.4 Effects changing the relative collision energy

Ion beam dragging

A process influencing the relative collision energy E is the so-called *beam dragging* which will be discussed in this part.

An ion beam stored in the TSR circulates with a revolution time of $\sim 5\,\mu$s and interacts each time with the electron beam when passing the electron cooler. In each collisione this interaction reduces the relative energy between the electrons and ions. This results in a dragging of the ion beam by the electrons towards the electron beam velocity and is therefore named *beam dragging.*

The relative collision energy E is given by Eq. 4.15:

$$E = \left(\sqrt{E_e} - \sqrt{\frac{m_e}{m_i}E_i}\right)^2 ,$$

where E_e and E_i are the electron and ion energy, respectively.
The shift of the relative collision energy with respect to changes in the ion energy is given by:

$$dE = -\sqrt{\frac{m_e}{m_i}}\sqrt{\frac{E}{E_i}}|dE_i|, \tag{4.27}$$

i.e.

$$dE = -\sqrt{EE_i\frac{m_e}{m_i}}\frac{1}{E_i}|dE_i|, \tag{4.28}$$

with $dE < 0$.
Consider a single collision of an ion of charge Z with an electron at a collision velocity v. The momentum transfer is then approximatively given by [92]

$$\Delta p = \frac{2Ze^2}{4\pi\epsilon_0 vb}, \tag{4.29}$$

at an impact parameter b, and the energy change of the ion is:

$$\Delta E_i(b) = \frac{(\Delta p)^2}{2m_e}. \tag{4.30}$$

Assuming a cylindric electron beam with the homogeneous density n_e, the energy change in an interval dx can then be written as (integrating over $n_e dA = n_e 2\pi b db$):

$$\left|\frac{dE_i}{dx}\right| = 2\pi\int_{b_{min}}^{b_{max}} n_e b\Delta E_i(b)\,db = \frac{4\pi Z^2 e^4}{(4\pi\epsilon_0)^2 m_e v^2}\, n_e\, L_C(v), \tag{4.31}$$

where $L_C(v)$ is the so-called Coulomb logarithm, defined as:

$$L_C := \ln\frac{b_{max}}{b_{min}}, \tag{4.32}$$

where b_{min} and b_{max} is the minimum and the maximum impact parameter, respectively. A typical value for the Coulomb-logarithm is $L_C \approx 10$ [88]
The change of the ion energy with time can be derived from Eq. 4.31 using $dx = v_i\,dt$ and taking into account the relative overlap $\eta = L/C$ of the electron beam with the ion beam in the storage ring. This transformation leads to the expression

$$\left|\frac{dE_i}{dt}\right| = \eta v_i \left|\frac{dE_i}{dx}\right|. \tag{4.33}$$

The relative change in the ion energy with time is therefore given by

$$\frac{1}{E_i}\left|\frac{dE_i}{dt}\right| = \frac{4\pi e^4}{(4\pi\epsilon_0)^2} Z^2 \eta L_C n_e \frac{v_i}{2EE_i} \tag{4.34}$$

$$= 2.606 \times 10^{-13}\mathrm{eV}^2\mathrm{cm}^2 Z^2 \eta L_C n_e \frac{v_i}{2EE_i} \tag{4.35}$$

and the shift in the collision energy dE can be calculated combining Eq. 4.28 and Eq. 4.35. For a more detailed study of the beam dragging the velocity distribution $f(v, \mathbf{v}')$ (Eq. 4.23) of the electrons as well as effects of the longitudinal magnetic fields in the electron cooler have to be considered [88, 92, 93].

Choosing typical electron and ion beam parameters (see Tab. 4.2) an adjusted collision energy $E = 100\,\mathrm{meV}$ changes by $dE \approx 1\,\mathrm{meV}$ in about 100 ms. Thus, the electron energy and therefore the collision energy gets switched between the measurement energy ($E > 0\,\mathrm{eV}$) and the cooling energy (i.e. $E = 0\,\mathrm{eV}$) to minimize ion beam dragging effects in rate coefficient measurements.

Toroid effects

The angle between the electron and ion beam is not zero in the toroid regions of the electron cooler (see Fig. 4.4). The non-relativistic relative electron-ion energy for a collision angle ϕ can be derived from Eq. 4.13 and results in

$$E = E_e + E_c - 2\sqrt{E_e E_c}\cos\phi, \tag{4.36}$$

where E_e is the electron energy in the laboratory frame-of-reference and $E_c = (m_e/m_i)E_i$. The electron beam moves inside the toroid section on a curvature with a radius $R_{\mathrm{Toroid}} = 800\,\mathrm{mm}$ changing the collision angle ϕ as a function of the position along the ion beam.

Moreover, the space-charge potential $U_{sc}(r)$ is changing with r, i.e. the distance to the center of the electron beam, see Eq. 4.19. It can be shown [94], that the relative electron energy E_{Toroid} inside the toroid section as a function of the position ΔL is

$$E_{\mathrm{Toroid}}(\Delta L) = E_c + E_e(r) - \sqrt{4E_c E_e(r)}\frac{R_{\mathrm{Toroid}}}{\sqrt{R^2_{\mathrm{Toroid}} + \Delta L^2}}, \tag{4.37}$$

with

$$r = \sqrt{R^2_{\mathrm{Toroid}} + \Delta L^2} - R_{\mathrm{Toroid}} \tag{4.38}$$

and $0 \leq \Delta L \leq \Delta L_{max}$. The length ΔL is maximal if $r = R_{eb}$, the radius of the electron beam, and given by

$$\Delta L_{max} = \sqrt{(R_{eb} + R_{Toroid})^2 - R^2_{Toroid}}. \tag{4.39}$$

The position ΔL is defined as the distance from the position where the angle between the electron and ion beam is zero and the projected position of recombination onto the ion beam axis, see Ref. [94] for a more detailed description. As can be seen from Eq. 4.37, $E_{\text{Toroid}} = 0$ for $\Delta L = E$ and is increasing with ΔL. At a collision energy $E = 0\,\text{eV}$, an ion beam energy $E_i \approx 2\,\text{MeV}$ and an electron beam radius $R_{eb} = 14\,\text{mm}$ the maximal change in the collision energy is $E_{Toroid} \approx 18\,\text{eV}$ at $\Delta L_{max} \approx 150\,\text{mm}$. The length where the electron-ion beams are collinear in the electron cooler is about $L = 1500\,\text{mm}$. The effects in the toroid region can be minimized by decreasing the size of the electron beam (R_{eb}), i.e. applying a small expansion factor α (Eq. 4.5). The increased collision energy in the toroid sections is usually not to critical for DR rate coefficient measurements at low collision energies ($E \leq 0.01\,\text{meV}$) due to the low DR cross section at collision energies of several eV, see for instance Fig. 6.6 in Sec. 6.2.1. The described effects in the toroid sections are taken into account in measurements of DR rate coefficient spectra using an iterative procedure, see discussion in Sec. 5.3.2.

4.5 DR fragment detector systems

The investigation of the DR requires detector systems which allow for determine either the final states of the dissociation fragments or the initial-to-final state correlation between the molecular ion and the atomic fragments. Two methods used for the study of DR will be discussed in this section.

The initial-to-final state correlation is determined by a specific kinetic energy release which is related to a fragment distance and can be measured using the recombination fragment imaging (RFI) technique [39], see also Sec. 3.3.

The RFI technique fails at low kinetic energy releases. i.e. small fragment distances, or if one atomic fragment is in a Rydberg state and gets field ionized before hitting the detector. The fieldionization in the fringe field of a dipole magnet occurs for each Rydberg state at a defined position and gives therefore a Rydberg state specific trajectory of the atomic ions.

This part will give a brief overview on the RFI technique and will present a detector system which allows for studying the Rydberg state of atomic fragment produced by DR.

4.5.1 The projected fragment imaging

The setup for the RFI is shown in Fig. 4.5 and consists of a MCP (diameter 80 mm) with a phosphor screen, some readout electronics and a data acquisition unit. The front side of the MCP was grounded and the back side of the MCP and the phosphor screen were set to +1.7 kV and +3.2 kV, respectively. The operating voltage of the photomultiplier (PMT) was $U_{PMT} = 500\,\text{V}$ at a current of $I_{PMT} = 0.13\,\text{mA}$.

A particle hitting the MPC produces a light spot on the phosphor screen (functionality, see Sec. 4.3). The output of the PMT oriented to the phosphor screen gives a short voltage signal (maximum voltage $\sim -200\,\text{mV}$) with a decay time of about 5 ms. This signal is amplified and shaped by a module (*ORTEC 572, Amplifier*). The unipolar output of that module is connected

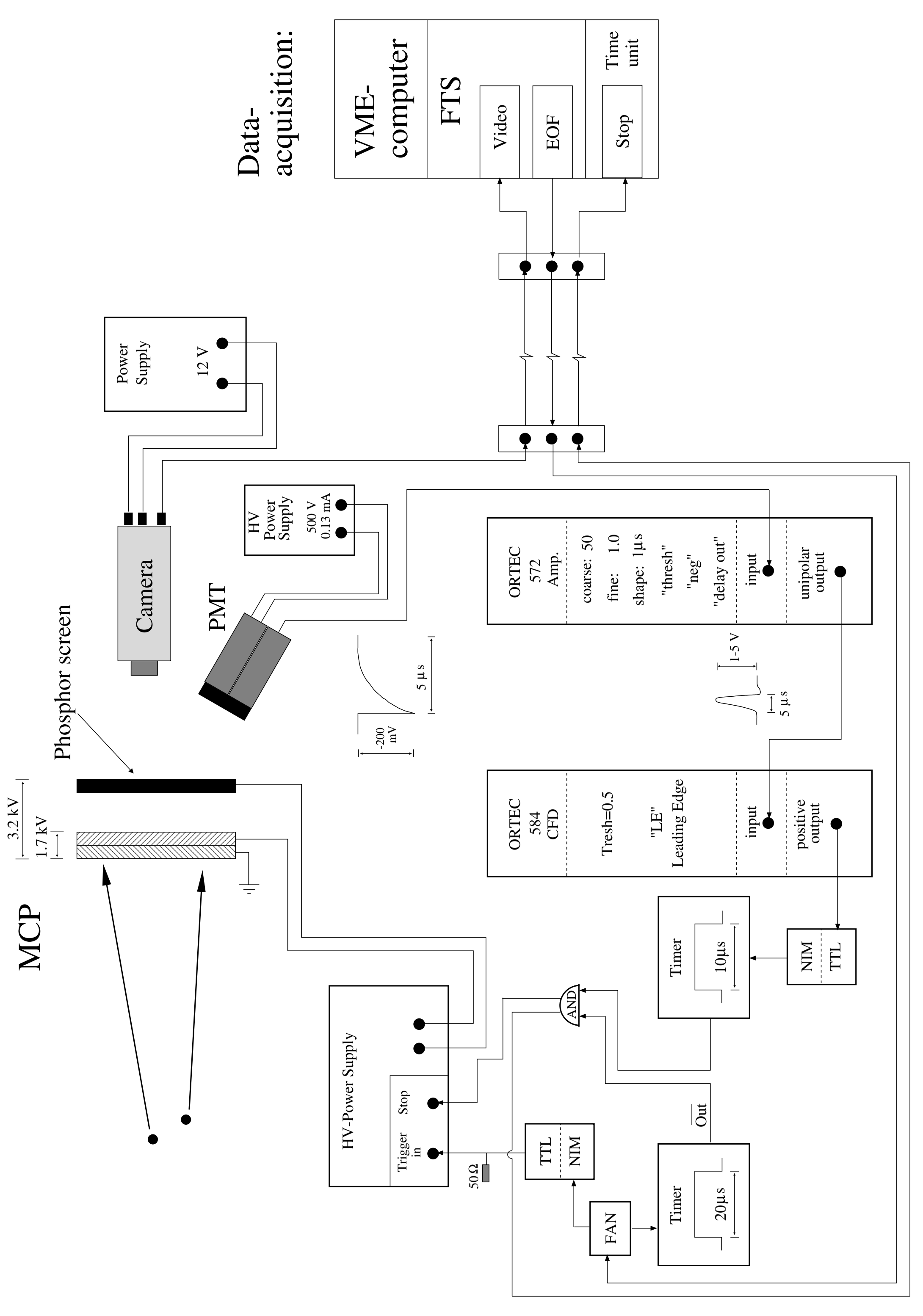

Figure 4.5: *Schematic drawing of the RFI setup.*

to a *Constant Fraction Discriminator* (CFD) (*ORTEC 584*). From the positive output signal of the CFD a gate signal (width 20 μs) is produced in a *timer-unit.* This gate signal is connected to an *AND-unit.*

The light spots on the phosphor screen are also imaged by a 50 Hz CCD camera working on an *interlaced mode*, i.e. the readout of odd and even frames occurs every 20 ms corresponding to an exposure time of 40 ms for each frame. Working in the so-called *25 Hz-mode* only even or odd frames are processed. The arrival time between two particles belonging to a DR event is several ns, whereas the switching time of the phosphor screen is about 1 μs. Each frame is processed by a *Frame Threshold Suppressor* (FTS) which is connected to a VME-computer providing the impact position of the particles on the MCP in units of pixels, see Sec. 4.3 for more details. The FTP sends a *End-of-Frame* (EOF) signal which is branched by a *logical fan-out-unit* into two signals. One signal switches on the high voltage of the phosphor screen and the second signal triggers a *timer-unit* giving a gate signal (width 20 μs). The inverse gate signal and the output gate signal from the other *timer-unit* (coming from the CFD) are connected to an *AND-unit* which again is connected to the switch of the power supply for the high voltage of the phosphor screen and to the data acquisition system which assigns to each event the time elapsed since the ion beam injection. Each time the *AND-unit* gives an output signal the high voltage of the phosphor screen is turned off (switching time $\sim 1\,\mu$s). Due to the setting it takes at least 20 μs from the EOF until the phosphor screen can be switched off. This dead-time is necessary since the switching of the high voltage induces a signal in the PMT such that each time the high voltage is turned on an "artificial" event is seen turning off immediately the high voltage again. If the inverse of the DR rate is small compared to the switching time of the phosphor only particles belonging to one DR event are seen in each frame. The spatial resolution of the RFI setup is ~ 0.1 mm, whereas the minimum distance of two clusters of pixels has to be ~ 1.5 mm to be distinguishable. Furthermore descriptions of the image processing is given in Ref. [94] where also a detector setup for measuring three-dimensional fragment distances is discussed.

4.5.2 The MCP detector for ion fragment measurements

The motional electric field felt by the neutral particles passing the dipole is proportional to the strength of the magnetic fringe field, see measured fringe field from Ref. [95] shown in Fig. 4.7. The neutral atoms enter the fringe field of the dipole magnet and get deflected once they undergo field ionisation. The critical electric field for field ionisation to occur is proportional to $1/n^4$, where n is the principal quantum number of the atom. The impact position of field ionized atoms at the MCP-detector is thus dependent on its Rydberg state. The rate of neutral particles passing straight through the dipole can be measured by a surface barrier detector (SBD) (size $40 \times 60\,\mathrm{mm}^2$).

The dipole chamber, the RFI-detector and the MCP-detector for atomic ions are shown schematically in Fig. 4.6. The molecular ions move in the dipole magnet on a curvature with a radius of

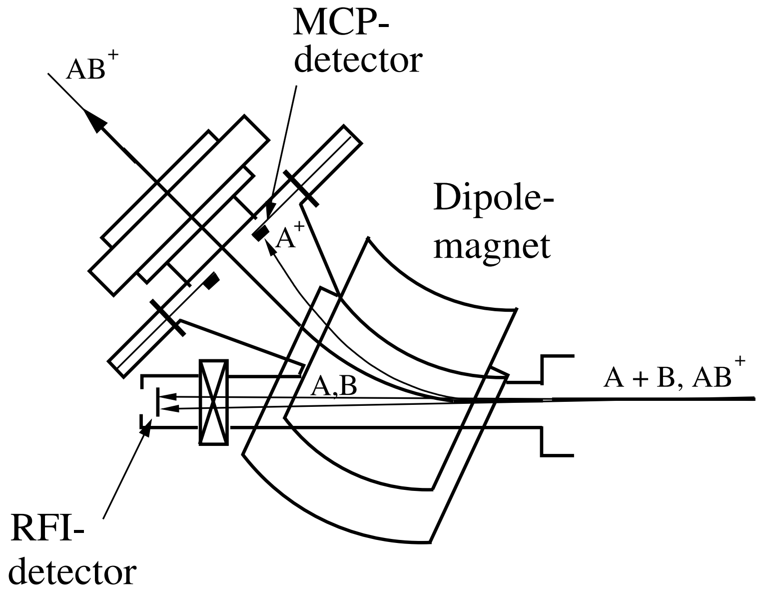

Figure 4.6: *Schematic drawing of the dipole chamber and the detectors. For the measurement of field ionized fragments (A^+) a MCP-(Multi Channel Plate)detector with spatial resolution was used. The neutral fragments (A,B) passing the dipole magnet hit the RFI-detector.*

$\rho = 1.15\,\mathrm{m}$ and get deflected by $\phi = 45°$, whereas a field ionized atom moves on a trajectory with a reduced radius $\rho_A = \rho m_A/(m_A + m_B)$; m_A and m_B are the masses of the field ionized and the neutral DR fragment, respectively. If the molecular ion ($m_i = m_A + m_B$) is much heavier than the field ionized fragment, the radius ρ_A becomes rather small and the fragment cannot reach the MCP-detector. The length of the dipole magnet is $d = 88\,\mathrm{cm}$ and the distance from the edge of the dipole magnet to the position where the MCP-detector crosses the ion beam is $l = 69\,\mathrm{cm}$. The MCP detector is movable perpendicular to the ion beam axis with an accuracy better than 1 mm.

The MCP detector consists of two MCPs (Chevron geometry) with an active diameter of 2.5 cm and a resistive anode which is connected to some electronics responsible for the calculation of the impact position, see Fig. 4.8. The electronics consists of a set of pre-amplifier for each of the four wires connected to the edges of the anode and a *Position-Computer* 2502A from Quantar Technology Inc. which calculates the impact position of the electrons on the anode from the ratio of the four voltage signals. The Position-Computer has two analog and two digital outputs (8 bit for x- and y-direction). Events on a detector can be visualized by connecting the analog outputs to a two channel oscilloscope and displaying channel one versus channel two. The spatial information about the impact position on the detector can be obtained using a CCD camera for taking images of the display of the oscilloscope and using the readout electronics discussed in Sec. 4.5.1. The phosphor screen is here replaced by the display of the oscilloscope. More information about the detector can be found in Ref. [96].

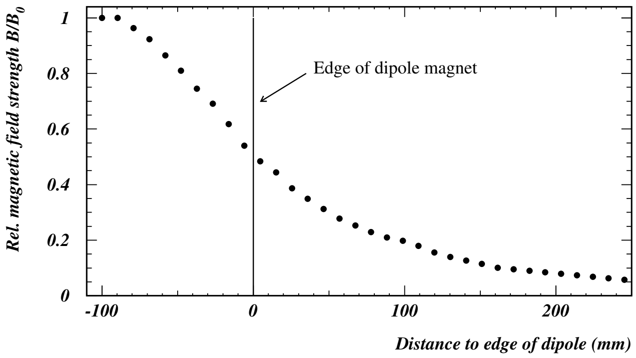

Figure 4.7: *Measured relative magnetic field strength in the fringe field of the dipole magnet as a function of the distance to the edge of the dipole; data taken from Ref. [95].*

4.6 Measurement of absolute rate coefficients

To measure absolute rate coefficients, e.g. for the DR of molecular ions with electrons, the storage ring technique turned out to be a powerful tool in the beginning of the early 90's. The stored molecular ions ($E_i = 1/2mv_i^2$) can be merged with an intense (density $n_e = 10^6 - 10^7\,\mathrm{cm}^{-3}$) and cold ($kT_\perp \approx 10 - 15\,\mathrm{meV}$, $kT_{||} \approx 0.1\,\mathrm{meV}$) electron beam inside the so-called electron cooler on a length of about 1.5 m. The neutral recombination fragments can be measured using an energy resolving surface barrier detector (SBD) (size $40\times60\,\mathrm{mm}^2$) down-stream the electron cooler. The energy resolution allows to distinguish between fragments belonging to DR and fragments from scattering with residual gas molecules in the storage ring. In the latter case usually only one of the two constituents of the molecular ion hits the detector and deposits therefore only part of the total molecular ion energy. By setting a window on the measured energy spectra around the peak corresponding to the total ion energy the DR fragment rate R can be obtained by normalizing the integrated number of events to the total measurement time. In case of the recombination of a molecular ion AB$^+$ the DR rate coefficient $\alpha(E)$ as a function of the collision energy E is given by

$$\alpha(E) = \frac{R_{AB}}{n_e(E)\eta N_i}, \tag{4.40}$$

where $n_e(E)$ is the electron density, N_i the number of stored ions and $\eta = 0.0269 \pm 0.0002$ the ratio between the overlap length of the electrons-ion beam in the electron cooler $l = 1.49\pm0.01\,\mathrm{m}$ and the ring circumference $L = 55.4\,\mathrm{m}$. The electron density varies with the adjusted relative collision energy, see Sec. 4.4. The number N_i of stored molecular ions is related to the ion current I_i by

$$N_i = \frac{I_i}{qef}, \tag{4.41}$$

with the elementary charge e, the charge state q of the ions and the orbital frequency $f = v_i/L$. The orbital frequency is obtained using a *Schottky* pickup electrode and ion currents higher than $1\,\mu A$ are measured by a *DC transformator*. The limitation of the sensitivity to ion beam currents higher than $1\,\mu A$ makes it difficult to measure absolute rate coefficients, as will be discussed in

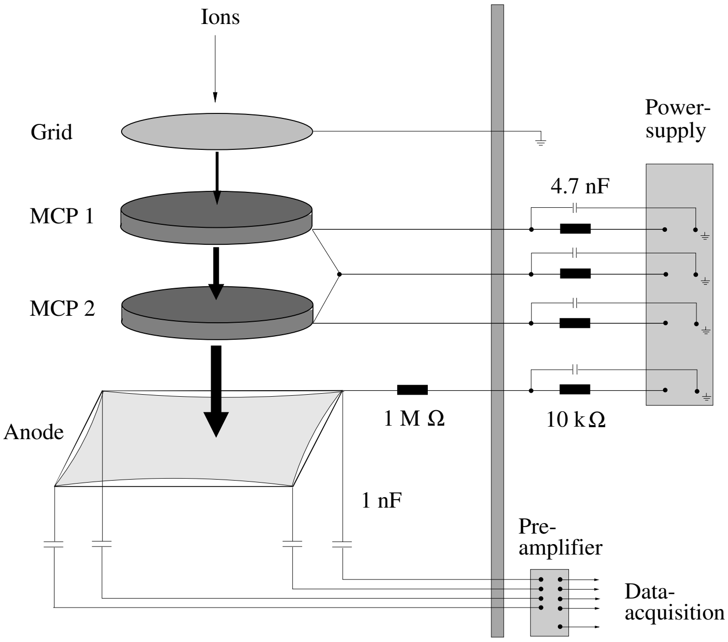

Figure 4.8: *Schematic drawing of the MCP detector. The spatial resolution is obtained by the resistive anode together with the* Position-Computer *2502A from Quantar Technology Inc. which is not shown here.*

Sec. 5.3.2.

4.6.1 Setup and data acquisition

In this section the measurement scheme as well as the setup for the measurement of DR rate coefficients will be briefly discussed, see Fig. 4.9 for a schematic drawing of the setup.

To obtain a DR rate coefficient the rate of DR fragments as well as the number of stored ions has to be measured, see Eq. 4.40. The number of ions in the ring is proportional to the ion current, see Eq. 4.41 which can either be directly measured by a DC transformator (for $I_i > 1\,\mu\text{A}$) or indirectly by the trigger signal rate from the beam profile monitor (BPM). The output voltage of the DC transformator is converted into a frequency by a volt-to-frequency converter (VFC). The measurement scheme is as follows.

At each injection the offset voltage of the electron cooler is set to 0 Volt, which is also called cooling voltage. At this voltage the ion beam gets phase-space cooled and reduces to a Gaussian-like shape with a size of 1 mm (FWHM). After a defined pre-cooling time the data acquisition gets started by a CAMAC interrupt (LAM 1)[3]. To avoid beam dragging effects, see Sec. 4.4, the electron cooler voltage is cyclic changed between the *reference*, the *measurement* and the *cooling* voltage every 25 ms; this procedure is called *wobbling.*

In the first step the offset voltage of the electron cooler is set to the reference voltage (REF) by the data acquisition software which also triggers a Gate Generator (GG). The GG is set such that it creates a gate signal with a width of 20 ms after a delay of 5 ms. The 5 ms delay is needed by the electron cooler to adjust the new voltage. While the gate is set the trigger signal from

---

[3] **LAM** stands for **L**ook **A**t **M**e

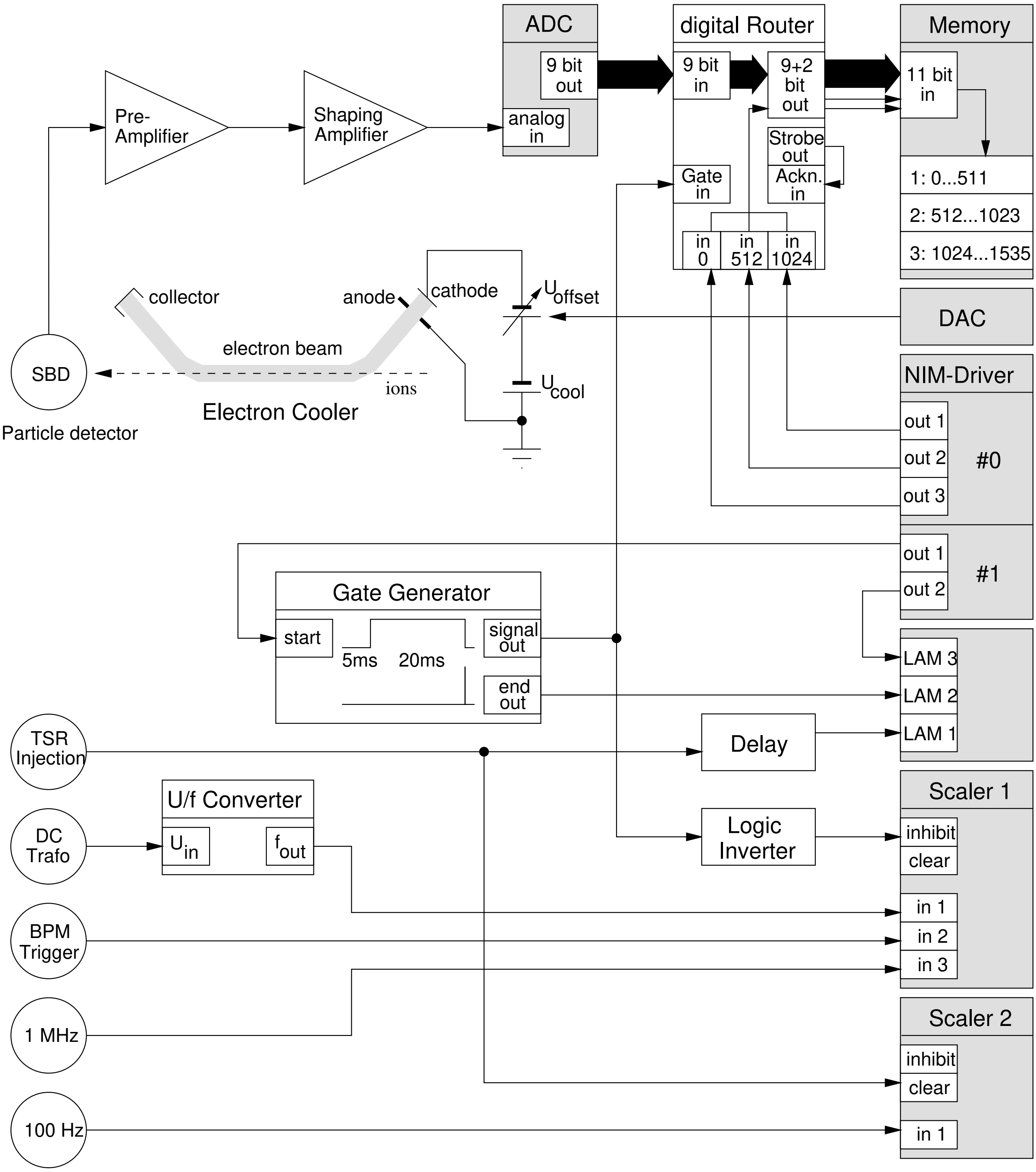

Figure 4.9: *Schematic drawing of the setup used for DR rate coefficient measurement; grey boxes: CAMAC modules, white boxes: NIM modules and circles: input signals.*

the BPM, the signal from the DC transformer and the gating time (1 MHz clock signal) itself is fed into Scaler 1 and read into a memory module after the LAM 2, generated by the end signal from the Gate Generator. The Scaler 1 gets cleared after each read-out. In the second and third step the measurement is repeated with the offset voltage set to the measurement voltage (MEAS) and the cooling voltage (COOL), respectively. This cycle is usually repeated 10 times, corresponding to a total measurement time of 0.75 s. When the last cycle is finished the software sends a LAM 3 signal instead of a LAM 2 and the data get transfered from the memory module to the measurement computer system. The data transfer lasts several ms while no data can be taken.

The data acquisition of the fragment rate is slightly different. The fragments hitting the surface barrier detector (SBD) produce an analog signal which gets pre-amplified (Pre-Amplifier) and shaped (Shaping Amplifier) before converted into a 9 bit signal by an analog-digital-converter (ADC) and fed into a Digital Router. The bit-value is proportional to the energy deposited in the SBD. The Digital Router is gated by the Gate Generator and adds 2 bit according to the wobble state (REF-MEAS-COOL) to the 9 bit from the ADC. The digital wobble state is set via a NIM-Driver by software. The 11 bit signal is send to a Histogram Memory Unit (HMU) whereas the additional 2 bit define the starting address (0 = REF, 512 = MEAS and 1024 = COOL). This way a separate histogram is assigned to each wobble state. The data in the HMU get accumulated until a LAM 3 is generated and then transfered to the measurement computer system together with the injection time information written into the Scaler 2. The Scaler 2 is connected to a 100 Hz clock signal and gets cleared with each injection.

At each injection only one defined measurement energy is set. To study the energy dependence of the rate coefficient the measurement energy is changed at each injection.

5. Recombination and super-elastic collisions of hydrogen molecular ions

This chapter is focused on the dissociative recombination (DR) and super-elastic collisions (SEC) of hydrogen molecular ions with electrons. Both processes give rise to a vibrational cooling which has been studied and used to derive absolute vibrational state specific DR and SEC rate coefficients. The unexpected large SEC rate coefficients lead to a complete vibrational cooling of an H_2^+ or D_2^+ ion beam in less than one minute of storage.

5.1 Observation of electron-induced vibrational cooling of H_2^+ and D_2^+

As discussed in Sec. 3.2, the vibrational population information can be obtained from the CEI measurements. Using a slow extraction scheme (Sec. 4.2.1), a small part of the stored beam was continuously extracted and steered towards a beam line where the CEI experiment took place. Two different target foils were used, a Formvar target of 70 Å [27] and a DLC target of 40 Å thickness [97] in the H_2^+ and D_2^+ experiment, respectively. The distance between the target foil and the detector was 2965 ± 5 mm for the H_2^+ experiment and 4615 ± 5 mm for the D_2^+ experiment.

In order to measure the vibrational state population of the H_2^+ (D_2^+) beam, and its change due to electron recombination processes, namely DR and SEC, the ion beam was stored in the ring and merged with electrons in the electron cooler for a time t. After this time, the electron beam was turned off, and a small fraction of the ion beam was continuously extracted toward the CEI setup, until the stored beam intensity became too weak and the rate of extracted ions too small. The remaining ion beam in the ring was kicked out before a new injection took place. The projected fragment distance spectra obtained with the CEI detector were measured after various times of storage and electron interaction. As pointed out in Sec. 3.2, these distributions directly represent superpositions of the initial nuclear probability distributions for the various vibrational states of H_2^+ (D_2^+) according to their population. Vibrational deexcitation of the molecular ions will hence show up as a narrowing of the measured fragment distance distributions.

In order to prove that the change in the vibrational state population is only due to the interaction

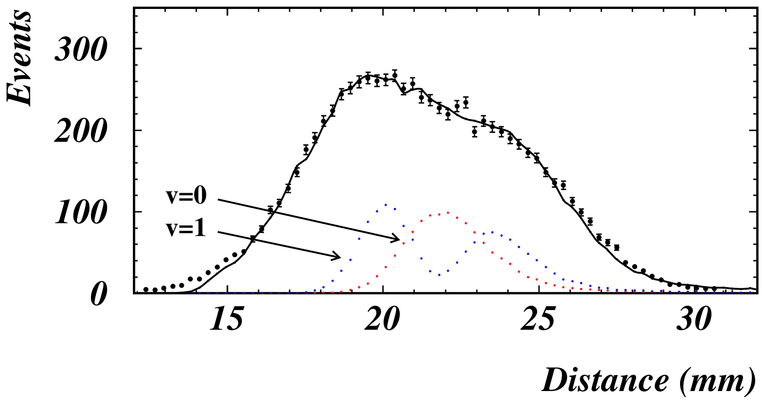

Figure 5.1: *Fragment distance spectrum from CEI of H_2^+ during the first 4 s of storage (no electron beam). The full line represents the fitted distribution $P(d;t)$ ($v_{max} = 10$) and the broken lines show the contributions for $v = 0$ and $v = 1$ as indicated.*

with the electron beam, a measurement was done with the electron beam switched off. In the experiment with the H_2^+ beam data were acquired over 12 s, whereas for D_2^+ the measurement time was, due to the higher beam intensity, up to 20 s. The acquired events were divided into three time slices. The time slices were $t = 0 - 4$ s, $t = 4 - 8$ s and $t = 8 - 12$ s for the H_2^+ measurement and $t = 0 - 6$ s, $t = 6 - 12$ s and $t = 12 - 20$ s for the experiment with the D_2^+ beam. Fig. 5.1 shows a fragment distance spectrum for H_2^+ measured during the first 4 seconds of storage. No changes in the shape of these distributions were observed during the whole storage period. The normalized fragment distance spectra were fitted by the function $P(d;t)$ (Eq. 3.12) including vibrational states $v = 0 \ldots 10$. The simulated functions $P_v^*(d)$ were derived following the procedure discussed in Sec. 3.2.3. A cosine-cut[1] was applied to the experimental and simulated data sets to diminish the influence of the wake effect as well as the worse spatial resolution parallel to the beam direction, see Sec. 3.2.2 for more details. On top of the measured fragment distance spectrum in Fig. 5.1 the fitted distribution $P(d;t)$ (full line) and the contributions of the two lowest vibrational states (broken lines) are plotted; all functions are scaled to fit the experimental spectrum. The bad agreement between the fitted function $P(d;t)$ and the measured distribution at small fragment distances is due to the contributions of higher vibrational states which were not taken into account. The results for the vibrational populations up to $v = 5$ for each of the time slices are shown in the Fig. 5.2 for the measurements with the H_2^+ and D_2^+ beam.

It can be seen that neither the collision-induced dissociation from the residual gas in the ring nor the motional electric fields of about 20 kV/cm (H_2^+) and 40 kV/cm (D_2^+) induced in the dipole magnets of the ring cause significant changes of the initial vibrational state distribution of both molecular ions. This observation is in good agreement with conclusions drawn from pure DR measurements at CRYRING [22].

---

[1] i.e. discarding events with a large component of the fragment distance parallel to the ion beam direction

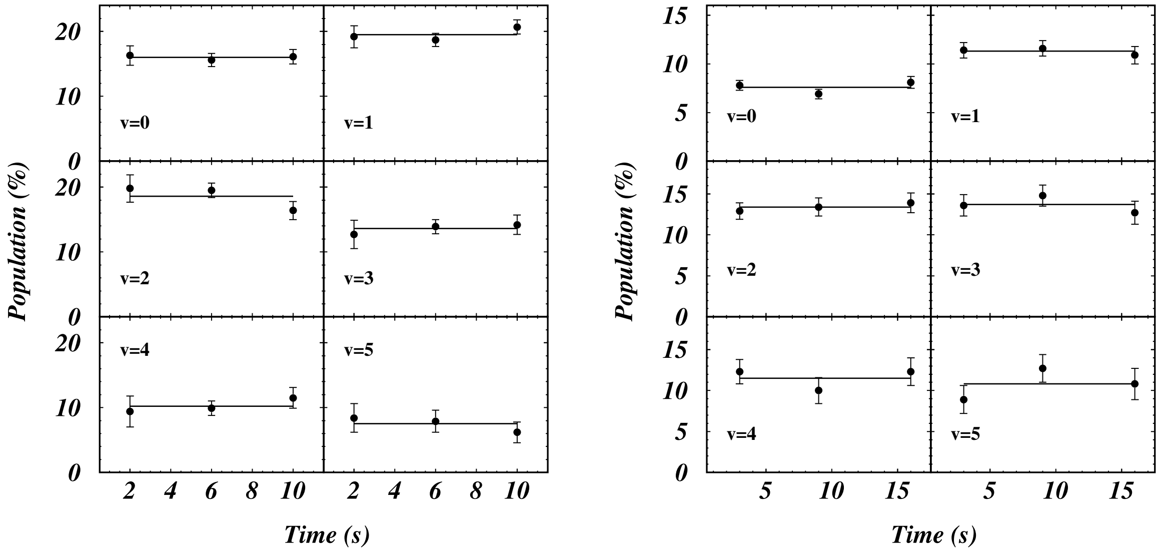

Figure 5.2: *Measured vibrational population distributions ($v = 0 - 5$) for H_2^+ (left) and D_2^+ (right) during 12 s and 20 s of storage without an electron beam. The straight lines drawn through the points are the average values of the population of each vibrational level.*

In Fig. 5.3 (H_2^+) the initial vibrational population distributions derived from the measured fragment distance spectra in absence of the electron beam and without applying time cuts are shown. Due to the strong cosine-cut many events were discarded in the measurement with the H_2^+ ion beam. To take advantage of better statistics when using all events (i.e. no cosine-cut) only the two-dimensional fragment distances D in the detector plane and not the three-dimensional fragment distances d were taken into account. The neglected spatial component is strongest influenced by the wake-effects (see. Sec. 3.1) and has a worse experimental resolution (see Sec. 4.3). The Monte-Carlo simulation was used to provide two-dimensional fragment distance distributions $P_v^*(D)$ for each vibrational state v instead of three-dimensional fragment distance distributions $P_v^*(d)$ (see Sec. 3.2.2). The vibrational population was then extracted by fitting a linear combination of the simulated functions $P_v^*(D)$ to the normalized experimental spectra, following the procedure explained in Sec 3.2.3 for the analysis of the full three-dimensional spectra. The results for H_2^+, shown in Fig. 5.3, agree within the statistical errors with the results of Fig. 5.2, obtained from the three-dimensional fragment distance spectra. For D_2^+ a fit to the three-dimensional fragment distance spectra was done. Both measured vibrational population distributions are compared with earlier results, obtained from photodissociation experiments with H_2^+ (D_2^+), carried out by Von Busch and Dunn [98], and with predicted populations calculated under the assumption that H_2^+ (D_2^+) is formed in the ion source by ionization of ground state H_2 (D_2) obeying the Franck-Condon principle. The populations of the first two vibrational states measured in the present experiments are several percent higher than the Franck-Condon

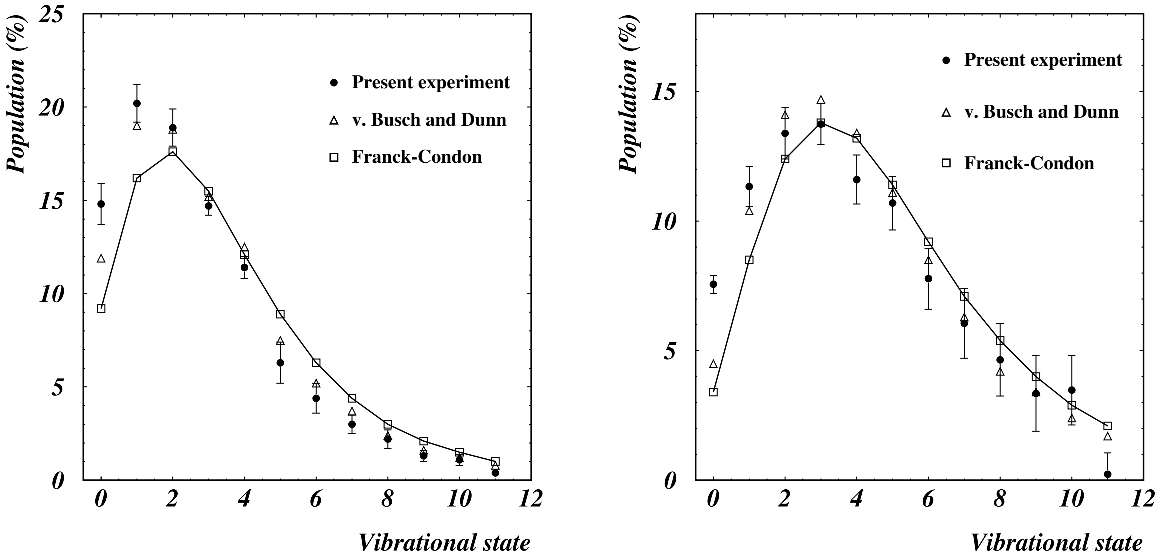

Figure 5.3: *Measured vibrational populations in the stored H_2^+ (left) and D_2^+ (right) beam as extracted from fragment distance spectra from CEI taken without electron beam. Also shown are the results from photodissociation experiments by Von Busch and Dunn [98] and from Franck-Condon calculations. The lines are drawn to guide the eye through the Franck-Condon values.*

populations. Similar deviations for the lowest vibrational states were also seen in the CEI measurement of HD^+ [34] carried out earlier with our setup. The photodissociation experiments on H_2^+ (D_2^+) by Von Busch and Dunn [98] show similar deviations from the Franck-Condon values. Possible reasons for the deviations have been discussed by Amitay *et al.* [34].

To study the influence of the DR and SEC processes on the vibrational state population, the fragment distance spectra were measured after several storage times during which the ion beam was continuously interacting with electrons. As the electron beam was turned off before starting the CEI measurement, the vibrational population distribution can be assumed to be "frozen", as was found for both molecular ions, see Fig. 5.2. Changes in the vibrational population distributions are therefore due to interactions with electron. Measured fragment distance spectra for different interaction times of electrons with H_2^+ and D_2^+ molecules are shown in Figs. 5.4 and 5.5, respectively. The experiment with D_2^+ molecules was performed with an improved experimental CEI setup which allowed a faster data acquisition and therefore higher statistics. Furthermore, the initial ion beam current stored in the TSR was higher which made it possible to obtain sufficient CEI count rates for longer interaction times with the electron-ion beam. For both molecular ions a clear change in the vibrational distribution can be seen (i.e. the width is getting narrower) with time which is an evident sign for vibrational cooling. The shift of the peak position towards higher distances is due to the anharmonicity of the potential well of the

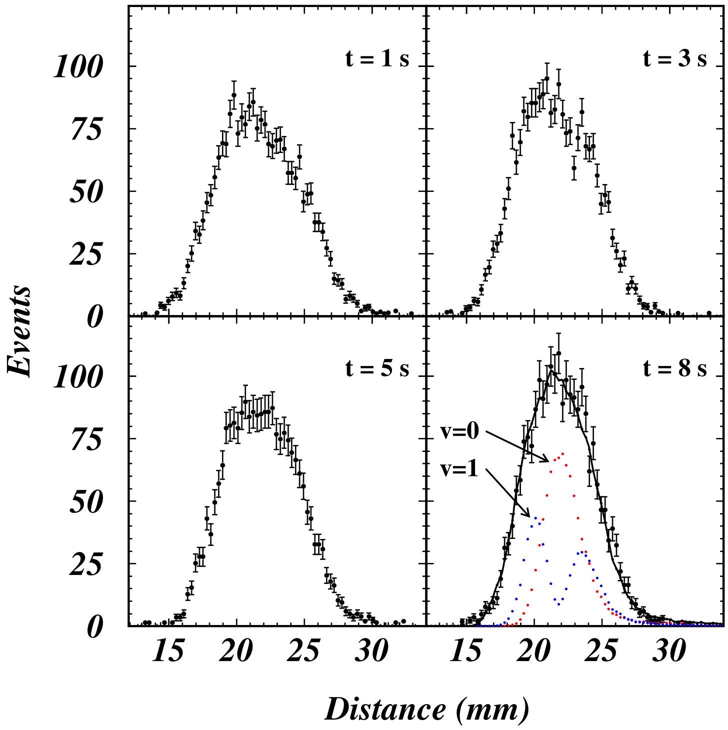

Figure 5.4: *Three-dimensional fragment distance spectra of H_2^+ from Coulomb explosion measured after different interaction times with near-zero relative energy electrons. For $t = 8\,s$ the full line represents the fitted distribution $P(d;t)$ ($v_{max} = 10$), the broken lines show the contributions from $v = 0$ and $v = 1$ as indicated.*

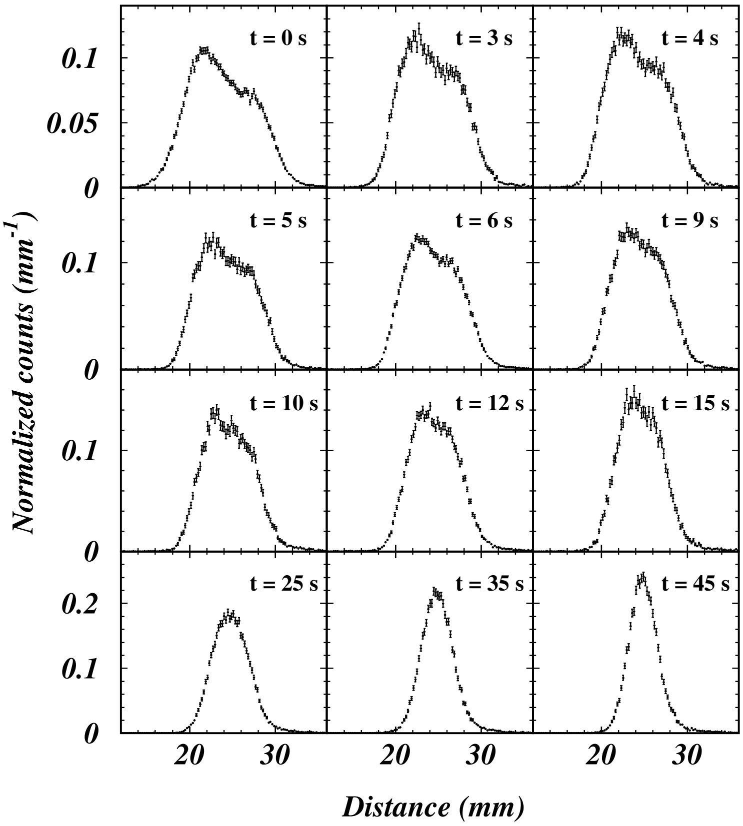

Figure 5.5: *Spectra of the three-dimensional fragment distance d for D_2^+ Coulomb explosion measured after different interaction times ($t = 0 - 45\,s$) with near-zero relative energy electrons (electron density $5.6 \times 10^{-6}\,cm^3/s$). The spectra are normalized to unit area.*

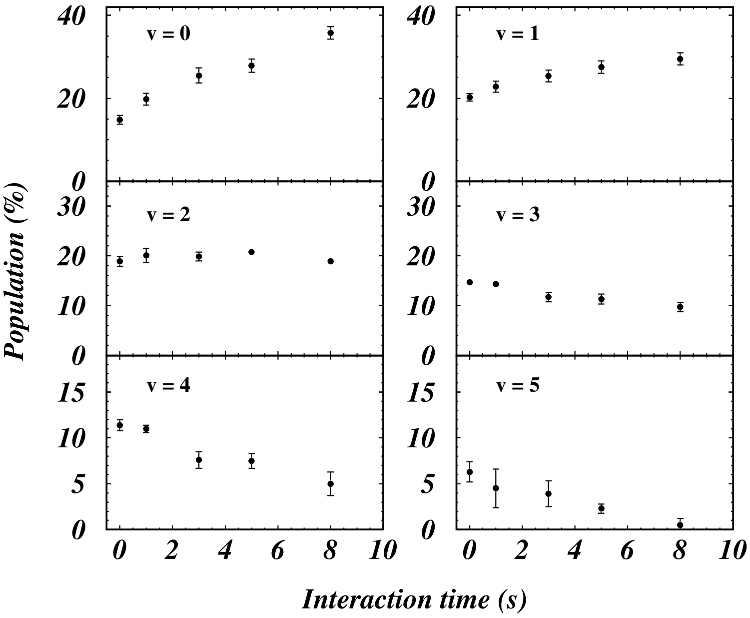

Figure 5.6: *Time evolution of the vibrational population for the first six vibrational states of* H_2^+ *as a function of the interaction time with near-zero relative energy electrons. The electron density was* $n_e = 6.07\times10^6\ cm^{-3}$.

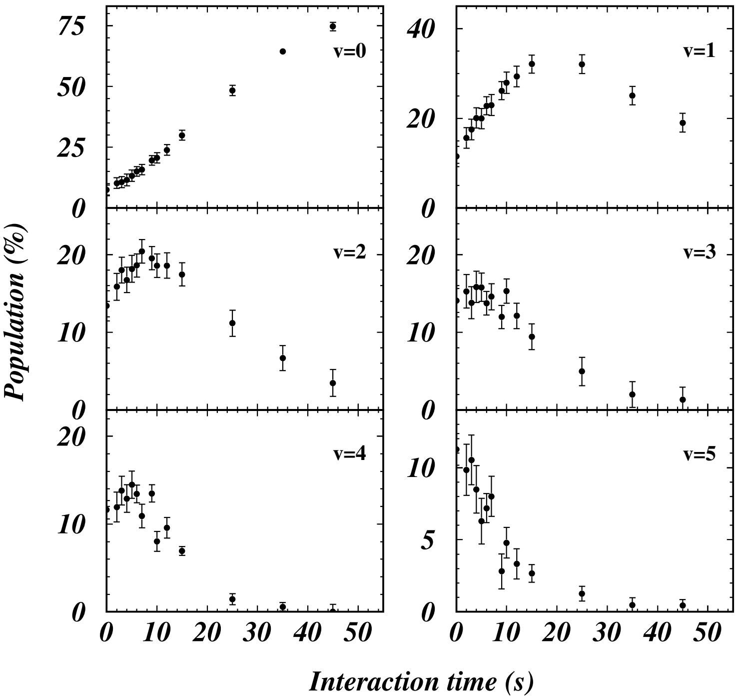

Figure 5.7: *Time evolution of the vibrational population for the first six vibrational states of* D_2^+ *as a function of the interaction time with near-zero relative energy electrons. The electron density was* $n_e = 5.55\times10^6\ cm^{-3}$.

molecular hydrogen ion causing, on the average, an increased internuclear separation which gives rise to smaller kinetic energy releases in the Coulomb explosion process and therefore smaller fragment distances.

For H_2^+ the two-dimensional theoretical fragment distance distributions $P_v^*(D)$ were again fitted to the measured two-dimensional fragment distributions (see discussion above) corresponding to different time slices, whereas for D_2^+ the full three-dimensional information was used to reveal the time evolution of the vibrational population. Figs. 5.4 and 5.5 show the three-dimensional fragment distance distributions as measured for the H_2^+ and D_2^+ beam, respectively. Only vibrational states lower than $v = 11$ have been taken into account. Additionally the fitted distribution $P(d;t)$ (solid line) and the contributions from $v = 0$ and $v = 1$ (dotted lines) are drawn. The three-dimensional fragment distance spectra for D_2^+ are normalized to unit area for a better comparison. The results are represented for the first six vibrational states of H_2^+ and D_2^+ in the Figs. 5.6 and 5.7, respectively. For both molecular ions a vibrational cooling can be seen, especially for D_2^+ the population of the vibrational ground state increases from initially less than 10 % to about 75 % in 45 s. The population of the first excited vibrational state of D_2^+ increases in the first 20 s to almost 35 % and decreases at longer storage times. After about 25 s only the lowest four vibrational states of D_2^+ are populated. Both experiments cannot directly be compared due to different initial vibrational population distributions (Fig. 5.3) and electron densities.

5.2 Vibrational state specific relative DR rate coefficients for H_2^+ and D_2^+

The CEI technique (Sec. 3.1) makes it possible to measure the vibrational population $p_v(t)$ of molecular ions stored in the TSR, as has been shown in the previous section, whereas the RFI technique (Sec. 3.3) provides information about the relative contribution $q_v(t)$ of different vibrational states to DR. These techniques have been used in previous experiments to study the DR of HD^+ [34]. A vibrationally excited HD^+ molecular ion cools radiatively to its vibrational ground state in less than 500 ms [33]. This radiative cooling cannot be observed for the homonuclear diatomic molecular ions H_2^+ and D_2^+ due to a missing dipole moment.

To obtain vibrational state specific relative DR rate coefficients both techniques, CEI and RFI, were combined. The relative contribution $q_v(t)$ of a vibrational state v to the DR rate obtained from the stored ion beam is proportional to the population p_v and the rate coefficient α_v of that state. Taking the DR rate coefficient α_1 as reference[2], relative DR rate coefficients can be yielded by

$$\frac{\alpha_v}{\alpha_1} = \frac{q_v(t)}{q_1(t)} \frac{p_1(t)}{p_v(t)}. \qquad (5.1)$$

---

[2] Usually the rate coefficient α_0 for the vibrational ground state is taken as reference, however as will be shown α_1 is about one order of magnitude larger than α_0 which reduces the statistical errors on the relative rate coefficients α_v/α_1.

The measurement of the relative contributions $q_v(t)$ of vibrational states to DR will be discussed and vibrational state specific relative DR rate coefficients will be derived for H_2^+ and D_2^+ in the following sections.

The two experiments were carried out at ion energies $E_i \approx 1\,\mathrm{MeV}$ and $E_i \approx 2\,\mathrm{MeV}$ for the H_2^+ and D_2^+ molecule, respectively. For the H_2^+ experiment the single-ended van-de-Graaff accelerator and for the D_2^+ experiment the RFQ accelerator was used. The longitudinal and the transverse electron temperatures were $kT_{||} \approx 0.1\,\mathrm{meV}$ and $kT_\perp \approx 12\,\mathrm{meV}$ for both molecules. The electron densities were $n_e = 6.1 \times 10^6\,\mathrm{cm}^{-3}$ and $n_e = 5.4 \times 10^6\,\mathrm{cm}^{-3}$ at electron beam diameters of about $d = 35\,\mathrm{mm}$ and $d = 30\,\mathrm{mm}$ for the H_2^+ and D_2^+ experiment, respectively. In all experiments, the velocities of the electron beams were set very close to that of the injected beams. Hence, the electron-ion collisions occurred at near-zero relative energies E and the average collision energies were given by the transverse electron temperatures $kT_\perp$. Small differences between the average velocities of electrons and ions were reduced by the friction force which rapidly drags the ion beam to a velocity matching the electron velocity (Sec. 4.4.4), such that the energy of average relative motion between the two beams becomes zero. The angular spread of the ion beam after injection into the TSR of at most ±7 mrad was reduced within several seconds of storage due to interactions in the merged electron-ion beam. At the same time the ion beam size was reduced from initially several millimeters to about 1 mm (FWHM).

5.2.1 DR of H_2^+ and D_2^+

The recombination fragment imaging (RFI) technique has been extensively used in recent years to study the initial-to-final state-to-state correlations in dissociative recombinations (see for instance Ref. [34]). The experimental method of the RFI technique has been discussed in Sec. 3.3. A specific kinetic energy release $E_k^{vJnn'}$ is related to each initial-to-final state-to-state DR channel; vJ denotes the initial ro-vibrational state and n and n' the final atomic fragment states. The kinetic energy release $E_k^{vJnn'}$ is converted into a macroscopic fragment distance d of up to several centimeters after a free flight of a few meters, obeying the relation

$$d \sim \sqrt{E_k^{vJnn'}}, \tag{5.2}$$

see Eq. 3.17 for the exact dependence. The concept of the RFI is based on the measurement of the distribution $P_{vJnn'}(D)$ of projected fragment distances D on the detector plane oriented perpendicular to the center-of-mass motion of the dissociating fragments. The shape of the expected projected fragment distance distributions $P_{vJnn'}(D)$ are discussed in Sec. 3.3 for different angular distributions of the fragment relative to the beam direction. It has been shown that the angular distribution is isotropic at matched electron-ion velocities [94]. Assuming a time independent Boltzmann distribution of the rotational excitation corresponding to $T = 600\,\mathrm{K}$, a projected fragment distance distribution $P_{vnn'}(D)$ (Eq. 3.23) can be given for each initial-to-final state-to-state DR channel[3], as derived in Sec. 3.3.

At matched average velocities of electron and ion beam ($E = 0\,\mathrm{eV}$) one of the atomic fragments is always produced in the ground state ($n' = 1$), whereas the final state of the other fragment is dependent on the ro-vibrational excitation of the molecular ion prior to recombination. For H_2^+ in a ro-vibrational state[4] $v < 5$ and $J < 6$, only the final asymptote corresponding to $n = 2$ is accessible. The $n = 1$ asymptote receives a negligible population as has been shown in previous experiments [39]. Due to the larger reduced mass of D_2^+ the vibrational and rotational energies are shifted with respect to the values for H_2^+ , see Append. B. Therefore, in D_2^+ the limits below which only the final asymptote ($n = 1$) $n = 2$ is accessible are $v < 7$ and $J < 8$. Assuming a rotational excitation corresponding to a Boltzmann distribution at $T = 600\,\mathrm{K}$ (measured ion source temperature $T = 600 \pm 100\,\mathrm{K}$ [34]) about 85 % of the H_2^+ molecules are in a rotational state $J < 6$ and about 75 % of the D_2^+ molecules are in a rotational state $J < 7$. The small contribution from higher J levels for the H_2^+ and D_2^+ ions in the vibrational states $v = 4$ and $v = 6$, respectively, is negligible and it was assumed that only the $n = 2$ asymptote is energetically accessible.

To compare the electron induced vibrational cooling and to extract relative DR rate coefficients for both molecular ions, the DR and CEI studies (discussed in the previous section) of each ion were performed in a separate experiment under the same experimental conditions. The experimental conditions, such as the ion beam energy and the electron cooler settings, can be found in Sec. 5.2 for both experiments.

The impact position of the DR fragments on the detector is obtained using an imaging system, consisting of a CCD camera, a frame threshold suppressor (FTS) and a VME computer, see Sec. 4.5.1 for a more detailed description. Each fragment hitting the detector produces a light spot on the phosphor screen mounted behind the MCP. The fragment positions, measured with the CCD, camera are given in units of camera pixels and need to be transformed into millimeters prior to a data analysis can be done. The distance between the CCD camera and the MCP is slightly different for each experiment. The so-called pixel-to-millimeter calibration is usually done by putting small metal discs of known diameter in front of the MCP blocking part of the DR fragments. This way a shadow of the metal disc is obtained in pixel-units. Fitting an ellipse[5] to the disc shadow yields a disc diameter in units of pixels which can be directly compared to the disc diameter in mm. Following this method a value for the pixel-to-millimeter transformation can be derived with a systematic error of approximately 3 %. The systematic error is due to the rather large MCP-disc distance of about 25 cm and the ion beam diameter of ≈ 1 mm (FWHM). This leads on one hand to a smeared contour of the disc profile on the MCP and on the other

---

[3] Each projected fragment distance distribution is convoluted with a defined rotational excitation distribution, see discussion in Sec. 3.3.

[4] For all calculations the rotational constant of the vibrational ground state (Tab. B.1) has been used.

[5] The pixel distances on the CCD chip are different in the vertical and horizontal direction and have a fixed ratio of $\sqrt{2}$ [75] for the cameras used in our experiments.

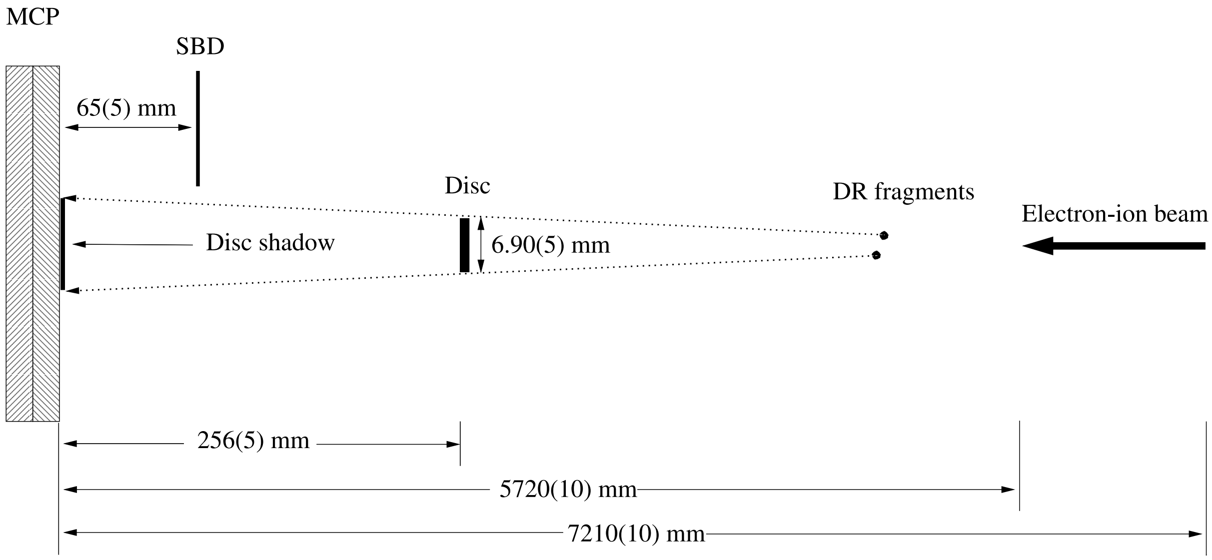

Figure 5.8: *Schematic drawing of the setup used to measure the projected distance of the DR fragments together with the positions of the metal disc, the surface barrier detector (SBD) and the electron-ion recombination region inside the electron cooler with respect to the MCP. It is possible to chose between discs of different diameters. Also depicted is the disc shadow which is enlarged due to the divergence of the dissociating DR fragments.*

hand to an enlarged diameter, as the DR fragments are not moving parallel, see Fig. 5.8. For the experiment with the D_2^+ ion beam, "images" have been taken from the lower edge of a surface barrier detector (SBD), movable in vertical direction, at different positions which can be precisely adjusted from outside the vacuum chamber. The smaller distance to the MCP reflects in a smaller systematic error of less than 2 %.

In the experiment with the H_2^+ ion beam, projected fragment images have been measured for electron-ion interaction times from $t = 0.5 - 13.5\,\mathrm{s}$, whereas for D_2^+ the measurements were performed up to times $t = 90\,\mathrm{s}$. Some measured projected fragment distance distributions for the DR of H_2^+ ions at matched electron-ion velocities are shown in Fig. 5.9 for different time slices. The changing shapes of the projected fragment distance distributions reflect the vibrational cooling already seen in the CEI measurement. The large contributions at small distances disappear with time and are due to DR producing fragments in an excited state with $n = 3$. As discussed before, these final asymptotes are energetically accessible only for vibrationally excited H_2^+ molecules $(v > 4)$. As in previous experiments [39] no contribution of DR with final asymptotes $n = 1$ has been observed.

The relative contribution $q_{vnn'}$ of each initial-to-final state-to-state DR channel was obtained by fitting the function $P(D;t)$ (Eq. 3.24) to the measured distributions which were normalized to unity. The calculated projected fragment distance distributions for the different vibrational states take into account rotational excitation and the length of the electron cooler. The ro-

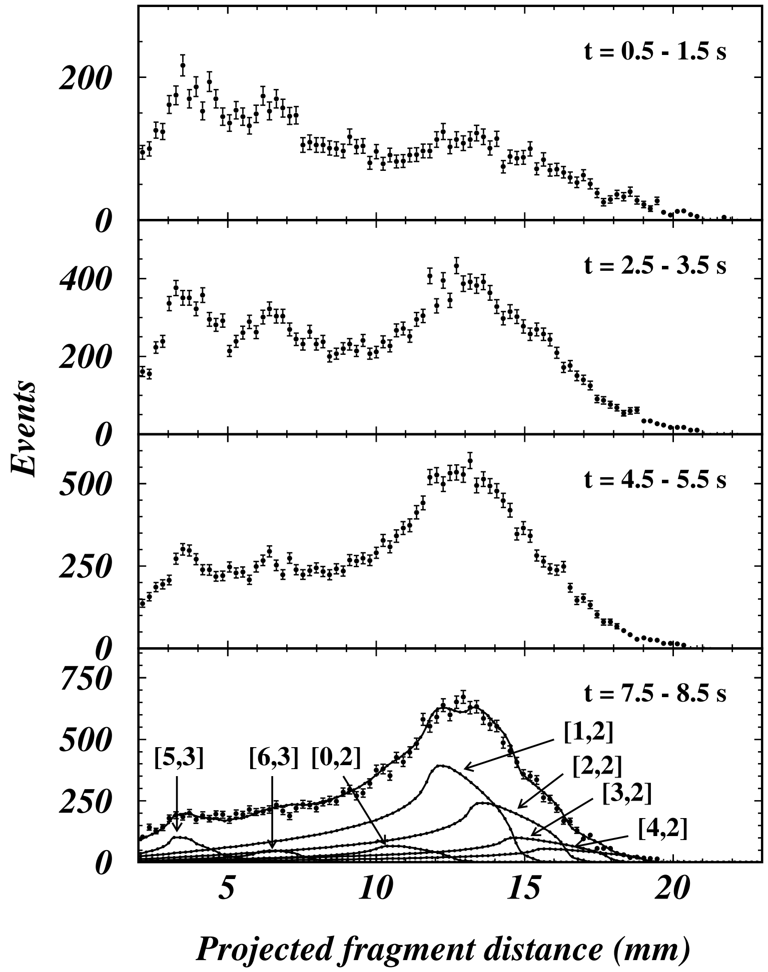

Figure 5.9: *Measured projected fragment distance distributions from the DR of H_2^+ with near-zero kinetic energy electrons at different interaction times. In the lowest panel some expected projected fragment distributions, including rotational excitation (T = 600 K) are shown, corresponding to DR of H_2^+ excited in an initial vibrational state v into H(1s)+H(n) ([v,n]). Additionally, the fitted linear combination of all considered fragment distributions are drawn.*

tational excitation was assumed to be Boltzmann distributed corresponding to a temperature of $T = 600\,\mathrm{K}$. In addition, the angular distribution of the DR fragments was assumed to be isotropic, see Sec. 3.3. A fixed value for the pixel-to-mm calibration was used. In the lowest panel ($t = 7.5 - 8.5\,\mathrm{s}$) of Fig. 5.9 the fitted function $P(D;t)$ as well as the individual contributions of some DR channels are drawn on top of the measured distribution. The shape of the individual contributions are expressed by the functions $P_{vnn'}(D)$ (Eq. 3.23). The peak position of the expected projected fragment distance distributions $P_{vnn'}(D)$ are well separated for all DR channels allowing for extracting their relative contributions $q_{vnn'}(t)$, where $\sum_{vnn'} q_{vnn'} \equiv 1$. The fitting results are summarized in Fig. 5.10. The relative contributions of the higher vibrational states ($v > 4$) disappear almost completely within about 10 seconds. The vibrational states $v > 4$ populate predominantly the final asymptotes with $n = 3$; this corresponds to the DR channel with the lowest kinetic energy release.

The DR measurement of D_2^+ was also carried out at near-zero kinetic energy collision energies. The analysis of the projected fragment distance spectra for D_2^+ followed the same procedure

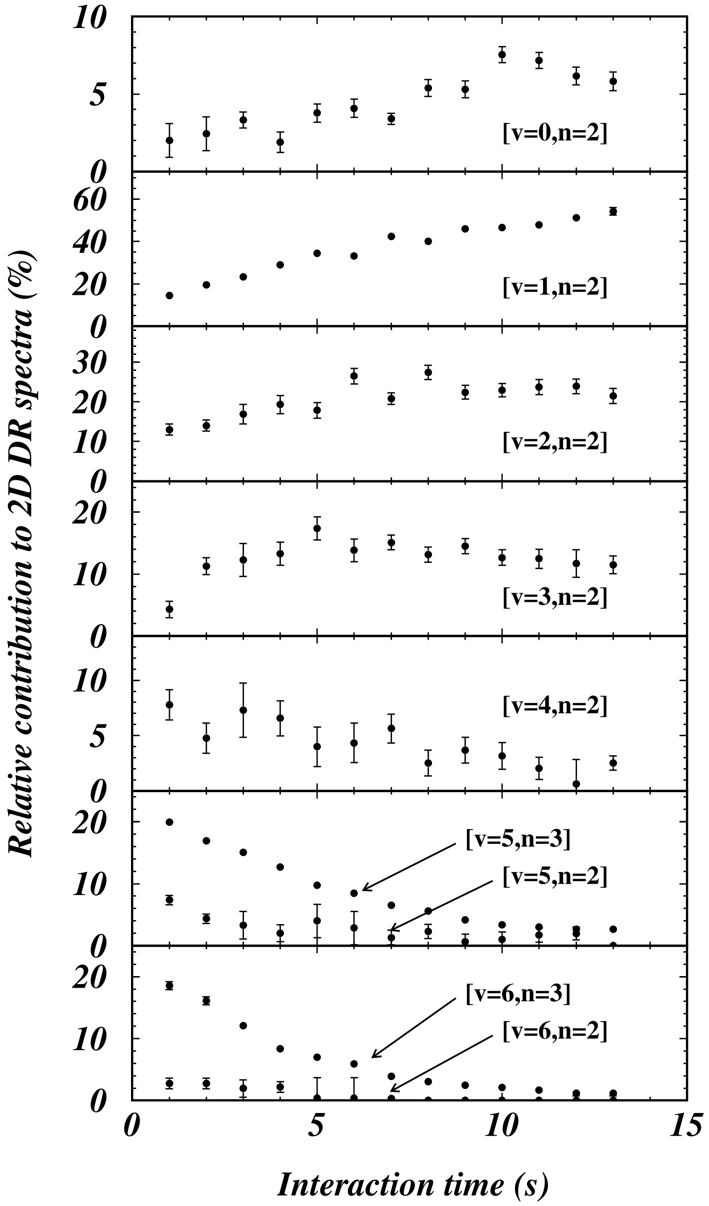

Figure 5.10: *Fitting results for the relative contributions $q_{vnn'}$ of each channel corresponding to DR of H_2^+ in an initial vibrational state v into H(1s)+H(n) ([v,n]) to the projected fragment distance distributions measured at $E \approx 0\,eV$ and different interaction times ($t = 0 - 13\,s$) with electrons.*

discussed for H_2^+ . Some of the measured spectra are presented in Fig. 5.11. The statistics was high enough for interaction times lower than 60 s to extract meaningful spectra for time windows of 1 s. Only for the longer storage times the fragment rate became too low such that larger time windows (4 s) were needed to obtain reasonable statistics. As for H_2^+ a strong vibrational cooling is visible and an almost complete disappearance of higher vibrational states (contributions at small distances) is observed within less than 10 s. The fitting results, presented in Fig. 5.12, reveal an almost complete cooling into the vibrational ground state. After about 40 s only the vibrational states $v = 0$ and $v = 1$ contribute to the DR. Due to the lower lying vibrational energy levels, the final asymptotes $n = 3$ are only accessible for vibrational states $v > 6$. As

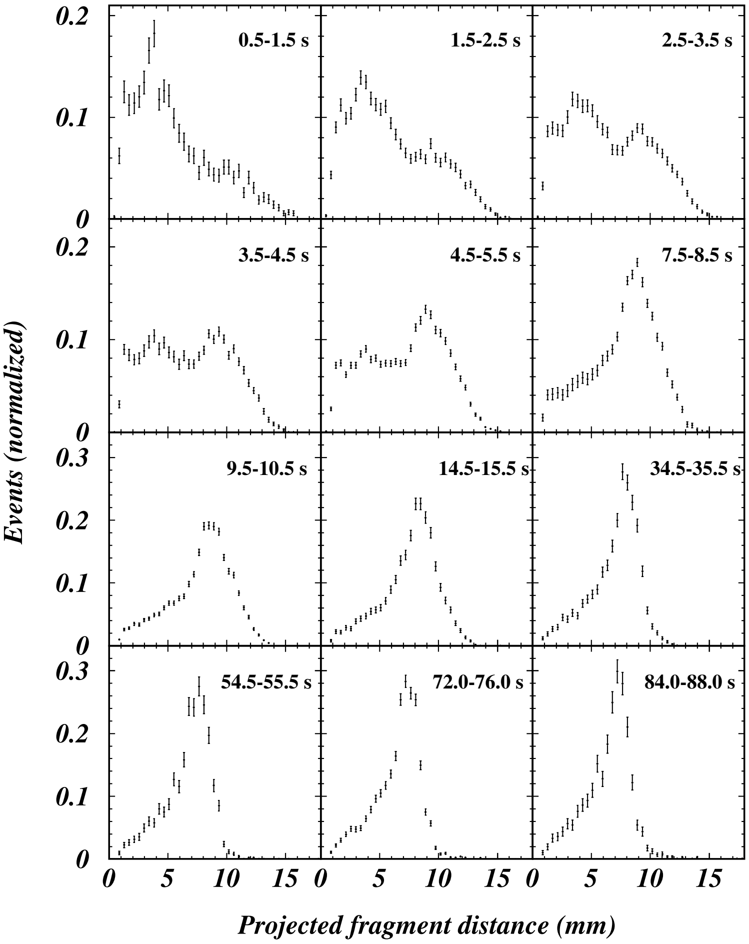

Figure 5.11: *Measured projected fragment distance distributions from the DR of D_2^+ with near-zero kinetic energy electrons at different interaction times.*

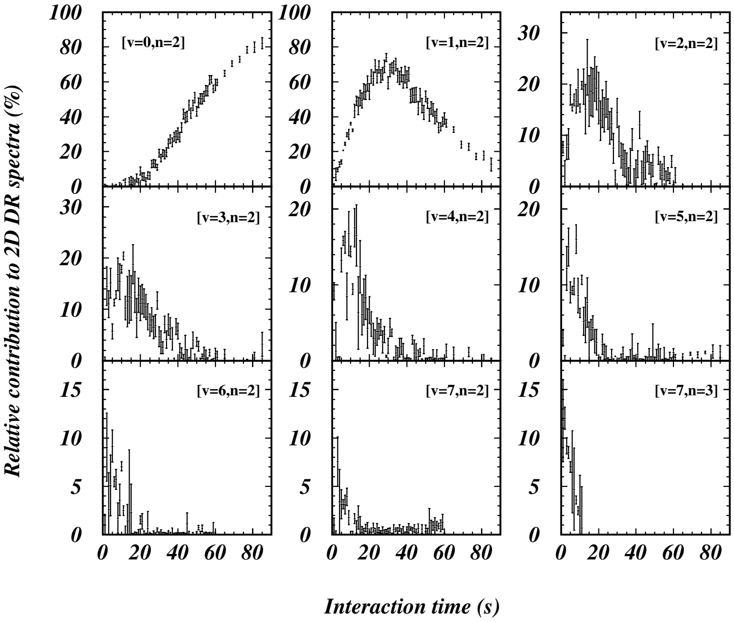

Figure 5.12: *Fitting results for the relative contributions $q_{vnn'}$ of each channel corresponding to DR of D_2^+ in an initial vibrational state v into D(1s)+D(n) ([v,n]) to the projected fragment distance distributions measured at $E \approx 0\,eV$ and different interaction times ($t = 0 - 85\,s$).*

for H_2^+ a predominant population of final asymptotes $n = 3$ is observed for $v = 7$. The expected projected fragment distance distributions $P_{vnn'}(D)$ (Eq. 3.23) are less separated from each other due to the smaller vibrational level spacing in D_2^+ compared to H_2^+ . Additionally, the total number of involved vibrational states is larger for D_2^+ . This made it particular difficult to extract reliable relative contributions for the first ten time slices (i.e. for $t < 11$ s) and gave rise to systematic variations in the results. Thus, only DR channels with final asymptotes $n = 2$ were fitted in a first step. In a second step, the relative contributions of DR channels with final asymptotes $n = 3$ were fitted keeping the relative contributions of the other channels fixed to the values obtained from the first fit. This procedure is possible since the kinetic energy release and therefore the fragment distance is small for DR channels with final asymptotes $n = 3$ and does not influence the shape of the spectra at large projected fragment distances; the shape at these distances is completely caused by the other DR channels, see lowest panel in Fig. 5.9. The relative contributions of vibrational states $v > 7$ to DR disappeared within a few seconds and are therefore not shown in Fig. 5.12.

A second experiment was carried out with an H_2^+ ion beam at higher storage energy and higher electron density. The experiment aimed at observing the time evolution of the relative contributions of the lower vibrational states for longer electron-ion interaction times. The two RFQ accelerators were used together with the seven-gap resonators (Sec. 4.1) to accelerate the H_2^+ ion beam produced in a CHORDIS ion source to an energy of $E_i \approx 2$ MeV. The electron density was $n_e = 1.09 \times 10^7$ cm^{-3}, about twice as high as in the first experiment, which decreased the time-constant for the electron induced vibrational cooling by almost a factor of two. The transverse and the longitudinal electron temperatures were $kT_\perp = 12.7$ meV and $kT_{||} \approx 0.1$ meV,

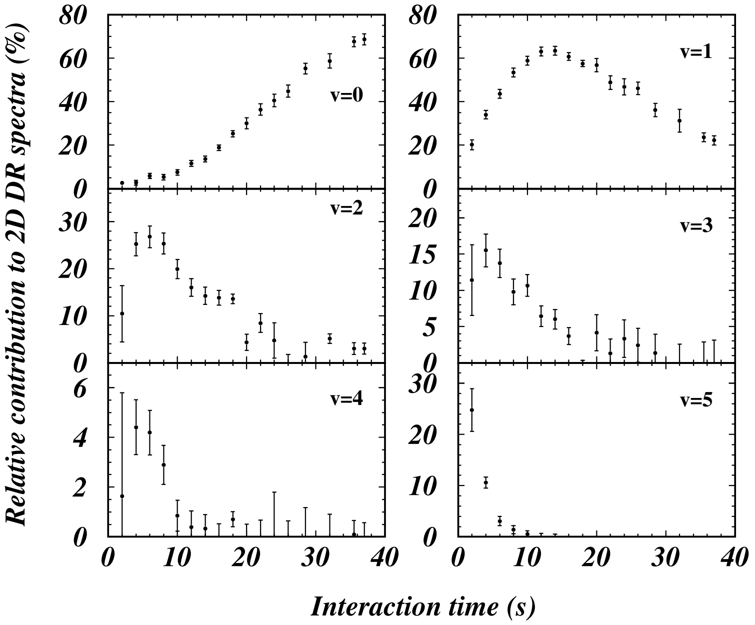

Figure 5.13: *Fitting results for the relative contributions $q_{vnn'}$ of each DR channel (with $n = 2$ and $n' = 1$) to the projected fragment distance spectra measured at near-zero electron-ion collision energies and interaction times up to $t = 37$ s.*

respectively. The measurement scheme as well as the data analysis were identical with the previous experiments, therefore only the final results are shown in Fig. 5.13. An almost complete vibrational cooling into the two lowest vibrational states was found in about 30 s.

5.2.2 Relative DR rate coefficients for H_2^+ and D_2^+

The information about the relative contribution $q_{vnn'}(t)$ of each initial-to-final state-to-state channel to DR at a given time can now be combined with the vibrational population $p_v(t)$ to derive state-to-state DR rate coefficients relative to that of $v = 1$ (final asymptote $n = 2, n' = 1$), i.e. $\alpha_{vn1}/\alpha_{121}$ (see Eq. 5.1). The DR rate coefficient of the first excited vibrational state has been chosen as reference instead of that for the vibrational ground state because of the small measured relative contributions $q_{021}(t)$ of $v = 0$ to DR (see Figs. 5.10 and 5.12) which cause large statistical errors. Figs. 5.14 and 5.15 present the relative DR rate coefficients for the lower vibrational states of H_2^+ and D_2^+ , respectively; after summation over all contributions of each vibrational state to the final fragment states energetically accessible by DR with near-zero kinetic energy electrons. For H_2^+ the relative DR rate coefficients are shown for all time slices for which the vibrational population was known from the CEI measurement, whereas for D_2^+ only those time slices were considered were either the vibrational population or the relative contribution to DR was significantly different from zero within their error bars. The lines drawn represent the weighted mean values used as the final results. The required time independence of the values is given within the statistical error bars and prove the reliability of the method to extract relative DR rate coefficients.

The final experimental results for the relative DR rate coefficients are shown in the Figs. 5.16 and 5.17 for H_2^+ and D_2^+ , respectively, as a function of the vibrational state v. The plotted error bars are larger than the statistical values. The results are summarized together with their systematic errors in Tab. 5.1. The systematic errors are due to the uncertainties in the factor for the pixel-to-millimeter transformation, discussed in the previous section and were obtained by a systematic study of the influence of the uncertainties in the pixel-to-millimeter calibration on the relative DR rate coefficients. The experimental results for H_2^+ as well as for D_2^+ are compared to earlier calculations, based on the multichannel quantum defect theory (MQDT), of the DR rate coefficients by Nakashima *et al.* [24] for $v = 0 - 4$. Furthermore shown are recent results from new MQDT calculations of the DR of H_2^+ at a collision energy $E = 0.01$ meV by Schneider *et al.* [99]. Rate coefficients become constant at collision energies lower than the longitudinal electron temperature of $kT_{||} \approx 0.1$ meV, such that the calculations for $E = 0.01$ meV represent the experimental conditions [100]. Theoretical studies of the DR of D_2^+ will probably also be performed in the near future. The calculations by Nakashima *et al.* considered only the ${}^1\Sigma_g^+$ dissociative state of molecular hydrogen, whereas the results by Schneider *et al.* were obtained taking into account also higher dissociative states, belonging to the so-called Q_1 series. But, both MQDT calculations did not include rotational excitations. The results by Schneider *et*

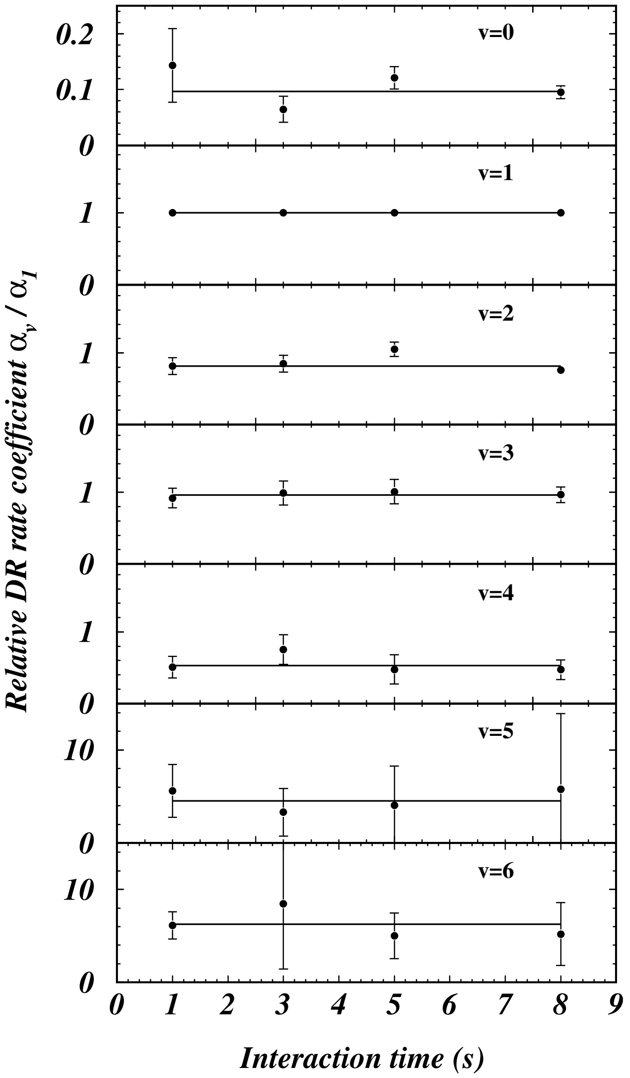

Figure 5.14: *Relative DR rate coefficients at $E = 0\,\mathrm{eV}$ for the first seven vibrational states of H_2^+. The straight lines represent the weighted mean values used as the final results. The displayed values have been added up over all possible final states.*

al. have been convoluted with our experimental (i.e. anisotropic) electron velocity distribution, whereas the results by Nakshima *et al.* were convoluted with an isotropic Maxwell-Boltzmann distribution corresponding to 100 K, the approximate transverse electron temperature in the present experiments. Takagi [101] included rotational excitations in his calculations of the DR cross section of HD^+ in $v = 0, 1$ and H_2^+ in the vibrational ground state. Further calculations of the DR cross section for H_2^+, HD^+ and D_2^+, using the projection operator technique, were carried out for the vibrational states $v = 0 - 4$ by Rai Dastidar and Rai Dastidar [102]. These calculations were performed for collision energies larger than 500 meV and cannot be compared to our results. Only for the first three vibrational states of H_2^+ a reasonable agreement between the calculations by Nakashima *et al.* and our results can be seen. Also the calculations by Schneider *et al.* cannot reproduce the measured relative rate coefficients and show almost no

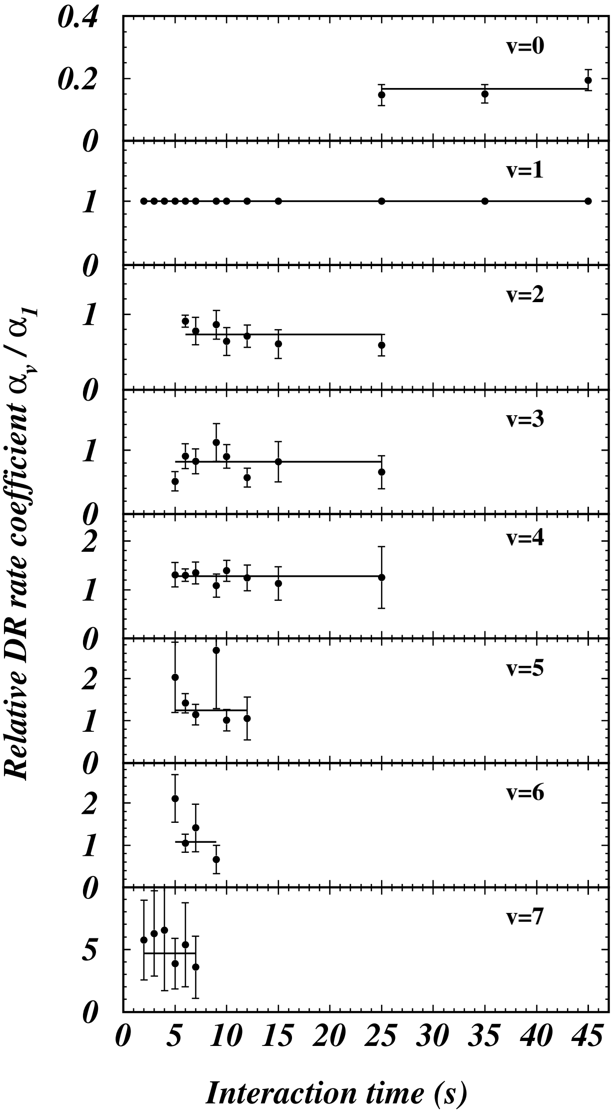

Figure 5.15: *Relative DR rate coefficients at $E = 0\,eV$ for the first eight vibrational states of D_2^+ . The straight lines represent the weighted mean values used as the final results. The displayed values have been added up over all possible final-states*

dependence on the vibrational state.

The theoretical results for D_2^+ do only agree for $v = 1$ and $v = 3$ within the experimental error bars. Nakashima *et al.* trace back the very low value for the ground vibrational state of D_2^+ to the small Franck-Condon factor between the continuum vibrational wavefunction of the $^1\Sigma_g^+$ dissociative state and the nuclear wavefunction for $v = 0$. The final experimental results for relative DR rate coefficients of H_2^+ , HD^+ and D_2^+ are summarized in Tab. 5.1. The electron-ion collision energy as well as the longitudinal electron temperature were identical in all three experiments and amounted to $E \approx 0\,\mathrm{meV}$ and $kT_{||} \approx 1\,\mathrm{K}$. The transverse electron temperatures varied slightly and are quoted in Tab. 5.1. The relative DR rate coefficients show similar trends for both studied molecular ions. The DR rate coefficients are almost constant for the vibrational states $v = 1 - 4$ of H_2^+ and $v = 1 - 6$ of D_2^+ and are about an order of magnitude higher than

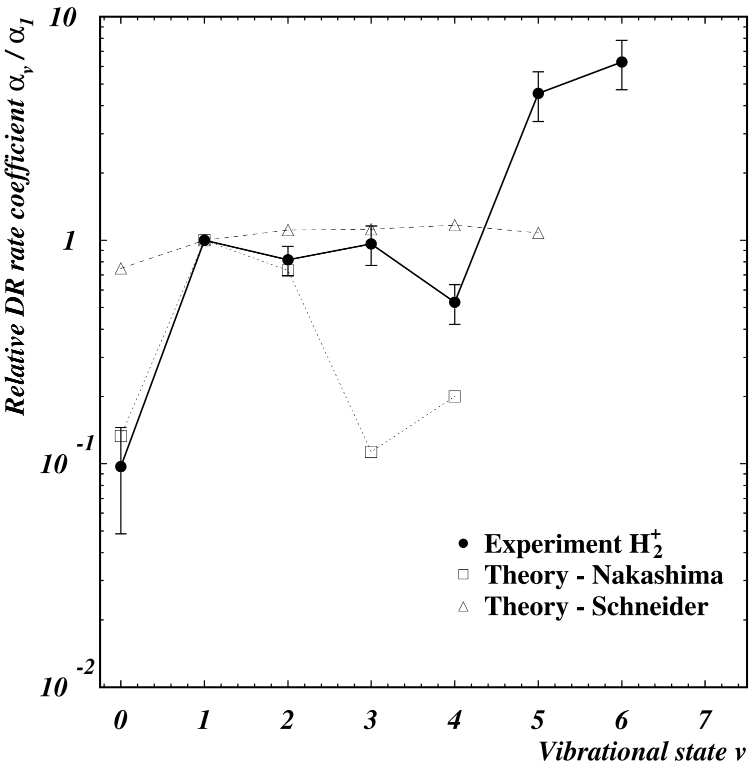

Figure 5.16: *Experimental results for the relative DR rate coefficients of H_2^+ at $E \approx 0\,eV$ as a function of the initial vibrational quantum number (solid circles). Together with the experimental results are also theoretical calculations by Nakashima* et al. *[24] (open boxes) and Schneider* et al. *[99] (open circles) shown, see text. Lines are drawn to guide the eye through the values.*

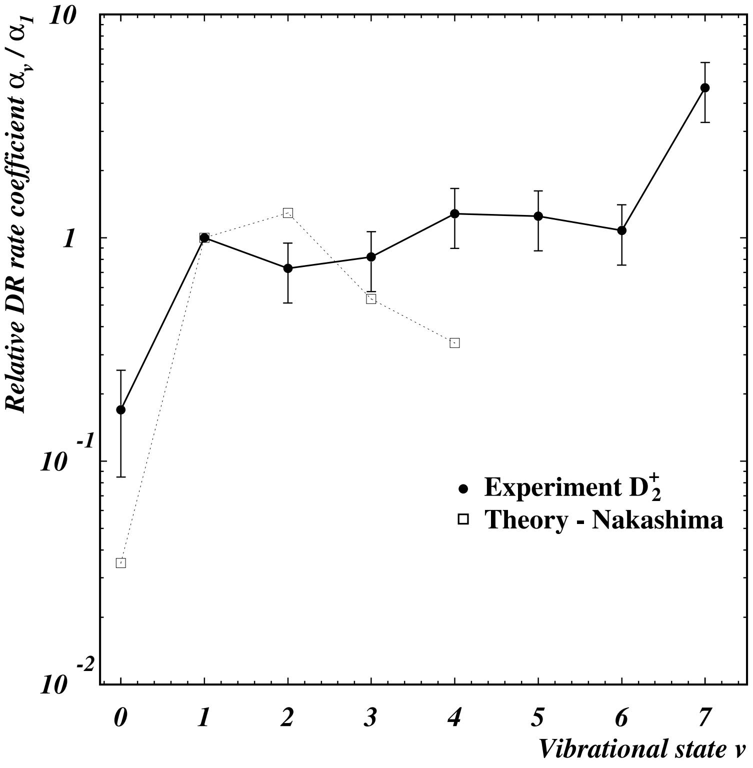

Figure 5.17: *Experimental results for the relative DR rate coefficients of D_2^+ at $E \approx 0\,eV$ as a function of the initial vibrational quantum number (solid circles). Together with the experimental results are also theoretical calculations by Nakashima* et al. *[24] (open boxes) shown. Lines are drawn to guide the eye through the values.*

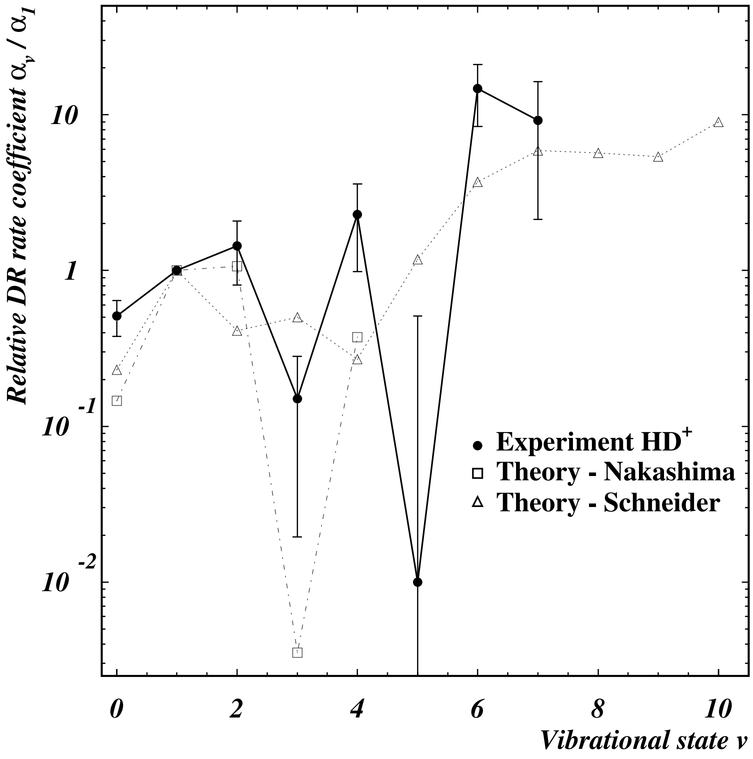

Figure 5.18: *Experimental results for the relative DR rate coefficients of* HD^+ *at* $E \approx 0\,eV$ *as a function of the initial vibrational quantum number (solid circles). Together with the experimental results are also shown theoretical calculations by Nakashima* et al. *[24] (open boxes) and Amitay* et al. *[40] (open triangles). Lines are drawn to guide the eye through the values.*

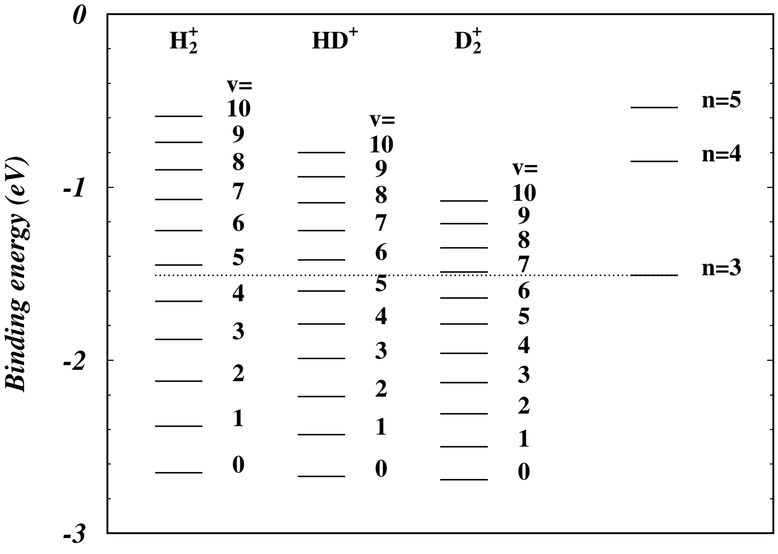

Figure 5.19: *Binding energies of* H_2^+ *,* HD^+ *and* D_2^+ *in the rotational ground state* $(J = 0)$ *and vibrational state* $v = 0 - 11$ *compared to the asymptotic fragment energies for* $n = 3 - 5$.

	H_2^+	D_2^+	HD^+ [34]
	$T_\perp$=139 K	$T_\perp$=139 K	$T_\perp$=116 K
α_0/α_1	0.10 ± 0.05	0.17 ± 0.09	0.51 ± 0.13
α_2/α_1	0.82 ± 0.12	0.73 ± 0.22	1.44 ± 0.63
α_3/α_1	0.96 ± 0.19	0.82 ± 0.20	0.15 ± 0.13
α_4/α_1	0.53 ± 0.11	1.28 ± 0.50	2.30 ± 1.30
α_5/α_1	4.5 ± 1.4	1.25 ± 0.63	0.01 ± 0.05
α_6/α_1	6.3 ± 1.9	1.08 ± 0.43	14.8 ± 6.3
α_7/α_1		4.69 ± 1.90	9.2 ± 7.1

Table 5.1: *Experimental relative DR rate coefficients of* H_2^+ *,* D_2^+ *and* HD^+ *[34] for collisions with near-zero kinetic energy electrons and transversal electron temperatures* $kT_\perp$*. The longitudinal electron temperature was* $kT_{||} \approx 1\,K$ *in all experiments.*

the values for the vibrational ground states. The steep increases in the DR rate coefficient for higher vibrational states, $v > 4$ and $v > 6$ in case of H_2^+ and D_2^+ , respectively, are due to the accessibility of additional channels through which DR can proceed. These vibrational states can couple to the higher lying dissociative states belonging to the Q_1 series, Fig. 2.4. This feature has also been seen for the relative DR rate coefficients of HD^+ . Fig. 5.18 shows the experimental results taken from Amitay *et al.* [34] and obtained at the same experimental setup. The MQDT calculations by Schneider *et al.* can qualitatively reproduce this trend in case of HD^+ [34], but not for H_2^+ [99], see Figs. 5.18 and 5.16. The possible DR via the higher dissociative states of the Q_1 series coincides with the energetic accessibility to the final asymptotes $n = 3$. The binding energies of the lower vibrational states ($v = 0 - 10, J = 0$) of the three hydrogen molecular ions are summarized and compared to the energies of the final asymptotes $n = 3 - 5$ in Fig. 5.19.

The comparison of the trend in the relative DR rate coefficients for HD^+ with those for H_2^+ and D_2^+ reveals a decisive difference. For HD^+ the relative DR rate coefficient of the vibrational ground state is by fare the largest for all three ions. Furthermore there is a striking variation in the values for the vibrational states $v = 1-5$ which was not found for H_2^+ and D_2^+ . The variations for $v = 0 - 4$ cannot be explained by Franck-Condon (FC) factors, as the FC dominated DR rate coefficients from Nakashima *et al.* barely reproduce the experimental results. The different behavior of the measured relative DR rate coefficient for the homonuclear hydrogen molecular ions H_2^+ and D_2^+ and the heteronuclear hydrogen molecular ion HD^+ is not yet understood.

5.3 Absolute DR rate coefficients for H_2^+ and D_2^+

H_2^+ and D_2^+ ion beams produced by electron impact ionization are vibrationally excited as discussed in the previous sections. This vibrational excitation and the absence of radiative cooling makes it difficult to obtain a DR rate coefficient for the vibrational ground state as it has been measured several times for HD^+, see for instance [71]. But, the process of electron induced vibrational cooling via SEC allows for cooling H_2^+ and D_2^+ ion beams to almost 100 % into their vibrational ground state in less than 60 s; the effective time for a complete vibrational cooling is inverse proportional to the electron density.

In this section a measurement of DR rate coefficients for the vibrational ground states of H_2^+ and D_2^+ will be discussed.

5.3.1 Monitoring the vibrational cooling

In Sec. 3.3 the principle of recombination fragment imaging (RFI) has been discussed. This technique allows for monitoring the relative contribution of each vibrational states to DR and therefore provides indirectly information about the vibrational population of a stored molecular ion beam. The relative contribution q_v of a vibrational state v to a RFI spectra is proportional to the population of that state and its DR rate coefficient α_v. The vibrational population $p_v(t)$ can therefore be written as

$$p_v(t) = \frac{q_v(t)/\alpha_v}{\sum_v q_v(t)/\alpha_v}. \tag{5.3}$$

Multiplying both, denominator and numerator with α_1, the DR rate coefficient for $v = 1$, leads to an expression for $p_v(t)$ only depending on the relative contribution $q_v(t)$ which can be measured using the RFI and the relative DR rate coefficients obtained from previous experiments, see Sec. 5.2. This way we used the RFI to monitore the vibrational population as a function of the storage time.

Both experiments were carried out at the same ion energy per nucleon (E_i=1 MeV/a.m.u.). The ions were produced in a CHORDIS ion source and accelerated using the RFQ accelerator together with the seven-gap resonators. The injection cycles were 60 s and 80 s for the experiments with the D_2^+ and H_2^+ beam, respectively. The electron density was $n_e = 1.6 \times 10^7\,\mathrm{cm}^{-3}$ and the transverse and longitudinal temperatures were $kT_\perp = 11.8\,\mathrm{meV}$ and $kT_{||} = 0.1\,\mathrm{meV}$, respectively, in both experiments. The electron cooler was adjusted to zero collision energy.

The $1/e$ ion beam lifetimes were about 20 s for both ions. A sufficient large fragment rate on the detector even after 80 s of storage was needed, therefore the number of injected ions had to be rather high. To protect the detector system from damage due to too high fragment rates a metallic shutter was used in the first 20 s to cover the MCP. Thus, only data for storage times longer than 20 s are available. In Sec. 5.2 the analysis of measured DR 2D spectra has been discussed in detail and the reader is referred to Sec. 3.3 for more extensive descriptions.

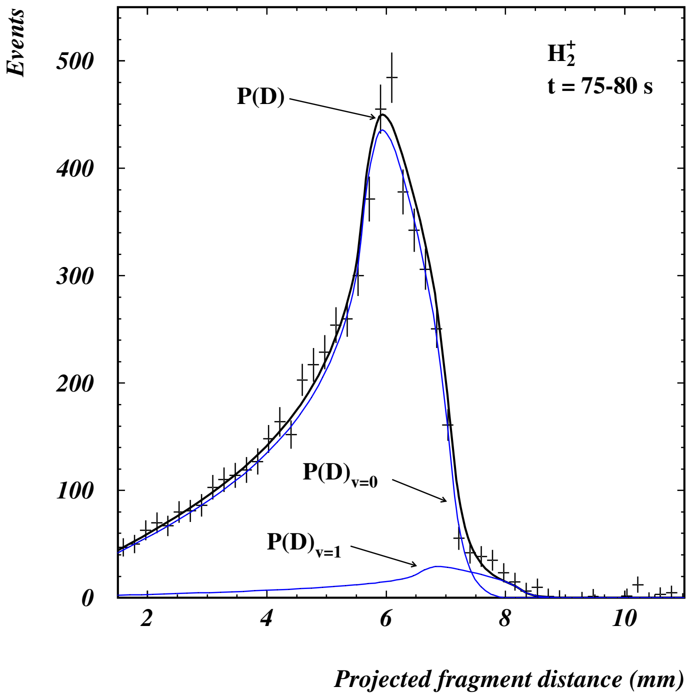

Figure 5.20: *Measured and background corrected distribution of projected fragment distances for H_2^+ taken between $75 - 80\,s$ after injection. Furthermore shown are the contributions of the theoretical fragment distance distributions $P(D)_{v=0}$ and $P(D)_{v=1}$ to the fitted distribution $P(D)$.*

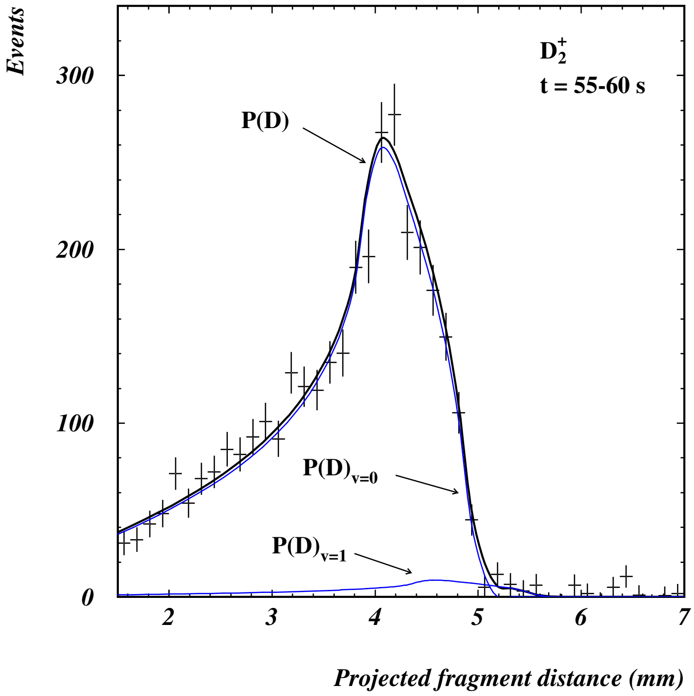

Figure 5.21: *Measured and background corrected distribution of projected fragment distances for D_2^+ taken between $55 - 60\,s$ after injection. Furthermore shown are the contributions of the theoretical fragment distance distributions $P(D)_{v=0}$ and $P(D)_{v=1}$ to the fitted distribution $P(D)$.*

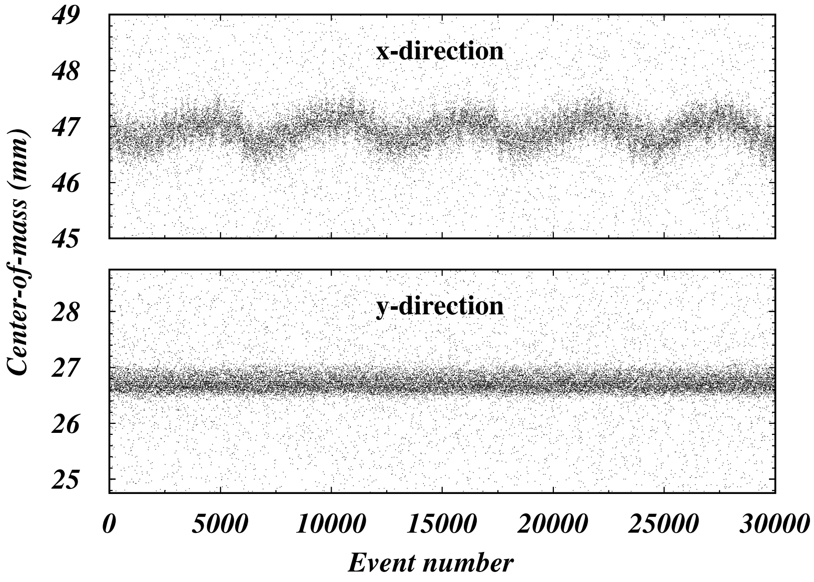

Figure 5.22: *Center-of-mass of the two DR fragments in x- and y-direction, corresponding to horizontal and vertical orientation, respectively, for the first 30000 DR events; taken from the H_2^+ measurement. The fluctuations in x-direction are due to temperature effects, see text.*

For both molecular ions measured projected fragment distance distributions are shown in Fig. 5.20 (H_2^+) and Fig. 5.21 (D_2^+). The spectrum for H_2^+ was taken between 75 and 80 s and for D_2^+ between 55 and 60 s after injection. Each spectrum shown has been corrected for background contributions coming from uncorrelated fragment pairs. Single neutral fragment can emerge from dissociative excitation (DE) or collisions with residual gas molecules. The center-of-mass position of two uncorrelated fragments in the detector differs from the position of two fragments coming from DR. Thus, a cut in the center-of-mass position can reduce the background contribution. In the present experiments an oscillation of the horizontal center-of-mass position was observed caused by periodic temperature drifts in the cooling water system making a precise cut rather difficult. Fig. 5.22 shows the center-of-mass position in y- and x-direction, corresponding to vertical and horizontal orientation, respectively, as a function of the acquired event number. These temperature drift leads to small changes in the ion beam orbital and gives rise to either a small variation in the angle between the electron-ion beam or a parallel shift of the ion beam with respect to the electron beam. The oscillations are therefore only observable in the horizontal component of the fragment position. For storage times longer than about 45 s the contribution of the vibrational ground state to DR convert to values lower than 100 %, see Fig 5.23[6]. In addition the time evolution of the vibrational ground state population of H_2^+ and D_2^+ is shown in Fig. 5.24, calculated using Eq. 5.3 and the relative DR rate coefficients from Tab. 5.1. Two possible explanations can be given for that observations.

Assuming the electron induced vibrational deexcitation to be in equilibrium with a vibrational excitation by residual gas scattering, i.e. both rates for vibrational excitation and deexcitation

---

[6] After 20 s of storage only the two lowest vibrational states, $v = 0$ and $v = 1$, contribute to the DR 2D spectra.

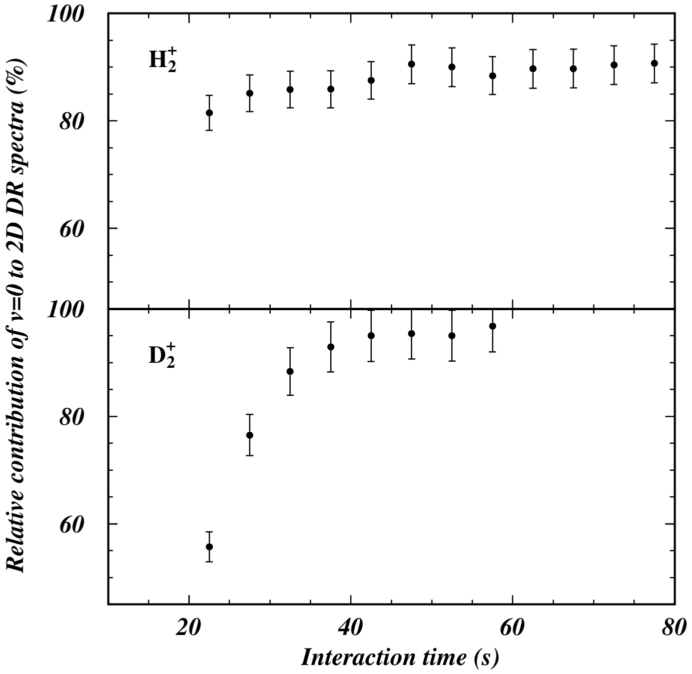

Figure 5.23: *Contribution of the vibrational ground state of H_2^+ and D_2^+ to the DR spectra of projected fragment distances as a function of the interaction time with electrons.*

have to be the same. Taken into account that about 99.5 % of the molecular ions are in the vibrational ground state (Fig. 5.24) and a residual gas density[7] of $n_{RG} = 1.3\times10^6$ cm^{-3} the rate coefficient for vibrational excitation by residual gas scattering is $\alpha_{RG} \approx 5\times10^{-9}$ cm^3/s. The $1/e$ lifetime for vibrational excitation of the vibrational ground state due to scattering on residual gas molecules is, for the given residual gas density, about 150 s and would cause a change in the vibrational population distribution of several percent in about 10 s even if there is no electron beam. This has not been observed in the CEI measurements, see discussion in Sec. 5.2. A second heading process, known from earlier experiments, is the electron induced vibrational excitation due to collisions in the toroid sections. But, the rate coefficients for this process is of the order of 10^{-11} cm^3/s as has been shown by M. Lange [71] and therefore much to small.

A second explanation for the subtotal cooling into the vibrational ground state could be some remaining background contributions. The fitted function $P(D)$ plotted in Fig. 5.20 cannot totally reproduce the measured projected fragment distance distribution in the region between 7-9 mm. The shape of the function $P(D)$ in that region is determined by the contribution of the first excited state $(P(D)_{v=1})$. This could be a hint that this part of the spectrum is caused be background events.

For storage times longer than 40 s the contributions of the vibrational ground states to DR are

---

[7] The residual gas density depends on the vacuum pressure inside the TSR which is typically 5×10^{-11} mbar.

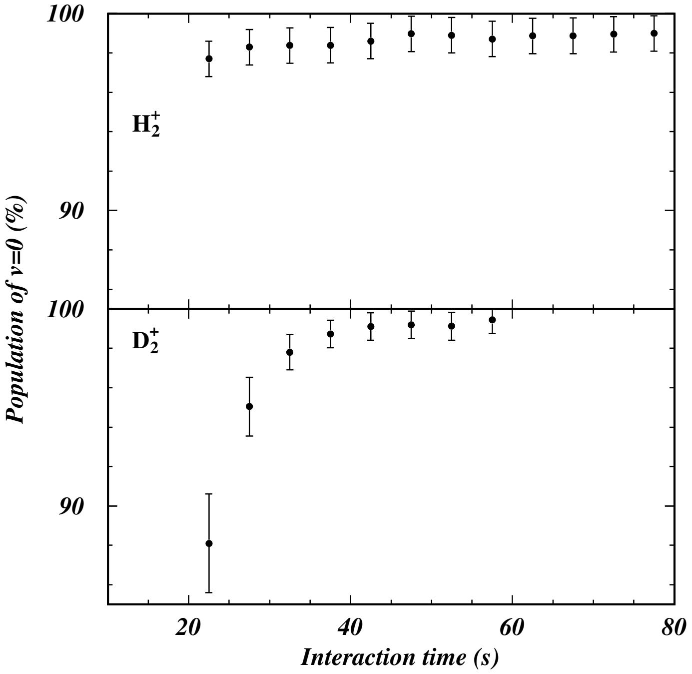

Figure 5.24: *Population of the vibrational ground state of H_2^+ and D_2^+ as a function of the interaction time with electrons.*

approximately constant for both molecules and amount to:

$$\mathrm{H}_2^+: \quad q_0(t > 40\,\mathrm{s}) = 89.6 \pm 1.4\,\% \tag{5.4}$$

$$\mathrm{D}_2^+: \quad q_0(t > 40\,\mathrm{s}) = 95.6 \pm 1.9\,\%. \tag{5.5}$$

The DR rate coefficients discussed in the following Section were measured after 40 s pre-cooling, They therefore represent not the value for the vibrational ground states and need to be corrected using the values from Eqs. 5.4 and 5.5, i.e. by factors 0.90 and 0.96, respectively.

5.3.2 DR rate coefficient measurements

The setup and the principle for rate coefficient measurements has been discussed in Sec. 4.6, therefore only a short overview on the measurement procedure is given here. The molecular ions were injected in the TSR and electron cooled for 40 s, i.e. the electron cooler was set to cooling energy ($E_{cool} = 0\,\mathrm{eV}$). After the pre-cooling period the electron energy wobbling was started, i.e. changing cyclic the collision energy every 25 ms from $E_{ref} \rightarrow E_{meas} \rightarrow E_{cool}$. The reference energy was set to $E_{ref} = 44.1\,\mathrm{eV}$ in the measurement runs with the H_2^+ beam. For the measurement runs with the D_2^+ beam the reference energy was either set to $E_{ref} = 93.1\,\mathrm{eV}$ or the electron beam was switched off. To obtain an energy spectrum for the DR rate coefficient the measurement energy was changed with each injection. The DR fragments were detected using an energy resolving surface barrier detector (SBD). The analog output signal from the

SBD is proportional to the deposited energy and was digitized by an ADC before written into a Histogram Memory Unit (HMU). To each wobbling mode a defined starting address in the HMU is assigned providing separated energy spectra. In case of an H_2^+ or D_2^+ beam basically two energy components show up in the ADC spectra, the total energy in case of DR and only half the energy in case of dissociative excitation (DE), where one of the dissociating fragments is chrges, in the toroid sections of the electron cooler or collisions with residual gas where typically only one fragment hits the SBD. If the fragment rate is too high uncorrelated particles might hit the SBD at the same time (i.e. within the resolution of the Shaping Amplifier) and give rise to additional peaks in the ADC spectra at higher energies. In the present experiments these contributions were less than 0.1 %. The total number of DR events for a wobbling state was obtained by integrating over all events in the full fragment energy region of the corresponding ADC spectrum. The integrated number of events at a wobbling state were then transformed into a DR rate by normalizing to the total measurement time at that state.

Ion current calibration

The DR rate coefficient $\alpha(E)$ at a collision energy E is given by

$$\alpha(E) = \frac{R(E)^{meas}}{n_e(E)\eta N_i}, \tag{5.6}$$

where R^{meas} denotes the DR fragment rate at measurement energy E, $n_e(E)$ the electron density at the energy E, N_i the ion current and $\eta = 0.0269 \pm 0.0002$[8], a TSR specific constant. To obtain a DR rate coefficient, the DR fragment rate R^{meas} as well as the number of stored ions have to be measured.

The number of stored ions is proportional to the ion current I_i and can be written as

$$N_i = \frac{I_i}{e\, f_{TSR}}, \tag{5.7}$$

with the elementary charge e and the revolution frequency f_{TSR} of the ions in the TSR. The ion energy was $E_i = 1.556\,\mathrm{MeV/a.m.u.}$ in both measurements corresponding to a revolution frequency of $f_{TSR} = 0.311\,\mathrm{MHz}$. The SBD used for measuring the DR fragment rate should not be exposed to rates higher than 2-3 kHz. Thus the injection had to be adjusted such that the maximum ion current in the ring was much less than $1\,\mu\mathrm{A}$, the minimum current which can be measured by the DC transformer. In the present experiment the DR fragment rate R^{cool} (i.e. the electron cooler was set to cooling; $E = 0\,\mathrm{eV}$) was used as a signal proportional to the ion current. The relation between both ion current and fragment rate is given by

$$I_i = \Phi R^{cool}. \tag{5.8}$$

---

[8] η is the ratio between the overlap length of the merged electron-ion beam in the electron cooler and the ring circumference.

To link I_i to the rate R^{cool}, the relation constant Φ had to be determined, which was done in several steps.

In a first step the DR fragment rate was related to the trigger rate R_{BPM} of the beam profile monitor (BPM) [89] by determining

$$\gamma = \frac{R_{BPM}}{R^{cool}} \tag{5.9}$$

for each measurement run. Fig. 5.25 shows the relation γ for different measurements. The BPM can be used to measure the residual gas ionization rate by the stored ion and is therefore sensitive to changes in the residual gas pressure. This fact gave rise to systematic fluctuations of γ in each measurement run. The error bars on the data points in Fig. 5.25 therefore represent the standard deviation of a single measurement. The mean values for both measurements amount to:

$$H_2^+: \quad \gamma = 1414 \pm 48, \tag{5.10}$$

$$D_2^+: \quad \gamma = 832 \pm 17. \tag{5.11}$$

In a next step the BPM trigger rate was connected to the rate of the volt-to-frequency converter (VFC). The VFC rate R_{VFC} is proportional to the output voltage of the DC transformator[9] and the ratio λ between BPM and VFC trigger rates is given by

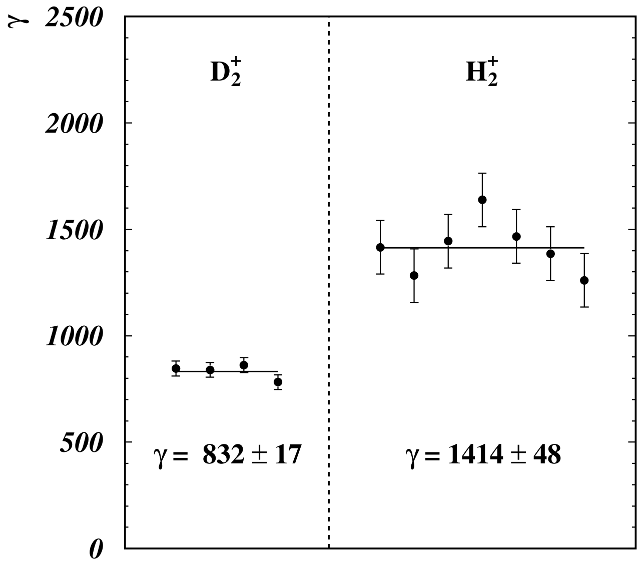

Figure 5.25: *Relation γ between the rate of H_2 (D_2) fragments when the electron cooler was set to cooling (i.e. E=0 eV) and the BPM trigger rate for different measurements. Furthermore the mean values and their standard errors are plotted. The errors on the data points represent the standard deviation of a single measurement.*

$$\lambda = \frac{R_{BPM}}{R_{VFC}}. \tag{5.12}$$

---

[9] This measurement was done with a higher ion current and closed shutter situated in front of the surface barrier detector

Fig. 5.26 shows the ratio λ obtained from different measurements with H_2^+ and D_2^+ ion beams. The weighted mean values are:

$$
\begin{aligned}
H_2^+: \quad \lambda &= 3.05 \pm 0.06, & (5.13)\\
D_2^+: \quad \lambda &= 3.05 \pm 0.03. & (5.14)
\end{aligned}
$$

The same ratio λ was found for both the H_2^+ and D_2^+ beam. This observation is consistent with the fact that the cross section for residual gas ionization is proportional to the ion energy per nucleon which was about 1 MeV/a.m.u. for both measurements[10]. The larger error in the mean value for the calibration with the H_2^+ beam is probably caused by stronger fluctuations in the ring pressure which has been already seen in the previous calibration step.

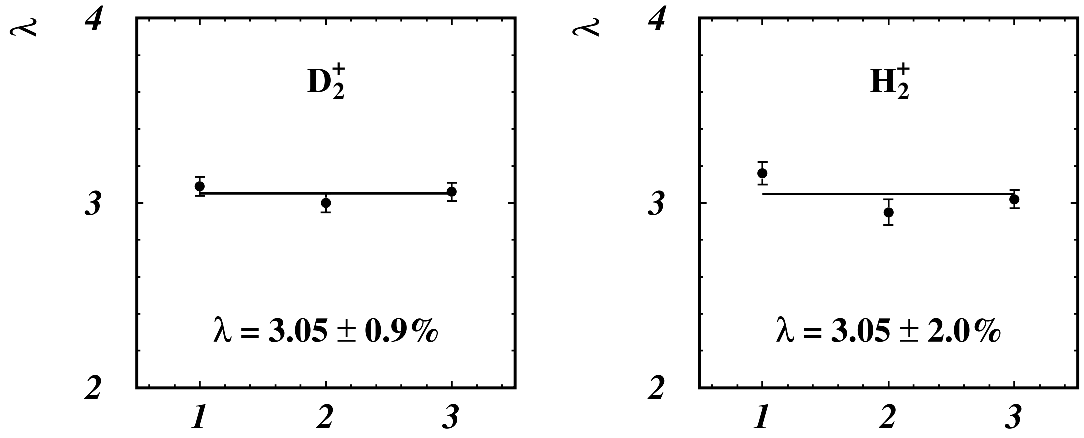

Figure 5.26: *Relation λ between the BPM signal trigger rate and the volt-to-frequency converter rate for different measurements and both molecular ion beams.*

The calibration of the VFC was done at several DC transformator output voltages, see Fig. 5.27; the accuracy of the DC is about ±0.5 mV. The relation between the DC voltage U_{DC} and the VFC rate R_{VFC} is defined as

$$\epsilon = \frac{\partial U_{DC}}{\partial R_{VFC}}. \tag{5.15}$$

The slope ϵ yielded from a linear fit to the measured values is:

$$\epsilon = 0.0228 \pm 0.001 \text{ mV/Hz}. \tag{5.16}$$

The DC transformator output voltage corresponds to an ion current according to the known

---

[10] The residual gas consists of about 90 % of H_2 and the cross section for ionization of H_2 can be approximated by: $\sigma \approx 4 \times 10^{-17} q^2 A/E\,\mathrm{cm}^2$, where E/A is the beam energy in MeV/a.m.u. and q the charge state of the stored ion [89].

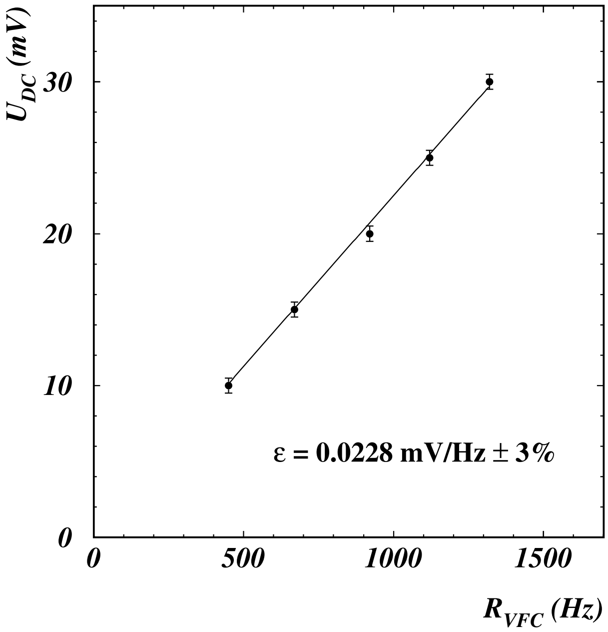

Figure 5.27: *Calibration of the volt-to-frequency converter (VFC). The relation between the DC voltage and the output frequency of the VFC is given by the slope ϵ.*

calibration factor:

$$\sigma = \frac{I_i}{U_{DC}} = 1\,\mu\text{A/mV}. \tag{5.17}$$

Using Eq. 5.8 the ion current can directly be related to the signal rate R^{cool} with the relation constant

$$\Phi = \frac{\sigma\epsilon}{\gamma\lambda}, \tag{5.18}$$

which amounts to

$$H_2^+ : \quad \Phi = 5.3 \pm 0.5\,\text{pA/Hz}, \tag{5.19}$$

$$D_2^+ : \quad \Phi = 9.0 \pm 0.5\,\text{pA/Hz}, \tag{5.20}$$

for the two different ion beams. The errors are obtained from the sum over the uncertainties in the different calibration steps and represent the maximum error in the calibration of the ion current with respect to the DR fragment rate R^{cool}. The number of stored ions can be derived combining Eqs. 5.7 and 5.8:

$$N_i = \frac{I_i}{e\,f_{TSR}} = \frac{R^{cool}}{e\,f_{TSR}}\Phi. \tag{5.21}$$

To get the correct DR rate coefficient uncorrelated fragment pairs from collisions between the molecular ions and residual gas molecules need to be subtracted. The DR rate coefficient at large collision energies, such as the reference energy in the experiments, is very low because of the small Franck-Condon overlap between the wavefunctions of the vibrational ground state of H_2^+ (D_2^+) and the Rydberg states of the so-called Q_2 series. The fragment pairs at reference energy can therefore be assumed to be uncorrelated and their rate $R(E)^{ref}$ was subtracted from the rate at measurement energy. Combining Eqs. 5.6 and 5.21, the background corrected DR rate coefficient is given by

$$\alpha(E) = \frac{ef_{TSR}}{n_e\eta}\,\frac{1}{\Phi}\,\frac{\langle\, R(E)^{meas} - R(E)^{ref}\,\rangle}{\langle\, R^{cool}\,\rangle}, \tag{5.22}$$

where all rates were averaged over the different measurement runs, expressed by $\langle\ \rangle$.

DR rate coefficients for H_2^+

Fig. 5.28 shows the measured DR rate coefficient of H_2^+ (black dots). The reference energy was $E_{ref} = 44.1\,\mathrm{eV}$ for all measurement runs. The two peaks at around 9 eV and 16 eV are due to recombinations via the so-called Q_1 and Q_2 series[11] and have approximately the same DR rate coefficient as for HD^+ [71]. This is consistent since at such high collision energies isotope effects should not play a role anymore. The error on the absolute scale is caused by the error in the ion current calibration and amounts to ±8.4 %, see Eq. 5.20. The increased collision energy in the toroid sections of the electron cooler (Sec. 4.4.4) gave rise to an enhanced DR rate coefficient in the collision energy regime between $E = 0.5 - 5\,\mathrm{eV}$, because of the large DR rate coefficient at collision energies of about $E = 8 - 10\,\mathrm{eV}$. Although the overlap length between the electron-ion beam in the toroid section is rather small compared to the total overlap length DR at these collision energies is much more likely and enhances the recombination rate at the adjusted energy E. To correct for the toroid effects an iterative procedure, first introduced for a dielectronic recombination experiment by A. Lampert [103], was applied to the experimental data. The corrected spectrum is shown in Fig. 5.28 (solid line with dots) together with the toroid contributions (dotted line). As has been found by analysing the RFI data (Sec. 5.3.1), the relative contribution of the ground vibrational state to DR stays constant and amounts to $q_0 = 89.6 \pm 1.4\,\%$ after a storage time of 40 s, thus the presented data were taken after 40 s of pre-cooling and the measured rate coefficient needs to be corrected for the contribution of the first excited vibrational state to obtain the correct value for $v = 0$. As discussed in Sec. 4.4.3 the experimental DR rate coefficient for merged-beam experiments is a convolution of the DR cross section with the anisotropic thermal electron velocity distribution. For our merged-beam conditions ($kT_\perp = 11.8\,\mathrm{meV}$ and $kT_{||} = 0.1\,\mathrm{meV}$) and taking into account the contribution of $v = 1$ (i.e. $q_0(t > 40\,\mathrm{s}) \approx 90\,\%$), we got a DR rate coefficient of

$$\begin{aligned} \alpha_{mb} &= 0.9\cdot(2.1 \pm 0.2)\times 10^{-8}\,\mathrm{cm}^3/\mathrm{s} \\ &= (1.9 \pm 0.2)\times 10^{-8}\,\mathrm{cm}^3/\mathrm{s}. \end{aligned} \tag{5.23}$$

Assuming a $1/E$ behavior of the DR cross section, this rate coefficient can be converted into a thermal rate coefficient (isotropic Maxwellian distribution) for $T = 300\,\mathrm{K}$ with

$$\alpha = (0.8 \pm 0.1)\times 10^{-8}\,\mathrm{cm}^3/\mathrm{s}, \tag{5.24}$$

---

[11] The dissociative Rydberg series of H_2 having a $2p\sigma_u$ and $2p\pi_u$ core are called Q_1 and Q_2, respectively [6].

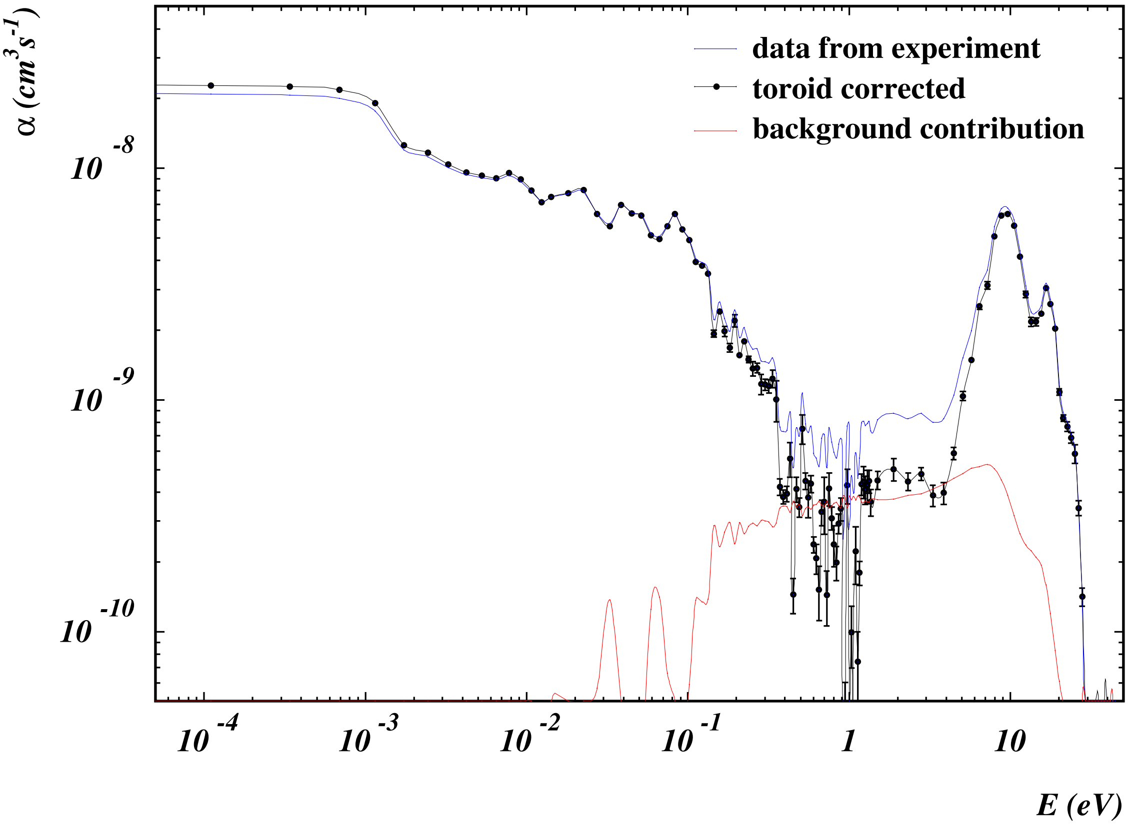

Figure 5.28: *Measured rate coefficient for DR of H_2^+ with electrons. The spectrum was measured after 40 s of pre-cooling. The systematic errors on the plotted rate coefficients are 8.4 %. The background contribution from collisions in the toroid region (dotted line) was subtracted from the experimental data (black dots). Furthermore, the background corrected rate coefficient is plotted (solid line with dots).*

using Eq. 4.26 and assuming

$$\alpha(T) \approx (1/T)^{0.5}. \tag{5.25}$$

M. Lange studied threshold effects in the DR of vibrationally cold HD^+ [71, 41] and presented DR rate coefficients for two different transverse electron temperatures; the longitudinal temperature was $kT_{||} \approx 0.1$ meV in both experiments. At electron-ion collision energies $E < 1$ meV the DR rate coefficient amount to $\alpha \approx (3.0 \pm 0.6) \times 10^{-8}$ cm^3/s and $\alpha \approx (1.3 \pm 0.3) \times 10^{-8}$ cm^3/s at transverse temperatures $kT_\perp = 4$ meV and $kT_\perp = 28$ meV, respectively. To compare the DR rate coefficients of HD^+ with that of H_2^+ the results need to be scaled to our merged-beam conditions ($kT_\perp \approx 12$ meV). Assuming again the dependence $\alpha(T) \approx (1/T)^{0.5}$ (Eq. 5.25) on the electron temperature, one obtains for the two DR rate coefficients a mean value $\alpha \approx (1.8 \pm 0.4) \times 10^{-8}$ cm^3/s, which is, within the error bars, the same as the DR rate coefficient for H_2^+ . This has been already seen before in DR experiments at CRYRING [22], where a convergence of the relative DR rates for HD^+ and H_2^+ to the same value was found after approximately 30 s of storage time and electron cooling. Recently, new MQDT calculations were performed by Schneider *et al.* [99] of absolute anisotropic ($kT_\perp = 12\,\mathrm{meV}$ and $kT_{||} = 0.1\,\mathrm{meV}$) DR rate coefficients at a collision energy $E = 0.01\,\mathrm{meV}$. The calculated DR rate coefficient amounts to

$$\alpha(E = 0.01\,\mathrm{meV}) \quad = \quad 4.54 \times 10^{-8}\,\mathrm{cm}^3/\mathrm{s}. \tag{5.26}$$

This values is about a factor of two higher than the experimental DR rate coefficient for vibrationally cold H_2^+ ions.

Due to the electron energy distribution the measured DR rate coefficient should be constant for collision energies of the order of the transverse (Sec. 4.4.3) electron temperature (i.e. at collision energies smaller than approximately 12 meV), whereas the measured DR rate coefficient further increases at lower collision energies. This feature could be caused by the actual shape of the DR cross section at very low collision energies. The measured DR rate coefficient is a convolution of the DR cross section $\sigma(E)$ with the flattened Maxwellian electron velocity distribution (Sec. 4.4.3) in our experiment and could be dominated by the longitudinal electron temperature at sub-thermal collision energies. J.R. Mowat [100] discussed the shape of DR rate coefficients at collision energies lower than the thermal electron temperature and different $1/E^n$ cross section behavior (with n=1.10, 1.15 and 1.20) and found for all values of n an increase in the DR rate coefficient at sub-thermal collision energies. The increase is becoming more pronounced with larger values for n. The increasing DR rate coefficient for $E < 10\,\mathrm{meV}$ could therefore be a hint for a DR cross section $\sigma \propto 1/E^n$ with $n > 1.0$ for low collisions energies.

Another explanation for that behavior could be a drop in the DR cross section at a collision energy $E \approx 1\,\mathrm{meV}$. It was not possible to assign a destructive window resonance (Sec. 2.1.1) to that energy.

DR rate coefficients for D_2^+

Fig. 5.29 shows the measured DR rate coefficient spectrum for D_2^+ taken after a pre-cooliong time of 40 s, i.e. no further vibrational cooling (Sec. 5.3.1). The spectrum is divided into two parts. The reference energy for the measurement at collision energies $E < 0.6\,\mathrm{eV}$ was $E_{ref} = 93.1\,\mathrm{eV}$, whereas for higher collision energies a negative cathode voltage offset[12] was chosen as reference energy, sufficient high enough that no electrons got extracted from the cathode. The positions and absolute rates of the peaks caused by capture states belonging to the Q_1 ($\approx$ 9 eV) and Q_2($\approx$ 16 eV) series (see discussion for the H_2^+ measurement) are approximately the same as for H_2^+ and HD^+ . The value for the DR rate coefficient drops dramatically in the collision energy range from $E \approx 10^{-4}$ to $E \approx 10^{-3}$. This strong effect has not been seen in the H_2^+ measurement

---

[12] The relative collision energy is defined by the cathode voltage of the electron cooler, see Sec. 4.4.

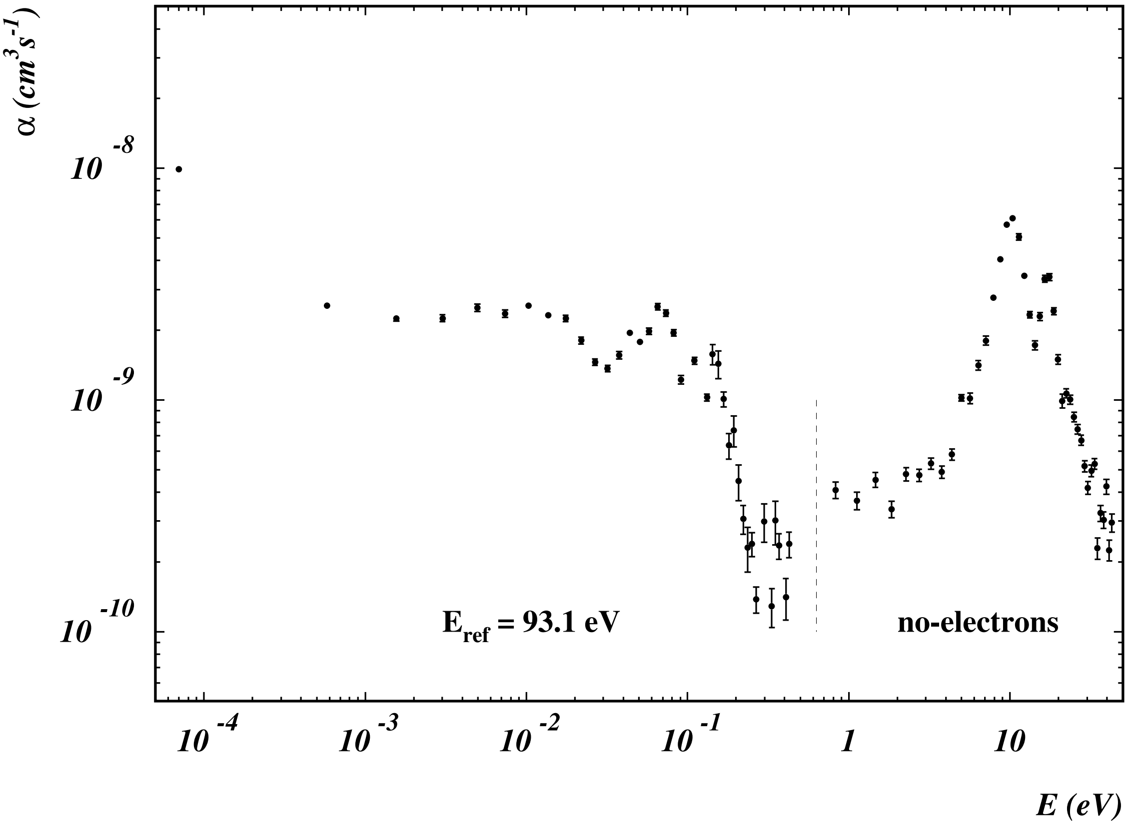

Figure 5.29: *Measured rate coefficient for DR of D_2^+ with electrons. The spectrum was measured after 40 s pre-cooling. The systematic errors on the plotted rate coefficients are 5.9 %. The reference collision energy in the left part of the plotted spectrum was $E_{ref} = 93.1$ eV, whereas the electron beam was turned off in the reference energy step at the measurement for collision energies $E > 0.55$ eV, see plot. No toroid background correction has been applied to the data.*

and is still not understood. A reason for that behavior might be problems with the reference energy. The time given to the electron cooler to adjust to the measurement energy before starting the data acquisition (5 ms, see Sec. 4.6.1) could have been to short. If the setting was too slow the collision energy could have been still too high and the DR fragment rate therefore too small. But this does not explain why the fragment rate at $E < 10^{-4}$ eV, corresponding to the cooling energy, was the same as in the next wobble step when the electron cooler was set to cooling energy. To fully understand the drop in the DR rate coefficient, new experiments are planed in the closer future. There are no toroid corrections applied to the spectrum because of the small number of data points and the problems in the understanding of the spectrum. If the problems discussed above are due to problems with the adjustment to the measurement energy and connected to the reference energy, the step to the cooling energy is not problematic and the DR rate coefficient can

	H_2^+	D_2^+
v	$kT_\perp = 11.9\,\mathrm{meV}$	$kT_\perp = 11.8\,\mathrm{meV}$
0	1.87 ± 0.15	1.18 ± 0.09
1	18.7 ± 11.2	6.9 ± 4.0
2	15.3 ± 9.5	5.1 ± 3.4
3	18.0 ± 11.5	5.6 ± 3.6
4	9.9 ± 6.3	8.9 ± 6.4
5	84 ± 57	8.7 ± 6.8
6	118 ± 80	7.5 ± 5.4
7	-	32.6 ± 23.4

Table 5.2: *Summarized results for the absolute DR rate coefficients (in units of* 10^{-8} *cm*^{3}*/s) for the lower vibrational states of* H_2^+ *and* D_2^+ *. The electron-ion collision energy was* $E \approx 0\,meV$ *and the temperature of the longitudinal electron velocity* $kT_{||} \approx 0.1\,meV$ *in both experiments. The transverse electron temperature was as stated on top of each column. For vibrational states below the drawn horizontal lines DR via the higher dissociative state belonging to the* Q_1 *series is energetically possible.*

be obtained from the DR fragment rate at the cooling energy. The DR rate coefficient at cooling energy E_{cool} is defined by our merged-beam conditions ($kT_\perp = 11.8\,\mathrm{meV}$ and $kT_{||} = 0.1\,\mathrm{meV}$). Taking into account the contribution of $v = 1$ (i.e. $q_0(t > 40\,\mathrm{s}) \approx 96\,\%$), the DR rate coefficient is

$$\begin{aligned} \alpha_{mb} &= 0.96 \cdot (1.2 \pm 0.1) \times 10^{-8}\,\mathrm{cm^3/s} \\ &= (1.2 \pm 0.1) \times 10^{-8}\,\mathrm{cm^3/s}. \end{aligned} \tag{5.27}$$

As for H_2^+ , this DR rate coefficient can be converted into a thermal rate coefficient (isotropic Maxwellian distribution) for $T = 300\,\mathrm{K}$ and amounts to

$$\alpha = (0.45 \pm 0.04) \times 10^{-8}\,\mathrm{cm^3/s}. \tag{5.28}$$

Taking the relative DR rate coefficients for H_2^+ and D_2^+ from Sec. 5.2.2 and the absolute DR rate coefficients for $v = 0$, discussed in this section, absolute values for the lower vibrational states can be derived. The final results for the absolute DR rate coefficients of H_2^+ and D_2^+ are summarized in Tab. 5.2.

5.4 Absolute SEC rate coefficients for H_2^+ and D_2^+

The vibrational cooling rates observed in an H_2^+ and D_2^+ ion beam interacting with electrons will be discussed in this section. There are two processes taking place in a merged electron-ion beam at near-zero collision energies, DR and SEC. In Sec. 5.3 absolute experimental DR rate coefficients for H_2^+ and D_2^+ are presented which can be used to obtain first absolute SEC rate coefficients for both molecular ions. In the first part a model describing the vibrational cooling will be developed and applied to estimate absolute SEC rate coefficients for H_2^+ . In the following two parts more elaborate studies of the vibrational cooling will be discussed and absolute SEC rate coefficients presented for H_2^+ and D_2^+ .

5.4.1 First estimated absolute SEC rate coefficients for H_2^+

The two processes, SEC and DR, affect the vibrational population distributions of H_2^+ and D_2^+ , but in different ways. While DR preferentially removes molecular ions in those vibrational states that have larger DR rate coefficients than the others, SEC transfers population from high to low vibrational states. No significant changes in the vibrational population are taking place in the absence of the electron-ion interactions (Sec. 5.1). Thus, it seems appropriate to use a simple model where only DR and SEC are affecting the vibrational population of the molecular ions interacting with electrons at approximately zero relative energies. Radiative transitions can be neglected. Dipole transitions are not allowed for H_2^+ and D_2^+ due to a missing static dipole moment and the estimated lifetime for quadrupole transitions from $v = 1$ to $v = 0$ in H_2^+ is of the order of 10^6 s [3]. The rates for radiative transitions between vibrational states are therefore much smaller than the smallest DR or SEC rates at the applied electron densities.
Assume an ensemble with $N_v(t)$ molecules in the different vibrational states v and initial ($t = 0$) occupation numbers N_v^0. Furthermore assuming there are $\tilde{n}$ vibrational states ($v = 0$ up to $v = \tilde{n} - 1$), the numbers $N_v(t)$ are given by a set of coupled differential equations:

$$\frac{dN_v(t)}{dt} = -\left(\alpha_v + \beta_v\right) n_e \eta N_v(t) + \beta_{v+1} n_e \eta N_{v+1}(t), \tag{5.29}$$

where n_e denotes the electron density, η the ratio between the electron cooler length and the ring circumference and β_v and α_v the SEC and DR rate coefficients, respectively, for a given vibrational level v, with $\beta_0 = 0$ and (neglecting feeding from higher states $v \geq \tilde{n}$) $\beta_{\tilde{n}} = 0$. It was assumed that the cooling can be described in good approximation by using only the SEC rate coefficients for $\Delta v = 1$. This assumption is consistent with theoretical calculations for SEC rate coefficients which predict SEC rate coefficients for each vibrational state v with $\Delta v = v - v' \geq 2$ which are almost an order of magnitude lower than the corresponding rates for $\Delta v = 1$ (see Tab.5.5). These calculations are based either on the MQDT (Schneider *et al.* [99] and Nakashima *et al.* [24]) or on the R-matrix theory (Sarpal and Tennyson [23]). This set of coupled differential equations can be solved following the procedure discussed in Append. E. The time evolution of the population of a vibrational state v can then be obtained by normalizing $N_v(t)$ to the total number of molecules:

$$p_v(t) = \frac{N_v(t)}{\sum_v N_v(t)}. \tag{5.30}$$

In a first step the measured vibrational population distributions for H_2^+ (Fig. 5.6) were compared to the modeled time dependence using DR and SEC rate coefficients predicted by theory [27]. For the DR rate coefficients α_v the values calculated by Nakashima *et al.* [24] were used for the first five vibrational states (corrected for the present electron velocity distributions and temperatures). For the SEC rate coefficients we used the values calculated by Sarpal and Tennyson [23]. Their calculations have been performed only for the vibrational states $v = 1, 2$, yielding $\beta_1 = 8.5{\times}10^{-8}$ cm^3 s^{-1} and $\beta_2 = 2.0{\times}10^{-7}$ cm^3 s^{-1}. In order to evaluate the time dependence of the vibrational population for $v = 0 - 5$ we have arbitrarily assumed the SEC rate coefficients for the levels $v = 3, 4, 5$ and 6 to be equal to the one calculated by Sarpal and Tennyson [23] for the $v = 2$ level. Sarpal and Tennyson assumed that the SEC rate coefficients for the higher vibrational states are smaller than for the first two vibrational states. For the DR rate coefficients, only the values for the $v = 5$ and 6 levels are missing, and they were set equal to the rate coefficient for the $v = 4$ level, as calculated by Nakashima *et al.* [24], assuming that their values are not very different from $v = 4$ It will be shown later, when the time evolution obtained from the model is compared to the experimental data, that the main conclusions do not depend on these assumptions. The initial number of ions N_v^0 in a vibrational state v were set to the measured values of the initial population p_v^0 (see Fig. 5.3); the level $v = 6$ was included ($\tilde{n} = 7$) to describe feeding of $v = 5$, and feeding from $v > 6$ was neglected.

Fig. 5.30 shows a comparison of the measured populations of the vibrational states $v = 0 - 5$ (taken from Fig. 5.6) with time evolutions for $p_v(t)$ as calculated for DR and SEC separately as well as for the combination of both processes, using the rate coefficients as calculated or assumed on the basis of available calculations and described above. Clearly, none of these modeled time evolutions (dashed and dotted lines) can explain the experimental data. To make sure the mismatch between experimental data and the modeled time evolutions is not caused by the applied restriction to SEC changing the vibrational quantum number by only one unit, we extended our model to transitions with $\Delta v > 1$. Additionally we used SEC rate coefficients by Schneider *et al.* [99], obtained from modified MQDT calculations; these SEC rate coefficients are summarized in Tab. 5.5. The time evolutions, obtained with the modified model and the new set of SEC rate coefficients ($E = 0.01$ meV), are very similar to the results shown in Fig. 5.30 and therefore not shown here[13]. The remaining mismatch between theory and experiment is not surprising since the SEC rate coefficients for $v = 1 - 3$ are of the same order of magnitude as the ones calculated by Sarpal and Tennyson. Additionally, the SEC rate coefficients for higher vibrational transitions are at most 25 % of the corresponding transition with $\Delta v = 1$ and have only small contributions to the vibrational cooling. In order to fit the data we kept the calculated DR rate coefficients fixed to the values given above and increased, by trial and error, the SEC rate coefficients until we archived a reasonable agreement with the experimental data. The full lines in Fig. 5.30 represent the calculated time dependence for SEC rate coefficients β_v set to the following values (in units of $1{\times}10^{-6}$ cm^{3}s^{-1}): β_1=0.6, β_2=1.2, β_3=2.2, β_4=2.4, and β_5=4.4 [27]. It seems that the SEC rate coefficients needed to reproduce the observed vibrational cooling are

---

[13] The experimental electron-ion collision energy was $E < 0.1$ meV. The SEC rate coefficients for this energy correspond to the values calculated for $E = 0.01$ meV, shown in Tab. 5.5

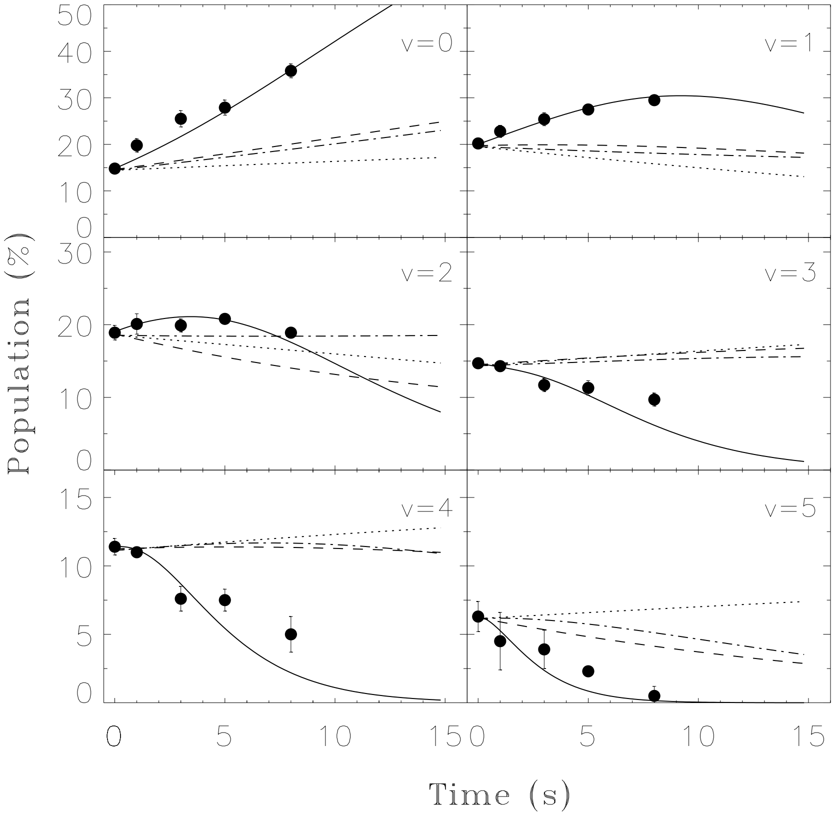

Figure 5.30: *Time evolution of the vibrational population for the first six vibrational states of* H_2^+ *as a function of the interaction time with near-zero relative energy electrons (filled symbols) in comparison to the model results for DR only (dotted lines), SEC only, based on Sarpal and Tennyson [23] (dashed lines), DR plus SEC as based on Sarpal and Tennyson [23] (dash-dotted lines), and DR plus SEC with modified SEC rate coefficients as given in the text (full lines).*

considerably larger, mostly by more than one order of magnitude, than the calculated values by Sarpal and Tennyson [23], were $\beta_1^{cal} = 0.085 \times 10^{-6}\,\mathrm{cm}^3/\mathrm{s}$ and $\beta_2^{cal} = 0.2 \times 10^{-6}\,\mathrm{cm}^3/\mathrm{s}$ [14].
The measurement of the absolute vibrational state specific DR rate coefficient of H_2^+ was performed after the publication of these SEC rate coefficients [27]. However, measurements by W. van der Zande *et al.* [22] had shown, that the DR rate coefficient for vibrationally cold H_2^+ is similar to the value for vibrationally cold HD^+ and of the order of $2 \times 10^{-8}\,\mathrm{cm}^3/\mathrm{s}$, which is in good agreement with the calculated value for $v = 0$ by Nakashima *et al.* [24]. This result justified the selection of the calculated DR rate coefficients and proved for the first time that SEC is the dominant vibrational cooling process.

---

[14] SEC rate coefficients for higher vibrational states were estimated to be even smaller [23].

5.4.2 Absolute SEC rate coefficients for H_2^+

With the relative DR rate coefficients determined in Sec. 5.2 the RFI technique can be used to obtain the time evolution of the vibrational population $p_v(t)$ of a vibrational state v by measuring its relative contribution $q_v(t)$ to DR. Thus, an additional DR experiment was carried out to study the longtime behavior of the vibrational cooling and was used to derive, together with the experimental absolute DR rate coefficients (see Tab 5.2), absolute SEC rate coefficients for H_2^+ . The RFI technique replaces a direct measurement of the vibrational population and has the advantage that the vibrational population distribution can be observed for all storage times, whereas the CEI technique allows the vibrational population distribution to be studied only for a fixed storage time interval following each injection. Hence, the CEI technique has a large duty circle. The applied DR measurement for an H_2^+ ion beam has already been discussed in Sec. 5.2.1. The relative contribution $q_v(t)$ of a vibrational state v to the DR with a DR rate coefficient α_v is expressed by

$$q_v(t) = \frac{p_v(t)\alpha_v}{\sum_v p_v(t)\alpha_v}, \tag{5.31}$$

where $p_v(t)$ is the time evolution of the population of that vibrational state. The functions $q_v(t)$ were simultaneously fitted (see Fig. 5.32) to the measured relative DR contributions of the first six vibrational states by least-square minimization, using the SEC rate coefficients as free parameters. The functions $p_v(t)$ were calculated using Eq. 5.30 and the model was restricted to $\tilde{n} = 7$ vibrational states and vibrational transitions $\Delta v = 1$. The DR rate coefficients were kept fixed and set to the their absolute values known from the relative DR rate coefficient measurement (Sec. 5.2.2) and the absolute DR rate coefficient measurement for the vibrational ground state; see Sec. 5.3. The initial vibrational population was set to the values plotted in Fig. 5.3. The fitted time evolutions $q_v(t)$ are plotted (full lines) on top of the experimental data (filled symbols) in Fig. 5.31. The thin lines show the time evolution using the calculated and estimated SEC and DR rate coefficients from Sarpal and Tennyson [23] and Nakashima *et al.* [24], respectively, as discussed before. It clearly turns out that the time constants[15] for vibrational cooling are too long and subsequently the calculated SEC rate coefficients too small. The fitting results for the SEC rate coefficients are summarized in Tab. 5.5 and compared to SEC rate coefficients calculated by Schneider *et al.* [99] for our experimental conditions, i.e. anisotropic electron velocity distribution with the transversal and longitudinal electron temperature $kT_\perp = 12\,\mathrm{meV}$ and $kT_{||} = 0.1\,\mathrm{meV}$, respectively. It should be mentioned again that the experimental SEC rate coefficients were obtained based on the assumption that *only* $\Delta v = 1$ transitions are allowed. This assumption is not supported by a *propensity rule* as the calculated

---

[15] The time constant τ for electron induced vibrational deexcitation is defined by the rate coefficient β, the electron density n_e and the constant $\eta = 0.027$ (see Sec. 4.6) and amounts to $\tau = (\beta n_e \eta)^{-1}$ (see Eq. 6.2).

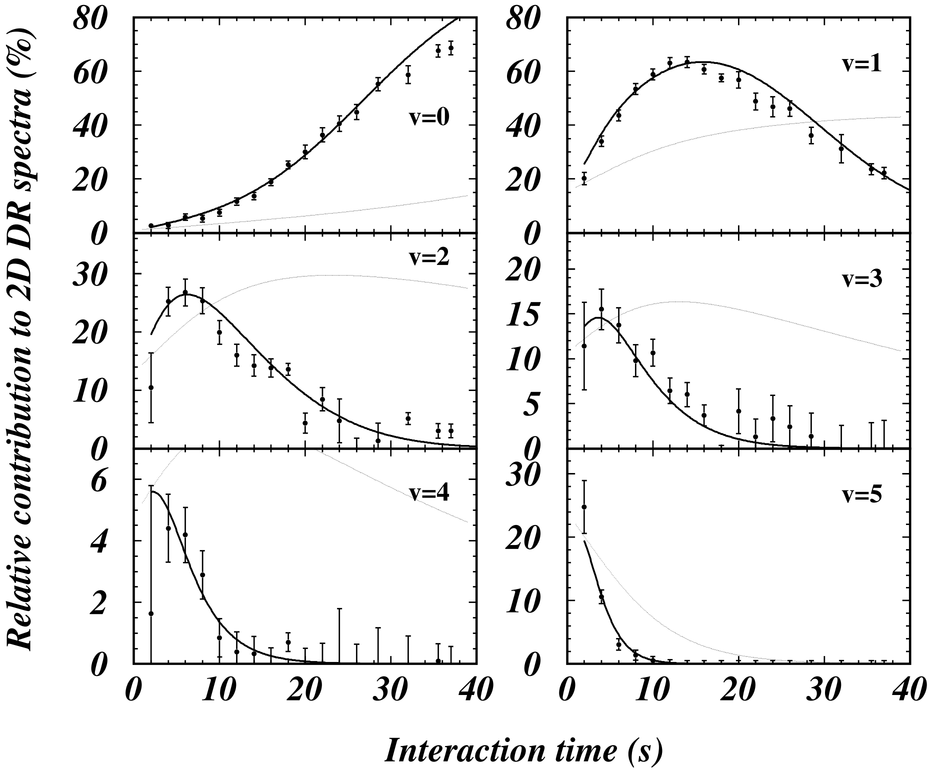

Figure 5.31: *Measured relative contributions of the first six vibrational states to the two-dimensional DR spectra (filled symbols) for* H_2^+*. The full lines represent the modeled time evolutions* $q_v(t)$ *as obtained from a simultaneous fit to the six projected fragment distance spectra. The fits were performed using the SEC rate coefficients as free parameters and keeping the DR rate coefficients fixed to the measured values. The thin lines represent the modeled time evolutions using the calculated DR and SEC rate coefficients.*

SEC rate coefficients in Tab. 5.5 show. Including also higher vibrational transitions ($\Delta v = 2$) in the model made the least square fitting procedure unstable.

The fitted SEC rate coefficients are systematically smaller than the estimated values published in Ref. [27] and discussed before, which is due to the different set of absolute DR rate coefficients. The experimental absolute DR and SEC rate coefficients were therefore used to model the vibrational population evolution under the experimental conditions (modified electron density and thus different time constants for the vibrational cooling) of the CEI measurement (see Fig. 5.6 in Sec. 5.1) used to derive first absolute SEC rate coefficients. The results are shown in Fig. 5.32. Besides for the vibrational ground state a rather good agreement between experimental and modeled data is discernible and proves the reliability of the model. The modeled time evolution for the vibrational ground state is systematic about 3-4 % lower than the measured data for $t > 0$ s which might be due to a systematic errors in the measurement of the initial

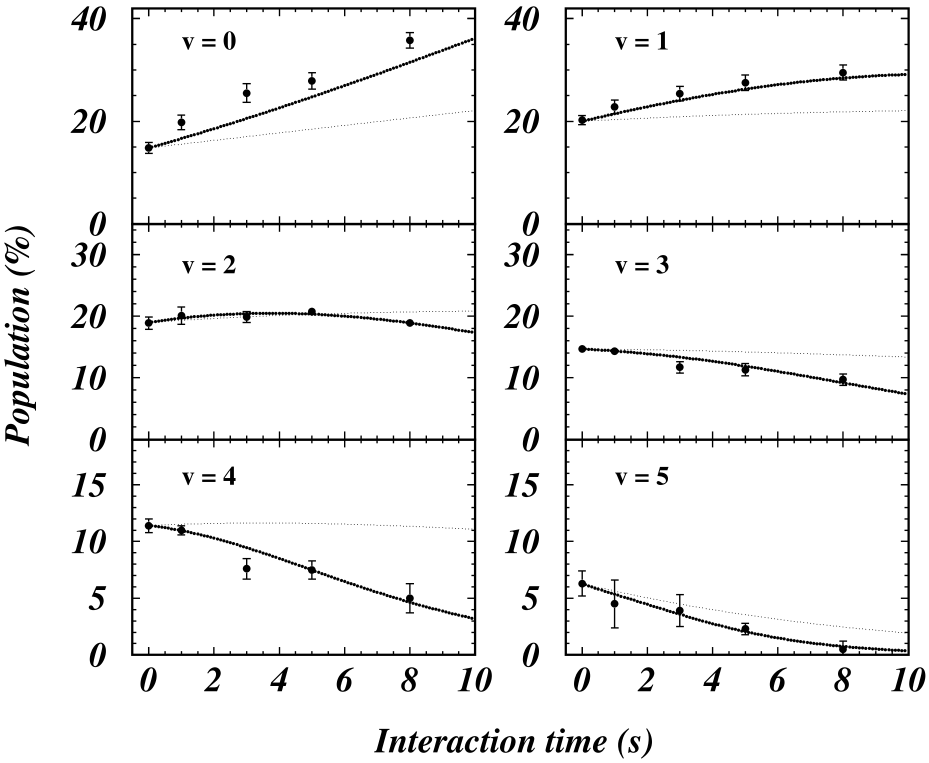

Figure 5.32: *Time evolution of the vibrational population for the first six vibrational states of H_2^+ as a function of the interaction time with near-zero relative energy electrons (filled symbols). The solid lines represent the modeled population evolutions. For the SEC rate coefficients the values from Tab. 5.5 and for the DR rate coefficients the experimental results were taken. The thin lines represent the time behavior of the population if the calculated SEC rate coefficients are used.*

vibrational population distribution (Fig. 5.3) which was used as an input to the model.

The statistical uncertainties on the SEC rate coefficients in Tab. 5.3 are less than 5 % for fixed DR rate coefficients. The rather large systematic errors on the relative DR rate coefficients, discussed in Sec. 5.2.2, need to be considered. Since no simple analytic expression can be found for $p_v(t)$ (Eq. 5.30) a simple calculation of the propagation of errors is not feasible. To estimate the errors on the absolute SEC rate coefficients the absolute DR rate coefficients were varied within their uncertainties and a new set of SEC rate coefficients obtained by following the fitting procedure discussed above. The uncertainties in the absolute SEC rate coefficients were found to be less than 20 % and are therefore much smaller than the errors on the relative DR rate coefficients which can be explained by the smaller contribution of DR to the vibrational cooling with respect to SEC.

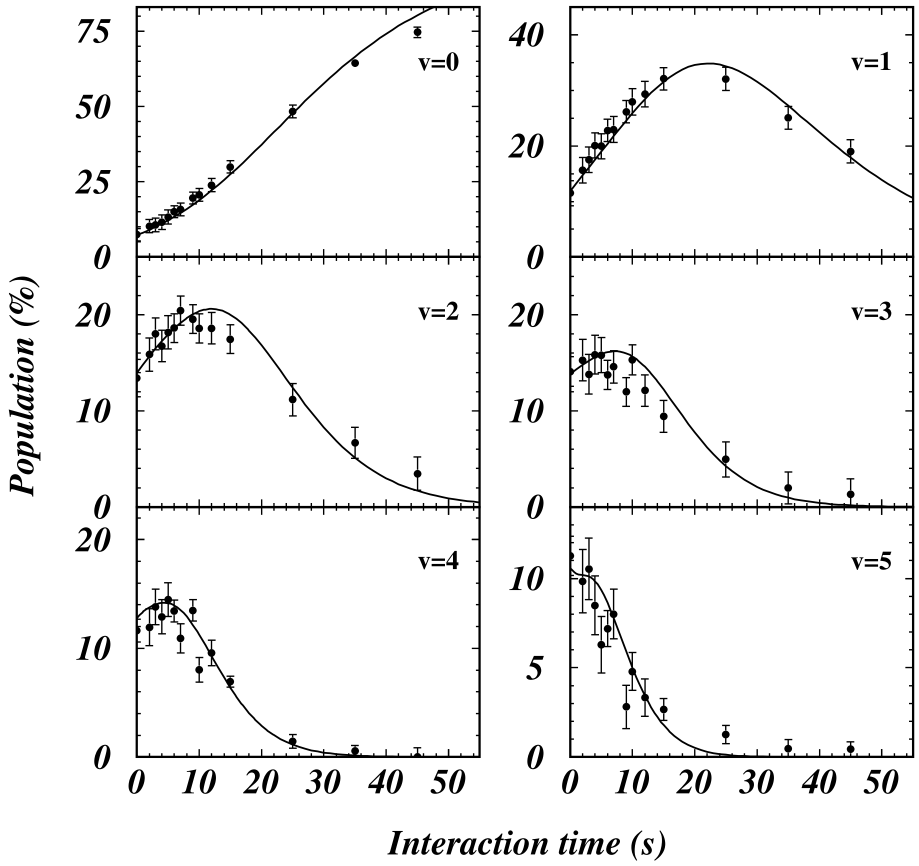

Figure 5.33: *Vibrational population evolution of the first six vibrational states of D_2^+ as a function of the interaction time with near-zero relative energy electrons (filled symbols). The full lines represent the modeled time behavior as obtained from a simultaneous fit to all shown spectra. The fits were performed using the SEC rate coefficients as free parameters and keeping the DR rate coefficients fixed to the measured values.*

5.4.3 Absolute SEC rate coefficients for D_2^+

The vibrational population evolution within the first 45 s of interaction between D_2^+ molecular ions and electrons (collision energy $E \approx 0\,\mathrm{eV}$) has been discussed in Sec. 5.1. These results are shown in Fig. 5.7. These data were used to obtain absolute SEC rate coefficients for D_2^+ by a simultaneous fit of the vibrational populations $p_v(t)$ (Eq. 5.30) to the measured data choosing the SEC rate coefficients as free parameters and keeping the absolute DR rate coefficients fixed. The absolute DR rate coefficients for vibrational states $v = 0-7$ are known from the experiment discussed in Sec. 5.1 and scaled with the absolute DR rate for the vibrational ground state, known from the DR rate coefficient measurement with an almost vibrationally cold D_2^+ ion beam (see Sec. 5.3). The functions $p_v(t)$ were calculated using Eq. 5.30 restricting the model for the vibrational cooling again to $\tilde{n} = 7$ vibrational states and vibrational transitions $\Delta v = 1$. The initial vibrational population was set to the values obtained from the CEI measurement without electron-ion interactions, see Fig. 5.3. The fitted time evolutions $p_v(t)$ are plotted in Fig. 5.33 (full lines) on top of the measured data (filled symbols) from Fig. 5.7. The absolute SEC rate coefficients are summarized in Tab. 5.3. The uncertainties for the absolute SEC rate coefficients were obtained following the procedure discussed for the SEC rate coefficients of H_2^+ and amount to about 20 %, see Tab. 5.3 for all vibrational states. The overall agreement between experimental data and fitted time evolutions proves that SEC is the dominant vibrational cooling process.

v	H_2^+ $kT_\perp = 12.7\,\mathrm{meV}$	D_2^+ $kT_\perp = 11.8\,\mathrm{meV}$
1	39 ± 8	36 ± 7
2	76 ± 16	89 ± 18
3	121 ± 26	125 ± 25
4	146 ± 30	150 ± 30
5	210 ± 42	220 ± 44

Table 5.3: *Summarized results for the absolute SEC rate coefficients (in units of 10^{-8} cm^3/s) for the lower vibrational states of H_2^+ and D_2^+. The size of the uncertainties are discussed in the text. The temperature of the longitudinal electron velocity $kT_{||} \approx 0.1$ meV in both experiments. The transverse electron temperature was as stated on top of each column.*

5.5 Discussion: experimental results versus theoretical predictions

The results for the absolute DR and SEC measurements are summarized in Tab. 5.4. The relative DR rate coefficients were scaled with the absolute values of DR rate coefficients for vibrationally cold H_2^+ and D_2^+ ions. The uncertainties on the values were obtained from the sum over the uncertainties of the different measurements and represent the maximum errors on the rate coefficients.

The SEC rate coefficients for the initial vibrational states $v = 1 - 5$ are identical for H_2^+ and D_2^+ within their error bars, whereas the DR rate coefficients for the first four vibrational states of H_2^+ are between 1.6 and 3.2 times larger than for D_2^+. A comparison of DR rate coefficients of vibrational states larger than $v = 4$ is difficult due to the additional dissociative DR channels energetically accessible from the vibrational states $v = 5$ and $v = 7$ for H_2^+ and D_2^+, respectively. Besides for the vibrational state $v = 4$ all rate coefficients for H_2^+ are larger than for D_2^+.

The recombination of an electron with a hydrogen molecular ion is a dielectronic process forming a doubly excited neutral hyrogen molecule. This state can either dissociate into two neutral fragments (DR) or autoionize again (inverse recombination process). The latter process corresponds to a SEC if the molecular vibrational state has changed. The cross section σ_{cap} for the recombination (Eq. 2.8) is proportional to the capture width $\Gamma(R)$ (Eq. 2.5) (R is the internuclear separation) and the square of the initial vibrational wavefunction, see Sec. 2.1.1. Within the

	H_2^+		D_2^+	
	DR	SEC	DR	SEC
v	$kT_\perp = 11.9\,\mathrm{meV}$	$kT_\perp = 12.7\,\mathrm{meV}$	$kT_\perp = 11.8\,\mathrm{meV}$	$kT_\perp = 11.8\,\mathrm{meV}$
0	1.87 ± 0.15	-	1.18 ± 0.09	-
1	18.7 ± 11.2	39 ± 8	6.9 ± 4.0	36 ± 7
2	15.3 ± 9.5	76 ± 16	5.1 ± 3.4	89 ± 18
3	18.0 ± 11.5	121 ± 26	5.6 ± 3.6	125 ± 25
4	9.9 ± 6.3	146 ± 30	8.9 ± 6.4	150 ± 30
5	84 ± 57	210 ± 42	8.7 ± 6.8	220 ± 44
6	118 ± 80	-	7.5 ± 5.4	-
7	-	-	32.6 ± 23.4	-

Table 5.4: *Summarized results for the absolute DR and SEC rate coefficients (in units of 10^{-8} cm^3/s) for the lower vibrational states of H_2^+ and D_2^+. The electron-ion collision energy was $E \approx 0\,meV$ and temperature of the longitudinal electron velocity $kT_{||} \approx 0.1\,meV$ in both experiments. The transverse electron temperature was as stated on top of each column. For vibrational states below the drawn horizontal lines DR via the higher dissociative state belonging to the Q_1 series is energetically possible.*

fixed nuclear, or adiabatic approximation $\Gamma(R)$ is independent of the nuclear mass, i.e. identical probabilities for the recombination of an electron with an H_2^+ and D_2^+ ion. The autoionization lifetime $\tau(R)$ is proportional to the inverse capture width (Eq. 2.5). Assumig a classical treatment of the nuclear motion, the probability for DR to occur is given by the product between the cross section σ_{cap} and the so-called survival factor $S(R)$ (Eq. 2.7), which describes the probability for DR to occur. The survival factor is dependent on the capture width and the velocity of the dissociating fragments and becoming larger with increasing velocities, see Eq. 2.7. The two molecular hydrogen isotopomers have different reduced masses, $\mu = 1/2$ (H_2^+) and $\mu = 1$ (D_2^+), and the relation between the dissociation velocities is given by $v_{H_2^+} = \sqrt{2}v_{D_2^+}$. The survival factor for H_2^+ is therefore larger than for D_2^+ and one would expect DR rate coefficients for H_2^+ to be larger than for D_2^+ and the SEC rate coefficients for H_2^+ to be smaller than for D_2^+. The observed larger DR rate coefficients for H_2^+ are consistent with this classical approach, whereas the rate coefficients for SEC do not show this isotope effects. This could be a hint that elastic collisions (EC), where initial and final vibrational state are identical, are more likely for D_2^+. Unfortunately, it is not possible to study EC with our experimental setup. Geddes *et al.* used photodissociation experiments to derive autoionization lifetimes of the superexcited $^1\Sigma_u^+$ states in hydrogen [104, 105]. They found isotope effects and measured a larger autoionization width for the superexcited states of D_2. We could not see this isotope effect in SEC, but cannot claim

	Experiment	$E = 0.01\,\mathrm{meV}$	$E = 12\,\mathrm{meV}$
$v \longrightarrow v'$	$10^{-8}\,\mathrm{cm}^3/\mathrm{s}$	$10^{-8}\,\mathrm{cm}^3/\mathrm{s}$	$10^{-8}\,\mathrm{cm}^3/\mathrm{s}$
$1 \longrightarrow 0$	39 ± 8	4.69	1.97
$2 \longrightarrow 1$	76 ± 16	9.85	5.41
$2 \longrightarrow 0$	-	0.63	0.44
$3 \longrightarrow 2$	121 ± 26	16.25	6.20
$3 \longrightarrow 1$	-	4.77	2.10
$3 \longrightarrow 0$	-	0.61	0.26
$4 \longrightarrow 3$	146 ± 30	26.10	13.49
$4 \longrightarrow 2$	-	4.50	2.96
$4 \longrightarrow 1$	-	3.33	2.16
$4 \longrightarrow 0$	-	0.47	0.32
$5 \longrightarrow 4$	210 ± 42	101.52	34.59
$5 \longrightarrow 3$	-	11.78	4.10
$5 \longrightarrow 2$	-	2.42	0.82
$5 \longrightarrow 1$	-	1.93	0.68
$5 \longrightarrow 0$	-	0.33	0.12

Table 5.5: *Comparison between experimental ($E \approx 0\,\mathrm{meV}$) and calculated [99] ($E = 0.01\,\mathrm{meV}$ and $E = 12\,\mathrm{meV}$) anisotropic SEC rate coefficients for H_2^+. The calculated SEC cross sections are convoluted with an anisotropic electron velocity distribution ($kT_\perp = 12\,\mathrm{meV}$ and $kT_{||} = 0.1\,\mathrm{meV}$), corresponding to the experimental conditions. The experimental SEC rate coefficients were obtained using a rate equation model neglecting transitions where an initial vibrational state v is changed by more than one unit, see text.*

that this is also true for EC. An explanation of the dominance of $\Delta v = 1$ transitions in SEC using the classical model failed. This shows already the problematic arising from a classical description of the two competing processes, SEC and DR.

Different calculations were performed in the past, based either on $R-$matrix theory [23] or on multichannel quantum defect theory (MQDT) [24, 99]. A comparison between experimental data for H_2^+ ($E \approx 0\,\mathrm{meV}$) and recent results from MQDT calculations of anisotropic SEC and DR rate coefficients for different electron-ion collisions energies ($E = 0.01\,\mathrm{meV}$ and $E = 12\,\mathrm{meV}$) by Schneider *et al.* [99] are shown in Tab. 5.5 and Tab. 5.6, respectively. The calculated SEC and DR cross sections are convoluted with our experimental anisotropic electron velocity distribution ($kT_\perp = 12\,\mathrm{meV}$ and $kT_{||} = 0.1\,\mathrm{meV}$).

Even though the uncertainties on the experimental DR rate coefficients are not small their values

v	Theory $10^{-8}\,\mathrm{cm^3/s}$	Experiment $10^{-8}\,\mathrm{cm^3/s}$
0	4.54	1.87 ± 0.15
1	6.03	18.7 ± 11.2
2	6.68	15.3 ± 9.5
3	6.75	18.0 ± 11.5
4	7.05	9.9 ± 6.3
5	6.56	84 ± 57

Table 5.6: *Comparison between experimental ($E \approx 0\,$meV) and calculated [99] ($E = 0.01\,$meV) anisotropic DR rate coefficients for H_2^+. The calculated DR cross sections are convoluted with an anisotropic electron velocity distribution ($kT_\perp = 12\,$meV and $kT_{||} = 0.1\,$meV), corresponding to the experimental conditions.*

are, besides for $v = 0$, larger than the calculated values for collision energies $E = 0.01\,\mathrm{meV}$. The increase in the experimental DR rate coefficient for the vibrational state $v = 5$, presumable due to the additional dissociative states belonging to the Q_1 series, is also not reproduced. The discrepancies range up to a factor of ≈ 3. For the SEC rate coefficients the mismatch between experiment and theory is even stronger. The experimental data are almost an order of magnitude higher than the values calculated for the electron-ion relative energy $E = 0.01\,\mathrm{meV}$. This comparison reveals underestimated rate coefficients for both processes, SEC and DR, whereas the disagreement for the SEC rate coefficients is even more striking. Possible reasons for the disagreement between experimental data and theoretical predictions could be the rotational excitation of the stored ions, which were not taken into account in the MQDT calculations. The overall underestimation of both rate coefficients could be due to a wrong capture width $\Gamma(R)$. The capture width used in the MQDT calculations for H_2^+ is the same as the one used for the calculations of the absolute DR rate coefficients for HD^+, published in Ref. [34]. This is somehow in contradiction to the isotope effects observed by Geddes *et al.* [105], see discussion above.

6. Final states of non-crossing mode recombination processes

In this chapter the DR of two further small two diatomic molecular ions, LiH^+ and $^4HeH^+$, proceeding by the non-crossing mode DR, will be discussed (see Sec. 2.1.2). Absolute DR rate coefficients as well as a new final-state measurement scheme will be presented for LiH^+. A high-resolution measurement of the energy dependence of final-state branching ratios at the opening of a new energetically allowed final channel will be presented for the DR of $^4HeH^+$.

6.1 DR of LiH^+: Rate coefficients and final states

This section is focused on the discussion of experiments exploring the non-crossing mode DR of LiH^+ ions with low-energy electrons. The results have been already published and can be found in Ref. [15]. In the first part experimental results for the absolute DR rate coefficient of LiH^+ and in the second part a measurement of the final-state populations revealed using fragment imaging and state-selective field ionization will be presented.

6.1.1 Experimental conditions

The LiH^+ ion beam was produced in the MPIK Tandem accelerator by gas stripping and dissociation of LiH_2^- ions from a cesium sputter source. After acceleration to an energy of 6 MeV and magnetic mass selection, the beam was injected into the TSR and kept circulating for up to about 17 s. In the electron cooler section, the ion beam (initial diameter ≈ 2 cm) was merged with a collinear electron beam of $\approx$1.5 cm diameter over an interaction region of 1.5 m length (2.7% of the ring circumference). The motional electric field due to stray transverse components of the magnetic guiding field in the straight overlap region amounted to $\lesssim 3$ V/cm. The stored LiH^+ ion beam was electron cooled during ≈ 5 s after the injection by Coulomb collisions in the merged electron-ion beam at matched velocities, yielding an ion beam diameter of $\lesssim$2 mm and a relative momentum spread of $\lesssim 10^{-4}$. The density of the electron beam was $n_e = 8.5 \times 10^6$ cm^{-3} and the flattened electron velocity distribution was characterized by a longitudinal and transverse temperature of $kT_{||} \approx 0.1$ meV and $kT_\perp = 12$ meV, respectively. The LiH^+ beam lifetime was ≈13 s when the electron beam was turned off and ≈5 s with the velocity-matched electron beam turned on. The pressure was $\approx 5 \times 10^{-11}$ mbar an all sections of the TSR.

6.1.2 DR rate coefficient measurement

The DR rate coefficient measurements were carried out using the experimental setup described in Sec. 4.6. The measurement scheme was the same as in the DR rate coefficient measurement for H_2^+ and D_2^+, see Sec. 5.3.2. Additionally, the radiative vibrational cooling of LiH^+ was studied using Coulomb exlosion imaging (CEI). The experiment has been already discussed by L. Knoll [54], therefore only the results are presented in Tab. 6.1 together with the modeled populations discussed in Sec. 2.3.3. In Sec. 2.3.3 the vibrational cooling of LiH^+ in a Planck radiation field was studied and shown was shown that a LiH^+ ion beam should have cooled down vibrationally almost completely towards the thermal equilibrium corresponding to 300 K after a storage time of about 7 s. The calculated value for the population of the vibrational ground state after 1.5 s is larger than the measured value, whereas for $v = 1$ the calculated population is lower than the measured population, see Tab. 6.1. The differences might be due to either the calculated dipole moment matrix elements in Ref. [55] or, more likely, due to systematic problems in the analysis of the CEI data [54]. The relative errors on the measured populations for $t = 1 - 2$ s are between $\approx 10\,\% - 50\,\%$. The actual time for cooling into thermal equilibrium might take longer than calculated. Unfortunately there are presently no further (CEI) data available for longer storage times. It should be mentioned that at this thermal equilibrium only $\approx 78\,\%$ of the molecular ions are in the ground vibrational state, $\approx 14\,\%$ in $v = 1$ and the residual $\approx 8\,\%$ are distributed over higher vibrational levels. This feature is due to the unusual shallow potential (dissociation energy of ≈ 116 meV from $v = 0$) of the ground electronic state of LiH^+.

	Population (%)			
	Experiment		Model	
v	t=0-1 s	t=1-2 s	t=0.5 s	t=1.5 s
0	42.1 ± 2.5	46.7 ± 4.3	42.1	54.3
1	35.4 ± 3.6	35.2 ± 6.3	35.4	25.4
2	10.7 ± 2.8	10.2 ± 4.5	10.7	10.5
3	9.8 ± 1.3	3.9 ± 1.6	9.8	7.3

Table 6.1: *Vibrational populations of a LiH^+ ion beam after $t = 0.5$ s and $t = 1.5$ s of storage without electron-interaction measured using Coulomb explosion imaging [54] compared to the calculated values using the rate equation model discussed in Sec. 2.3.3. The measured populations for $t = 0 - 1$ s have been used as the initial populations in the calculations.*

The measurement procedure was similar to the one discussed in the Secs. 4.6 and 5.3.2. The electron energy wobbling (i.e. changing cyclic the collision energy every 25 ms from $E_{ref} \rightarrow E_{meas} \rightarrow E_{cool}$) was started after a pre-cooling time of 7 s. The energy dependence of the DR rate coefficient on the electron-ion collision energy was measured by changing the *measurement* energy E_{meas} for each injection. The DR fragments were detected by an energy resolving surface barrier detector (SBD) as a function of the time elapsed since injection. The SBD allowed to distinguish between DR events where pairs of neutral Li and H atoms were produced from events yielding only single Li or H atoms, similar to the H_2^+ and D_2^+ cross section mesurements in Sec. 5.3.2. At matched electron-ion energy a large rate of single H fragments was observed, whereas the rate on Li and H fragment pairs was only $\approx 15\,\%$ of H signal rate. Both signal rates revealed the same energy dependence, i.e. constant ratio between rate of single H fragments and rate of Li and H fragment pairs at different collision energies. Thus, both the H and the Li+H signal were assigned as being due to low-energy DR. It will be shown that the occurrence of a single H fragment in $\approx 85\%$ of all events is due to field ionization of Rydberg ($n \geq 8$) Li atoms in the dipole magnet (see Sec. 6.1.3). Fig. 6.1 shows the measured energy dependence of the DR rate coefficient for collisions energies ranging between $E = 0.1$ meV and $E = 300$ meV, obtained by evaluating the H plus Li + H fragment rate. The single H fragment rate measured at zero relative collision energy was used as a reference signal proportional to the number of stored ions. Additionally shown in Fig. 6.1 is the calculated dependence of the DR rate coefficient on the collision energy E assuming a DR cross section $\sigma \propto 1/E$ and using the experimental electron temperatures (solid line). The measured spectrum was scaled to the value for the absolute DR rate coefficient measured at zero relative collision energy, see below, and shows no prominent structures at electron-ion collision energies lower than 300 meV. However, a shoulder occurs at ≈ 50 meV. Starting from its values at $E \leq 10^{-4}$ eV the DR fragment rate drops to $\approx 1/4$ of the maximum value already at 5 meV (less than the transverse electron temperature) and to $<3\,\%$ at 50 meV, whereas the calculated rate drops to $\approx 1/2$ of the maximum value at 5 meV and to $\approx 30\,\%$ at 50 meV. This could be an indication for a strong resonance in the DR cross section at sub-thermal collision energies, see discussion in Sec. 5.3.2. The energy dependence of the calculated and the measured DR rate coefficients for collision energies larger than ≈ 50 meV are similar. The absolute DR rate coefficient at matched electron-ion velocities (i.e. $E = 0$) was derived from the lifetimes of the LiH$^+$ ion beam at different applied relative collision energies. The decrease of the beam current was monitored, using the time dependence of the H fragment yield as a signal proportional to the ion beam current. The lifetime of the LiH$^+$ ion beam could therefore be derived from the rate of single H fragments on the SBD. The ion beam lifetime $\tau(E = 0)$ with the velocity-matched electron beam (i.e. $E = 0$ eV) turned on can be written as

$$\frac{1}{\tau(E=0)} = \frac{1}{\tau_{DR}} + \frac{1}{\tau_{RG}}, \tag{6.1}$$

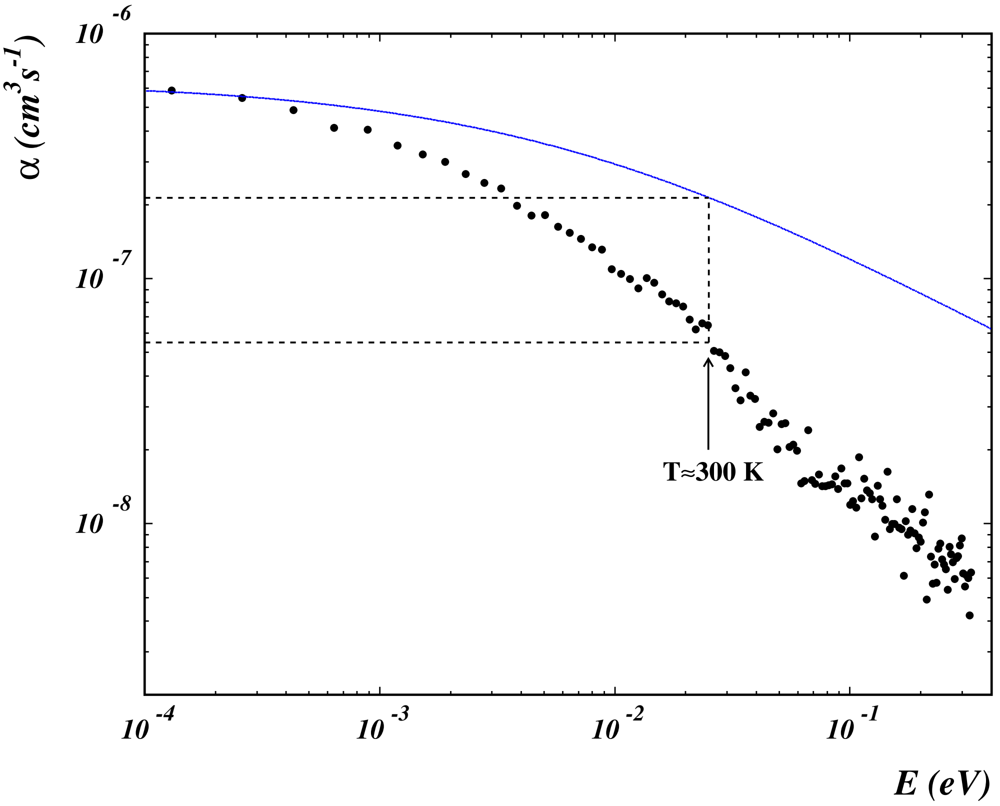

Figure 6.1: *Energy dependence of the rate coefficient for DR of LiH$^+$ with electrons, obtained by measuring the single H fragment plus Li + H fragment pair rate. The error on the rate coefficients amounts to 33 %. The measurement were performed after a pre-cooling time of 7 s. The solid line represents the calculated dependence of the DR rate coefficient on the collision energy E assuming a DR cross section $\sigma \propto 1/E$. The dashed lines mark the measured and calculated DR rate coefficients for a collision energy E corresponding to $T \approx 300\,K$.*

were $1/\tau_{DR}$ and $1/\tau_{RG}$ are the single H fragment rates due to DR and residual gas scattering. Increasing the relative electron-ion energy to values larger than ≈ 100 meV led to the reduction of the DR fragment rate by about two orders of magnitude, see Fig. 6.1. The ion beam lifetimes $\tau(E > 100\,\mathrm{eV})$ at these collision energies are in a good approximation identical with the beam lifetime τ_{RG} determined by residual gas scattering. The lifetime due to DR can therefore be derived from Eq. 6.1, using the measured values for τ_{RG} and $\tau(E = 0)$ and amounted to $\tau_{DR} = (7.14 \pm 2.55)$ s. An absolute DR rate coefficient α can be derived from the electron density n_e, the ratio of the electron-ion interaction region to the ring circumference $\eta = 0.027$ and the beam lifetime τ using the relation

$$\alpha = \frac{1}{n_e \eta \tau}. \tag{6.2}$$

Hence, the absolute DR rate coefficient α_{mb} for our merged-beam conditions (anisotropic thermal electron velocity distribution with $kT_\perp = 12\,\mathrm{meV}$ and $kT_{||} = 0.1\,\mathrm{meV}$ and zero relative collision energy) can be calculated from the lifetime τ_{DR} and amounts to

$$\alpha_{mb} = (6 \pm 2) \times 10^{-7}\,\mathrm{cm}^3/\mathrm{s}. \tag{6.3}$$

It has been shown in Fig. 6.1 that the DR cross section σ_{DR} does not vary as $\propto 1/E$ (i.e. $\alpha \propto 1/\sqrt{T}$) at collision energies $E \leq 50\,\mathrm{meV}$. Hence, the calculation of a thermal rate coefficient (isotropic Maxwell-Boltzmann distribution) using Eq. 4.24 is not correct. However, the measured DR rate coefficient is larger than the value used in recent early universe models [106] and the DR of LiH$^+$ is therefore one of the fastest reaction among those taken into account in the different models (see Tab. I in Ref. [106]). The estimated thermal DR rate coefficient for LiH$^+$ in that table amounts to $\alpha = 2.6 \times 10^{-8}\,\mathrm{cm}^3/\mathrm{s}$ for $T = 300\,\mathrm{K}$ [106]. However, it is important to recall that the LiH$^+$ ion beam is expected to be still in a superposition of vibrational states as discussed in Sec. 2.3.3. As will be shown in Sec. 6.1.3 the vibrational population distribution was found in a steady-state after about 7 s of cooling. This observation is consistent with the modeled vibrational cooling (Sec. 2.3.3). The CEI measurements were performed without merging the ion beam with electrons. The electron-ion interaction in these measurements might have caused some additional electron induced vibrational cooling. To check this open question some additional CEI measurements for longer storage times are needed. Results from CEI measurements with and without electron cooling could reveal the influence of the electron-ion interaction on the vibrational cooling. At the moment it is not yet clear if both, electron cooling and extraction of LiH$^+$ molecules, is feasible because of the weak LiH$^+$ ion beam produced in the Tandem.

6.1.3 Final fragment states

This section deals with the study of the final fragment states in the DR of LiH$^+$ with low-energy electrons which can be depicted as

$$\mathrm{LiH}^+(v) + e^-(E) \rightarrow \mathrm{Li}(nl) + \mathrm{H}(1s) + E_k, \tag{6.4}$$

where v, n and l denote the initial vibrational state of the molecular ion and the principal and orbital quantum numbers of the Li product, respectively, while E_k is the kinetic energy release. A very uncommon characteristics of LiH$^+$ is the low dissociation energy ($\approx$116 meV from the $v = 0$ level in the $X^2\Sigma^+$ ground state state potential). The ionization energy of atomic lithium is 5.39 eV (see Append. F). This small dissociation energy leads to an exceptionally large number of energetically allowed final states for the neutral Li fragment, where (see Fig. 6.2) Rydberg levels up to 11s can be reached even from the $v = 0$ level at near-zero electron energy. It has been already mentioned in the discussion of the DR rate coefficient measurement that the vibrational level spacings of LiH$^+$ are so small that already at the temperature inside the TSR

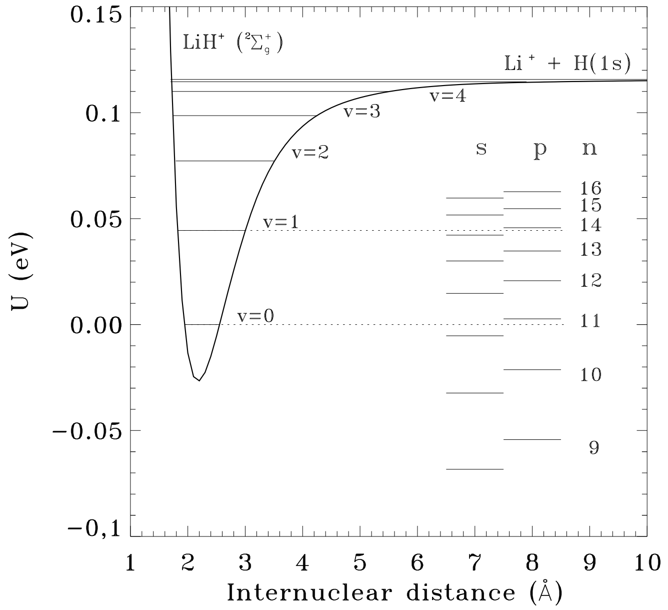

Figure 6.2: *Potential energy curve for the $X^2\Sigma^+$ state of the LiH$^+$ molecule (Berriche* et al. *[51]) with positions of the vibrational levels and the fragment energy levels for the $H(1s) + Li(nl)$ channel with $l = 0$ and 1 (s and p).*

($T \approx 300\,$K) several excited vibrational levels are populated. Even higher Rydberg levels can therefore be reached energetically by recombination with slow electrons.

Detector setup

Fragments resulting from the DR of LiH$^+$ ions, as well as from their collisions with residual gas molecules, were detected behind the first dipole magnet following the electron cooler. The distance from the center of the interaction region to the dipole magnet is about 6.5 m. Neutral fragments passing straight through the dipole magnet were analyzed either by the SBD (see Sec. 6.1.2) or by the RFI detector system (see Sec. 4.5.1). Due to its energy resolution the SBD could distinguish DR events where pairs of neutral Li and H atoms were produced from those yielding only a neutral H or Li fragment. Li fragments reaching the dipole magnet (field strength ≈0.87 T) in Rydberg states $n \geq 8$ can get field ionized by its strong (≈100 kV/cm) motional electric field[1]. Li$^+$ ions produced by interactions with the background gas or by field ionization of neutral Li fragments were counted on a spatially resolving MCP detector located on the inner side of the closed ion orbit (see Fig. 6.3). The detector was movable along an axis perpendicular to the ion beam direction. The spatial resolution of the ion fragment detector was obtained by a resistive anode mounted on the back of the MCP, see Sec. 4.5.2. All measurements were performed after a pre-cooling time of 7 s which was sufficient to reach thermal equilibrium

---

[1] The motional electric field $\vec{F}$ is related to the magnetic field strength $\vec{B}$ and the fragment velocity $\vec{v}$ by $\vec{F} = \vec{v} \times \vec{B}$.

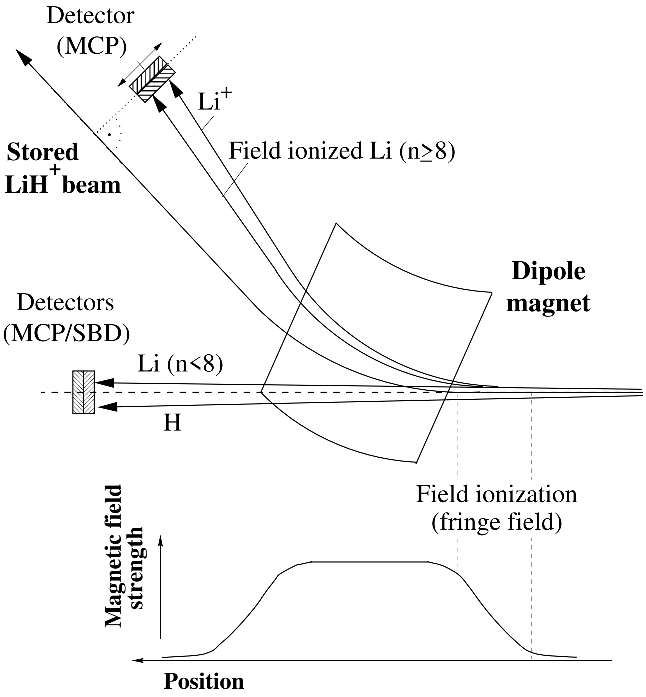

Figure 6.3: *Schematic drawing of the detector arrangement and the principle of analyzing the field ionization of Li fragments [15]. The ionization point in the linearly rising fringe field of the dipole is reflected by the impact position of the field ionization product on the MCP detector.*

with the storage ring walls, see modeled vibrational cooling in the Sec. 2.3.3. Two methods were applied to analyse the Li fragment states formed in the DR process at zero relative beam energy.

Recombination fragment imaging

The method of RFI, discussed in Sec. 4.5.1, which consists in measuring event-by-event the projected distance between pairs of neutral products, using the zero-degree MCP detector (see Fig. 6.3). A measured projected fragment distance distribution reveals the relative contribution of each intial-to-final state-to-state channel to DR (see Sec. 3.3). The measured projected distance distribution of neutral Li and H fragment pairs which were not affected by field ioniziation and thus could reach the imaging detector is shown in Fig. 6.4. The dashed line represents the expected projected fragment distance distribution for the DR of LiH$^+$ with electrons at matched electron-ion velocities into the product states Li($2\,s$) and H($n = 1$). The measured distribution reveals that Li fragments in states with $n \leq 5$ are essentially absent ($\lesssim 1\%$ of the total counts in the fragment distance spectrum) and that final channels up to $n \approx 10$ are more and more populated as n increases. The observation that a significant fraction ($\approx 15\,\%$ according to the SBD measurements described above) of the Li atoms formed in high ($n \geq 8$) Rydberg states can escape field ionization is consistent with the calculated radiative lifetimes of Li Rydberg states [107] (see Tab. F.3 in Append. F.3), which for $n = 8 - 10$ and $l = 0$ are comparable with the time-of-flight from the electron cooler to the dipole magnet of $\approx$ 500 ns. The RFI distribution in Fig. 6.4 cannot reproduce any contributions with $n \geq 10$ since the efficiency for

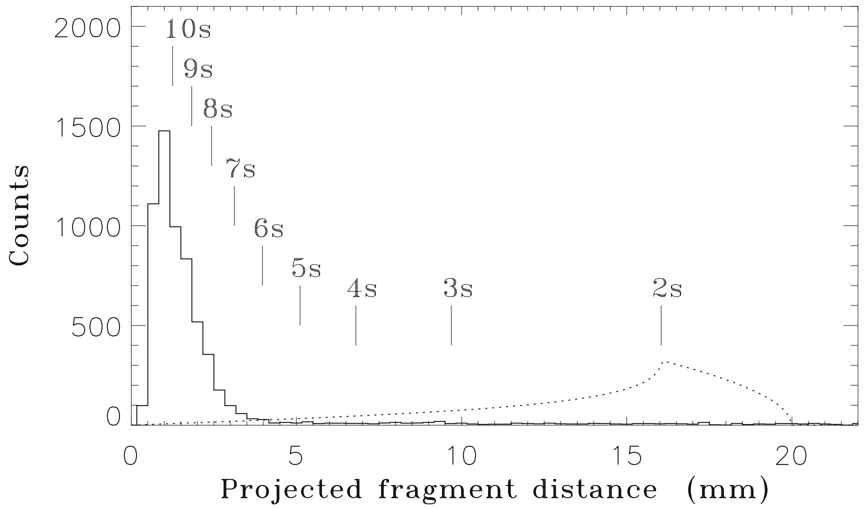

Figure 6.4: *Histogram of observed projected distances of neutral Li and H fragments, measured between 7 to 11 s after injection, and the expected shape of the histogram for the Li(2s) final channel (dashed line). Also indicated are the maxima of the expected distributions from higher final states.*

detecting fragment pairs with a very small distance drops dramatically from 100 % to 0 % within about 0.2 mm at a distance of ≈ 1.5 mm, as discussed in Sec. 4.5.1.

Detection of field ionized fragments

The spatially resolved observation of the Li^+ fragments behind the dipole magnet allowed to distinguish between ions generated by field ionization of Li atoms (resulting from DR) and ions directly produced by the dissociation of LiH^+ in collisions with residual gas molecules. The Li^+ ions directly produced in the residual gas before entering the dipole magnet get bent immediately when entering its fringe field, whereas Li atoms that undergo field ionization fly along a straight trajectory until they reach a point where the motional electric field becomes high enough to cause field ionization (see Fig. 6.3). The exact shape of the magnetic fringe field has been measured along the ion beam trajectory by Holzer [95] and is plotted in Fig. 4.7 (Sec. 4.5.2). The trajectory through the magnetic field and therefore the impact position on the MCP detector is dependent on the position where the field ionization occurred in the fringe field. Thus, an unique relation exists between ionization field strength and impact position on the MCP detector. The DR fragments were found to be distributed over a band of ≈ 10 cm. The diameter of the MCP is 2.5 cm wherefore several measurements with overlapping observation

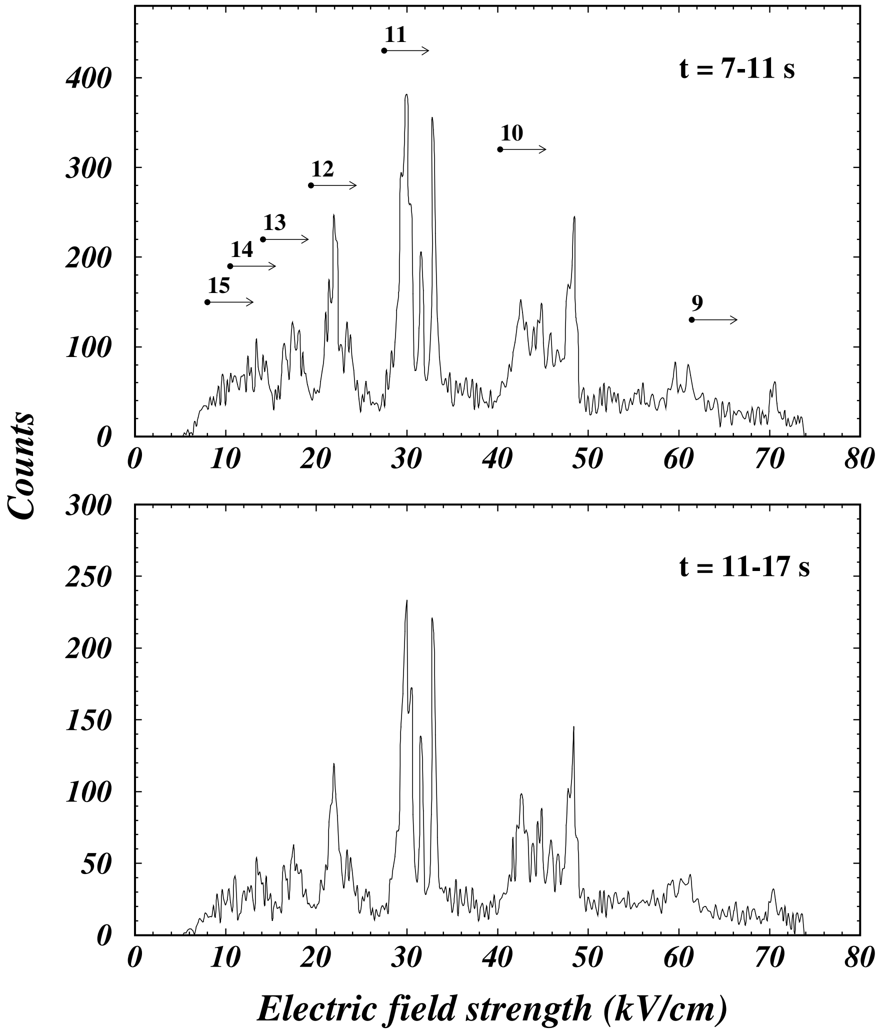

Figure 6.5: *Field ionization spectra measured between 7 s and 11 s and between 11 s and 17 s after injection. Critical field strengths* $F_c = C/n^4$ *with* $C = 1/12.8$ *(see text) are indicated for various* n *(*$t = 7$*-11 s).*

ranges were needed to scan the whole fragment distribution. The single spectra were connected applying cross-normalization through the H count rate on the zero-degree SBD.

Distributions of impact positions of the field ionized DR fragments on the MCP are shown in Fig. 6.5 for two different time intervals (7-11 s and 11-17 s after injection). The transformation from the impact position scale to a scale representing the critical ionization field strength was done by a numerical calculation of trajectories including the fringe field from Fig. 4.7. A nearly linear relation was found between impact position and critical electric field. The zero of the position scale and hence the electric field scale is uncertain within a few kV/cm, since the position of the stored ion beam with respect to the detector position could not be measured. The inaccuracy in the measurement of the distance between the detector and the edge of the dipole magnet gave rise to an additional uncertainty in the transformation to critical field strength, due to the divergence of the ion trajectories behind the dipole magnet. This additional uncertainty in the experiment leads to a compression or stretching of the measured distribution of $\approx \pm 1.5\,\mathrm{kV/cm}$. Li atoms formed in the electron-ion interaction region pass already through smaller motional electric fields before reaching the dipole magnet; hence, no signal due to field ionization in the dipole is expected for electric fields below $\approx 7\,\mathrm{kV/cm}$. The low-field shoulder of the observed distributions were therefore shifted to this point. The MCP was moved towards the LiH^+ ion beam until the injected ion beam got blocked by the metal frame on which the MCP was mounted. This caused the cut in the spectra at an electric field of about $75\,\mathrm{kV/cm}$. The relative peak heights in the two spectra plotted in Fig. 6.5 are identical within the statistical errors on the measured events. This proves the existence of an equilibrium in the vibrational population distribution for $t \geq 7\,\mathrm{s}$. Additionally shown (upper spectrum, Fig. 6.5) are critical field strengths for ionization of various Rydberg states which will be derived in the following section.

Assignment of Rydberg levels from the field ionization spectrum

Most of the Li atoms represented in the field ionization spectra of Fig. 6.5 get field ionized in the near-linear region of the fringe field (cf. Fig. 6.3), where the field strength rises with a slew rate of $S \approx 4.4$ kV $(\mathrm{cm\,ns})^{-1}$. The critical ionization fields F_c are expected [108] to depend on the initial quantum state of the Li atom as well as on the quantum mechanical time evolution of the system during the field is ramped. For low slew rates field ionization occurs *adiabatically* whereas at high slew rates the field ionization process is getting more and more *diabatically*, such that one defined Rydberg state may have several critical electric fields at which it gets ionized [109].

The $n-$dependence of the critical electric field required for ionization will be derived first neglecting level shifts caused by the electric and magnetic fields. Applying an electric field[2] F along the z axis to an H atom gives rise to an effective Coulomb-Stark potential[3],

$$V = -\frac{1}{r} + Fz, \tag{6.5}$$

with $r = \sqrt{x^2 + y^2 + z^2}$ and a saddle point on the z axis at $z = -1/\sqrt{F}$. The potential energy at the saddle point is $V = -2\sqrt{E}$ and the binding energy of an hydrogen atom with a principal quantum number n is $E = 1/2n^2$. Thus, for an atom in a Rydberg state n and vanishing angular momentum along the z axis (i.e. $m = 0$) the field F for classical saddle point ionization

---

[2] F is given in atomic units, where $1\,\mathrm{a.u.} \equiv 5.14 \times 10^9\,\mathrm{V/cm}$.

[3] All following equations are given in atomic units.

is, neglecting Stark splitting, given by

$$F = \frac{1}{16n^4}. \tag{6.6}$$

Eq. 6.6 reveals the dependence of the electric field on the principal quantum number of the ionizing Rydberg state. The additional centrifugal term for atoms in a higher $|m|$ state increases the threshold field and gives rise to a relative change in the required field of [110]

$$\frac{\Delta F}{F} = \frac{|m|\sqrt{E}}{\sqrt{2}} = \frac{|m|}{2n}. \tag{6.7}$$

The field ionization of an hydrogen atom is always diabatic [108] whereas the field ionization of alkali atoms is strongly dependent on the slew rate and may occur either adiabatically or diabatically. The field ionization of the hydrogen atom will therefore be discussed in a first step as an example for the diabatic process. An applied electric field leads to a Stark structure (see for instance Ref. [111], Fig. 5, or Ref. [112] for Stark effects to arbitrarily high order). It has been shown [108] that the strongest bound Stark states get field ionized once the binding energy is above the potential energy at the saddle point. The relation between the principal quantum number of that Stark state and the critical electric field is

$$F = \frac{1}{9n^4}. \tag{6.8}$$

Stark states with a lower binding energy do not field ionize once their energy levels are above the saddle point energy, as has been shown by Bailey *et al.* [113] who calculated the field ionization probabilities for the hydrogen atom, also including tunnelling. Data on tunnelling effects in the field ionization of Li are presented in Ref. [114]. This unexpected behavior can be explained by a strong localisation of the electrons along the z axis. Electrons belonging to Stark states with decreasing binding energy are located more and more away from the saddle point in the effective Coulomb-Stark potential, such that an effective potential can be related to each Stark state with an increased saddle point energy, see Ref. [108], Chapter 6. Eq. 6.8 represents therefore the lowest electric field needed for the ionization of a hydrogen atom in a Rydberg state with a corresponding principal quantum number n.

There are two main differences between the Stark structure and the field ionization properties of alkali atoms and the hydrogen atom. Firstly, the Stark manifolds of adjacent Rydberg states in alkali atoms do not cross [115] as they do in H. Secondly, the field ionization of Stark states of alkali atoms occurs rapidly once their binding energy is above the classical saddle point limit. The second difference can be understood as a scattering of the Rydberg electron on the core electrons which gives rise to their spatial de-localisation along the electric field axis. The s states of Li atoms are the strongest bound components of the Stark manifolds due to their largest quantum defect. Thus, they need the highest electric field to overcome the saddle point barrier. The field ionization is called adiabatic if all crossings are avoided and ionization takes place at the classical saddle point limit for the Stark shifted level energy. Dynamical effects at avoided crossings are becoming more and more important with increasing slew rate for the ramped electric field. The probability for a diabatic transition at an avoided crossing is given by the Landau-Zener transition probability. The validity of the Landau-Zener theory has been demonstrated at an avoided crossing in Li by Rubbmark *et al.* [116]. The criterion for the critical slew rate for a crossing may be written as [108]

$$S_c = \frac{\omega_0^2}{\frac{dE_1}{dF} - \frac{dE_2}{dF}}, \tag{6.9}$$

where ω_0 denotes the separation between the two Stark levels, E_1 and E_2, at the avoided crossing, which can be approximated [108] by

$$\omega_0 \approx 1/n^4. \tag{6.10}$$

The largest possible value for the denominator in Eq. 6.9 is proportional to n^2. The critical slew rate can therefore be approximated for a Rydberg state using the scaling law

$$S_c \propto 1/n^{10}. \tag{6.11}$$

Rubbmark *et al.* [116] studied the dynamics of traversing an avoided energy level crossing in a Rydberg state of lithium ($n = 19$) and found diabatic transitions to start at a critical rate $S_c \approx 0.2\,\mathrm{kV(cm\ ns)}^{-1}$. The rate S_c can be used together with Eq. 6.11 to estimate the Rydberg state from which diabatic transitions can be occur. At our slew rate of $S \approx 4.4\,\mathrm{kV(cm\ ns)}^1$ we expect diabatic transitions to set in for $n \geq 11$, i.e. some of the crossings are traversed diabatically whereas other crossings are avoided. Based on these considerations field ionization of Li atoms in a defined inital state can therefore proceed via different paths under the existent experimental conditions. The reader is referred to the books on Rydberg atoms by Stebbings and Dunning (editors) [117] and Gallagher [108] for more detailed descriptions of the adiabatic and diabatic processes in the field ionization of Rydberg atoms.

Conclusions about the Rydberg state populations were obtained from the measured field ionization spectrum (Fig. 6.5) using the semiclassical scaling law $F \propto 1/n^4$ (Eq. 6.6).

Influence of magnetic fields on Rydberg atoms

The energy shift of Rydberg levels caused by the magnetic field present in the dipole magnet was not taken into account. It will be shown that these shifts are small compared to the Stark splittings. A magnetic fields can lead to a linear energy shift as well as to a diamagnetic shift which is often called *quadratic Zeeman effect.*

To show the small effect of the magnetic field compared to the induced electric field we estimate the linear and quadratic energy shifts for an H atom in a magnetic field B. Considering the

Hamiltonian for an H atom in a magnetic field[4] B it can be shown that the level shift of a Rydberg state is given (in atomic units) by [118]

$$\Delta E = \frac{mB}{2} + \frac{B^2}{8}(1+m^2)n^4. \tag{6.12}$$

The quadratic diamagnetic term is not negligible if $n^4 B \gg 1$ [108]. The magnetic field strength in the dipole magnet was $B = 0.855\,\mathrm{T}$ and the highest Rydberg state contributing to the measured spectra of field ionized Li atoms was $n \approx 16$. Replacing n by the effective quantum number $n_l^* = n - \delta_l$ (see Append. F.1 for quantum defect parameters) for Li atoms one obtains $n_p^{*4} B \approx 0.24$ for Li atoms in a p state and $n = 16$. The quadratic energy shift can therefore be neglected and Eq. 6.12 reduces to the expression for the *linear Zeeman* effect. The *Zeeman* shift at our experimental conditions was $\Delta E = 1.82 \times 10^{-6}$ (a.u.) $= 0.05\,\mathrm{meV}$ and small compared the a Stark shift of the order of several meV [115].

Results for final fragment states and conclusions

Considering completely adiabatic field ionization of a low-l initial Rydberg state, as calculated for Li($n = 19$) by Rubbmark *et al.* [116], ionization is expected to take place at fields, described by $F_c \approx 1/12.8n^4$. These fields are marked in Fig. 6.5 for some Li Rydberg states n. The spacing between the critical fields F_c as well as their positions are in a reasonable agreement with the low-field limits of several multiplets. On the other hand progressively diabatic evolution of low-l initial states through the field region where avoided crossings between different n manifolds occur [116] leads to increasing ionization fields $F_c \approx 1/9n^4$, as discussed above. As a consequence, the peak structure in the n multiplets is likely to originate from Rydberg states with different l or $|m|$ states (see Eq. 6.7) that evolve adiabatically to the field ionization limit. In contrast, the diffuse tails of the multiplets towards higher ionization fields probably correspond to systems evolving via random alternative paths where the level crossings are partly traversed diabatically. The variety of possible evolution paths along the Stark manifolds gives rise to a complex structure of the field ionization spectra. In a future experiment it would appear possible to obtain a better understanding of the structure of these spectra by depleting Li fragments in a well defined Rydberg state by induced radiative transition to lower lying state which do not get field ionized. The difference in two field ionization spectra taken with and without applying induced radiative transitions could reveal the contribution of the chosen Rydberg state. Another approach to improve the assignment of states could be experiments at lower ion energies. The lowered maximum motional electric fields and ion velocities result in smaller slew rates of the electric field in the dipole magnet and therefore diminished probabilities for diabatic field ionization. Nevertheless, already the present interpretation of the field ionization spectra indicates that the DR of LiH$^+$ ions with low-energy electrons populates predominantly Rydberg levels of neutral Li

---

[4] B is given in atomic units, where $1\,\mathrm{a.u.} \equiv 2.35 \times 10^5\,\mathrm{T}$.

with $n \approx 10 - 12$. The lack of sensitivity of the field ionization method to the population of low lying Rydberg states ($n \leq 8$) can be compensated using the RFI technique, as discussed above. The RFI measurement indicates that these levels are indeed not populated significantly. Hence, these results clearly demonstrate the strong tendency for this non-crossing DR mode to produce, among all the energetically accessible states, the *highest possible* excited fragments (cf. Fig. 6.2). Such a situation also exists in the non-crossing mode DR of ^{4}HeH$^+$, where the predominant branching to the final channel He($1s^2$) + H($2l$) was observed in several DR experiments [119, 120] and explained by nonadiabatic couplings at small internuclear distances [18, 19].

6.2 DR of ^{4}HeH$^+$: Branching ratio at the opening of a new final fragment state

The DR of ^{4}HeH$^+$ is a further process following the non-crossing mode. The experiments presented in this section aim at the understanding of the DR at the threshold of a new accessible final fragment state. The DR of vibrationally cold ^{4}HeH$^+$ ions with low kinetic energy electrons ($E \lesssim 5\,\text{eV}$) is discussed in more detail in Sec. 2.1.2 and will be therefore only briefly reviewed here. The DR can be depicted by the reaction

$$^4\text{HeH}^+(v = 0; J) + e^-(E) \rightarrow \text{He}(1s^2) + \text{H}(n), \tag{6.13}$$

where J is the initial rotational state. Two final fragment states of the hydrogen atom are energetically accessible at near-zero collision energies, H(n=1) and H(n=2). Previous recombination fragment imaging (RFI) measurements, carried out at the CRYRING [4, 120] and the TSR [120] revealed the dominance of the formation of excited hydrogen atoms (i.e. H(n=2)), as has been predicted by MQDT calculations performed by Guberman [19]. The next final fragment state H(n=3) is energetically accessible at a collision energy $E = 333\,\text{meV}$ and a complete switch-over to this state was observed at a collision energy $E = 577\,\text{meV}$ [120]. The experiment discussed in this section was focused on the question how the branching ratio into the new possible final fragment state rises directly at the threshold to that final channel when studied with higher energy resolution.

The ^{4}HeH$^+$ ion beam was produced in a CHORDIS ion source and accelerated to an energy of $E_i = 2.41\,\text{MeV}$ using both RFQ accelerators (Sec. 4.1). The diameter of the electron cooled ion beam was $\approx 1\,\text{mm}$. The electron density was $n_e = 1.3 \times 10^7\,\text{cm}^{-3}$ and the transverse and longitudinal electron temperature amounted to $kT_\perp = 28.5\,\text{meV}$ and $kT_{||} \approx 0.1\,\text{meV}$, respectively. The pressure inside all sections of the TSR was on average $\approx 5 \times 10^{-11}$ mbar.
In the first part a measured DR rate coefficient spectrum will be presented and the observed structure discussed. The second and third part address the measurement of RFI spectra at collision energies between $E \approx 250\,\text{meV}$ and $E \approx 380\,\text{meV}$ and their interpretation.

6.2.1 DR rate coefficient spectrum

The collision energy dependence of the DR rate coefficient was measured using the experimental setup discussed in Sec. 4.6. In order to avoid ion beam dragging effects (Sec. 4.4.4), which reduce the adjusted electron-ion collision energy significantly, the experiment was carried out in the wobbling mode, i.e. changing cyclic in the collision energy every 25 ms, see Secs. 5.3.2 and 6.1.2 for more details. The time needed for a complete vibrational relaxation of all stored ^{4}HeH$^+$ ions into the ground state is less than 100 ms (see Tab. D.3 for the radiative lifetimes of the lower vibrational states) and for a radiative rotational cooling into thermal equilibrium with

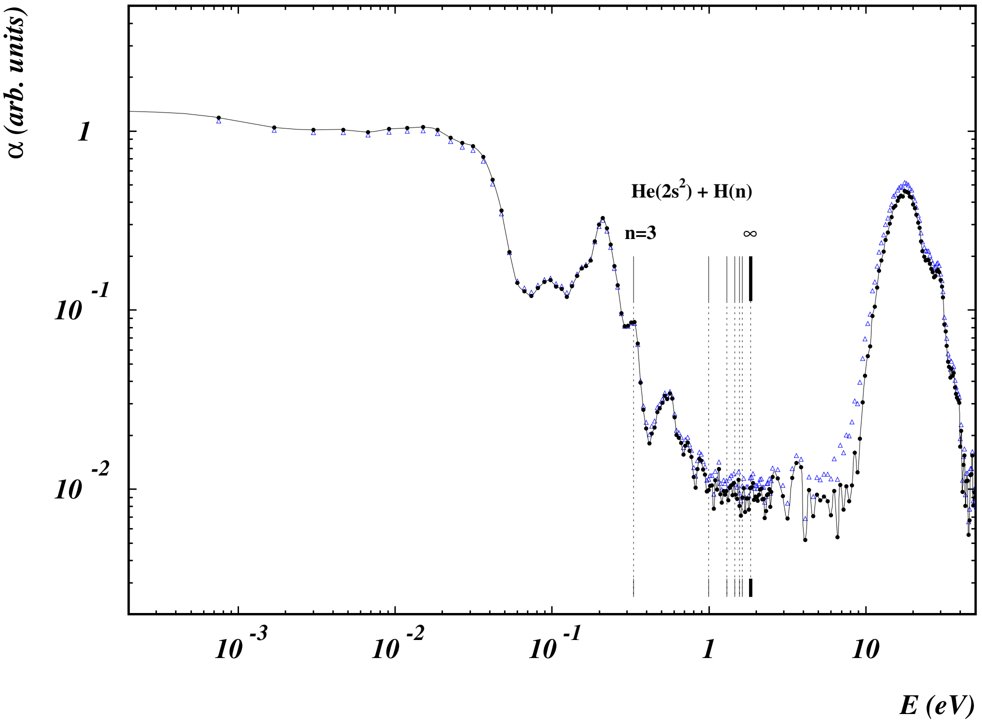

Figure 6.6: *Measured (open triangles) and background corrected (solid circles) DR rate coefficient spectrum for ^{4}HeH$^+$. The statistical errors on the experimental data are not plotted and amount to $\approx 1.5\,\%$ at $E < 200\,\mathrm{meV}$ and $\approx 15\,\%$ at $E \approx 2\,\mathrm{eV}$. The threshold energies for the production of excited hydrogen fragments H(n) as well as the energies of Rydberg resonant states (fragment states He(2s^2) + H($n = \infty$) and vibrational excitation v) of ^{4}HeH are shown, see text. The absolute value for the DR rate coefficient at about 10 meV is $\alpha \approx 7 \times 10^{-9}$ cm^3/s [4].*

the TSR walls corresponding to a temperature of $T \approx 300\,\mathrm{K}$ is about 7 s, see Sec. 2.3.2. Hence, all experiments were carried after a pre-cooling time of 7 s. The surface barrier detector (SBD) (see Sec. 4.6) was used in this measurements and DR event were identified by requiring the full energy on this detector. Fig. 6.6 shows the measured (open circles) and background corrected (full circles) DR rate coefficient spectra. The expansion factor and therefore the radius of the electron beam were small, see Tab. 4.2. Thus, background contributions of DR in the toroid sections (see Sec. 4.4.4) were strongly reduced which can be seen by the rather small difference between the measured and background corrected spectrum. The DR fragment rate measured at cooling energy was used as a reference signal which is proportional to the number of stored ions, whereas no ion current calibration was performed for the presented spectrum which therefore is shown in arbitrary units. The absolute value for the DR rate coefficient at about 10 meV was found in other experiments to be $\alpha \approx 7 \times 10^{-9}\,\mathrm{cm^3/s}$ [4]. The peak structure at collision energies larger than $\approx 7\,\mathrm{eV}$ has been observed in several measurements [4, 119, 121, 122] and explained by the capture of an electron into repulsive, doubly excited Rydberg states of the neutral HeH [45, 123] molecule. The peak structure at collision energies lower than 1 eV has been studied in several DR experiments with an ^{4}HeH$^+$ [4, 124] and an ^{3}HeH$^+$ [124, 125, 126] ion beam. Strömholm *et al.* compared their measured spectrum with the theoretical predictions of Sarpal, Tennyson and Morgen [18] and Guberman [20] and could not find a reasonable agreement. Tanabe *et al.* [124] assigned the structure at energies below 0.3 eV to a new indirect mechanism. The incident electron gets first captured into a vibrationally excited Rydberg state ($n > 2$) which then couple to the dissociative $n = 2$ Rydberg state. An overall understanding of the structure at low collision energies ($E < 1$ eV) is not yet achieved and improved theoretical models are needed.

In addition, in Fig. 6.6 are shown some threshold energies for the production of excited atomic hydrogen ($n = 3 - \infty$ for $v = 0$). The RFI measurement discussed in the following section was performed at collision energies around the threshold energy $E = 333$ meV where the production of hydrogen in $n = 3$ starts to become energetically possible. Exactly at that energy a small peak appears in the DR rate coefficient spectrum, which will be discussed below.

6.2.2 RFI at collision energies $E \approx 250$ - 380 meV

For a more detailed study of the observed [120] switch-over in the final state branching ratios at the opening of the H($n = 3$) channel we used the RFI technique, discussed in Sec. 4.5.1. This technique allows to measure, with high resolution, the small kinetic energy release of the DR into the H($n = 3$) channel at collision energies slightly above the threshold energy. The disadvantage of the RFI technique is the vanishing detection efficiency for fragment distances on the MCP smaller than ≈ 1.5 mm. This detection efficiency problem arises from the average spot size of an impinging DR fragment on the phosphor screen of ≈ 1.5 mm.

RFI measurements and results

The measurement scheme was as follows. A new ^{4}HeH$^+$ ion beam was injected every 18 s and the measurement was started after a pre-cooling time of 7 s, a time sufficiently long for a total radiative cooling into the vibrational ground state and an almost complete radiative rotational cooling into thermal equilibrium with the TSR walls corresponding to temperature of $T \approx 300$ K, see Sec. 2.3.2. Thus, it is reasonable to assume that the rotational population follows a Boltzmann distribution. The electron beam parameters can be found in Tab. 4.2. To minimize changes in the collision energy due to ion beam dragging effects (Sec. 4.4.4), the electron energy was set to matched electron-ion velocities in the first 7 s of pre-cooling and then cyclic varied between the required collision energy and the cooling energy. The dwell time on the cooling (i.e. $E = 0$) and measuring energy was 1 s and 0.5 s, respectively. The changes in the adjusted collision energies ($E \approx 250 - 350$ meV) due to ion beam dragging were estimated to be less than

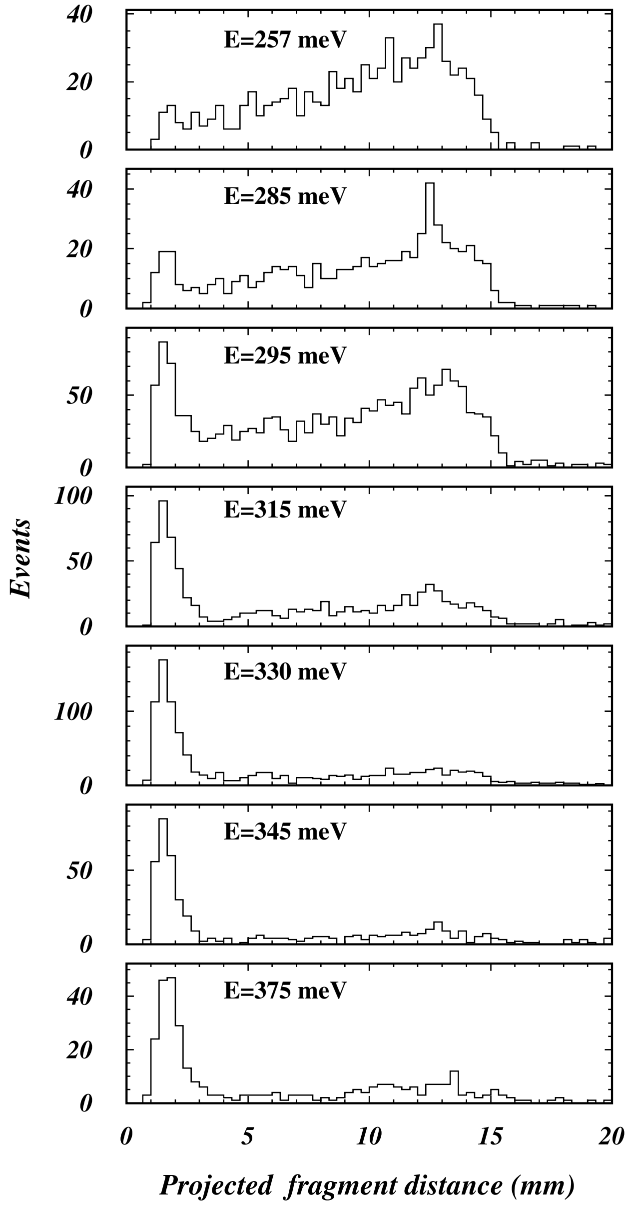

Figure 6.7: *Projected fragment distance distributions measured at different electron-ion collision energies E. The ion beam dragging gave rise to a decrease in the adjusted collision energy E of $\approx 5\,\mathrm{meV}$ in the measurement time of 0.5 s, see text.*

5 meV. This shift in the collision energy ΔE was calculated combining Eqs. 4.28 and 4.35 and using the electron beam parameters shown in Tab. 4.2 and a value for the Coulomb logarithm of $L_C = 10$ [88]. Different projected fragment distance spectra have been taken at collision energies around the threshold energy $E = 333\,\mathrm{meV}$ and are represented in Fig. 6.7. The statistics is very low due to the small DR rate coefficient of less than $\approx 4 \times 10^{-10}\,\mathrm{cm}^3/\mathrm{s}$ at these collision energies. Clearly, a two peak structure is observable in the distributions corresponding to energies $E \geq 285\,\mathrm{meV}$. The peak at small fragment distances can be assigned to DR into the H($n = 3$) fragment channel and the other peak to the H($n = 2$) fragment channel. A clear change in the fragment distance distribution towards smaller distances with increasing collision energies is

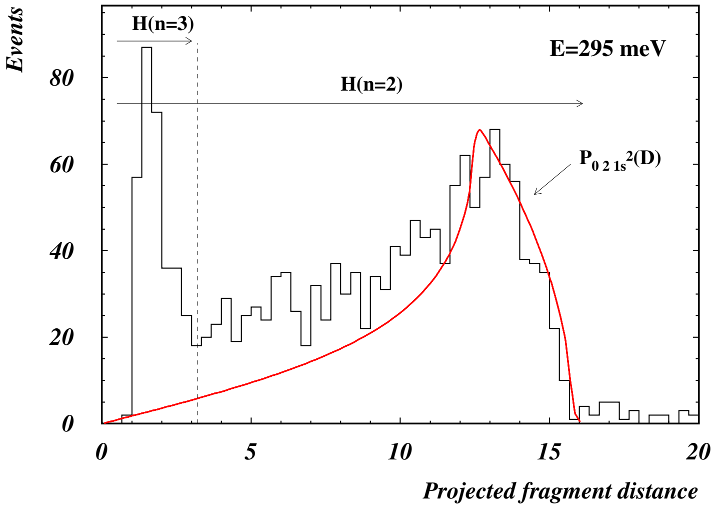

Figure 6.8: *Measured fragment distance distribution at $E = 295\,meV$. The plotted function $P_{0\,2\,1s^2}(D)$ represents the expected distance distribution assuming isotropic angular distribution of the DR fragments, see Sec. 3.3. The plotted arrows mark the range of possible fragment distances for the two final fragment states.*

discernible. This is already a sign for a fast switch-over into the higher excited fragment state. The exact distribution of electron energies in the vicinity of the given nominal collision energies (see Sec. 4.4.2) is discussed below (see Fig. 6.11). The projected fragment distance distribution $P_{0\,2\,1s^2}(D)$ (Eq. 3.23) (including rotational excitation) for an isotropic angular distribution of the fragments relative to the beam direction corresponding to DR into the H($n = 2$) channel was fitted to the individual spectra. The results of these fits are shown in Fig. 6.8 for the spectrum taken at $E = 295\,$meV. The fitted function cannot explain the additional contributions at distances $\approx 3 - 12\,$mm; the deviations could not be explained by a possible anisotropy in the angular distribution of the DR fragments, see Sec. 3.3. Similar contributions to a PFI spectrum were already observed in an earlier TSR experiment, see Semaniak *et al.* [120] (Fig. 2). The production of H($n = 3$) fragments in DR reactions taking place in the toroid regions at larger collision energies (cf. Sec. 4.4.4) are also not expected to play a significant role, due to the small electron beam diameter, see discussion above (Sec. 6.2.1). The relative contribution of the H($n = 2$) channel to DR was therefore obtained by integrating over *all* events having a fragment distance larger than the maximum possible distance for DR into the H($n = 3$) channel (dashed line in Fig. 6.8) plus an *estimated* number of events, also belonging to the H($n = 2$) channel at smaller distances. These numbers were obtained by a linear extrapolation of the measured contributions of the H($n = 2$) channel towards smaller fragment distances. Then the complete spectrum was integrated and the H($n = 2$) contribution was normalized to the total number of events. The energy dependence of the relative contributions to the H($n = 2$) channel is presented in Fig. 6.9. The systematic errors on the nominal collision energy E are estimated values and caused by the uncertainties in the electron beam parameters. To estimated the systematic errors on the relative contributions shown in Fig. 6.9, the projected fragment distance distribution $P_{0\,2\,1s^2}(D)$ (see Eq. 3.23) for the corresponding collision energy E was fitted to the normalized spectra. The relative contribution to the H($n = 2$) channel was used as the fit parameter. The difference between the relative contributions plotted in Fig. 6.9 and values obtained from the fit determined the systematic errors.

The relative contributions to the H($n = 2$) channel, presented in Fig. 6.9, show a decrease to about 40 % at the threshold energy $E = 333\,\text{meV}$ with increasing collision energies and are approximately constant at higher collision energies. It should be mentioned no experimental data for higher collision energies are available due to the fast decrease in the DR rate, see Fig. 6.6. The observed decrease in the relative contributions to the H($n = 2$) channel at collision energies already below the expected threshold of $E = 333\,\text{meV}$ can be explained by (a) the rotational excitation of the $^4\text{HeH}^+$ ions (see Tab. 6.2), which gives rise to a reduction of the collision energies required to access the H($n = 3$) final fragment state, and (b) the collision energy distribution shown in Fig. 6.11 for a nominal collision energy E. The rotational levels as well as the Boltzmann distributed rotational populations ($T \approx 300$) are shown in Tab. 6.2. As can be seen in Tab. 6.2, approximately 50 % of the $^4\text{HeH}^+$ ions have rotational energies of 25 meV and more.

The vanishing detection efficiency for fragment pairs with distances smaller than $\approx 1.5\,\text{mm}$ gives rise to a too small number of events belonging to the H($n = 3$) channel. Thus, the relative contributions of the H($n = 2$) channel to DR derived from the described method and shown in Fig. 6.9 are larger than the actual contributions. The presented relative contributions are in fact

J	E_J meV	p_J %
0	0	15.2
1	8.3	31.2
2	25.0	29.0
3	49.9	15.5
4	83.2	5.5
5	124.8	1.3
6	174.7	0.2

Table 6.2: *Excitation energies E_J for the lower rotational states $J = 0 - 6$, as well as the Boltzmann distribution of the rotational population p_J corresponding to a temperature of $T = 300\,K$.*

a convolution of the actual branching ratios for both populated final channels and the experimental conditions. To extract information about the branching ratios into the final fragment channels a Monte-Carlo simulation was developed, taking into account the well known experimental conditions and allowing for testing different models for the energy dependence of the branching ratios. Thus, by comparing the energy dependence of simulated relative contributions to the H($n = 2$) channel to the experimental results information about the energy dependence of the branching ratios the can be retrieved. The Monte-Carlo simulation as well as the result

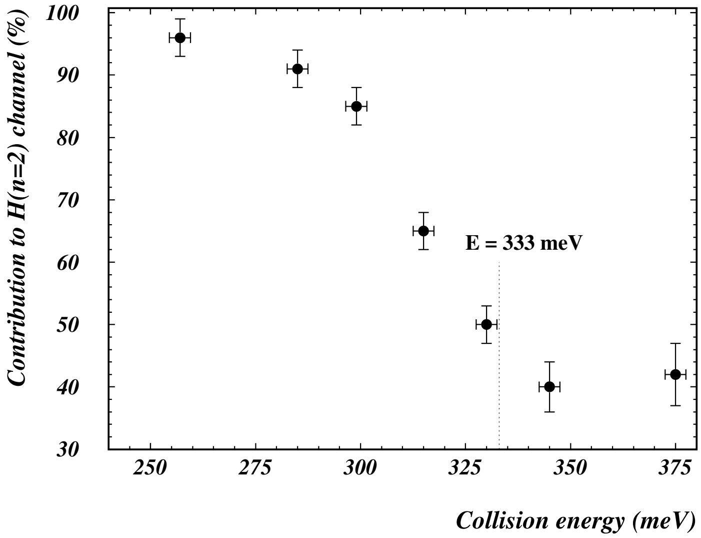

Figure 6.9: *Relative contribution of the H($n = 2$) channel to DR at different collision energies. The errors on the data are discussed in the text.*

for the energy dependence of the branching ratios will be discussed in the following section.

Monte-Carlo simulation of the DR

The Monte-Carlo simulation included all conditions of the experiment considered to be relevant. The energy dependence of the branching ratio for $J = 0$ ^{4}HeH$^+$ ions into the final fragment state H($n = 3$) is defined as

$$B(E) = \begin{cases} 0 & E < E_3 \\ B_3(E) & E \geq E_3 \end{cases} \tag{6.14}$$

where $E_3 = 333\,\text{meV}$ is the threshold energy for the accessibility of the final state H($n = 3$) for ro-vibrationally cold ^{4}HeH$^+$ and the function $B_3(E)$ which will be discussed later. For collisions with rotationally excited ^{4}HeH$^+$ ions ($v = 0$) the threshold energy E_3 is reduced by the rotational excitation energy E_J presented in Tab. 6.2. All conditions included in the simulation are summarized in the following list:

- exact geometry of the experimental setup (1.5 m interaction region and distances from electron cooler to MCP detector, see Fig. 4.4)
- shape of the ion beam (Gaussian like shape, FWHM ≈ 1 mm)
- isotropic angular distribution of the DR fragments
- transverse and longitudinal electron temperatures ($kT_\perp = 30\,\text{meV}$ and $kT_{||} = 0.1\,\text{meV}$), see energy distribution in Fig. 6.11
- Boltzmann distributed rotational excitation ($T = 300\,\text{K}$), see populations in Tab. 6.2

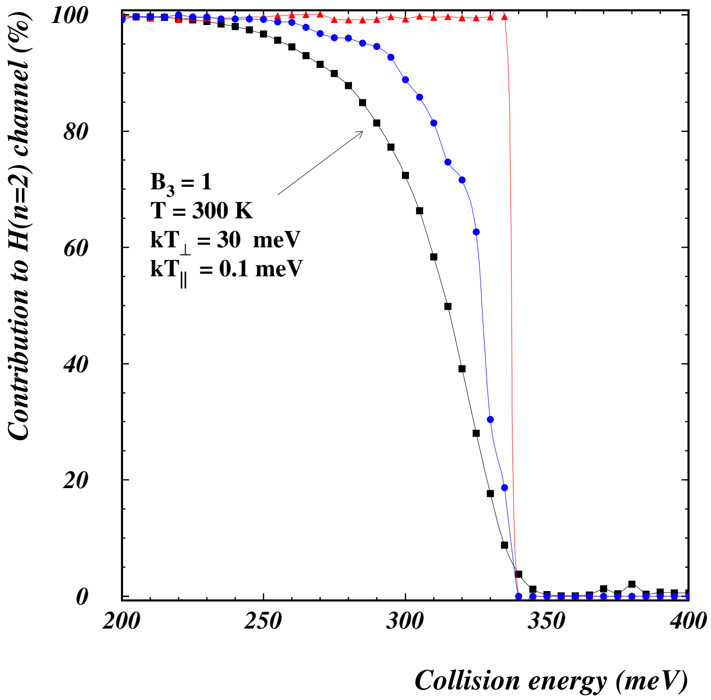

Figure 6.10: *Comparison between different simulated contributions to the H(n = 2) channel. The constant branching ratio was $B_3(E) = 1$ in all simulations. The solid triangles represent the energy dependence for zero transverse ($kT_\perp = 0$) and longitudinal ($kT_{||} = 0$) electron temperatures and zero rotational excitation ($T = 0\,K$). The solid circles show the results of the simulation including rotational excitation ($T = 300\,K$). The settings in the third simulation (solid boxes) were as stated in the plot.*

- detector efficiency for fragment distances D near the cut-off distance $D = 1.5\,\text{mm}$, as found in previous measurements
- ion beam dragging effects (linear energy changes as a function of the time by $\Delta E/\Delta t = 10\,\text{meV/s}$)
- branching ratio $B(E)$, as defined in Eq. 6.14
- the DR cross section was assumed to be constant over the simulated energy range (i.e. $E = 200 - 400\,\text{meV}$)
- DR cross section independent of the rotational excitation

The influence of the energy dependence of the DR cross section $\sigma(E)$ on the results has not yet been thoroughly tested and needs to be implemented in a next step in the Monte-Carlo

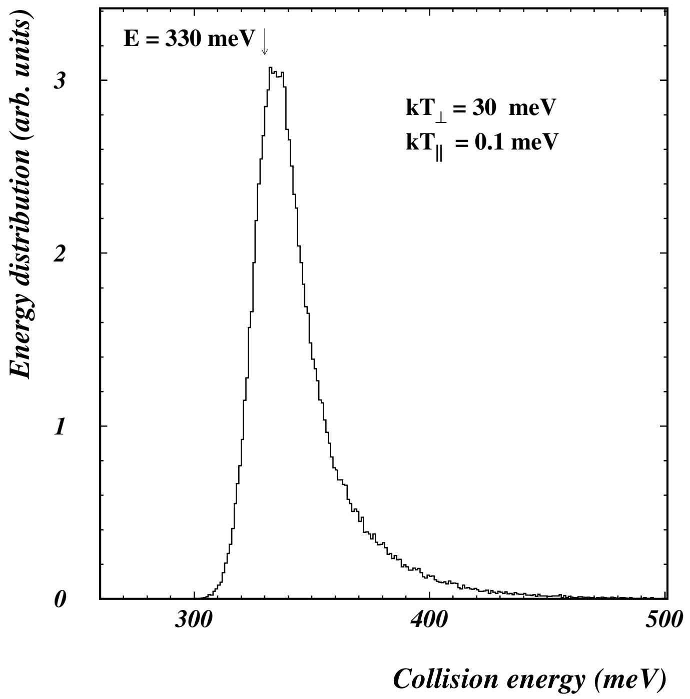

Figure 6.11: *Simulated collision energy distribution for a flattened Maxwellian velocity distribution of the electrons. The collision energy was set to $E = 330\,meV$ and the transverse and longitudinal electron temperatures were set as stated in the plot.*

simulation. In addition, recombinations in the toroid sections were not taken into account in the simulation; however, they do not play a significant role in the studied collision energy region, as can be seen in Fig. 6.6. Several models for the energy dependence of $B(E)$ have been tested, e.g. $B_3(E) = 1 - exp(-(E - E_3)/\sigma)$, where E_3 is the threshold energy for the H($n = 3$) channel and σ a constant which could be varied. A very good agreement between the simulated and the measured data was achieved using a constant value for the branching ratio B_3, i.e. the branching ratio for the population of the fragment state H($n = 3$) jumps from zero to the value B_3 once this channel is open. Recently, a wave packet treatment of the dissociation dynamics, performed by A. Orel [127], revealed such a step in the branching ratio $B(E)$ with $B_3 \approx 0.5$. The simulations were performed for collision energies between $E = 200\,\mathrm{meV}$ and $E = 400\,\mathrm{meV}$ in steps of $5\,\mathrm{meV}$ and various values for B_3. The relative contribution of the H($n = 2$) channel at the different collision energies and branching ratios B_3 was obtained by a fit of the projected fragment distance distribution function $P_{0\,2\,1s^2}(D)$ (Eq. 3.23) to the simulated and normalized spectra. Fig. 6.10 shows the results for different experimental conditions and a probability of 100 % (i.e. $B_3 = 1$) to populate the H($n = 3$) once this channel is energetically accessible. Neglecting rotational excitation (i.e. $T = 0\,\mathrm{K}$) and a spread in the electron velocity distribution in the simulation gives rise to a step-like shape at the threshold energy $E = 333\,\mathrm{meV}$ as presented by the solid triangles. Taking into account a rotational excitation in the simulation ($T = 300\,\mathrm{K}$) leads to an decrease in the relative contribution starting already at an energy $E \approx 260\,\mathrm{meV}$ (solid dots), which corresponds to DR of ^{4}HeH$^+$ in $J > 3$, see Tab. 6.2. The decrease of

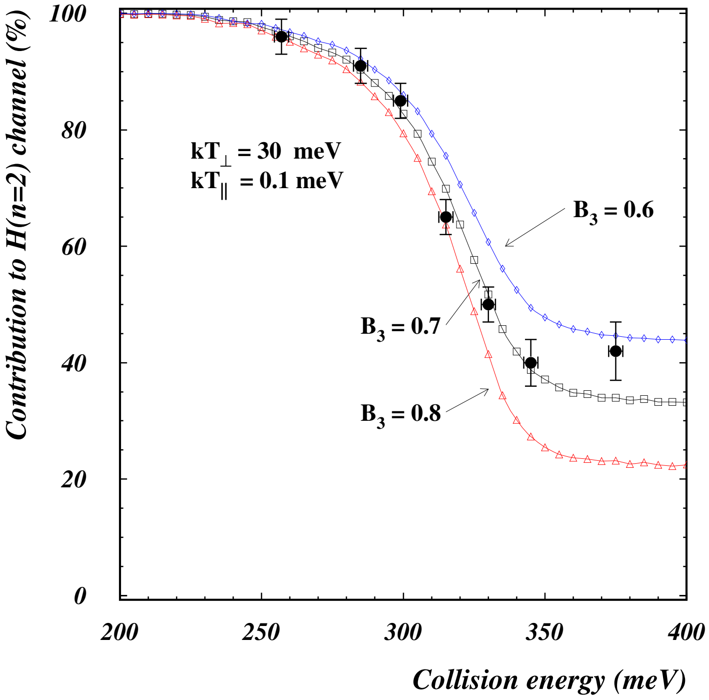

Figure 6.12: *Simulated contributions to the H(n = 2) channel as a function of the collision energy for various constant branching ratios* $B_3 = 0.6\,,0.7$ *and* 0.8 *as indicated in the plot, compared to the measured contributions (solid circles). The transverse and the longitudinal electron temperatures were set to the experimental values.*

the relative contribution to the H(n = 2) channel is becoming even more pronounced if the velocity distribution of the electrons is included (solid boxes). Fig. 6.11 represents the simulated electron energy distribution for a flattened Maxwellian velocity distribution of the electrons at an adjusted collision energy of 330 meV. The asymmetric shape of the energy distribution in Fig. 6.11 is caused by the transformation of the transverse and longitudinal electron velocity distributions in the co-moving frame of reference, see discussion in Sec. 4.4.3. This, together with the definition of the nominal collision energy, leads to the effect that the electron energy is in about 78 % of the recombinations larger than the nominal value.

The experimental data (see Fig. 6.9) are compared in Fig. 6.12 to the results obtained from the Monte-Carlo simulation, were the branching ratio B_3 was set to a constant value. In the simulation, the rotational temperature was set to $T = 300$ K and the longitudinal and transversal temperature was set to $kT_{||} = 0.1$ meV and $kT_{\perp} = 30$ meV, respectively. The detector efficiency at small (≤ 1.5 mm) distances is not known precisely, but it could be shown that the uncertainties on the simulated values are negligible. The best agreement between experimental and simulated data is found for a branching ratio $B_3 = 0.70 \pm 0.02$. However, as has been mentioned before, for a collision energy $E = 577$ meV a branching ratio $B_3 = 1.0$ was measured by Semaniak *et*

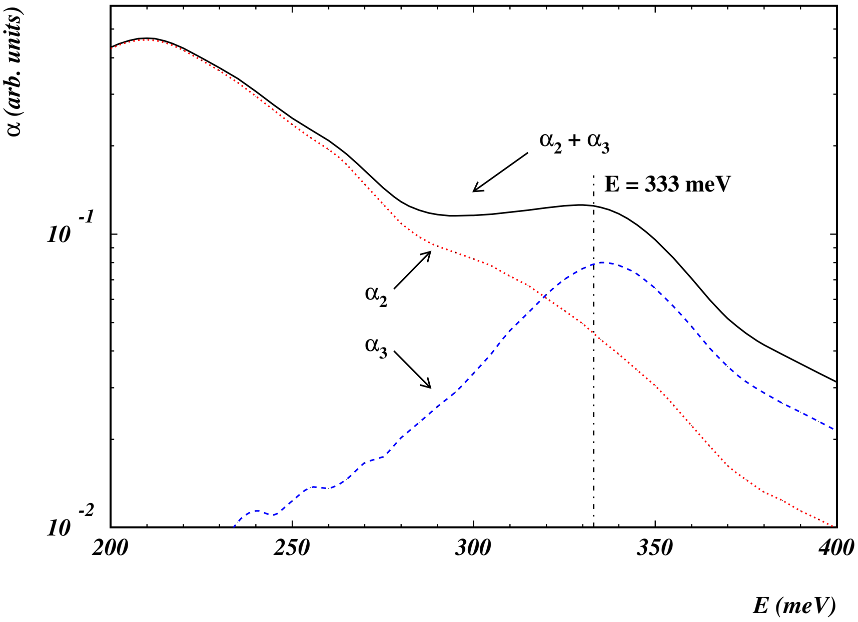

Figure 6.13: *Smoothed DR rate coefficient $\alpha(E) = \alpha_2(E) + \alpha_3(E)$ (in arbitrary units) from Fig. 6.6 in the energy region from $E = 200\,\mathrm{meV}$ to $E = 400\,\mathrm{meV}$ (solid line) and the rate coefficients $\alpha_2(E)$ and $\alpha_3(E)$ of the two final fragment state channels H($n = 2$) (dotted line) and H($n = 3$) (dashed line), respectively. The dash-dotted line marks the threshold energy.*

al. [120]. Since there are presently no further PFI data available for the energy region between $E = 360\,\mathrm{meV}$ and $E = 577\,\mathrm{meV}$ no statement can be done on the energy dependence of the branching ratio $B_3(E)$ in that energy region.

The measured spectrum of the DR rate coefficient $\alpha(E)$ in Fig. 6.6 has a small hump around the threshold energy $E = 333\,\mathrm{meV}$. As will be shown, this hump is due to the opening of the additional final fragment state H($n = 3$) at that energy. Since there are only two final fragment states populated, H($n = 2$) and H($n = 3$), the DR rate coefficient $\alpha(E)$ can be written

$$\alpha(E) = \alpha_2(E) + \alpha_3(E), \tag{6.15}$$

where $\alpha_2(E)$ and $\alpha_3(E)$ are the rate coefficients for the DR channels related to the final state H($n = 2$) and H($n = 3$), respectively. With $q_2(E)$ and $q_3(E) = 1 - q_2(E)$ being the individual relative contributions of the final fragments H($n = 2$) and H($n = 3$), respectively, to DR, Eq. 6.15 can be written as

$$\alpha(E) = \underbrace{q_2(E)\alpha(E)}_{=\alpha_2(E)} + \underbrace{(1 - q_2(E))\alpha(E)}_{=\alpha_3(E)}. \tag{6.16}$$

The relative contribution $q_2(E)$ can be obtained using the Monte-Carlo simulation as has been shown above. However, in the rate coefficient measurement a surface barrier detector (SBD) was used. Compared to the imaging detector system used in the RFI technique the SBD does not have efficiency problems for the detection of fragment pairs with small distances. Thus, in a new simulation the detection efficiency was set to 100 % for all fragment distances and the branching ratio into the higher final fragment state was set to $B_3(E) = 0.7$, see above. In Fig. 6.13 the smoothed measured DR rate coefficient $\alpha(E)$ (Fig. 6.6) is plotted for the energy region from $E = 200\,\text{meV}$ to $E = 400\,\text{meV}$ together with the individual contributions of the two final fragment channels $\alpha_2(E)$ and $\alpha_3(E)$, obtained using Eq. 6.16 and the energy dependence of the relative contribution $q_2(E)$ from the Monte-Carlo simulation. Clearly, the rate coefficient $\alpha_2(E)$ falls off exponentially and the additional DR rate is caused by the new accessible final fragment state H$(n = 3)$. This unexpected fast decreasing DR rate with increasing collision energy is not yet understood.

In summary, a large switch-over into the H$(n = 3)$ final fragment channel was found at collision energies $E \geq 333\,\text{meV}$, which can explain the hump in the DR rate coefficient starting at around $E = 300\,\text{meV}$, see Fig. 6.13.

Both molecular ions, ^{4}HeH$^+$ and LiH$^+$, are examples for the non-crossing mode DR. The experimental studies of this process revealed a favoured population of the highest energetically possible fragment states. This behavior seems to be a common trend in the DR via the non-crossing mode.

7. Conclusions and perspectives

In this thesis several experiments are presented focused on inelastic collisions and recombination processes between slow electrons and different molecular ions. All experiments were carried out at the heavy ion storage ring TSR at the Max-Planck Institut für Kernphysik in Heidelberg. The results of these experiments and some conclusions are summarized in the following section. The last section gives some perspectives on possible future experiments.

7.1 Summarized results and conclusions

This work was focused on one hand on the study of the competition between super-elastic collisions (SEC) and dissociative recombination (DR) in collisions between slow electrons with the hydrogen molecular ions H_2^+ and D_2^+ and on the other hand on the investigation of the non-crossing mode DR.

The main results of the collision experiments of zero kinetic energy electrons with hydrogen molecular ions are summarized in the following list:

- The electron induced vibrational cooling of the non-polar molecular ions H_2^+ and D_2^+ was observed using the Coulomb explosion imaging (CEI) technique. It was proven that the vibrational cooling is caused by electron-ion interactions in the electron cooler. Two processes can be responsible for the observed cooling, namely SEC, an inelastic scattering process in which internal excitation energy is transferred to the scattered electron, and the vibrational state specific DR which preferentially depletes hydrogen molecular ions in excited vibrational states.
- The recombination fragment imaging (RFI) technique allowed the time evolution of the individual contributions of the different vibrational states to DR to be monitored. The experimental data from CEI and RFI were combined to derive first relative DR rate coefficients for the lower vibrational states $v = 0-6$ and $v = 0-7$ of H_2^+ and D_2^+, respectively. A comparison of the experimental relative DR rate coefficients to calculated values revealed a disagreement for several vibrational states.

- The electron induced vibrational de-excitation was used in two experiments to prepare vibrational cold ion beams of H_2^+ and D_2^+ . For these vibrationally cold ions first absolute DR rate coefficients were measured. The absolute DR rate coefficient for D_2^+ is smaller than for H_2^+ which can be explained by the smaller overlap between the nuclear wavefunction and continuum wavefunction. For H_2^+ a good agreement with recent calculations, based on the multichannel quantum defect theory (MQDT), was found, whereas for D_2^+ no new MQDT calculations are presently available.

- It was shown that the observed vibrational cooling is predominately caused by SEC and that the experimental SEC rate coefficients of both molecular ions studied are of the order of $10^7 - 10^{-6}\,\mathrm{cm}^3/\mathrm{s}$, about an order magnitude larger than the rates predicted by MQDT or R-matrix calculations. The absolute SEC rate coefficients were obtained using a rate equation model based on the DR and SEC processes, whereas the SEC were restricted to transitions with $\Delta v = 1$. Based on the experimentally known absolute DR rate coefficients the modeled time evolutions of the vibrational populations were fitted to the experimental data varying the absolute SEC rate coefficients as free parameters.

The molecular ions LiH^+ and $^4\mathrm{HeH}^+$ recombine with slow electrons via the non-crossing mode process. The final state population in the DR proceeding by such processes was of specific interest in this work. The experimental results are summarized in the following list:

- The LiH^+ molecular ion was investigated experimentally for the first time. The DR of a LiH^+ ion beam with low kinetic energy electrons was studied. A measurement of the DR rate coefficient yielded an absolute value of the order of $10^{-7}\,\mathrm{cm}^3/\mathrm{s}$. Additionally, the final fragment state population was studied by measuring the spectra of field ionized Li Rydberg atoms from the DR. An exact assignment of atomic states to the spectra was not possible due to the complexity of the field ionization process. However, the results indicate a predominant population of the very high Rydberg states with $n = 10 - 12$, which are among the highest energetically possible final states.

- Experimental studies of the DR of a vibrationally cold $^4\mathrm{HeH}^+$ ion beam with electrons at collision energies around the threshold of a new final fragment state (i.e. $\mathrm{He}(1s^2)$ + $\mathrm{H}(n = 3)$) were concentrated on the population of that state. A branching ratio of ≈ 0.7 into that final state was found for collision energies above the threshold. It could be shown that the accessibility of that new final fragment state causes an increased DR rate around the threshold energy.

- The predominant population of the highest energetically accessible final state in the DR of LiH^+ and $^4\mathrm{HeH}^+$ indicates a common trend for molecular recombination via the non-crossing mode.

7.2 Perspectives

Based on the presented results and the recent technical progress at the TSR and the DR imaging system a variety of open questions might be approached. Three basic improvements concerning the study of DR are presently in preparation, a new electron target[86], a faster two-dimensional imaging system ($\approx$ 950 frames/s) and a new three-dimensional imaging system[128]. Several interesting physical questions are itemized and discussed below.

- Is it possible to cool the rotational degree of freedom of H_2^+ (D_2^+) by SEC?
  Using the new electron target SEC could cool an H_2^+ ion beam to a temperature of the order of the transversal electron temperature ($kT_\perp \approx 1\,\mathrm{meV}$), i.e. the ion beam would be ro-vibrationally cold.
  The rotational cooling could be observed by adjusting the electron-ion collision energy slightly below the threshold energy for the accessibility to the next higher fragment state (i.e. H($3l$) + H($1s$)) from the vibrational ground state. Thus, only rotationally excited ions can access that DR channel. The disappearance of that channel from a RFI spectra would prove the rotational cooling. Monte-Carlo simulations of such experiments taking into account the detector efficiency at short fragment distances ($\approx$ 1 mm) have been made and show the feasibility.

- Can SEC be studied at other homonuclear diatomic molecular ions, such as O_2^+ or N_2^+?
  For the required observation of the vibrational cooling it might be difficult to use CEI as it was done for molecular hydrogen. Presently, the CEI technique is not yet sufficiently enough developed to determine the exact internuclear separation of many-electron molecular ions prior to the electron stripping, which is essential for the CEI technique to work as a method to probe vibrational populations. These problems were studied by L. Knoll[54] for the molecular ions LiH^+ , $^4HeH^+$ and CH^+ and some further tests are needed.

- What are the dominant vibrational transitions in SEC?
  The preparation of an H_2^+ ion beam in a defined vibrational state prior to injection into the TSR and the relaxation of that state could answer this question. A possible procedure to prepare an H_2^+ ion beam in such a defined initial vibrational state could be as follows. Recently, the construction of a 22-pole ion trap has been started[129], which allows for preparing a vibrationally cold H_2^+ ion beam. The development of new lasers with short wavelength (UV) could be used to apply the **STI**mulated **R**aman **A**diabatic **P**assage (STIRAP)[130] technique which allows for a coherent population transfer to a defined excited vibrational state. A feasibility study of this procedures needs to be done in a first step. The preparation of an ion beam in such a well defined excited vibrational state is very complex. Hence, it is reasonable to prepare an ion beam with an initial vibrational population distribution different from that produced in the ion source using for instance

ion-atom collisions. It is a strong hint that $\Delta v = 1$ transitions in SECs are dominant if the measured vibrational cooling of such an ion beam can be reproduced by the modeled (i.e. only $\Delta v = 1$ transitions) time evolutions based the measured SEC rate coefficients presented in this work.

- How fast is the actual vibrational cooling of a LiH^+ ion beam and is a cooling due to electron-ion interactions competitive with radiative processes?
  The actual vibrational population distribution in the presented DR rate coefficient measurements is not known. The population was assumed to be Boltzmann distributed which should be verified in further experiments. Even though the analysis of CEI data from LiH^+ is problematic the CEI technique can be used to monitor the vibrational population over storage times of up to at least 10 s. The influence of the electron-ion interaction on the vibrational population could be studied similar to SEC with the H_2^+ and D_2^+ ion beams.
- Is it possible to study the collision energy dependence of the branching ratios in the DR of $^4\mathrm{HeH}^+$?
  Using the new electron target together with the present electron cooler ion beam dragging effects could be reduced. In addition, the development of a faster imaging system is in preparation which allows for the acquisition of higher fragment rates. Hence, a scan over a larger collision energy region with sufficiently high statistics would be possible.

The presented experimental results on the DR and SEC of H_2^+ and D_2^+ and the DR of $^4\mathrm{HeH}^+$ and LiH^+ have the potential for giving new inside into the chemistry of the primordial gas in the Early Universe and lead to a better understanding of the physics of inelastic collisions and recombination between electrons and molecular ions.

Appendix

A Diatomic molecular ions

In this section the Born-Oppenheimer approximation will be briefly introduced and the calculation of ro-vibrational wavefunctions for diatomic molecules discussed.

A.1 The Born-Oppenheimer approximation

The forces on the electrons and nuclei in a molecule are of the same order of magnitude, whereas the masses are rather different. The velocity of the nuclei is therefore slow compared to the velocity of the electrons and the motion of electrons and nuclei can be considered to be independent. This separate treatment of the electron and nuclei motion is commonly known as the Born-Oppenheimer approximation. A more formal derivation of that separation will be presented here. The full molecular Hamiltonian can be written as:

$$\begin{aligned}\mathbf{H}(r,R) &= \sum_i \frac{\hat{p}_i^2}{2m_e} + \sum_{j>i} \frac{e^2}{|r_i - r_j|} + \sum_i \frac{\hat{P}_i^2}{2M} + \sum_{j>i} \frac{Z_i Z_j e^2}{|R_i - R_j|} - \sum_{ij} \frac{Z_j e^2}{|r_i - R_j|} & \text{(A.1)}\\ &\equiv \mathbf{T}_e + \mathbf{V}_e + \mathbf{T}_N + \mathbf{V}_N + \mathbf{V}_{e,N}, & \text{(A.2)}\end{aligned}$$

where $\{r, \hat{p}\}$ refers to the electronic coordinates and momenta and the $\{R, \hat{P}\}$ to the nuclear coordinates and momenta. Z_i and M_i are the charge and mass of the nucleus i and m_e is the electron mass. The notations in Eq. A.2 describe the operators for the electron kinetic energy ($\mathbf{T}_e$), the electron-electron potential energy ($\mathbf{V}_e$), the nuclear kinetic energy ($\mathbf{T}_N$), the nuclear-nuclear potential energy ($\mathbf{V}_N$) and the electron-nuclear potential energy ($\mathbf{V}_{e,N}$). The time independent Schrödinger equation has the form:

$$\mathbf{H}(r,R)\,|\,\Psi(r,R)\,\rangle = E\,|\,\Psi(r,R)\,\rangle\,, \tag{A.3}$$

where $|\,\Psi(r,R)\,\rangle$ is the energy eigenfunction in the full coordinate space; i.e. nuclear and electronic coordinates. This wavefunction can be written as

$$|\,\Psi(r,R)\,\rangle = |\,\psi(r;R)\,\rangle\,|\,\chi(R)\,\rangle\,, \tag{A.4}$$

where $|\,\psi(r;R)\,\rangle$ is the electronic part of the total wavefunction for a given nuclear wavefunction $|\,\chi(R)\,\rangle$. The electronic potential energy $E(R)$ at a fixed value of R is

$$\mathbf{H}_e(r,R)\,|\,\psi(r;R)\,\rangle = E(R)\,|\,\psi(r;R)\,\rangle\,, \tag{A.5}$$

with

$$\mathbf{H}_e(r,R) = \mathbf{T}_e + \mathbf{V}_e + \mathbf{V}_{eN}. \tag{A.6}$$

Substituting $|\,\Psi(r,R)\,\rangle = |\,\psi(r;R)\,\rangle\,|\,\chi(R)\,\rangle$ back into the time independent Schrödinger equation (Eq. A.3) and using Eq. A.5 one obtains:

$$\begin{aligned}\mathbf{H}(r,R)\,|\,\psi(r;R)\,\rangle\,|\,\chi(R)\,\rangle = E(R)\,|\,\psi(r;R)\,\rangle\,|\,\chi(R)\,\rangle \quad &+\\ V_N(R)\,|\,\psi(r;R)\,\rangle\,|\,\chi(R)\,\rangle \quad &+\\ T_N\,|\,\psi(r;R)\,\rangle\,|\,\chi(R)\,\rangle \quad &,\end{aligned} \tag{A.7}$$

where $V_N(R)$ and T_N are the energy eigenvalues of the nuclear-nuclear potential energy operator $\mathbf{V}_N$ and nuclear kinetic energy operator $\mathbf{T}_N$, respectively. The nuclear kinetic energy operator acts on both wavefunctions $|\,\psi(r;R)\,\rangle$ and $|\,\chi(R)\,\rangle$:

$$\begin{aligned}&\mathbf{T}_N\,|\,\psi(r;R)\,\rangle\,|\,\chi(R)\,\rangle =\\ &-\frac{\hbar^2}{2\mu}\left\{|\,\chi(R)\,\rangle\,\frac{\partial^2\,|\,\psi(r;R)\,\rangle}{\partial R^2} + 2\frac{\partial\,|\,\psi(r;R)\,\rangle}{\partial R}\frac{\partial\,|\,\chi(R)\,\rangle}{\partial R} + |\,\psi(r;R)\,\rangle\,\frac{\partial^2\,|\,\chi(R)\,\rangle}{\partial R^2}\right\},\end{aligned} \tag{A.8}$$

with the reduced mass μ of the molecule.
Within the Born-Oppenheimer approximation the terms including derivatives of the electronic wavefunction with respect to the nuclear coordinates are neglected since the size of these terms goes approximately as the mass ratio of electrons to nuclei. The nuclear kinetic energy operator $\mathbf{T}_N$ does therefore not act on the electronic wavefunction $|\,\psi(r;R)\,\rangle$ and the full Hamiltonian for the nuclear motion has the form

$$\mathbf{H}\,|\,\chi(R)\,\rangle = \{\underbrace{E(R) + V_N(R)}_{V(R)} + T_N\}\,|\,\chi(R)\,\rangle\,, \tag{A.9}$$

with the potential energy $V(R)$.

A.2 Ro-vibrational wavefunctions for diatomic molecular ions

In this part a simple expression for the Schrödinger equation of diatomic molecules is presented within the Born-Oppenheimer approximation, allowing the calculation of ro-vibrational wavefunctions. As been shown in the previous section the potential energy of the nuclei and electrons is expressed by $V(R)$. With the internuclear distance R and the angles ϕ and θ, defined by the orientation of the internuclear distance relative to the laboratory coordinate system, the nuclear kinetic energy operator ($\mathbf{T}_N$), expressed in spherical coordinates, is given by [131]

$$\mathbf{T}_N(R,\theta,\phi) = -\frac{\hbar^2}{2\mu}\frac{1}{R^2}\frac{\partial}{\partial R}R^2\frac{\partial}{\partial R} - \frac{\hbar^2}{2\mu R^2}\left[\frac{1}{\sin\theta}\frac{\partial}{\partial\theta}\left(\sin\theta\frac{\partial}{\partial\theta}\right) + \frac{1}{\sin^2\theta}\frac{\partial^2}{\partial\phi^2}\right], \tag{A.10}$$

where

$$\mu = \frac{m_1 m_2}{m_1 + m_2}, \tag{A.11}$$

is the reduced mass of the diatomic molecule. The nuclear angular momentum $\mathbf{J}$ expressed in spherical coordinates has the form [32]:

$$\mathbf{J}^2 = -\hbar^2 \left[\frac{1}{\sin\theta} \frac{\partial}{\partial\theta} \left(\sin\theta \frac{\partial}{\partial\theta} \right) + \frac{1}{\sin^2\theta} \frac{\partial^2}{\partial\phi^2} \right] . \tag{A.12}$$

The nuclear kinetic energy operator $\mathbf{T}_N$ can therefore be written as a sum of operators describing the vibrational ($\mathbf{T}_N^v(R)$) and the rotational ($\mathbf{T}_N^J(R,\theta,\phi)$) motion,

$$\mathbf{T}_N = \underbrace{-\frac{\hbar^2}{2\mu} \frac{1}{R^2} \frac{\partial}{\partial R} R^2 \frac{\partial}{\partial R}}_{\mathbf{T}_N^v(R)} + \underbrace{\frac{\mathbf{J^2}}{2\mu R^2}}_{\mathbf{T}_N^J(R,\theta,\phi)} . \tag{A.13}$$

The molecular ions studied in this thesis are all in an electronic state where the projection of the total electronic orbital angular momentum on the internuclear axis vanishes. The effective potential energy curve $V(R)'$ can be found in literature and the wanted ro-vibrational wavefunctions $|\,\chi_{vJ}(R)\,\rangle$ can be obtained by solving the one-dimensional Schrödinger equation:

$$\left[-\frac{\hbar^2}{2\mu} \left(\frac{d^2}{dR^2} - \frac{J(J+1)}{R^2} \right) + V(R)' - E_{vJ} \right] |\,\chi_{vJ}(R)\,\rangle = 0, \tag{A.14}$$

where J denotes the rotational quantum number. The nuclear wavefunctions and energy levels needed in the framework of this thesis where calculated using either a very convenient numerical technique proposed by Cooney *et al.* [132] or a more sophisticated program package called *Level7.0* [63].

The total energy of a diatomic molecule in a ro-vibrational state $|\,vJ\,\rangle$ relative to the minimum potential energy $V(R_0)'$ is

$$\begin{aligned} E_{vJ} &= E_v + E_J && \text{(A.15)} \\ &= E_v + \frac{\hbar^2}{2\mu R_0^2} J(J+1) && \text{(A.16)} \\ &= E_v + BJ(J+1), && \text{(A.17)} \end{aligned}$$

where B is the *rotational constant* and R_0 the equilibrium distance of the molecule.

B Dissociation energies and rotational constants for H_2^+, HD^+ and D_2^+

Dissociation energies and rotational constants are presented for the different isotopomers of the molecular hydrogen ion. All calculations were performed using the program *Level7.0* [63]. This program calculates the ro-vibrational energy levels and wavefunctions as well as the ro-vibrational state specific rotational constants for diatomic molecules. As an input to the program the the ground electronic potential curve from Sharp [5] has been used.

B.1 Rotational constants for H_2^+, HD^+ and D_2^+

The rotational constants $B_{v,J}$ for the lower ro-vibrational states are presented in Tab. B.1.

	H_2^+		HD^+		D_2^+	
	cm^{-1}	meV	cm^{-1}	meV	cm^{-1}	meV
$B_{0,0}$	29.18	3.62	21.97	2.72	14.72	1.83
$B_{1,0}$	27.64	3.42	20.97	2.60	14.17	1.76
$B_{2,0}$	26.15	3.24	20.00	2.48	13.64	1.69
$B_{3,0}$	24.68	3.06	19.03	2.36	13.11	1.63
$B_{4,0}$	23.29	2.89	18.10	2.24	12.59	1.56

Table B.1: *Rotational constants $B_{v,J}$ for the lower ro-vibrational states of H_2^+, HD^+ and D_2^+.*

B.2 Dissociation energies for H_2^+, HD^+ and D_2^+

The dissociation energies for the different isotopomers of the hydrogen molecule are presented in Tab. B.2. The differences in the dissociation energies are due to the reduced masses of H_2^+, HD^+ and D_2^+.

The computed dissociation energies for HD^+ by Esry and Sadeghpour [28] and Balint-Kurti *et al.* [133] using more elaborated methods show a systematic shift of $\sim 1.5\,\text{meV}$ towards smaller dissociation energies and a difference of $\sim 0.1\,\%$ in the level spacings of the lower vibrational states.

v	H_2^+		HD^+		D_2^+	
	cm^{-1}	eV	cm^{-1}	eV	cm^{-1}	eV
0	-21376	-2.650	-21529	-2.669	-21710	-2.692
1	-19186	-2.379	-19616	-2.432	-2013	-2.496
2	-17123	-2.123	-17800	-2.207	-18622	-2.309
3	-15186	-1.883	-16079	-1.993	-17173	-2.129
4	-13370	-1.658	-14452	-1.792	-15789	-1.958
5	-11667	-1.447	-12910	-1.601	-14467	-1.794
6	-10084	-1.250	-11455	-1.420	-13198	-1.636
7	-8601	-1.066	-10090	-1.251	-11987	-1.486
8	-7237	-0.897	-8798	-1.091	-10846	-1.345
9	-5955	-0.738	-7602	-0.942	-9750	-1.209
10	-4792	-0.594	-6465	-0.802	-8709	-1.078
11	-3771	-0.467	-5402	-0.670	-7733	-0.959
12	-2890	-0.358	-4444	-0.551	-6789	-0.842
13	-2148	-0.266	-3588	-0.445	-5892	-0.730
14	-1541	-0.191	-2840	-0.352	-5061	-0.628

Table B.2: *Dissociation energies for the lower vibrational levels of* H_2^+, HD^+ *and* D_2^+, *calculated using* Level7.0 [63].

C Spectroscopic data for the lithium hydrides LiH$^+$ and LiH

C.1 Vibrational level spacing of LiH$^+$

Comparison between different calculated vibrational level spacings. For the calculation with *Level7.0* [63] the adiabatic ground electronic potential curve of LiH$^+$ from Berriche *et al.* [51] has been used.

	Ref. [63]		Ref. [51]		Ref. [134]	
v	$E_v - E_{v-1}$		$E_v - E_{v-1}$		$E_v - E_{v-1}$	
	cm^{-1}	meV	cm^{-1}	meV	cm^{-1}	meV
1	357.3	44.30	357.43	44.32	335	41.5
2	265.5	32.92	265.61	32.93	245	30.4
3	173.0	21.45	172.96	21.45	152	18.8
4	92.4	11.45	92.20	11.43		
5	37.6	4.66	37.45	4.64		
6	9.3	1.15	9.22	1.14		

Table C.1: *LiH$^+$ electronic ground state vibrational level spacings.*

C.2 Rotational constants

The rotational constants of LiH$^+$ in the electronic ground state where calculated using the program *Level7.0* [63].

	cm^{-1}	meV
$B_{0,0}$	3.78	0.469
$B_{1,0}$	3.23	0.400
$B_{2,0}$	2.62	0.325
$B_{3,0}$	1.92	0.238

Table C.2: *Calculated rotational constants $B_{v,J}$ for the lower ro-vibrational states of LiH$^+$.*

C.3 Radiative transition probabilities

The transition probability for a spontaneous emission from an initial state $|\, i\,\rangle$ to a final states $|\, f\,\rangle$ can be expressed by the Einstein A_{if} coefficient and the radiative lifetime of the initial state

$|\, i\,\rangle$ time is given by

$$\tau_i^{-1} = \sum_f A_{if}. \tag{C.1}$$

The Einstein coefficient is given by (in units of s^{-1})

$$A_{if} = 3.137 \times 10^{-7}\, |\mu_{if}|^2\, \nu_{if}^3, \tag{C.2}$$

where μ is the dipole moment matrix element in Debyes [1] and ν_{if} the transition frequency in reciprocal centimeters.

The dipole moment matrix element for a ro-vibrational transition is defined as

$$\mu_{vJ,v'J'} = \int_0^\infty \Psi^*_{v'J'}(R)\, \mu(R)\, \Psi_{vJ}(R)\, dR, \tag{C.3}$$

where R is the internuclear separation, Ψ_{vJ} and $\Psi_{v'J'}$ are the normalized initial and final wavefunctions, respectively, and $\mu(R)$ the dipole moment function.
The total Einstein coefficient for transitions in a $\mathrm{X}^1\Sigma^+ \longrightarrow \mathrm{X}^1\Sigma^+$ system can be simply obtained by (in units of s^{-1}) [135]

$$A_{vJ} = \frac{1}{2J+1}\left\{ J \sum_{v'=0}^{v} A_{vJ,v'J-1} + (J+1) \sum_{\substack{v'=0\\ v=1}} A_{vJ,v'J+1} \right\}. \tag{C.4}$$

The total Einstein coefficients for LiH$^+$ in a initial vibrational state $v = 1$ and $J = 0 - 3$ can be computed using the transition frequencies obtained from calculations using the program *Level7.0* (see Tab. C.1) and the rotational excitation energies. The rotational excitation energy is expressed by

$$E_J = B_{v,J} J(J+1), \tag{C.5}$$

where $B_{v,J}$ denotes the rotational constants from Tab. C.2 and J the rotational state.
To estimate the lifetime of the different vibrational states v it is sufficient to calculate the Einstein coefficient for the rotational ground state, as can be seen from Tab. C.3. The calculated lifetimes are summarized in Tab. C.4.
Radiative transition with $\Delta v > 1$ have a dipole moment matrix element which is small compared to that for transition with $\Delta v = 1$ [55] and were therefore neglected in the presented calculation.

---

[1] 1 Debyes = 0.3935 a.u. = 3.336 $\times 10^{-30}$ Coulomb m

$\mid v, J\,\rangle$	$\mid v', J'\,\rangle$	$\lvert\mu_{v,J;v',J'}\rvert^2$ Debyes^2	$\nu_{v,J;v',J'}$ cm^{-1}	$A_{v,J}$ s^{-1}
$\mid 1,0\,\rangle$	$\mid 0,1\,\rangle$	0.0322	349.7	0.432
$\mid 1,1\,\rangle$	$\mid 0,0\,\rangle$	0.0296	363.8	
	$\mid 0,2\,\rangle$	0.0338	341.1	0.430
$\mid 1,2\,\rangle$	$\mid 0,1\,\rangle$	0.0284	369.0	
	$\mid 0,3\,\rangle$	0.0355	331.3	0.419
$\mid 1,3\,\rangle$	$\mid 0,2\,\rangle$	0.0274	373.4	
	$\mid 0,4\,\rangle$	0.0376	320.5	0.408

Table C.3: *Total Einstein coefficients for the possible ro-vibrational transitions from $v = 1$ and $J = 0 - 3$. The dipole moment matrix elements were computed by Gianturco* et al. [55].

$\mid v, J\,\rangle$	$\mid v', J'\,\rangle$	$\lvert\mu_{v,J;v',J'}\rvert^2$ Debyes^2	$A_{v,J}$ s^{-1}	$\tau_{v,J}$ s
$\mid 1,0\,\rangle$	$\mid 0,1\,\rangle$	0.0322	0.432	2.3
$\mid 2,0\,\rangle$	$\mid 1,1\,\rangle$	0.0797	0.435	2.3
$\mid 3,0\,\rangle$	$\mid 2,1\,\rangle$	0.1400	0.207	4.8
$\mid 4,0\,\rangle$	$\mid 3,1\,\rangle$	0.2050	0.045	22.4
$\mid 5,0\,\rangle$	$\mid 4,1\,\rangle$	0.2520	0.004	277.9

Table C.4: *Total Einstein coefficients and radiative lifetimes for the vibrational states $v = 1 - 4$ and $J = 0$. The dipole moment matrix elements were calculated by Gianturco* et al. [55].

C.4 The neutral lithium hydride LiH

The neutral lithium hydride LiH has been studied theoretically and a short summary of these publications will be given here. Ab initio calculations of adiabatic and diabatic potential energy curves for nearly all states below the ionic limit (i.e., Li($2s, 2p, 3s, 3p, 3d, 4s$ and $4p$) + H($1s$)) have been performed by Boutalib and Gadéa [50]. Yiannopoulou *et al.* [136] extented their calculations to higher excited electronic states (i.e., Li($3s, 3p, 3d, 4s, 4p, 4d, 4f, 5s$ and $5p$) + H($1s$)). Additional calculations concerning the LiH molecule have been done by Gemperle and Gadéa [137], Gadéa and Boutalib [138] and a general overview about spectroscopy and structure of the lithium hydride diatomic molecules and ions has been published by Stwalley and Zemke [53].

D Rotational lifetimes for ^{4}HeH$^+$ in its vibrational ground state

In this part calculated dissociation energies and rotational constants for the lower vibrational states are presented. All calculations were performed using the program *Level7.0* [63]. The $X^1\Sigma^+$ ground state for ^{4}HeH$^+$ has been calculated by Kolos and Peek [139].

D.1 Dissociation energies and rotational constants for ^{4}HeH$^+$

In Tab. D.1 the calculated dissociation energies for the vibrational states of ^{4}HeH$^+$ up to the vibrational state $v = 10$ are shown.

v	cm^{-1}	eV
0	-14881.7	-1.845
1	-11969.6	-1.484
2	-9365.1	-1.161
3	-7068.8	-0.876
4	-5085.7	-0.631
5	-3424.0	-0.425
6	-2094.8	-0.260
7	-1108.6	-0.137
8	-467.3	-0.058
9	-140.3	-0.017
10	-25.4	-0.003

Table D.1: *Dissociation energies for the vibrational states of* ^{4}*HeH*$^+$, *calculated using* Level7.0 [63].

The rotational constants of ^{4}HeH$^+$ were calculated using *Level7.0* [63] and are shown in Tab. D.2. Matsushima *et al.* [140] measured the rotational constants for the lower rotational states J and different istotopomers of the molecule HeH$^+$. Their results are in a reasonable agreement with the calculated values from Tab. D.2.

D.2 Radiative lifetimes for (v, J) levels of ^{4}HeH$^+$

^{4}HeH$^+$ cools within several ms in its vibrational ground state because of its short radiative lifetimes, see Tab. D.3. To estimate the time for rotational cooling of ^{4}HeH$^+$ in its vibrational ground state into thermal equilibrium at T=300 K, radiative lifetimes for rotational transitions need to be known. In Tab. D.3 only the lifetime for $J = 5$ is presented. The radiative lifetimes of rotational states smaller than $J = 5$ can be estimated assuming the integral over the dipole

	cm^{-1}	meV
$B_{0,0}$	33.55	4.16
$B_{1,0}$	30.83	3.82
$B_{2,0}$	28.10	3.48
$B_{3,0}$	25.30	3.14
$B_{4,0}$	22.40	2.78

Table D.2: *Rotational constants* $B_{v,J}$ *for the lower ro-vibrational states of* ^{4}*HeH*$^+$.

	radiative lifetimes (ms)				
v	$J = 0$	$J = 5$	$J = 10$	$J = 15$	$J = 20$
0	∞	110.70	4.24	4.67	2.47
1	1.09	2.32	2.50	2.43	2.22
2	0.64	2.39	1.70	2.00	2.48
3	0.52	1.14	1.45	2.04	
4	0.48	1.08	1.47	2.51	
5	0.50	1.16	1.73		
6	0.58	1.40	2.48		
7	0.77	1.99	5.50		
8	1.27	3.84			
9	2.98	14.64			
10	10.82				
11	119.64				

Table D.3: *Radiative lifetimes calculated for various* (v, J) *levels of the* $X^{`}\Sigma^+$ *state of* ^{4}*HeH*$^+$, *from Ref.* [49].

moment function $\mu(R)$ in Eq. C.3 to be independent of J.

$$\int_0^\infty \Psi^*_{vJ}(R)\,\mu(R)\,\Psi_{v'J'}(R)\,dR \approx const \quad \text{for } J \leq 5 \tag{D.1}$$

The Hamiltonian in the Schrödinger equation (Eq. A.14) for the ^{4}HeH$^+$ molecule has a *centrifugal distortion* term V_{cd}. This term is given by

$$V_{cd} = \frac{\hbar^2}{2\mu}\frac{J(J+1)}{R^2} \tag{D.2}$$

where μ is the reduced mass of the ^{4}HeH$^+$ molecule and R the internuclear distance of the two atoms. This term is small for lower rotational states and the nuclear wavefunctions $\Psi_{vJ}(R)$ become, in first order, independent of the rotational state J. Therefore the function in Eq. D.1

can be assumed to be approximately constant.
The transition probability for a pure rotational transition where $\Delta J = -1$ is given by the Einstein coefficient (see Eq. C.2) weighted with the appropriate *Hönl-London* factor [141]

$$\begin{aligned} A_{v,J;v,J-1} &= 3.137 \times 10^{-7} \frac{J}{2J+1} \left|\mu_{v,J;v,J-1}\right|^2 \nu^3_{v,J;v,J-1} && \text{(D.3)} \\ &= \tau_{v,J;v,J-1} && \text{(D.4)} \end{aligned}$$

The dipole moment matrix element $\mu_{0,5;0,4}$ in Eq. D.3 can be calculated using the lifetime $\tau_{0,5;0,4}$ from Tab. D.3. The lifetime of the lower rotational states can then simply be obtained from Eq. D.4 using that matrix element and the transition frequencies $\nu_{v,J;v,J-1}$. The calculated values are presented in Tab. D.4.

J	$\tau_{0,J;0,J-1}$ ms
1	18870
2	1966
3	544
4	221
5	110

Table D.4: *Calculated rotational lifetimes for ^{4}HeH$^+$ in the ground vibrational state.*

The exact values for the lifetimes are probably higher than the numbers given in Tab. D.4 since the position of the nuclear wavefunctions moves slightly to smaller R for lower J and the dipole moment function $\mu(R) \sim R$ [49]. Therefore, the integral in Eq. D.1 becomes smaller and the lifetime longer.

E Technique for solving coupled differential equations

In this part it will be explained how coupled differential equations can be solved. In a first step a simple example for such a set of n rate equations, similar to the equations solved in this thesis, will be given and in a next step a general solution will be presented.

Assuming a system with n different states and two processes changing the number of particles N in a certain state i, which are for instance dissociative recombination (DR) and super-elastic collisions (SEC). These processes have rate coefficients α (DR) and β (SEC) and the rate equation for a state i has the form:

$$\frac{d}{dt} N_i(t) \quad = \quad -C\,(\alpha_i + \beta_i)\, N_i(t) + C\,\beta_{i+1}\, N_{i+1}(t), \qquad \text{(E.1)}$$

with $\beta_0 = \beta_n = 0$. The constant factor C transforms the rate coefficients into inverse lifetimes τ for both processes and is defined as the product between the electron density n_e and the ratio $\eta = 0.027$ between the electron cooler length and the ring circumference.

These differential equations may be written in a matrix form as

$$\frac{d}{dt}\mathbf{N}(t) = \mathcal{A}\ \mathbf{N}(t), \qquad \text{(E.2)}$$

with $\mathbf{N}^{\top}(t) = (N_n(t), \cdots, N_1(t))$ and the matrix $\mathcal{A}$ composed of the rate coefficients:

$$\mathcal{A} = C \begin{pmatrix} -(\alpha_n + \beta_n) & 0 & \cdots & \cdots & \cdots & \cdots & 0 \\ \beta_n & -(\alpha_{n-1} + \beta_{n-1}) & 0 & \cdots & \cdots & \cdots & 0 \\ \vdots & \vdots & \ddots & \ddots & \ddots & \vdots & \vdots \\ 0 & \cdots & \cdots\ 0 & \beta_3 & & -(\alpha_2 + \beta_2) & 0 \\ 0 & \cdots & \cdots & \cdots & 0 & \beta_2 & -\alpha_1 \end{pmatrix}. \qquad \text{(E.3)}$$

The equations can be uncoupled by determine the eigenvectors and eigenvalues of the matrix $\mathcal{A}$. Assuming there are no degenerate eigenvalues of $\mathcal{A}$ (which can be expected for the problem faced here), the solution for $\mathbf{N}(t)$ is given by

$$\mathbf{N}(t) \ = \ \mathcal{S}\ \exp(\mathbf{T} \cdot t)\ \mathcal{S}^{-1}\ \mathbf{N^0}, \qquad \text{(E.4)}$$

where $\mathcal{S}$ is the matrix of the eigenvectors and $\mathbf{T}$ is a vector with the eigenvalues τ_i of $\mathcal{A}$. The vector $\mathbf{N^0}$ is defined by the initial amount of particles in each state i and the expression $\exp(\mathbf{T}\cdot t)$ describes a diagonal matrix,

$$\exp(\mathbf{T} \cdot t) = \begin{pmatrix} e^{\tau_n t} & 0 & \cdots & \cdots & 0 \\ \vdots & \vdots & \ddots & \vdots & \vdots \\ 0 & \cdots & \cdots & 0 & e^{\tau_1 t} \end{pmatrix}. \qquad \text{(E.5)}$$

F Quantum defects and radiative lifetimes of Li

F.1 Quantum defect of a nlj state in Li

The term energies T_{nlj} for alkali atoms can be represented by the empirical formula

$$T_{nlj} = \frac{Ry_{alk}}{(n - \delta_{nlj})^2}, \tag{F.1}$$

where Ry_{alk} denotes the Rydberg constant for alkali atoms ($Ry_{alk} = 109728.64\,\mathrm{cm}^{-1}$ for ^{7}Li). The quantities δ_{nlj} are called quantum defects which for an nlj state can be parameterized with a modified Rydberg-Ritz expression[142] and are given explicitly by

$$\delta_{nlj} = \delta_0 + \frac{\delta_2}{(n-\delta_0)^2} + \frac{\delta_4}{(n-\delta_0)^4} + \frac{\delta_6}{(n-\delta_0)^6} + \frac{\delta_8}{(n-\delta_0)^8}, \cdots. \tag{F.2}$$

The parameters $\delta_0, \delta_2, \cdots, \delta_\infty$ for ^{7}Li are given in Tab. F.1. The coefficients of higher order in Eq. F.2 are usually neglectable for high n states. As can be seen from Eq. F.2 the quantum defects are not only dependent on the orbital angular momentum and the magnetic quantum numbers l and m, respectively, but also on the principal quantum number n.

^{7}Li	δ_0	δ_2	δ_4	δ_6
$n\mathrm{s}_{1/2}$	0.399468	0.030233	-0.0028	0.0115
$n\mathrm{p}_{1/2,3/2}$	0.047263	-0.02613	0.0221	-0.0683
$n\mathrm{d}_{3/2,5/2}$	0.002129	-0.01491	0.1759	-0.8507
$n\mathrm{f}_{5/2,7/2}$	0.0003055(40)	-0.00126(5)		

Table F.1: *Quantum defect parameters for ^{7}Li, taken from Ref. [108].*

F.2 Energy levels for ^{7}Li

The term energies of atomic lithium can be calculated using Eq. F.1 and the quantum defect parameters from Tab. F.1. In Tab. F.2 the term energies for ^{7}Li in $n = 2 - 20$ and $l = 0 - 2$ are presented.

	Ionisation energy (eV)		
n	s	p	d
2	5.3917	3.5439	-
3	2.0186	1.5574	1.5119
4	1.5078	0.8704	0.8507
5	0.6432	0.5539	0.5445
6	0.4339	0.3834	0.3781
7	0.3123	0.2814	0.2778
8	0.2355	0.2151	0.2127
9	0.1839	0.1697	0.1680
10	0.1476	0.1373	0.1361
11	0.1211	0.1340	0.1125
12	0.1011	0.0952	0.0945
13	0.0857	0.0811	0.0805
14	0.0736	0.0699	0.0694
15	0.0638	0.0608	0.0605
16	0.0559	0.0535	0.0532
17	0.0494	0.0473	0.0471
18	0.0439	0.0422	0.0420
19	0.0393	0.0379	0.0377
20	0.0354	0.0342	0.0340

Table F.2: *Ionisation energies for* ^{7}*Li in different* n, l *states.*

F.3 Radiative lifetimes of Li Rydberg states

The lifetime of the Li Rydberg states calculated by Theodosiou [107] are summarized in Tab. F.3. The calculations included the blackbody radiation corresponding to 0 K and 720 K. The values for 300 K were obtained by a linear interpolation between the calculated values for 0 K and 720 K.

It should be mentioned that the typical time-of-flight of neutral DR fragments from the electron cooler to the dipole magnet is about 500 ns. This time is comparable to the radiative lifetime of Li atoms in a *s*- or *d*-state.

	0 K	**300 K**	720 K
	τ (ns)	τ **(ns)**	τ (ns)
8 *s*	403.3	**383.0**	354.6
9 *s*	574.8	**538.7**	488.3
10 *s*	783.4	**726.3**	646.4
11 *s*	1057.1	**966.5**	839.7
12 *s*	1369.5	**1239.2**	1056.7
8 *p*	1848.2	**1622.8**	1307.2
9 *p*	2509.5	**2154.0**	1656.2
10 *p*	3328.0	**2797.6**	2055.0
11 *p*	4310.1	**3565.9**	2523.9
12 *p*	5490.3	**4474.5**	3052.4
8 *d*	252.4	**247.7**	241.1
9 *d*	357.0	**348.2**	336.0
10 *d*	487.3	**472.5**	451.8
11 *d*	656.7	**632.9**	599.7
12 *d*	835.0	**800.6**	752.4

Table F.3: *Radiative lifetimes τ of Li Rydberg states in a Planck radiation field calculated by Theodosiou [107]. The lifetimes for 300 K were obtained by a linear interpolation between the values for 0 K and 720 K.*

References

[1] T.W. Hartquist and D.A. Williams, *The chemically controlled cosmos*, Cambridge University Press, Cambridge, 1995.

[2] D. Galli and F. Palla, *The chemistry of the early universe*, Astron. Astrophys. **335** (1998), 403 – 420.

[3] J.M. Peek, A.-R. Hashemi-Attar, C.L. Beckel, *Spontaneous emission lifetimes in the ground electronic states of* HD^+ *and* H_2^+, J. Chem. Phys. **71** (1979), no. 12, 5382 – 5383.

[4] C. Strömholm, J. Semaniak, S. Rosén, H. Danared, S. Datz, W. van der Zande, and M. Larsson, *Dissociative recombination and dissociative excitation of* $^4HeH^+$*: Absolute cross sections and mechanisms*, Phys. Rev. A **54** (1996), no. 4, 3086 – 3094.

[5] T.E. Sharp, *Potential-energy curves for molecular hydrogen and its ions*, Atomic data and Nuclear data tables **2** (1971), 119.

[6] S. L. Guberman, *The doubly excited autoionizing states of* H_2, J. Chem. Phys. **78** (1983), 1404 – 1413.

[7] D.R. Bates, *Dissociative recombination*, Phys. Rev. **78** (1950), 492 – 493.

[8] J.M. Bardsley and M.A. Biondi, *Dissociative recombination*, Adv. At. Mol. Phys. **6** (1970), 1 – 57.

[9] J.M. Bardsley, *Configuration interaction in the continuum states of molecules*, J. Phys. B **1** (1968), 349 – 364.

[10] ______, *The theory of dissociative recombination*, J. Phys. B **1** (1968), 365 – 380.

[11] A. Giusti, *A multichannel quantum defect approach to dissociative recombination*, J. Phys. B: Atom. Molec. Phys. **13** (1980), 3867 – 3894.

[12] A. Giusti-Suzor, J. N. Bardsley, and C. Derkits, *Dissociative recombination in low-energy e-*H_2^+ *collisions*, Phys. Rev. A **28** (1983), no. 2, 682 – 691.

[13] U. Fano, *Effects of configuration interaction on intensities and phase shifts*, Phys. Rev. **124** (1961), no. 6, 1866 – 1878.

[14] S. L. Guberman and A. Giusti-Suzor, *The generation of O(1S) from the dissociative recombination of* O_2^+, J. Chem. Phys. **95** (1991), 2601 – 1413.

[15] S. Krohn, M. Lange, M. Grieser, L. Knoll, H. Kreckel, J. Levin, R. Repnow, D. Schwalm, R. Wester, P. Witte, A. Wolf, and D. Zajfman, *Rate coefficients and final states for the dissociative recombination of* LiH^+, Phys. Rev. Lett. **86** (2001), no. 18, 4005 – 4008.

[16] M. Larsson, H. Danared, J.R. Mowat, P. Sigray, G. Sundström, L. Broström, A. Filevich, A. Källberg, S. Mannervik, K.G. Rensfelt, and S. Datz, *Direct high-energy neutral-channel dissociative recombination of cold* H_3^+ *in an ion storage ring*, Phys. Rev. Lett. **70** (1993), no. 4, 430 – 433.

[17] M.J. Jensen, H.B. Pedersen, C.P. Safvan, K. Seiersen, X. Urbain, and L.H. Andersen, *Dissociative recombination and excitation of* H_3^+, Phys. Rev. A **63** (2001), 052701.

[18] B. K. Sarpal, J. Tennyson, and L.A. Morgan, *Dissociative recombination without curve crossing: study of* HeH^+, J. Phys. B **25** (1994), 5943 – 5953.

[19] S.L. Guberman, *Dissociative recombination without curve crossing*, Phys. Rev. A **49** (1994), no. 6, R4277 – R4280.

[20] ______, *New mechanisms for dissociative recombination*, XIXth International Conference on the Physics of Electronic and Atomic Collisions, AIP Conf. Proc. No.360 (Whistler, Canada) (J.W. McConkey L.J. Dubé, J.B.A. Mitchell and C.E. Brion, eds.), AIP, New York, 1995, p. 307.

[21] M. Larsson, M. Carlson, H. Danared, L. Broström, S. Mannervik, and G. Sundström, *Vibrational cooling of* D_2^+ *in an ion storage ring as revealed by dissociative recombination*, J. Phys. B: At. Mol. Opt. Phys. **27** (1994), 1397 – 1406.

[22] W.J. van der Zande, J. Semaniak, V. Zengin, G. Sundström, S. Rosén, C. Strömholm, S. Datz, H. Danared, and M. Larsson, *Dissociative recombination of* H_2^+*: Product state information and very large cross sections of vibrationally excited* H_2^+, Phys. Rev. A **54** (1996), no. 6, 5010 – 5018.

[23] B. K. Sarpal and J. Tennyson, *Calculated vibrational excitation rates for electron -* H_2^+ *collisions*, Mon. Not. R. Astron. Soc. **263** (1993), 909 – 912.

[24] K. Nakashima, H. Takagi, and H. Nakamura, *Dissociative recombination of* H_2^+, HD^+, *and* D_2^+ *by collisions with slow electrons*, J. Chem. Phys. **86** (1987), no. 2, 726 – 737.

[25] T. Tanabe, H. Takagi, I. Katayama, K. Chida, Y. Arakaki, Y. Haruyama, M. Saito, I. Nomura, T. Honma, K. Noda, and K. Hosono, *Evidence of superelastic electron collisions from* H_2^+ *studied by dissociative recombination using an ultracold electron beam from a cooler ring*, Phys. Rev. Lett. **83** (1999), no. 11, 2163 – 2166.

[26] M. Saito, Y. Haruyama, T. Tanabe, I. Katayama, K. Chida, T. Watanabe, Y. Arakaki, I. Nomura, T. Honma, K. Noda, and K. Hosono, *Vibrational cooling of* H_2^+ *and* D_2^+ *in a storage ring studied by means of two-dimensional fragment imaging*, Phys. Rev. A **61** (2000), 062707.

[27] S. Krohn, Z. Amitay, A. Baer, M. Lange, L. Knoll, J. Levin, D. Schwalm, R. Wester, A. Wolf, and D. Zajfman, *Electron-induced vibrational deexcitation of* H_2^+, Phys. Rev. A **62** (2000), 032713.

[28] B.D. Esry and H.R. Sadeghpour, *Adiabatic formulation of heteronuclear hydrogen molecular ion*, Phys. Rev. A **60** (1999), no. 5, 3604 – 3616.

[29] M. Madsen and J.M. Peek, Atomic Data **2** (1971), 171.

[30] L. Wolniewicz and K. Dressler, *Adiabatic potential curves and nonadiabatic coupling functions for the first five excited* $^1\Sigma_g^+$ *states of the hydrogen molecule*, J. Chem. Phys. **100** (1994), no. 1, 444 – 451.

[31] D. Zajfman, Z. Amitay, M. Lange, U. Hechtfischer, L. Knoll, D. Schwalm, X. Urbain, R. Wester, and A. Wolf , *Curve crossing and branching ratios in the dissociative recombination of* HD^+, Phys. Rev. Lett. **79** (1997), no. 10, 1829 – 1832.

[32] B. H. Bransden and C. J. Joachain, *Physics of atoms and molecules*, Longman Group Limited, 1983.

[33] Z. Amitay, P. Forck, and D. Zajfman, *Rotational and vibrational lifetime of isotopically asymmetrized homonuclear diatomic molecular ions*, Phys. Rev. A **50** (1994), no. 3, 2304 – 2308.

[34] Z. Amitay, A. Baer, M. Dahan, J. Levin, Z. Vager, D. Zajfman, L. Knoll, M. Lange, D. Schwalm, R. Wester, and A. Wolf, *Dissociative recombination of vibrationally excited* HD^+*: State-selective experimental investigation*, Phys. Rev. A **60** (1999), no. 5, 3769 – 3785.

[35] P. Forck, M. Grieser, D. Habs, A. Lampert, R. Repnow, D. Schwalm, A. Wolf, and D. Zajfman, *Dissociative recombination of cold* HD^+ *at the Test Storage Ring*, Phys. Rev. Lett. **70** (1993), no. 4, 426 – 429.

[36] ______, *Molecular physics in a storage ring: dissociative recombination and excitation of cold HD$^+$*, Nucl. Instrum. Methods B **79** (1993), 273 – 275.

[37] C. Strömholm, I.F. Schneider, G. Sundström, L. Carata, H. Danared, S. Datz, O. Dulieu, A. Källberg, M. af Ugglas, X. Urbain, V. Zengin, A. Suzor-Weiner, and M. Larsson, *Absolute cross section for the dissociative recombination of HD$^+$: comparison of experiments and theory*, Phys. Rev. A **52** (1995), no. 6, R4320 – R4323.

[38] T. Tanabe, I. Katayama, H. Kamegaya, K. Chida, Y. Arakaki, T. Watanabe, M. Yoshizawa, M. Saito, Y. Haruyama, K. Hosono, K. Hatanaka, T. Honma, K. Noda, S. Ohtani, and H. Takagi, *Dissociative recombination of HD$^+$ with an ultracold electron beam in a cooler ring*, Phys. Rev. Lett. **75** (1995), no. 6, 1066 – 1069.

[39] D. Zajfman, Z. Amitay, C. Broude, P. Forck, B. Seidel, M. Grieser, D. Habs, D. Schwalm, and A. Wolf , *Measurement of branching ratios for the dissociative recombination of cold HD$^+$ using fragment imaging*, Phys. Rev. Lett. **75** (1995), no. 5, 814 – 817.

[40] Z. Amitay, A. Baer, M. Dahan, L. Knoll, M. Lange, J. Levin, I.F. Schneider, D. Schwalm, A. Suzor-Weiner, Z. Vager, R. Wester, A. Wolf, and D. Zajfman, *Dissociative recombination of HD$^+$ in selected vibrational quantum states*, Science **281** (1998), 75 – 78.

[41] M. Lange, J. Levin, G. Gwinner, U. Hechtfischer, L. Knoll, D. Schwalm, R. Wester, A. Wolf, X. Urbain, and D. Zajfman, *Threshold effects and ion-pair production in the dissociative recombination of HD$^+$*, Phys. Rev. Lett. **83** (1999), no. 24, 4979 – 4982.

[42] H.T. Schmidt, L. Vejby-Christensen, H.B. Pedersen, D. Kella, N. Bjerre, and L.H. Andersen, *Dissociative-recombination for vibrationally excited H$_2^+$ ions: the effect of laser photodissociation on the initial vibrational distribution*, J. Phys. B: At. Mol. Opt. Phys. **29** (1996), 2485 – 2496.

[43] L.H. Andersen, P.J. Johnson, D. Kella, H.B. Pedersen, and L. Vejby-Christensen, *Dissociative-recombination and excitation measurements with H$_2^+$ and HD$^+$*, Phys. Rev. A **555** (1997), no. 4, 2799 – 2808.

[44] J.A. Coxon and P.H. Hajigeorgiou, *Experimental Born-Oppenheimer potential for the $X^1\Sigma^+$ ground state of HeH$^+$: Comparison with the ab initio potential*, J. Mol. Spectrosc. **193** (1999), 306 – 318.

[45] A.E. Orel, K.C. Kulander, and T.N. Rescigno, *Effects of open inelastic channels in the resonant dissociative recombination of HeH$^+$*, Phys. Rev. Lett. **74** (1995), no. 24, 4807 – 4810.

[46] U. Hechtfischer, Z. Amitay, P. Forck, M. Lange, J. Linkemann, M Schmitt, U. Schramm, D. Schwalm, R. Wester, D. Zajfman, and A. Wolf, *Near-threshold photodissociation of cold CH^+ in a storage ring*, Phys. Rev. Lett. **80** (1998), no. 13, 2809 – 2812.

[47] U. Hechtfischer, *UV-Photodissoziation gespeicherter CH^+-Molekülionen*, Diplomarbeit, Universität Heidelberg, 1996.

[48] ———, *Photofragmentationsspektroskopie gespeicherter Molekülionen an der Dissoziationsschwelle*, Ph.D. thesis, Universität Heidelberg, 2000.

[49] S. Datz and M. Larsson, *Radiative lifetimes for all vibrational levels in the $X^1\Sigma^+$ state of HeH^+ and its relevance to dissociative recombination experiments in ion storage rings*, Physica Scripta **46** (1992), 343 – 347.

[50] A. Boutalib and F.X. Gadéa, *Ab initio adiabatic and diabatic potential-energy curves of the LiH molecule*, J. Chem Phys. **97** (1992), 1144 – 1156.

[51] H. Berriche and F.X. Gadéa, *Ab initio study of the LiH^+ molecules, electronic interaction analysis and LiH UV photoelectron spectrum*, Chem. Phys. **191** (1995), 119 – 131.

[52] H.R. Ihle and C.H. Wu, *Mass spectrometric determination of the ionization potential and dissociation energy of LiD*, J. Chem. Phys. **63** (1975), no. 4, 1605 – 1608.

[53] W.C. Stwalley and W.T. Zemke, *Spectroscopy and structure of the lithium hydride diatomic molecules and ions*, J. Phys. Chem. Ref. Data **22** (1993), no. 1, 87 – 112.

[54] L. Knoll, *Dissociation dynamics in Coulomb explosion imaging of diatomic molecules*, Ph.D. thesis, Universität Heidelberg, 2000.

[55] F.A. Gianturco, P.G. Giorgi, H. Berriche, and F.X. Gadéa, *Computed distributions of the rotovibrational transitions in LiH($\mathrm{X}^1\Sigma^+$) and LiH^+($\mathrm{X}^2\Sigma^+$)*, Astron. Astrophys. Suppl. Ser. **117** (1996), 377 – 392.

[56] A. Wolf, *Heavy-ion storage rings*, Atomic physics with heavy ions (H.F. Beyer and V.P. Shevelko, eds.), Springer, 1999.

[57] Z. Vager, R. Naaman, and E.P. Kanter, *Coulomb explosion imaging of small molecules*, Science **244** (1989), 426 – 431.

[58] D. Zajfman, G. Both, E. P. Kanter, and Z. Vager, *Multiple scattering of MeV atomic and molecular ions traversing ultrathin films*, Phys. Rev. A **41** (1990), no. 5, 2482 – 2488.

[59] D. Zajfman, T. Graber, E. P. Kanter, and Z. Vager, *Influence of multiple scattering on the Coulomb explosion imaging of fast molecules*, Phys. Rev. A **46** (1992), no. 1, 194 – 200.

[60] P. Sigmund, *Scaling laws governing the multiple scattering of diatomic molecules under Coulomb explosion*, Phys. Rev. A **46** (1992), 2596 – 2606.

[61] Z. Vager and D. S. Gemmell, *Polarization induced in a solid by the passage of fast charged particles*, Phys. Rev. Lett. **37** (1976), 1352.

[62] R. Wester, *Spatial structure of stored molecular ions by Coulomb explosion imaging*, Ph.D. thesis, Universität Heidelberg, 1999.

[63] R.J. LeRoy, *Level7.0, A computer program solving the radial Schrödinger equation for bound and quasibound levels*, University of Waterloo Chemical Physics Research Report No.CP642 (1996).

[64] Z. Amitay, D. Zajfman, P. Forck, U. Hechtfischer, B. Seidel, M. Grieser, D. Habs, R. Repnow, D. Schwalm, and A. Wolf, *Dissociative recombination of* CH^+*: Cross section and final states*, Phys. Rev. A **54** (1996), no. 5, 4032 – 4050.

[65] P.W. Atkins, *Physical Chemistry, 5th edition*, Oxford University Press, 1994.

[66] Sin-itiro Tomonaga (translated by T. Oka), *The story of spin*, The University of Chicago Press, 1997.

[67] M. Grieser, H. Deitinghoff, D. Habs, R. von Hahn, E. Jaeschke, C.-M. Kleffner, V. Kössler, S. Papureanu, R. Repnow, M.-H. Rhee, D. Schwalm, and A. Schempp, *Upgrading of the Heidelberg accelerator facility with a new high current injector*, Nucl. Instr. and Meth. A **328** (1993), 160 – 163.

[68] R. von Hahn, M. Grieser, D. Habs, E. Jaeschke, C.-M. Kleffner, J. Liebmann, S. Papureanu, R. Repnow, D. Schwalm, and M. Stampfer, *Development of seven-gap resonators for the Heidelberg high current injector*, Nucl. Instr. and Meth. A **328** (1993), 270 – 274.

[69] R. Keller, P. Spadtke, and F. Nohmayer, Proc. Int. Ion Engineering Congr., Kyoto, Japan (1983), 25.

[70] M. Madert, *Entwicklung und Aufbau des RFQ-Beschleunigers für den Heidelberger Hochstrominjektor*, Ph.D. thesis, Universität Heidelberg, 1998.

[71] M. Lange, *Competition between reaction channels in collisions of stored* HD^+ *ions with electrons*, Dissertation, Universität Heidelberg, 2001.

[72] D. Habs, W. Baumann, J. Berger, P. Blatt, A. Faulstich, P. Krause, G. Kilgus, R. Neumann, W. Petrich, R. Stokstad, D. Schwalm, E. Szmola, K. Welti, A. Wolf, S. Zwickler, E. Jaeschke, D. Krämer, G. Bisoffi, M. Blum, A. Friedrich, C. Geyer, M. Grieser, H. W. Heyng, B. Holzer, R. Ihde, M. Jung, K. Matl, W. Ott, B. Povh, R. Repnow, M. Steck,

E. Steffens, D. Dutta, T. Kühl, D. Marx, S. Schröder, M. Gerhard, R. Grieser, G. Huber, R. Klein, M. Krieg, N. Schmidt, R. Schuch, J. F. Babb, L. Spruch, and A. Noda, *First Experiments with the Heidelberg Test Storage Ring TSR*, Nucl. Instrum. Methods B **43** (1989), 390.

[73] F. Albrecht, *Langsame Extraktion am Heidelberger Schwerionenspeicherring TSR*, Dissertation, Universität Heidelberg, 1996.

[74] F. Albrecht, M. Beutelspacher, M. Grieser, R. von Hahn, L. Knoll, R. Repnow, D. Schwalm, K. Tetzlaff, and R. Wester, *Slow Extraction at the Heidelberg Heavy Ion Storage Ring TSR*, Fifth European Particle Accelerator Conference (Barcelona), vol. 3, 1996, p. 2459.

[75] R. Wester, F. Albrecht, M. Grieser, L. Knoll, R. Repnow, D. Schwalm, A. Wolf, A. Baer, J. Levin, Z. Vager, and D. Zajfman, *Coulomb explosion imaging at the heavy ion storage ring TSR*, Nucl. Instrum. Methods A **413** (1998), 379 – 396.

[76] G. Wissler, *Untersuchungen zur langsamen Extraktion am Heidelberger Schwerionenspeicherring TSR*, Diplomarbeit, Universität Heidelberg, 1998.

[77] G. Both, E. P. Kanter, Z. Vager, B. J. Zabransky, and D. Zajfman, *Ultrathin foils for Coulomb explosion experiments*, Rev. Sci. Instrum. **58** (1987), 424.

[78] V. Kh. Liechtenstein, T. M. Ivkova, E. D. Olshanski, I. Feigenbaum, R. DiNardo, and M. Doebeli, *Preparation and evaluation of thin diamond-like carbon foils for heavy-ion tandem accelerators and time-of-flight spectrometers*, Nucl. Instrum. Methods A **397** (1997), 140.

[79] J. Levin, L. Knoll, M. Scheffel, D. Schwalm, R. Wester, A. Wolf, A. Baer, Z. Vager, D. Zajfman, and V. Kh. Liechtenstein, *Application of ultrathin diamond-like-carbon targets to Coulomb explosion imaging*, Nucl. Instrum. Methods B **168** (2000), 268 – 275.

[80] L. Lammich, *Coulomb Explosion Imaging von dreiatomaren Molekülen am Beispiel von* CH_2^+, Diplomarbeit, Universität Heidelberg, 2001.

[81] A. Baer, *The angular distribution of quasilinear molecules measured by Coulomb explosion imaging*, Ph.D. thesis, Weizmann Institute of Science, 2000.

[82] M. Scheffel, *Untersuchung orts- und zeitauflösender Mehrteilchen-Detektoren mit Laserpulsen*, Diplomarbeit, Universität Heidelberg, 1999.

[83] M. Steck, G. Bisoffi, M. Blum, A. Friedrich, C. Geyer, M. Grieser, B. Holzer, E.Jaeschke, M. Jung, D. Krämer, K. Matl, W. Ott, and R. Repnow, *Electron cooling of heavy ions*, Nucl. Instrum. Methods A **287** (1990), 324 – 327.

[84] G. Barking, *Entwurf, Aufbau und Test einer neuen Elektronenkanone für den Elektronenkühler am TSR*, Diplomarbeit, Universität Heidelberg, 1996.

[85] S. Pastuszka, U. Schramm, M. Grieser, C. Broude, R. Grimm, D. Habs, J. Kenntner, H.-J. Miesner, T. Schüßler, D. Schwalm, and A. Wolf, *Electron cooling and recombination experiments with an adiabatically expanded electron beam*, Nucl. Instrum. Methods A **369** (1996), 11 – 22.

[86] M. Schmitt, *Erzeugung energiescharfer Elektronenstrahlen*, Ph.D. thesis, Universität Heidelberg, 2000.

[87] G. Kilgus, N.R. Badnell, D. Habs, A. Müller, D. Schwalm, and A. Wolf, *High-resolution measurement of dielectronic recombination of lithiumlike* Cu^{26+}, Phys. Rev. A **46** (1992), no. 9, 5730 – 5740.

[88] M. Beutelsbacher, *Systematische Untersuchungen zur Elektronenkühlung am Heidelberger Schwerionenspeicherring TSR*, Ph.D. thesis, Universität Heidelberg, 2000.

[89] B. Hochadel, F. Albrecht, M. Grieser, D. Habs, D. Schwalm, E. Szmola, and A. Wolf, *A residual-gas ionization beam profile monitor for the Heidelberg Test Storage Ring TSR*, Nucl. Instrum. Methods A **343** (1994), 401 – 414.

[90] P. Forck, *Dissoziative Rekombination und dissoziative Anregung intern kalter Molekülionen*, Dissertation, Universität Heidelberg, 1994.

[91] U. Schramm, T. Schüssler, D. Habs, D. Schwalm, and A. Wolf, *Laser-induced recombination studies with the adiabatically expanded electron beam of the Heidelberg TSR*, Hyperfine Int. **99** (1996), 309 – 316.

[92] H. Poth, *Electron cooling: Theory, experiment, application*, Phys. Rep. **196** (1990), 135 – 297.

[93] A. Wolf, *Elektronenkühlung für niederenergetische Antiprotonen*, Ph.D. thesis, Universität Karlsruhe (T.H.), 1985.

[94] M. Lange, *Verzweigungsverhältnisse und Winkelabhängigkeit der dissoziativen Rekombination von* HD^+*-Ionen*, Diplomarbeit, Universität Heidelberg, 1997.

[95] B. Holzer, *Präzisionsmessungen an den Magneten des TSR-Speicherrings (TSR)*, Diplomarbeit, Universität Heidelberg, 1988.

[96] J. Linkemann, *Elektronenstoßionisation und Rekombination hochgeladener Natrium-ähnlicher Ionen*, Ph.D. thesis, Universität Stuttgart, 1995.

[97] L. Lammich, private communication.

[98] F. von Busch and G.H. Dunn, *Photodissociation of H_2^+ and D_2^+: Experiment*, Phys. Rev. A **5** (1972), no. 4, 1726 – 1743.

[99] I. Schneider *et al.*, private communication.

[100] J.R. Mowat, *Cross section measurements at sub-thermal energies*, Dissociative Recombination: Theory, Experiment and Applications III (D. Schwalm D. Zajfman, J.B.A. Mitchell and B.R. Lowe, eds.), World Scientific, Singapore, 1996, pp. 226 – 229.

[101] H. Takagi, *Theoretical study of dissociative processes in HD^+/H_2^+-e collisions with the energy up to 10 eV*, Dissociative Recombination: Theory, Experiment and Applications III (D. Schwalm D. Zajfman, J.B.A. Mitchell and B.R. Lowe, eds.), World Scientific, Singapore, 1996, pp. 174 – 183.

[102] K. Rai Dastidar and T.K. Rai Dastidar, *Dissociative recombination of H_2^+, HD^+ and D_2^+ molecular ions*, J. Phys. Soc. Japan **46** (1979), no. 4, 1288 – 1294.

[103] A. Lampert, A. Wolf, D. Habs, J. Kenntner, G. Kilgus, M.S. Pindzola, N.R. Badnell, and D. Schwalm, *High-resolution measurement of the dielectronic recombination of fluorinelike selenium ions*, Phys. Rev. A **53** (1996), no. 3, 1413 – 1423.

[104] C. J. Latimer, K. F. Dunn, N. Kouchi, M. A. McDonald, V. Srigengan, and J. Geddes, *A dissociative photoionization study of the autoionization lifetime of the lowest $^1\Sigma_u$ superexcited state in hydrogen and deuterium*, J. Phys. B: At. Mol. Opt. Phys. **26** (1993), L595 – L600.

[105] J. Geddes, K.F. Dunn, N. Kouchi, M.A. McDonald, V. Srigengan, and C.J. Latimer, *Isotope effects in the autoionization of superexcited $^1\Sigma_u^+(Q_1)$ states in hydrogen*, J. Phys. B: At. Mol. Opt. Phys. **27** (1994), 2961 – 2970.

[106] P.C. Stancil, S. Lepp, and A. Dalgarno, *The lithium chemistry of the early universe*, Astrophys. J. **458** (1996), 401 – 406.

[107] C.E. Theodosiou, *Lifetimes of alkali-metal-atom Rydberg states*, Phys. Rev. A **30** (1984), no. 6, 2881 – 2909.

[108] T. Gallagher, *Rydberg atoms*, Cambridge University Press, Cambridge, 1994.

[109] J.H.M. Neijzen and A. Dönszelmann, *Diabatic field ionization of highly excited indium atoms*, J. Phys. B: At. Mol. Opt. Phys. **15** (1982), L87 – L91.

[110] W.E. Cooke and T.F. Gallagher, *Dependence of Rydberg-state field-ionization thresholds on $|m_l|$*, Phys. Rev. A **17** (1978), no. 3, 1226 – 1228.

[111] E. Luc-Koenig and A. Bachelier, *Systematic theoretical study of the Stark spectrum of atomic hydrogen I: density of continuum states*, J. Phys. B: At. Mol. Opt. Phys. **13** (1980), 1743 – 1767.

[112] H.J. Silverstone, *Perturbation theory of the Stark effect in hydrogen to arbitrarily high order*, Phys. Rev. A **18** (1978), no. 5, 1853 – 1864.

[113] D.S. Bailey, J.R. Hiskes, and A.C. Riviere, *Electric field ionization probabilities for the hydrogen atom*, Nuclear Fusion **5** (1965), 41 – 46.

[114] M.G. Littman, M.K. Kash, and D. Kleppner, *Field-ionization processes in excited atoms*, Phys. Rev. Lett. **41** (1978), no. 2, 103 – 107.

[115] M.L. Zimmerman, M.G. Littman, M.M. Kash, and D. Kleppner, *Stark structure of the Rydberg states alkali-metal atoms*, Phys. Rev. A **20** (1979), no. 6, 2251 – 2275.

[116] J.R. Rubbmark, M.M. Kash, M.G. Littman, and D. Kleppner, *Dynamical effects at avoided level crossings: A study of the Landau-Zener effect using Rydberg atoms*, Phys. Rev. A **23** (1981), no. 6, 3107 – 3117.

[117] R.F. Stebbings, and F.B. Dunnings, *Rydberg states of atoms and molecules*, Cambridge University Press, Cambridge, 1983.

[118] L.I. Schiff and H. Snyder, Phys. Rev. A **55** (1939), 59.

[119] T. Tanabe, I. Katayama, N. Inoue, K. Chida, Y. Arakaki, T. Watanabe, M. Yoshizawa, M. Saito, Y. Haruyama, K. Hosono, T. Honma, K. Noda, S. Ohtani, and H. Takagi, *Origin of the low-energy component and isotope effect on dissociative recombination of* HeH^+ *and* HeD^+, Phys. Rev. A **49** (1994), no. 3, R1531 – R1534.

[120] J. Semaniak, S. Rosén, G. Sundström, C. Strömholm, S. Datz, H. Danared, M. af Ugglas, M. Larsson, W.J. van der Zande, Z. Amitay, U. Hechtfischer, M. Grieser, R. Repnow, M. Schmidt, D. Schwalm, R. Wester, A. Wolf, and D. Zajfman, *Product-state distributions in the dissociative recombination of* $^3HeD^+$ *and* $^4HeD^+$, Phys. Rev. A **54** (1996), no. 6, R4617 – R4620.

[121] G. Sundström, S. Datz, J.R. Mowat, S. Mannervik, L. Broström, M. Carlson, H. Danared, and M. Larsson, *Direct dissociative recombination of* HeH^+, Phys. Rev. A **50** (1994), no. 4, R2806 – R2809.

[122] T. Tanabe, I. Katayama, N. Inoue, K. Chida, Y. Arakaki, T. Watanabe, Y. Yoshizawa, S. Ohtani, and K. Noda, *Dissociative Recombination of* HeH^+ *at large center-of-mass energies*, Phys. Rev. Lett. **70** (1993), no. 4, 422 – 425.

[123] Å. Larson and A.E. Orel, *Dissociative recombination of HeH$^+$: Product distributions and ion-pair formation*, Phys. Rev. A **59** (1999), no. 5, 3601 – 3608.

[124] T. Tanabe, I. Katayama, S. Ono, K. Chida, T. Watanabe, Y. Arakaki, Y. Haruyama, M. Saito, T. Odagiri, K. Hosono, K. Noda, T. Honma, and H. Takagi, *Dissociative recombination of HeH$^+$ isotopes with an ultra-cold electron beam from a superconducting electron cooler in a storage ring*, J. Phys. B: At. Mol. Opt. Phys. **31** (1998), L297 – L303.

[125] J.R. Mowat, H. Danared, G. Sundström, M. Carlson, L.H. Andersen, L. Veijby-Christensen, M. af Ugglas, and M. Larsson, *Direct dissociative recombination of HeH$^+$*, Phys. Rev. Lett. **74** (1995), no. 1, 50 – 53.

[126] A. Al-Khalili, H. Danared, M. Larsson, A. Le Padellec, R. Peverall, S. Rosén, J. Semaniak, M. af Ugglas, L. Viktor, and W. van der Zande, *Dissociative recombination of ^{3}HeH$^+$: comparison of spectra obtained with 100, 10 and 1 meV temperature electron beams*, Hyperfine Int. **114** (1998), 281 – 287.

[127] A. Orel *et al.*, private communication.

[128] D. Strasser, *in preparation*, Ph.D. thesis, Weizmann Institute of Science.

[129] H. Kreckel, PhD thesis in preparation, Universität Heidelberg.

[130] K. Bergmann, H. Theuer, and B.W. Shore, *Coherent population transfer among quantum states of atomes and molecules*, Rev. Mod. Phys. **70** (1998), no. 3, 1003 – 1025.

[131] H. Lefebvre-Brion and R.W. Field, *Perturbations in the Spectra of Diatomic Molecules*, Academic Press, Orlando, 1986.

[132] P. J. Cooney, E. P. Kanter, Z. Vager, *Convenient numerical technique for solving the one-dimensional Schrödinger equation for bound states*, Am. J. Phys. **49** (1981), 76.

[133] G.G. Balint-Kurti, R.E. Moss, I.A. Sadler, and M. Shapiro, *Calculations of vibration-rotation energy levels of HD$^+$*, Phys. Rev. A **41** (1990), no. 9, 4913 – 4917.

[134] O. Grabandt, H.J. Bakker, C.A. de Langes, and I. Paidarova, *The temperature dependence of the LiH photoelectron spectrum*, Chem Phys. Letters **189** (1992), no. 2, 291 – 296.

[135] G. Herzberg, *Molecular spectra and molecular structure: I. Spectra of diatomic molecules*, Van Nostrand Reinhold, 1950.

[136] A. Yiannopoulou, G.-H. Jeung, S.J. Park, H.S. Lee, and Y.S. Lee, *Undulations of the potential-energy curves for the highly excited electronic states in the diatomic molecules related to the atomic orbital undulations*, Phys. Rev. A **59** (1999), no. 2, 1178 – 1186.

[137] F. Gemperle and F.X. Gadéa, *Beyond Born-Oppenheimer spectroscopic study for the C state of LiH*, J. Chem Phys. **110** (1999), no. 23, 11197 – 11205.

[138] F.X. Gadéa and A. Boutalib, *Computation and assignment of radial couplings using accurate diabatic data for the LiH molecule*, J. Phys. B:At. Mol. Opt. Phys. **26** (1993), 61 – 74.

[139] W. Kolos and J.M. Peek, *New ab initio potential curve and quasibound states of* $^4HeH^+$, Chem. Phys. **12** (1976), 381 – 386.

[140] F. Matsushima, T. Oka, and K. Takagi, *Observation of the rotational spectra of* $^4HeH^+$, $^4HeD^+$, $^3HeH^+$, *and* $^3HeD^+$, Phys. Rev. Lett. **78** (1997), no. 9, 1664 – 1666.

[141] H. Hönl and F. London, *Über die Intensitäten der Bandenlinien*, Z. Physik **33** (1925), 803 – 809.

[142] C.-J. Lorenzen and K. Niemax, *Quantum defects of the* $n^2P_{1/2,3/2}$ *levels in* ^{39}KI *and* ^{85}RbI, Physica Scripta **27** (1983), 300 – 305.

Danksagung

Die vorliegende Arbeit hätten nicht ohne die vielfältige Unterstützung und Hilfe vieler Personen entstehen können. An dieser Stelle möchte ich mich dafür und die angenehme Arbeitsatmosphäre, sowohl am MPI als auch am Weizmann Institut, während der letzten drei Jahre gleichermaßen bedanken.
Mein herzlicher Dank gilt Andreas Wolf, Daniel Zajfman und Dirk Schwalm für ihre Betreuung. Besonderer Dank gilt Andreas Wolf, der mit seiner freundliche und hilfsbereiten Art bei manchen Problemen geholfen hat. Insbesondere möchte ich mich bei ihm für das gründliche Durchlesen dieser Arbeit und die zum besseren Verständnis sicherlich hilfreichen Korrekturen bedanken. Daniel Zajfman möchte ich für die vielen Diskussionen, insbesondere während der Zeit am Weizmann Institut und den diversen Strahlzeiten, und seine freundschaftliche Art danken. Mein herzlicher Dank gilt auch Dirk Schwalm, zum einem für die Möglichkeit die hier diskutierten Experimente in seiner Gruppe ausführen zu können und zum anderen für die vielen Anregungen, die er mir in diversen Gesprächen gegeben hat. Herrn Frank Arnold danke ich sehr für seine Bereitschaft, das Zweitgutachten dieser Arbeit zu übernehmen. Die Vorbereitung und insbesondere die Durchführung der verschiedenen Messungen am TSR wäre ohne die Zusammenarbeit mit meinen Kollegen nicht denkbar gewesen. Ganz besonders möchte ich mich an dieser Stelle bei den noch "aktiven" Mitgliedern der Molekülgruppe, Holger Kreckel, Lutz Lammich, Daniel Strasser, Peter Witte und Michael Lange bedanken. Aber auch den "ehemaligen", Adam Baer, Yasha Levin, Roland Wester, Ulrich Hechtfischer und Marcus Scheffel sei hier gedankt. Allen Gruppenmitgliedern, sowohl am MPI als auch am Weizmann Institut, danke ich für das sehr gute Arbeitsklima und die vielen leckeren Geburtstagskuchen. Die Experimente am TSR wären nicht ohne die umfangreiche Unterstützung vieler Personen möglich gewesen. Ganz besonders möchte ich mich bei Manfred Grieser und Kurt Horn bedanken, ohne die kein Strahl den Weg zum Detektor gefunden hätte. Auch möchte ich allen Technikern und Operateuren unter der Leitung von Herrn Repnow und Robert von Hahn danken für ihr Engagement und Geduld bei der Erzeugung der unterschiedlichen Molekülstrahlen. Herrn Vogt von der MPI Bibliothek sei an dieser Stelle für das wundersame Beschaffen einiger Veröffentlichungen gedankt, von denen ich kaum mehr als den Namen das Autors wußte.

Schließlich gilt mein besonderer Dank meinen Eltern, meiner Schwester und Caroline, die mich während der letzten drei Jahre mit ihrem Interesse und insbesondere einer Menge Geduld unterstützt haben.